Probing microRNA Activity *in vitro* and inside Cells Using Single Molecule Microscopy

by

Sethuramasundaram Pitchiaya

A dissertation submitted in partial fulfillment
of the requirements for the degree of
Doctor of Philosophy
(Chemistry)
in The University of Michigan
2012

Doctoral Committee:

Professor Nils G. Walter, Chair

Professor Carol A. Fierke

Professor Anna K. Mapp

Associate Professor Kristen J. Verhey

2012

To Mom, Dad, Eashwar and Visha

Acknowledgements

I feel honored and privileged to have Dr. Nils Walter as my advisor. His guidance and insights have been instrumental in shaping and expanding my ken. I have always been amazed and inspired by his patience, sagacity and supportive nature among others. Thank you for being an exceptional mentor and hats off to you Nils!!

I would like to especially thank all the members of the Walter lab, past and present, for creating a great environment to do research. I wish you all the very best in your scholarly pursuits and other endeavors. I am also very grateful to my co-workers, collaborators and other thesis committee members for all their help, advice and support.

I thank my friends for their company and for making Ann Arbor another home away from home. They have piqued my scientific curiosity, tickled my funny bone and have given me a helping hand during times of distress. You guys are the best!!

I feel truly blessed to have a wonderful family. They have stood by my side through all facets of life. Their support, encouragement and unconditional love have made me strive harder and explore higher grounds. Without their hard work and sacrifice I wouldn't have reached the position that I am currently in. Mom, Dad, Eashwar and Visha, this thesis is dedicated to you.

Table of Contents

List of Figures

List of Appendices

Abstract

Probing microRNA Activity *in vitro* and inside Cells Using Single Molecule Microscopy

By

Sethuramasundaram Pitchiaya

Chair: Nils G. Walter

Non-coding RNAs (ncRNAs) outnumber their protein-coding counterparts, yet their presumably diverse functions are still ill-understood. This thesis reports the development of two novel single-molecule methods to probe the activity of microRNAs (miRNAs), a class of regulatory ncRNAs, in pursuit of their elusive mechanism of action.

miRNAs associate with components of the RNA induced silencing complex (RISC) to assemble on messenger RNA (mRNA) targets and regulate protein expression in higher eukaryotes. Here, I describe a method for the intracellular single molecule, high resolution localization and counting (iSHiRLoC) of miRNAs. Microinjected, singly fluorophore labeled, functional miRNAs were tracked within diffusing particles, a majority of which contained single miRNA molecules. Observed mobility and mRNA dependent assembly changes support a model of multiple target turnovers by miRNAs, revealing the dynamic nature of an important gene regulatory pathway and paving the way towards its single molecule systems biology.

miRNAs accumulate in processing bodies (PBs), sub-cellular foci enriched in RNA processing enzymes, as a cause or consequence of post-transcriptional gene silencing. Despite numerous observations, quantitative analysis of miRNA localization within PBs has been lacking. iSHiRLoC of miRNAs revealed that only a small fraction of miRNAs localized to PBs and majority of PBs contained only one or two fluorophore labeled miRNA molecules. Moreover, miRNAs resided in PBs only for a few hundred milliseconds, suggesting the preponderance of unstable interactions. Heterogeneous distribution of miRNAs in PBs coupled with the observation that miRNAs docked onto PBs either stably or transiently suggests an underlying diversity in the composition of these two complexes.

Some mRNAs contain multiple binding sites for a specific miRNA, presumably for enhanced regulation. To quantify the binding stoichiometry between miRNAs and such mRNAs, I developed a single-molecule *in vitro* assay based on the step-wise photobleaching of fluorescent probes. Our data, in two different cell extracts, showed that a majority of mRNAs are either bound by zero or a single miRNA under conditions of maximal repression. Computational mRNA structure analysis predicted low accessibility of miRNA binding sites. Together, these data suggest that a higher number of binding sites corresponds to a higher probability of binding, not multiple occupancy.

Chapter 1

Surveying the RNA World: One Molecule at a Time

1.1 Introduction

Following its isolation in 1869 by Friedrich Miescher (1), research on “nuclein”, now known as DNA, took a meteoric leap. Seminal work, including the elucidation of its composition and double-helix structure, the Avery-Mcleod-Mcarthy transformation experiment, and the Hershey-Chase hereditary experiments, soon followed and culminated in the central dogma of biology as we know it; DNA, not protein, is the carrier of genetic information, which is transferred to functional proteins by way of RNA. Since then, the line separating science fiction from science has been blurred, largely owing to the advent of molecular cloning and genetic engineering. The possibility that ‘life’ can be created or tweaked within a test-tube (2-4), as exemplified by the cloning of a mammal - ‘dolly’ the sheep – from adult somatic cells by Wilmut and coworkers (3), has made the word ‘DNA’ commonplace in every household.

The insight that DNA is the storehouse of (inheritable) genetic information holds the promise of explaining disease susceptibility and progression, genetic variation and human complexity. Initially proteins, built from a more diverse set of 20 amino acids as compared to the 4 building blocks of nucleic acids, are complementarily deemed the workhouse of the cell that catalyzes all biochemical reactions. RNA was merely considered an information messenger involved in the transcription of the genetic information stored in DNA into proteins. The discovery of independently functioning catalytic RNAs or ribozymes (5) shattered this misconception and thus heralded an era wherein RNA takes more of a ‘center stage’. The emergence of ribozymes also gave rise to the hypothesis of a

primordial RNA world, according to which RNA was the original genetic material that could both self-replicate and catalyze the enzymatic reactions necessary to sustain life.

1.2 Non-coding RNAs at the Forefront of Biology

Despite the fact that the human genome is 30-fold larger than that of *C. elegans*, the number of protein coding genes in humans is only ~1.2-fold larger than in the worm (6, 7). In addition, sequencing of the human genome has shown that only ~1.5% of the entire human genetic material codes for proteins (6, 7). These observations lead to an interesting and important question; what criteria distinguish organisms that are as complex as humans from relatively simpler ones such as the worm? The answer lies in the other 98.5% of the human genome that does not encode proteins and previously was perceived as 'junk'. The complexity of organisms, i.e. a qualitative measure of the intricacy involved in organismal development, body plan organization and cellular diversity, is now known to be related to the amount of non-protein coding sequences within the genome (**Fig. 1.1**). Furthermore, the fundamental reason behind complexity is not the mere presence of such sequences, but also their transcription into RNA. Current estimates place the fraction of the mammalian genome that is transcribed at ~30–60% (6-8). Considering that only ~1.2% of the entire genome is protein coding, non-coding RNAs (ncRNAs) are predicted to be one of the most abundant molecular species within a eukaryotic cell. As they do not code for proteins, these ncRNAs were initially thought of as 'transcriptional noise', i.e. a basal amount of erroneous transcription accompanying the fruitful synthesis of protein-coding messenger RNAs (mRNAs), but at least some of them were later found to exhibit profound regulatory roles (6-8), thus forming the basis for cellular homeostasis rather than constituting an aberration.

ncRNAs are a diverse group of RNA molecules, both structurally and functionally. These RNAs also vary in size from several kilo bases (kb), as in the case of long ncRNAs (9) and intronic regions of precursor messenger RNAs (pre-

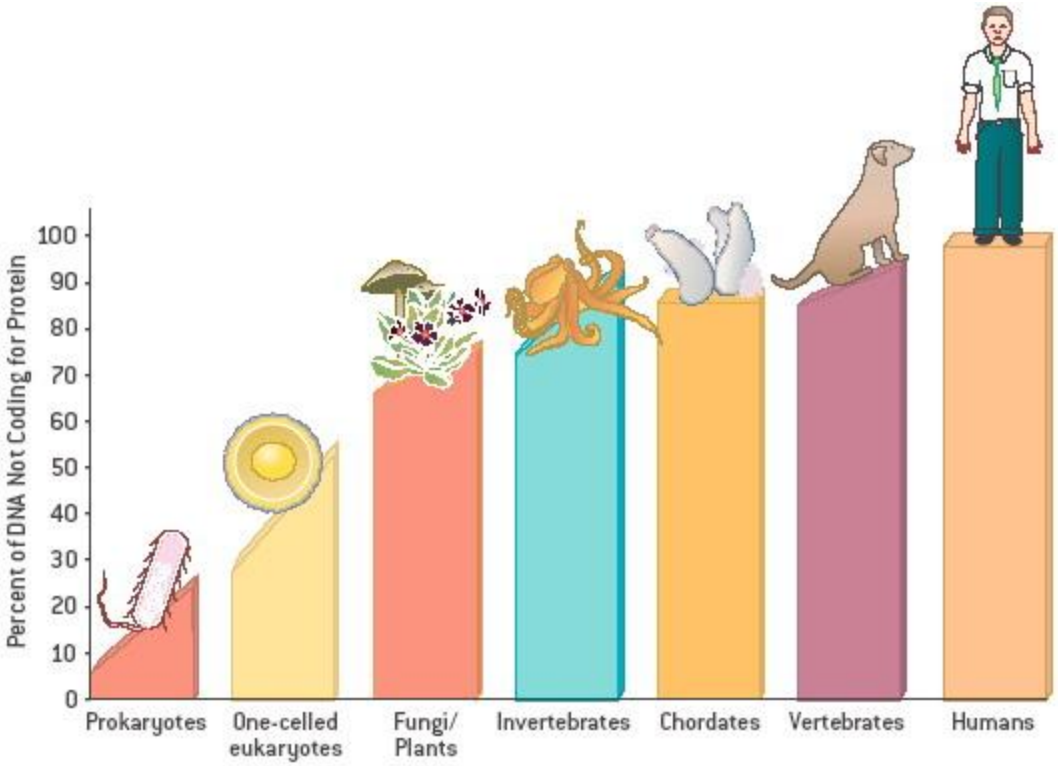

Figure 1.1. Percent of genomic DNA not coding for proteins plotted against the complexity of organisms. Reprinted from reference (10) with permission from Scientific American, Inc.

mRNAs), to small silencing or microRNAs (siRNAs or miRNAs) that are ~22 nucleotides (nt) in length (11, 12). Moreover, they perform a combination of structural, catalytic and regulatory roles, and are widely distributed through all life forms. Structural ncRNAs include small nuclear RNAs (snRNA), small nucleolar RNAs (snoRNAs), transfer RNAs (tRNAs) and ribosomal RNAs (rRNA). These RNAs act as structural scaffolds for the organization of large RNA protein complexes, often referred to as ribonucleoproteins (RNPs), which as a complex elicit a biological function. For instance, snRNAs associate with several proteins to form the spliceosome (13), which catalyzes the removal of non-coding intronic regions from a pre-mRNA in eukaryotes, resulting in a mature mRNA bearing the appropriate information for protein synthesis. Based on similar principles of ordered assembly, the ribosome also forms a functional RNP from greater than 50 proteins and 3 or 4 rRNAs, which with assistance from tRNAs (molecules that are enzymatically 'charged' with amino acids and decode the genetic information of mRNAs) synthesize cellular proteins (14). As the active sites of both of these machineries contain RNA, they have often been described as ribozymes that require protein cofactors (13-15) .

The first functional ribozymes were discovered in the 1980's by Tom Cech and Sidney Altman, who were investigating the functions of *Tetrahymena* group I introns (5) and bacterial RNase P (16), respectively, for which they shared the 1989 Nobel Prize in Chemistry. Group I introns catalyze their own excision from between protein coding regions in pre-mRNAs, whereas RNase P mediates the 5`trimming of precursor-tRNAs to produce the functional tRNA. To date, several other self-cleaving catalytic RNAs have been identified, initially in sub-viral particles and now also more broadly through all life forms (17, 18). The hairpin, hammerhead, hepatitis delta virus (HDV) and the *Neurospora crassa* Varkud satellite (VS) ribozymes are the four classical examples of such self-cleaving catalytic RNAs (19). These ribozymes undergo a series of conformational changes (20-22) and eventually dock into a catalytically active structure to cleave their own backbone. In sub-viral particles, self-cleavage causes the monomerization of longer multi-copy genomes synthesized via rolling circle

replication (19). More recently, a variant of the HDV ribozyme termed the CPEB3 ribozyme, has been discovered in the human transcriptome (23, 24). This and similar discoveries suggest that evolutionary remnants or precursors of viral ribozymes appear to be buried within the mammalian genome.

In contrast to other self-cleaving RNA enzymes, the *glmS* ribozyme, which is present in the 5`untranslated region (UTR) of genes responsible for glucoseamine-6-phosphate (GlcN6P) biosynthesis in bacteria, catalyzes self-cleavage of its backbone only when bound by GlcN6P as a cofactor (25, 26). Under conditions of elevated GlcN6P concentration, the ribozyme binds this cofactor and catalyzes its own cleavage, resulting in the destabilization of the GlcN6P synthesis genes (26). In this fashion, the ribozyme senses cellular GlcN6P abundance and creates a negative feedback loop to regulate GlcN6P biosynthetic enzymes. Such metabolite-binding ncRNAs, which regulate the activity of mRNAs in which they are embedded, are called riboswitches (27). The vast majority of riboswitches, however, lack catalytic activity and mediate gene regulation by inhibiting transcription or translation of their host mRNA (27). The S-adenosyl methionine (SAM), thiamin pyrophosphate (TPP), pre-queuosine-1 (PreQ1) and glycine riboswitches are a few examples of gene regulatory bacterial ncRNAs (27).

Conceptionally related to riboswitches, 5` and 3`UTRs of mRNAs as well as intronic regions in pre-mRNAs can similarly be classified as *cis*-acting regulatory ncRNAs (7). These ncRNAs, unlike riboswitches, are present only in eukaryotes and act in *cis* as receivers of *trans*-acting signals, by forming secondary structures that recruit regulatory proteins. In addition to serving regulatory roles, introns can have significant sequence diversity and can mediate alternative splicing, recombination of exons in multiple ways, to increase protein diversity. Interestingly, the length of UTRs (28) and the fraction of alternatively spliced genes (29) scale with the developmental complexity in animals, indicative of the greater sophistication of mRNA regulation in higher organisms.

Long ncRNAs (lncRNAs) (9), also known as long-intervening ncRNAs (lincRNAs), are regulatory RNA molecules greater than 500 nt in length. These ncRNAs can function as *cis*- or *trans*-acting elements to elicit epigenetic regulation by recruiting chromatin remodeling factors at appropriate genomic foci. Classical examples of lncRNAs include *XIST* (30) and *HOTAIR* (31), **the former** silences one of the two X chromosomes in all eutherian females to achieve proper X-linked gene dosage, whereas the latter is proposed to promote cancer metastasis.

In summary, we are in the midst of a fundamental revolution in our understanding of cellular gene expression. Small (<500 nucleotides) regulatory ncRNAs have only over the past 10 years been recognized as abundant key elements of the cellular machinery responsible for the maintenance, regulation, and modification of genetic information (9, 32, 33). At the forefront of this revolution stand two classes of small regulatory ncRNAs; silencing RNAs (siRNAs) and microRNAs (miRNAs).

1.3 Small RNAs, Big Impact: miRNA Mediated Gene Regulation

In 1993, two research groups independently arrived at the conclusion that protein coding genes are regulated by endogenously expressed, non-protein coding genes, via the hybridization of their complementary RNAs (34, 35). Within a few years, Andrew Fire and Craig Mello published a pair of seminal articles (36, 37) that provided an explanation for the previously observed suppression (38, 39) of endogenous genes, which they found to be mediated by the introduction of homologous RNA. These and several other key findings (40-43) marked the inception of the RNA silencing or RNA interference (RNAi) field.

RNA silencing is an evolutionarily conserved cellular phenomenon wherein small non-coding RNA fragments act as triggers to either repress or destroy complementary mRNA targets (12). Consequently, RNAi has become a tool that exploits the introduction of exogenous siRNAs into the cellular RNA silencing pathway to mediate mRNA cleavage (44). As a tool, RNAi provides a

rapid means of depleting specific mRNAs by introducing double-stranded RNA homologous to a particular message leading to its sequence-specific degradation with profound implications in functional genomics and therapeutics. Additionally, the observation that viral RNAs can be targeted effectively via RNAi (45) implicates this pathway as an evolutionarily ancient, intracellular antiviral immune response.

By contrast, miRNAs are endogenously expressed and processed small RNAs, ~20-30 nt in length, that bind to short (6-8 nt) so-called “seed” sequences in the 3’UTRs of target mRNAs to typically downregulate the gene expression of target mRNAs at the post-transcriptional level (11, 12). As abundant high-level gene regulators they play key roles in almost all cellular processes (11, 12, 46, 47), and their aberrant expression has been associated with several human pathologies, including cancer (48, 49). About 50% of all human genes (~11,000) are computationally predicted to be controlled by ~1,000 different miRNAs, while the rest of the human genes appear to evolve to avoid such control (47, 50, 51). As an additional layer of complexity, a single miRNA is thought to typically regulate several hundred mRNAs, whereas a single mRNA is predicted to often be regulated by multiple miRNAs of the same or different sequence. A picture thus emerges of a complex regulatory network that allows for rapid adaptation of the whole transcriptome to changing environmental cues during, for example, cell development or cancer onset. However, tools to experimentally verify this regulatory network are only slowly emerging.

Biosynthesis of functional miRNAs follows a tightly regulated multi-step pathway (**Fig. 1.2**) (47). Bioinformatic annotations show that most miRNA genes are located in intergenic regions with their own promoters and are transcribed as primary transcripts (pri-miRNA) by RNA polymerase II (RNAPII) or RNAPIII (52, 53). It was also observed that 50% of known miRNAs are in close proximity to other miRNAs, leading to the proposition that clustered miRNAs might be transcribed from a single polycistronic transcription unit (54). Pri-miRNAs fold into one or several stem-loop structures containing imperfectly base-paired stems,

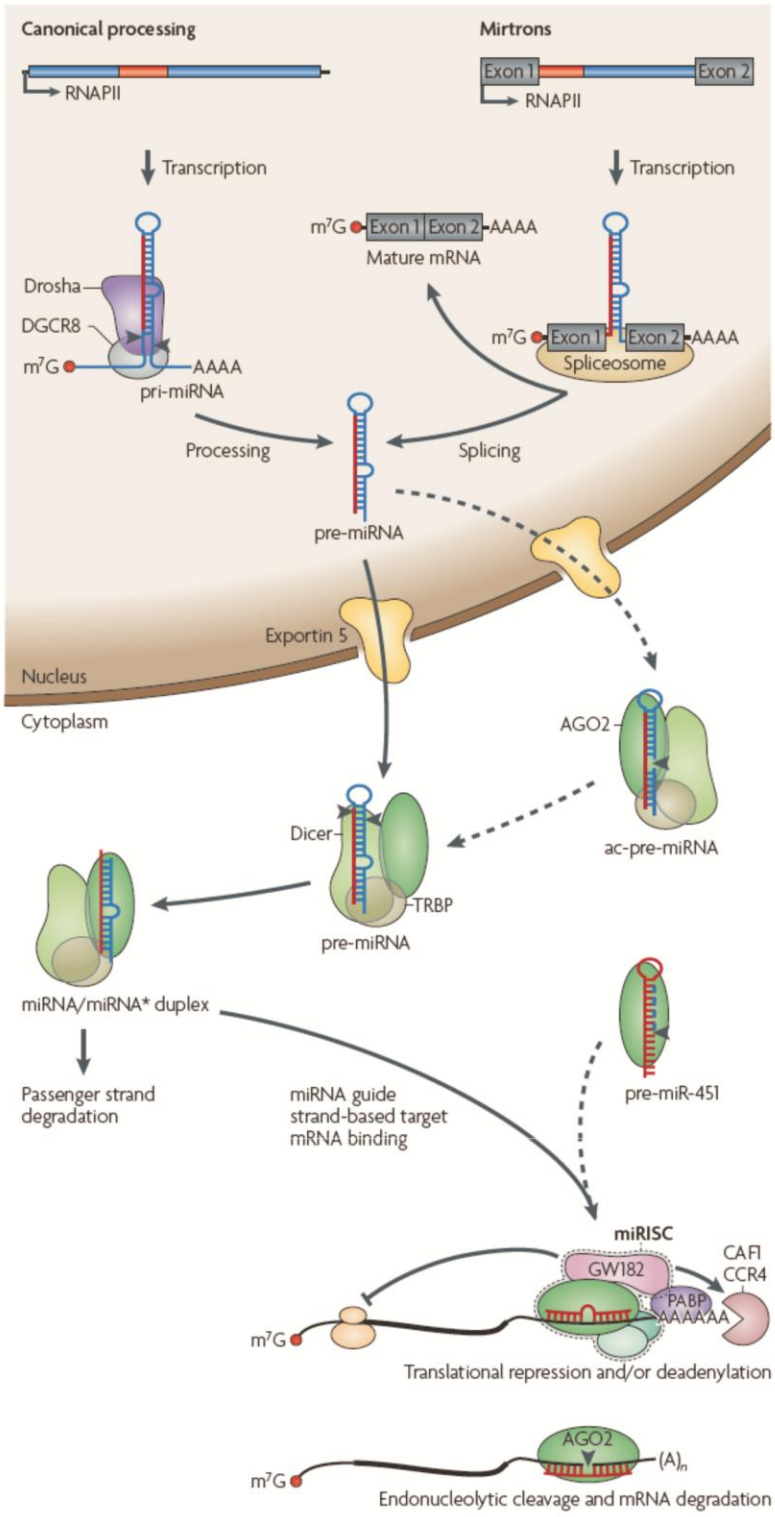

Figure 1.2. miRNA biogenesis pathway. Reprinted from reference (47) with permission from the Nature publishing group.

which are cleaved in the nucleus by a protein complex that contains Drosha (an RNAse III type endonuclease) and DGCR8 (the microprocessor). This enzymatic reaction results in the formation of precursor-miRNAs (pre-miRNA) that are ~70 nt long and contain a 2-nt overhang on their 3`end. Some pre-miRNAs are produced from very short introns (mirtrons) of protein coding pre-mRNAs as a result of splicing and debranching, thereby bypassing the Drosha–DGCR8 step (55). pre-miRNAs contain a single stem-loop and are transported by Exportin-5 via the nuclear pore complex (NPC) into the cytoplasm, where they are cleaved by protein complexes containing the enzyme Dicer to yield ~22-bp miRNA duplexes. In general, this product of Dicer has 2-nt overhangs on the 3`end of each strand, with the overhang on one end resulting from Drosha cleavage. In mammals, the protein argonaute 2 (AGO2), which has robust RNaseH-like endonuclease activity, can support Dicer processing by cleaving the 3′ arm of some pre-miRNAs, thus forming an additional processing intermediate called AGO2-cleaved precursor miRNA (ac-pre-miRNA) (56). Processing of pre-miR-451 also requires cleavage by AGO2, but is independent of Dicer cleavage and its 3′ end is generated by exonucleolytic trimming (57, 58). Following processing, one strand of the miRNA duplex (the guide strand) is preferentially incorporated into the miRNA-induced silencing complex (miRISC), whereas the other strand (passenger or miRNA*) is released and degraded. Generally, the retained strand is the one that has the less stably base-paired 5′ end in the duplex. Passenger strands are not always byproducts of miRNA biogenesis; they can also be loaded into miRISC to function as miRNAs (59-61).

As part of miRISC, miRNAs base pair with target mRNAs to mediate their repression (**Fig. 1.3**) (62). In the relatively rare case where the miRNA binds with complete complementarity, the mRNA target is endonucleolytically cleaved by Ago2, leading to a complete knockdown of protein expression as expected for RNAi. In contrast, mRNAs bound by partially complementary miRNAs are repressed via translational repression or deadenylation and degradation. Initially, translational repression was considered a hallmark of gene regulation mediated by only partially base-paired miRNAs (63, 64). Translation repression is thought

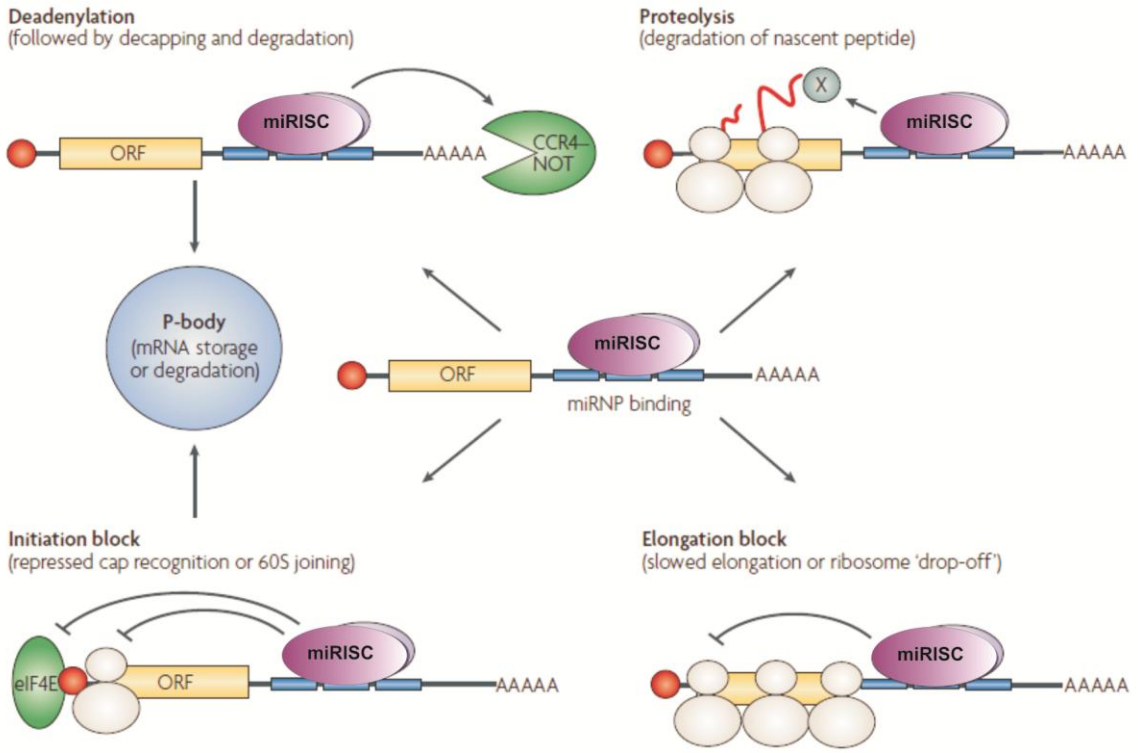

Figure 1.3. Possible mechanisms of miRNA mediated gene regulation in mammals. Adapted from reference (65) with permission from nature publishing group.

to occur via inhibition of translation initiation or elongation. It was first observed that only m^7G-capped, not ApppN capped or IRES containing, mRNAs underwent miRNA-mediated repression. Polysome gradient analyses have also shown that m^7G-capped miRNAs containing a functional let-7 miRNA binding site move up the gradient, indicating reduced or no ribosome loading onto the mRNA and thus supporting suppression at the translation-initiation step (66, 67). Moreover, there is substantial evidence that proteins of miRISC disrupt the essential eIF4E-eIF4G interaction or bind directly to the 5`cap, thus impeding the formation of the translation initiation complex. One of the proteins that disrupt initiation complex formation is believed to be from the AGO family, which are core components of miRISC, as it contains a domain of (limited) homology to the cap-binding domain of eIF4E (68). This suggests that AGO may compete with eIF4E for cap binding, thus preventing effective PABP-eIF4G interaction. In addition, it was shown that either the 40S subunit (66, 69) or 60S (70, 71) subunit are inhibited from binding to repressed mRNAs, further corroborating the initiation block model. In contrast to earlier reports, studies in *C. elegans* showed that *lin14* and *lin28* mRNAs, which are targets of *lin4* miRNA, remained associated with polysomes even though the protein level was strongly repressed (72). Additionally, miRNAs and AGO proteins co-sedimented with their mRNA targets and polysomes in human cells (73-75). These results show that ribosomes can still be associated with the miRISC-mRNA complex, thus instead supporting a post-initiation repression model.

The notion that mRNA destabilization and decay is a mode of miRNA-mediated repression was initially supported by microarray analysis of transcript levels in cells and tissues (76). The miRNA pathway was inhibited in these cells, resulting in a marked increase in the abundance of several mRNAs validated as miRNA targets. Since then several groups have found evidence that miRNAs act by predominantly degrading their targets (77, 78). These results recently were further validated using high throughput sequencing and ribosome profiling, which showed that only 7% of all miRNA targets were translationally repressed (79). However, mRNA degradation is initiated by a gradual decrease in the length of

the poly-A-tail and can either proceed by 3` to 5` decay or by decapping followed by 5` to 3` decay (80); AGO hypothetically can bind to the 5`cap, preventing circularization of the mRNA, which in turn can render the poly-A tail vulnerable to cleavage.

Sequestration of miRNA-bound mRNA complexes to processing bodies (PBs) (67, 81), intracellular foci enriched in RNA degrading enzymes (82), was initially deemed an attractive mechanism of miRNA mediated gene regulation, in part because the hypothesis exemplifies spatial organization of cellular function. However, it still remains possible that repressed targets localize to PBs only as a consequence of other modes of repression (83).

In summary, a number of competing hypothesis regarding the mechanism of miRNA-induced gene repression have been proposed (**Fig. 1.3**). It is a distinct possibility that this divergence simply arises from the fact that experiments on different systems (cells, cell-free extracts, etc.) using different methodologies give different answers. In addition, it is not yet clear whether miRNAs repress their target in a specific cell either by a single mechanism or by several parallel mechanisms. These questions arguably can be answered only by direct observation of the repression of single mRNA targets in real-time. To this end, I resorted to single molecule fluorescence microscopy in live cells and *in vitro*.

1.4 Single Molecule Fluorescence Microscopy

The cell is a complex mixture of single molecules that function in a highly organized and concerted manner to forge life. Conversely, each molecule within the cell is, in principle, a local reporter on the nature and dynamics of its surroundings. Yet studies of biomolecules, such as probing their structure, measuring their reaction kinetics or determining their intracellular distribution, have mostly been conducted on the ensemble level, reporting the “average” structure, mechanism or cellular organization. Important information hidden within this average, as a seemingly homogenous population of molecules can, in fact, be composed of surprising heterogeneity. This fact is exemplified by the recent realization that the flow of genetic information is spatially and temporally

organized through the transport of single mRNA molecules to discrete regions in an organ (84) or even a single cell (85, 86) to synthesize proteins in the region where they are needed most. For example, as seen by live-cell fluorescence microscopy, a significant fraction of the mRNA encoding the cytoskeletal protein actin localizes to the leading edge of the cell. Upon tracking the diffusion of single actin mRNA molecules, multidirectional movements with net displacement vectors pointing towards the leading edge of the cell were observed, thus rationalizing the average cellular organization of the mRNA (87).

Single-molecule fluorescence microscopy (SMFM) generally reveals rare events and transient species or intermediates on a reaction pathway, like those found in protein (88, 89) or RNA folding landscapes (20, 90), without the need to perturb or synchronize the molecules of the system to generate a signal. Such information is easily lost by averaging in regular ensemble measurements. According to the ergodic theorem, the time average of any observable obtained from visualizing a single molecule is equivalent to the population average, provided the molecule is visualized over a sufficiently long period of time. Yet, single-molecule studies have also shown that some RNA and protein enzymes exhibit so-called static heterogeneity with conformationally and functionally distinguishable molecular species that only slowly exchange on an experimental time scale (20-22, 91). The types of information obtained from SMFM thus provide unprecedented insights into the functional mechanisms, dynamic properties, and sub-cellular localization of biomolecules, with only limited perturbation of the underlying biology.

Two major aspects of microscopy, accuracy and resolution, define the quality of imaging in a quantitative manner. On one hand, accuracy describes the radius of the circle (or sphere in the case of three-dimensional localization) within which it is certain that an object is localized (i.e., the error associated with localizing an object). On the other hand, resolution is the distance below which two closely located objects cannot be distinguished as separated from one another. In 1873, Ernst Abbe observed the failure of a lens-based optical microscope to distinguish two features closer than half of the wavelength of the illumination light on the

lateral plane. This imposes a theoretical limit on the resolution of fluorescence microscopy of 200–300 nm (using visible, ~500-nm illumination light). This relationship is more accurately described by:

$$\Delta \boldsymbol{d} = \frac{\lambda}{2n\sin\alpha} \qquad \text{(Eq. 1)}$$

where Δ*d* is the distance between two closely located spots, *λ* is the wavelength of light used for illumination, *n* is the refractive index of the medium in which the lens is working and *α* is the half-angle of the maximum cone of light that enters or exits the lens. The obtainable axial resolution as then described by:

$$\Delta z = \frac{\lambda}{2n\sin^2\alpha} \qquad \text{(Eq. 2)}$$

is almost threefold higher than the resolution limit in the lateral dimension (~500–600 nm).

For over a century, Abbe's law (also referred to as "Rayleigh's resolution limit") was considered a fundamentally limiting factor in intracellular imaging. This problem is exacerbated for single molecules: their intracellular density is often much higher than that commonly used in SMFM, leading to severe overlap of their images. Given that a typical human cell contains ~10^{10} protein molecules (92) of ~2.5-nm radius and the cell by itself has a volume of ~4x10^{12} nm^3, a conservative estimate of ~20% of the total cell volume is filled with just proteins. Factoring in other molecules, such as lipids, nucleic acids, inorganic ions and small metabolites, the density of molecules, in general, within a cell is astoundingly high. Even in such a crowded environment biomolecules often diffuse at speeds of several nanometers per second, frequently colliding with other molecules and changing direction. Studying single molecules under such conditions necessitates the need for higher accuracy and resolution than that obtained from conventional optical microscopy.

Single-molecule techniques can be broadly classified into two groups, those based on optical observation, which encompasses all SMFM approaches including single molecule fluorescence resonance energy transfer (SM-FRET) (93), and others based on mechanical interaction, such as manipulation by optical tweezers and imaging by atomic force microscopy (AFM) (94). Of these, SMFM has especially proven to be valuable in probing molecular properties in environments as complex and dense as those within cells. Currently available ultra-high-resolution microscopy methods can be categorized as: 1.) methods pertaining to localization of a few single molecules with nanometer-scale precision (super-accuracy imaging (95)); and 2.) methods resolving many single molecules within a densely populated sample by localizing only a sparse subset of them at a time through repeated super-accuracy imaging (often termed super-resolution imaging (95)). With a focus on super-accuracy imaging, a general outline of the important requirements for performing single-molecule experiments, in addition to a broad overview of well-established single-molecule techniques that localize molecule with nanometer scale precision, is given in the following.

Experimental Design in Single-Molecule Fluorescence Microscopy. The sensitivity required to detect single molecules is achieved by carefully selecting the sample concentration, instrumentation, and probe used to label the molecule. The concentration of molecules should be kept low enough, in the nanomolar to picomolar range, to distinguish one molecule from another. While controlling sample concentration *in vitro* is relatively easy, it presents a major challenge *in vivo*. Another important parameter to be optimized in SMFM is the signal-to-noise ratio (SNR) (i.e., the ratio of useful signal (photons) emitted by single molecules and unwanted, spurious background signal (noise)). Noise can arise from impurities in the sample, from fluorescent molecules in the sample that are not in focus, or from shot noise (dark counts) of the detector. From its definition, it is clear that having a high SNR is preferred, but several factors can markedly affect this value (as discussed under section “Probes”). A whole arsenal of solutions, in

the form of improved optical configurations (illumination methods, light sources, and detectors) and fluorescent probes, is currently available and constantly being refined to overcome low SNR.

Modes of illumination. Schemes to illuminate a sample can be primarily divided into two categories: far-field illumination and near-field illumination. In far-field imaging, the distance between the objective lens and sample is at least an order of magnitude greater than the wavelength of light used. Conversely, in near-field imaging, the sample is separated from the illuminating focusing lens or fiber optics by a distance much smaller than the illumination wavelength. Additionally, the diameter of the lens or fiber is smaller than the wavelength of light used (typically ~80 nm) (96, 97). Such a configuration ensures that the light interacts with the sample before effects of diffraction come into play, leading to higher resolution. Near-field illumination requires very flat samples for the lens or fiber optics to scan over it, making it less useful for intracellular imaging. In the following, we focus on some of the more popular far-field illumination schemes used in SMFM imaging (**Fig. 1.4**).

Wide-field epi-illumination. In wide-field epi-illumination schemes, light passes through the objective's optical axis, illuminating all molecules in the light path. Although a specific plane of the sample can be focused, molecules present in other focal planes also get excited, contributing significant background. This illumination method is suitable for SMFM only when bright molecules are sparsely distributed, such that background contribution from out of focus molecules is negligible.

Total internal reflection (TIR) illumination. TIR was first used in 1981 by Daniel Axelrod in conjunction with fluorescence (TIRF) and fluorescence microscopy (TIRFM) to image the lipid probe 3,3´-diocta-decyclindocarbocyanine (diI) in human skin fibroblasts (98). When light is transmitted through a medium of higher refractive index (n_i; e.g., glass) into one of lower refractive index (n_r; e.g., water) at incident angles (θ_i) greater than the critical angle given by $\theta_c = \sin^{-1}(n_r/n_i)$ (Snell's Law), light is totally reflected within the first medium. However, because of its wave properties, some light will be transmitted into the medium of

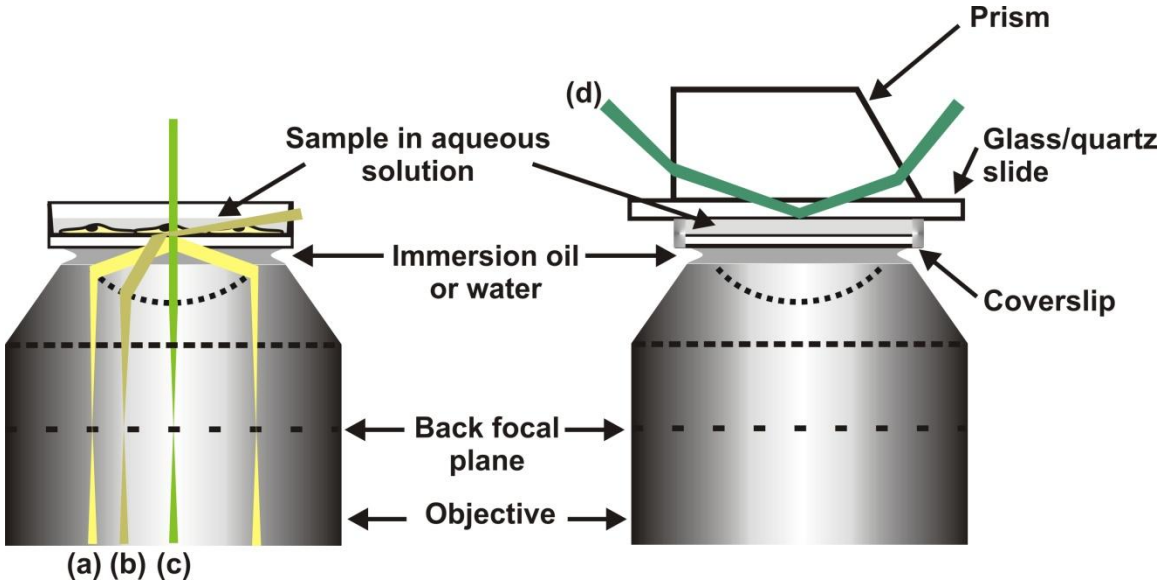

Figure 1.4. Wide-field Illumination methods**.** In live cell imaging, typically, OTIRF (a), HILO (b) or wide-field epi-illumination (c) is used. By simply moving the excitation light away from the optical axis, one can switch from wide-field epi-illumination to HILO or OTIRF. In all three cases, the incident light and the fluorescent light pass through the same objective. By contrast, in PTIRF (d) the incident light is directed to the sample through a prism. The fluorescent light passes through the depth of the sample and the coverslip before being collected by the objective. As the sample has to be sandwiched between the slide and the coverslip, PTIRF is not suitable for live cell imaging, which demands frequent media change and precise control of O_2/CO_2 gas.

lower refractive index in the form of a “standing” or “evanescent” wave. The intensity of this light field decreases exponentially from the interphase, establishing only a thin lamina of ~150-nm depth within the aqueous sample, effectively reducing background fluorescence from outside regions. TIR can be achieved by illumination through either a high numerical aperture (NA) objective (objective-type TIRFM, or OTIRFM) or a quartz prism that couples the incident light into the glass surface (prism-type TIRFM, or PTIRFM). In OTIRFM, the incident laser light is focused onto the back focal plane (BFP) of the objective so that it is away from and parallel to the optical axis, thus θ_c is achieved without needing an inclined light source. Since the incident light and the fluorescent light are focused by the same objective, scattering of laser light within the objective leads to some background in the image. PTIRFM avoids this background, but poses geometric constraints due to the greater challenge to couple the incident light at the right angle and the fact that both sides of the sample need to be optically accessed. TIRFM is especially useful in imaging surface immobilized molecules or, in the case of (intra)cellular imaging, the basal plasma membrane and ~100 nm of the adjacent cytoplasm.

Highly inclined and laminated optical sheet (HILO) illumination. Although TIRFM provides image quality greatly improved over that obtained by traditional epi-illumination, it is restricted to imaging molecules near an optically transparent surface. HILO microscopy (HILOM), also termed variable angle epi-fluorescence microscopy (VAEM) or near-TIRFM, overcomes this limitation by greater penetration into the sample without significantly compromising the signal-to-noise ratio (SNR) (99, 100). Similar to OTIRF, the light source is focused onto the BFP of the objective but at a smaller radial distance from the optical axis so that the incident angle does not exceed the critical angle. This way, light is refracted into the sample at high inclination from the optical axis, thus illuminating a small lamina within the sample, the width of which is dependent on the diameter of the field of view (FoV) and the angle of incidence. The laminar width of the beam is maintained by using a field stop, essentially decreasing the FoV, to prevent excessive divergence of the incident beam. Due to the transmission of the

refracted beam through the objective into the sample, as in epi- and narrow-field illumination, any movement of the objective along the optical axis results in focusing on a different plane in the sample along the z-dimension, enabling imaging in 3D (99, 100). The excitation beam path for epi-illumination, OTIRFM and HILOM are relatively similar so that a single microscope can be used to implement all three schemes.

Narrow-field epi-illumination. In narrow-field epi-illumination light is focused onto a small volume element within the sample, thus exciting only molecules in the excitation volume and not those outside of it. Confocal laser scanning microscopes work by this principle, wherein focusing of light to a specific volume is achieved by introducing pinholes (or apertures) in the excitation and emission paths. Higher resolution as compared to wide-field illumination can be achieved by decreasing the width of the pinholes, but this comes at the cost of lower photon collection. The method also suffers from slow sample readout rates as scanning an entire specimen occurs at one volume element at a time. A significant improvement in the scanning rate can be achieved by using spinning-disc or Nipkow-disc confocal microscopy. A disk consisting of several microlenses spins at typically 3,500 rpm to create virtual pinholes for confocal detection (101), essentially exciting several distinct regions of the sample simultaneously.

Light sources and detectors. Lasers are preferred over lamps for high-resolution optical microscopy because of their monochromatic, coherent and collimated light. Laser power should be high enough to excite all molecules optimally without damaging the sample. The wavelength of light spans anywhere from the far ultra-violet (UV) to the near-infra-red (NIR) region of the electro-magnetic spectrum (350–1000 nm), depending on the nature of the fluorescent probe and sample used. However, wavelengths from the visible part of the spectrum (450–680 nm) are used most frequently, mainly for two reasons. First, the transmission properties of available optics are best in the visible range, and second, most well-documented fluorescent probes (fluorophores) have their spectral properties in this region of the electromagnetic spectrum. Moreover, UV

light is not suitable for imaging living cells: it induces DNA damage and sometimes even apoptosis (102). IR lasers are slowly gaining popularity, however, because they scatter the least, thus significantly improving sample penetration depth.

Charge coupled devices (CCDs) and avalanche photodiodes (APDs) or photomultiplier tubes (PMTs) are most commonly used in SMFM, and depending on the type of imaging performed, one or the other is preferred. In wide-field illumination, CCDs are the detectors of choice, whereas for narrow-field illumination where photons from only a small region of the entire sample are collected, APDs or PMTs are used. CCDs contain a large matrix of photosensitive elements (or pixels) that simultaneously collect photons over the entire detector surface. Photon flux information at each pixel is stored as an electronic charge (photoelectron) that is first converted to an analog voltage by an amplifier, and then digitized. Intensified (I-)CCDs and electron-multiplying (EM-)CCDs amplify the number of photoelectrons through an external amplifier and on-chip, respectively, such that the digital number is (marginally) linearly dependent on the number of photons collected, making intensity values semi-quantitative at the (sub-)pixel level. APDs and PMTs are point detectors sensitive enough to detect and accurately count single photons, but have to be used in laser scanning microscopes to generate images of two-dimensional samples, limiting their time resolution. The time resolution obtainable with CCDs is primarily limited by the frame rate (number of frames or images per unit time), whereas the spatial resolution is dependent on the number of pixels and the quantum efficiency (i.e., the fraction of detected versus collected photons). A typical CCD used in SMFM has 512 x 512 pixels. While CCDs with higher numbers of pixels are available (e.g., 1024 x 1024), they are often less sensitive due to lower quantum yields.

Probes. The sample or the single molecule(s) under inquiry must be conjugated to a (fluorescent) probe or carry strong inherent fluorescence to be visualized. Synthetic dyes (Cy dyes, Alexa dyes, various forms of rhodamine dyes), fluorescent beads, quantum dots, and fluorescent proteins (FPs) are among the

common fluorescent probes used in SMFM. FPs are the mainstay of intracellular fluorescence microscopy. The cloning and expression of fluorescent proteins fused to cellular targets have become routine practices. However, this method of labeling comes at the cost that the protein fusion must be expressed exogenously, often resulting in overexpression as compared to endogenous copies. Using inducible expression systems (103) is one of the many possible tricks that can be employed to mitigate overexpression. Non-fluorescent beads, especially ones of large size, can be imaged with high precision even using microscopes with simple optics, making them an attractive alternative to synthetic dyes and FPs in single particle tracking (SPT). Conjugating biomolecules to beads and to a certain extent FPs, however, comes with the caveat that the attachment of a bulky load could skew the molecule's function, localization, and/or diffusion. The development of various bioorthogonal labeling strategies (104) and fluorogenic photo-affinity probes (105, 106) has made the specific labeling of single molecules with small fluorescent probes a viable option, even in living cells. A more detailed description and comparison of conjugation chemistries and the different organic dyes and FPs used in SMFM can be found in several reviews (107-109).

A fluorophore suitable for SMFM should have high brightness, favorable photophysical properties and sufficient inertness so that the label does not interfere with the function of the molecule to be tagged. The first two criteria have a direct impact on the localization accuracy of single molecules. Brightness, a value of photon output that is calculated as the product of a fluorophore's extinction coefficient and quantum yield, should be high enough to delineate signal from noise. Undesirable photophysical processes, such as intersystem crossing (triplet state excitation) and photobleaching, markedly affect the quality and length of a single-molecule recording. Although the precise mechanism is unclear, molecular oxygen is thought to be primarily responsible for photobleaching via photo-oxidation of the fluorophore. Several chemical agents (e.g., cyclooctatetraene (COT), trolox and 4-nitobenzyl alcohol (110)) and enzymatic oxygen scavenging systems (e.g., those containing glucoseoxidase

and catalase (22) or protocatechiuc acid and protocatechuate-3,4-dioxygenase (111)) can be used to prevent fast photobleaching and quench triplet state excitation. Attaching multiple fluorophores per molecule can also increase brightness and fluorescence longevity, but it also increases the risk of rendering the molecule non-functional.

Imaging living biological samples presents a unique set of problems, including phototoxicity and autofluorescence. Fluorophores, in their excited states, react with molecular oxygen in the cell, resulting in the accumulation of phototoxic free radicals that can compromise sub-cellular compartments or even the entire cell's livelihood (112). Thus, a balance has to be struck between the excitation laser power (and wavelength) used and the time for which the sample is illuminated, especially for long time-lapse experiments. In addition, naturally fluorescent molecules present inside cells, such as NADH, FADH and heme, absorb visible light and fluoresce, contributing to a high background level of autofluorescence during imaging. One way to circumvent autofluorescence and simultaneously enhance photostability of FPs is by using cell culture media that do not contain any fluorescent molecules, especially vitamins (113). Arguably the best solution is, however, to use fluorophore probes that absorb light in the far-red visible or NIR part of the spectrum where cellular components show minimal absorption (114, 115).

Imaging Single Molecules with Nanometer Scale Localization Accuracy. Even before the advent of single-molecule detection methods, there was a widespread interest in tracking the movement or diffusion of molecules, especially membrane proteins and motor proteins, in solution and in living cells. Ensemble methods to calculate molecular velocities and diffusion coefficients have existed in the form of fluorescence correlation spectroscopy, or FCS (116), and fluorescence recovery after photobleaching, or FRAP (117). Tracking the movement of individual molecules with high spatio-temporal resolution seemed like a logical extension.

During the late 1980s, three different groups independently tracked the displacement of single beads over time by high-speed video microscopy both *in vitro* (118) and within living cells (119, 120) with ~10–100 nm lateral accuracy and sub-second temporal resolution. Around the same time, the optical absorption spectrum of single pentacene molecules was recorded in p-terphenyl crystalline matrices at liquid-helium temperature (121). Single-molecule fluorescence detection of cryo-cooled pentacene molecules soon followed (122-124). In an effort to enhance resolution and extend single molecule detection to the 3rd dimension, Van Oijen *et al.* (125) used a combination of confocal microscopy and spectrally selective imaging (SSI) to localize single pentacene molecules embedded in p-terphenyl crystals. SSI involves sequentially exciting individual pentacene molecules of distinct absorption maxima (caused by matrix effects), so that each molecule can be localized independent of the presence of another within a densely populated, otherwise un-resolvable region. The abilities to track beads with high accuracy and to visualize single fluorescent molecules with high resolution, together with a continual expansion of the available repertoire of optical instrumentation, have converged over the past two decades into what is now termed super-accuracy and super-resolution imaging.

A single fluorescent probe (or a cluster of closely positioned probes) can be considered to be a point source of emitted light whose image is, due to diffraction, spread over a much larger area on the detector than the actual size of the object. Such an image, referred to as a diffraction limited spot, appears as an airy disc, composed of a central bright spot surrounded by concentric rings of diminishing intensities. The intensity distribution of such an image can be mathematically described by what is termed a point spread function (PSF). By approximating the PSF with a simple two-dimensional (2D) Gaussian function, the intensity maximum, that is, the center of the Gaussian curve, can be localized with an accuracy similar in magnitude to the size of the fluorescent emitter, effectively breaking the diffraction barrier and Abbe's law.

Fluorescence imaging with one nanometer accuracy (FIONA). FIONA is a super-accuracy method that is used to localize and track single, typically fluorescently labeled, molecules with nanometer accuracy in the x-y plane (126). Fluorescence from single emitters is detected by a CCD and the intensity is plotted as a function of the spatial coordinates x and y (**Fig. 1.5A**). The resulting PSF is fit with a 2D Gaussian function:

$$P_g(x,y;z_0,A,x_0,y_0,s_x,s_y) = z_0 + A\exp\left[-\frac{1}{2}\left[\left(\frac{(x-x_0)^2}{s_x}\right)+\left(\frac{(y-y_0)^2}{s_y}\right)\right]\right] \qquad \text{(Eq. 3)}$$

where z_0 is a constant term due to background fluorescence, A is the amplitude or maximal signal, x_0 and y_0 are the coordinates of the center of the distribution, and s_x and s_y are the standard deviations along the axes. The full width at half-maximum (FWHM) of the Gaussian depicts the variance of the PSF, and the (central) peak pinpoints the mean (**Fig. 1.5A**). The variance divided by the number of photons collected results in the most simplistic form of the standard error of the mean (s.e.m.), or the precision by which the molecule can be localized (127, 128):

$$\left\langle(\Delta x)^2\right\rangle = \frac{s^2}{N} \qquad \text{(Eq. 4)}$$

where Δx is the error in localization, $\langle(\Delta x)^2\rangle$ is the s.e.m., s^2 is the variance and N is the number of photons. The s.e.m. also depends on other important parameters, including the detector noise, background noise and the effective pixel size (128):

$$\left\langle(\Delta x)^2\right\rangle = \frac{s^2+\left(\frac{a^2}{12}\right)}{N} + \frac{8\pi s^4 b^2}{a^2 N^2} \qquad \text{(Eq. 5)}$$

where *a* is the effective pixel size, which is simply the CCD pixel size divided by the overall magnification used, and *b* represents noise of any form. This equation shows that greater localization accuracy can be achieved by increasing the number of photons collected, decreasing the noise, and/or reducing the effective pixel size. High (1.2–1.65) NA objectives and back-thinned CCDs are typically used to collect as many photons as possible with minimal detector noise. Decreasing the effective pixel size requires a corresponding increase in magnification, which in turn reduces the number of photons collected per unit square area of the detector, significantly compromising the SNR. Therefore, a localization precision of 1–2 nm can be achieved under ideal conditions by collecting 5,000–10,000 photons using a CCD with effective pixel size of 80–120 nm. The same principles can be applied to each frame of a movie (or series of multiple frames), tracking the movement of a single molecule with ~1-nm accuracy, hence the name FIONA. Depending on the frame rate at which the movie is recorded, a temporal resolution of up to 1 ms can be achieved (126).

Perhaps one of the most convincing proof-of-concepts for FIONA and a spearhead for the broader adoption of single molecule techniques, originated from the investigation of motor protein movements. The mechanism by which motor proteins translocate on a cytoskeletal “path” was under debate for several years. Myosin V is a dimeric-motor protein that contains a catalytic (“head”) domain, a light chain “arm” that is composed of six calmodulins, and a cargo binding domain on each of its monomers that is held together by a coiled-coil “stalk” (**Fig. 1.5B**). One study (129) postulated that kinesin, another motor protein, moves over microtubules by an “inchworm”-type mechanism, where one of the arms always leads, while another study (130) hypothesized a hand-over-hand mechanism, in which the two heads alternately move past one another. Yildiz *et al.* (126) resorted to FIONA to resolve the controversy. They used a similar myosin-light-chain-domain labeling strategy to that used by Goldman and coworkers (130). Rhodamine-labeled calmodulin was added to myosin V monomers so that each dimeric motor protein contained a single fluorophore

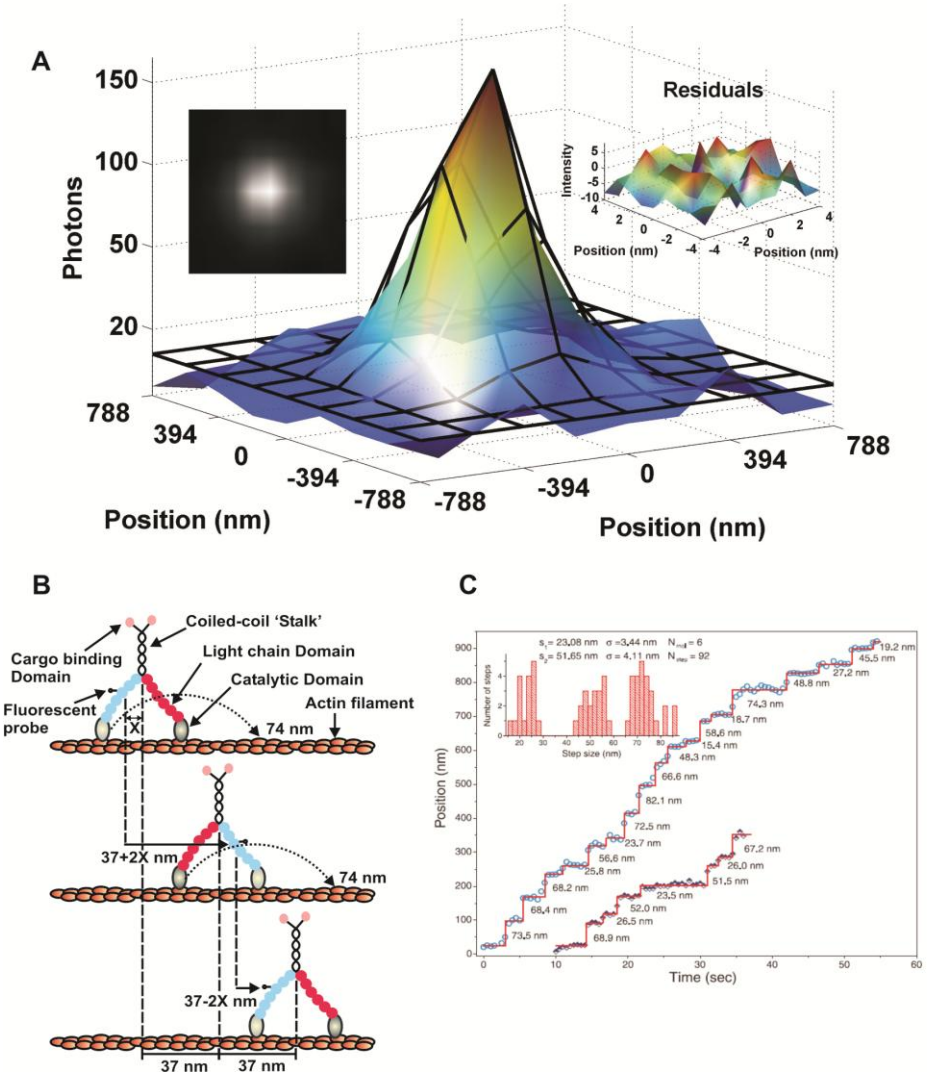

Figure 1.5. FIONA and its application. (A) CCD image of a single Cy5 labeled RNA (left inset) and its corresponding PSF fit to a 2D Gaussian. Residuals from the fit, which depicts the deviation of data points from the fitted curve, are also shown (right inset). (B) The hand-over-hand translocation model of myosin V as evident from single molecule step traces of myosin V labeled with bifunctional rhodamine on one of the twelve calmodulin light chains (126). On average, the protein alternates between 52 nm and 23 nm steps as it moves. This stepping pattern suggests that X, the distance along the direction of motion between the center of the coiled-coil stalk and labeled calmodulin, is 7.5 nm, i.e., the third calmodulin from the top is labeled. Sometimes, the speed of myosin V translocation is much faster than the frame rate of image acquisition, due to which, some 52 nm and 23 nm steps combine to yield ~74 nm apparent steps. A histogram of six myosin V molecules taking a total of 92 steps, representing the frequency of occurrence of specific step-sizes, is shown in the inset. (Panel C reproduced with permission from (126)).

(i.e., one fluorophore per two arms). The labeled arm is expected to take alternative 37-2X nm and 37+2X nm steps if it translocates by a hand-over-hand mechanism, where X is the distance of the fluorophore from the stalk. For a labeled calmodulin closest to the head, X would be ~18.5 nm, and hence, the motor should take alternating 74 nm and 0 nm steps. Alternatively, if the motor moves by an inchworm type mechanism, the step size should be a constant ~37 nm. Not only could the authors convincingly show that the protein moved via a hand-over-hand mechanism by plotting the position of the fluorophore with time, they could also distinguish between molecules that had the labeled calmodulin at different positions with respect to the stalk (**Fig. 1.5C**). Similarly, FIONA has also been used to track the path taken by kinesin as it "walks" over microtubules *in vitro* (131).

Multi-label imaging and particle tracking. In an effort to extend the use of FIONA to densely populated samples in which the PSFs overlap, both Paul Selvin's group (132) and Norbert Scherer's group (133) developed a method that exploits the quantized photobleaching behavior of single fluorophores to perform FIONA localization, and termed it Single-molecule high-resolution imaging with photobleaching (SHRImP) and nanometer localized multiple single molecules (NALMS), respectively.

The principle of SHRImP/NALMS can be explained by considering a sample that contains two molecules A and B whose PSFs overlap (PSF_A + PSF_B). If both fluorophores photobleach, the signal reduction in a plot of intensity over time will typically be in the form of two consecutive steps, each step representing the photobleaching of a single fluorophore, since it is highly unlikely for multiple fluorophores to photobleach at the same time. This step-wise photobleaching can be used to count the number of fluorophores with overlapping PSFs (134, 135). Once A has photobleached, the image only contains PSF_B, which can now be localized with high accuracy using FIONA. The resultant image can then be subtracted from the original image (PSF_A + PSF_B) to derive PSF_A, another single PSF to which the FIONA can be applied, thus localizing both molecules with high

accuracy in different images of a movie. The same concept can be applied to a sample that contains more than two overlapping PSFs, enabling localization of molecules that are separated by as low as ~10 nm (132, 133).

Gordon *et al.* (132) used SHRImP to resolve double-stranded (ds) DNA molecules each labeled with one Cy3 at both 5´ends. Upon imaging immobilized biotin-tagged DNA molecules of different lengths (30–50 bp) with TIRF, they deduced the expected length for each molecule of 3.4Å per base pair. Qu *et al.* (133) used NALMS to arrive at a similar conclusion, but in addition to using short dsDNA also used long λ-DNA hybridized to multiple Cy3-PNA conjugates to resolve up to ~20 serially overlapping PSFs, each separated by ~7 nm.

Single-molecule high-resolution colocalization (SHREC), on the other hand, resolves overlapping PSFs originating from molecules labeled with spectrally distinct fluorescent dyes. Unlike SHRImP/NALMS, SHREC does not depend on photobleaching of fluorescent probes so that the observation window for imaging can be significantly extended (136). However, it requires the precise mapping of images from channels of distinct spectral range (color) onto one another, which is non-trivial due to chromatic aberrations of the optics. Spudich and coworkers therefore developed a mapping calibration for SHREC that uses fiduciary markers to measure the registration between the color detection channels. To this end, surface immobilized beads of sub-diffraction (100 nm) diameter labeled with both Cy3 and Cy5 (fiduciary markers) were imaged at such a low density that only a single bead was visible per FoV. This bead was then moved in 0.5-µm steps in the pattern of a 12x26 grid with a piezoelectric stage. The resultant 312 images were stacked to create a single image containing 614 regularly spaced PSFs (312 each in the Cy3 and Cy5 channels). Each PSFs in each channel was independently fit with a 2D Gaussian function and localized by a FIONA-like algorithm. Combining all locations thus determined, a local weighted mean transformation (137) was calculated to map any point in the Cy5 channel precisely onto its corresponding point in the Cy3 channel. The resultant map is used as a template to localize single dual-labeled molecules.

To benchmark their SHREC technique, the authors used Cy3/Cy5 doubly-labeled dsDNA similar to that used in the SHRImP and NALMS studies and obtained very similar results (136). They then went on to use SHREC to concomitantly visualize the movement of both legs of myosin V in real-time. To this end, they exchanged the native calmodulines with a mixture of either Cy3- or Cy5 labeled calmodulins so that, on occasion, the two legs of a myosin would carry each a different fluorophore. As expected, they observed leg step sizes of ~74 nm, shifted by ~37 nm between the two color channels (136). More recently, Singer and coworkers have used a similar super-registration approach to track the transport of β-actin mRNAs through the nuclear pore complex (NPC). By achieving an unprecedented ~20-nm lateral accuracy at ~20-ms time resolution in living cells, they observed and measured the kinetics of a fast three-step mRNA transport process taking no more than 200-ms total time (138).

Of note, the multi-fluorophore super-accuracy imaging methods SHRImP, NALMS and SHREC are closely related to and likely inspired the super-resolution imaging techniques, such as Stochastic optical reconstruction microscopy (STORM) and Photo-activation localization microscopy (PALM) (REF). The primary goal of the former methods is to localize and track single a few molecules over time with high precision, whereas the latter tools aim to resolve ~10^3 times higher densities of single molecules over consecutive imaging cycles where only few molecules are turned on at any given time, accumulating data for a super-resolution image over time.

Localization and tracking of single molecules in 3D. Initial efforts in SPT involved systems that were either two-dimensional in nature, such as labeled lipid molecules in the basal membrane of a cell, or the information obtained were 2D projections of objects moving in 3D. Verkman and co-workers developed a unique method for 3D SPT by introducing a cylindrical lens in the optical path of an epi-fluorescence microscope (139). The PSF of a particle in focus then is circular in shape and becomes larger and more ellipsoidal when the particle moves out of the focal plane. The major axis of the ellipsoid formed when the particle is above the focal plane is perpendicular to that formed when the particle

is below the focal plane. Using this method, the authors localized red fluorescent beads of 100-nm diameter in living cultured cells with ~5-nm lateral and ~12-nm axial accuracy at ~500 ms time resolution (139).

Another powerful method for tracking particles in 3D is off-focus or defocused imaging. Developed by Florin and coworkers this method is based on the principle that the diameter and pattern of a PSF varies as the object is defocused (140). Particles that are slightly out-of-focus have a larger PSF diameter than when in focus and those even further from the focal plane give rise to a complex ring patterned PSF. The distance of the particle from the image plane can be deduced from the intensity pattern of the rings (i.e., the number, diameter, and relative intensity of rings). Schutz *et al.* used this method to record the trajectory of single potassium channels labeled with Cy5-tagged hongotoxin ligands in living T-lymphocyte cells (141). Although the method yielded lower axial accuracy than bead tracking (~40 nm versus ~3 nm), it was the first report of 3D SPT of molecules tagged with small fluorescent probes. Toprak *et al.* (142) used a variation of the above method to track phagocytosed beads with ~2.7 nm lateral accuracy and ~3.7-nm accuracy along the optical axis at 50-ms time resolution. In this technique, termed bifocal imaging, only 30% of the emitted light is focused, leaving the other 70% defocused, both of which are then split onto different regions of a CCD camera. The focused and defocused PSFs of a single particle are first mapped onto one another and then used to record the trajectory of the particle in the x-y plane and the z-axis, respectively.

Another approach for 3D SPT is based on the relative displacement of a pair of split images of the PSF onto distinct regions of the CCD. Appropriately named *Parallax* by Goldman and coworkers, either a wedge prism (143) or two closely spaced, parallel mirrors (144) are introduced at the back-focal-plane of the objective to view a fluorescent particle from two sides of the optical axis of the objective. With this optical configuration, the image of a particle moving in only the x-y plane is equally displaced in the x and y directions on either region of the CCD. By contrast, movements along the z-direction are reflected by the two images moving towards or away from each other in the x- (143) or y-direction

(144). The authors localized fluorescent particles with ~3-nm accuracy along the optical axis, including glucose-transporter containing vesicles in living adipocytes and single myosins walking along actin filaments (144, 145).

Finally, Moerner and coworkers recently introduced a so-called 4*f* imaging system composed of two achromatic lenses and a reflective liquid crystal phase-only spatial light modulator that convolves the microscope image with a double-helical PSF (146, 147). As a result, the camera image obtained of a single fluorescent particle shows two spots whose relative x,y-positions will twist around each other as the z-position of the tracked particle changes (like the two backbones of a dsDNA viewed along the double-helical axis). The authors were able to localize brightly fluorescent 200-nm beads with ~5–10-nm precision in the z-dimension and weaker emitters with up to ~30-nm precision (147).

Super-Resolution Microscopy – Hardware (Optics)-Based Methods. Beginning with confocal microscopy, several imaging techniques were developed starting in the 1990's with the vision of increasing resolution by reducing the focal spot size. These methods use specialized optical setups and can be considered 'hardware-based' solutions for super-resolution imaging, as opposed to 'software-based' methods like STORM/PALM/F-PALM, which rely instead on mathematical processing of a series of acquired diffraction limited images. Spot-scanning 4Pi microscopy (4PiM) (148) and wide-field I^5M (149) are two hardware-based techniques that can achieve ~3-7-fold greater axial resolution than traditional confocal microscopy. 4PiM uses two opposing high-NA objective lenses to illuminate a single focal spot. The coherent addition of wavefronts from both lenses narrows the focal dimension across the optical axis, resulting in higher resolution. I^5M implements the same opposing lens aperture enhancement for the detection of fluorescence but uses plane-parallel standing waves to illuminate the entire FoV.

Reversible saturable optical fluorescence transitions (RESOLFT) techniques. RESOLFT techniques utilize sophisticated excitation configurations

to physically decrease the width of the excitation volume and thus decrease the size of the PSF below theoretical limits of diffraction (150). These techniques can be described as targeted illumination/readout methods that do not require detection of single molecules, whereas STORM/PALM/F-PALM are stochastic readout methods based on the very features of single molecule detection. Implementation of RESOLFT can be loosely divided into three categories—stimulated emission depletion (STED) (151), ground state depletion (GSD) (152, 153), and saturated pattern excitation microscopy (SPEM)/saturated structured illumination microscopy (SSIM) (154, 155). In STED, two laser beams are used (**Fig. 1.6A**), an excitation beam and a comparatively red-shifted "depletion" beam. The excitation laser is first applied, followed immediately (within picoseconds) by a doughnut-shaped depletion beam that depletes the excited state of all fluorophores except those at the very centre of the original excitation beam. Fluorescence from the remaining molecules in the centre of the focal volume is then detected. The intensity of the depletion beam can be increased to "squeeze" the final detection volume to a smaller size. The two beams are raster-scanned across the entire sample to form the complete image, as is generally done in scanning laser confocal fluorescence microscopy (94). Using STED microscopy, GFP-labeled viruses and endoplasmatic reticulum were imaged in fixed PtK2 cells with a lateral resolution of ~70 nm (156). Recently, Hell and coworkers implemented STED in a 4Pi microscope to achieve 40–45 nm in all three spatial dimensions by generating a spherical focal spot of the same diameter (157). Axial scanning of fixed Vero cells with this configuration revealed that immunologically labeled Tom20 (a subunit of the TOM complex) formed distinct clusters on the mitochondrial membrane. The group also implemented a dual-color imaging scheme in which they used a combination of two excitation-one depletion events to image both Tom20 and mtHsp70 (a mitochondrial matrix protein) simultaneously with ~40-nm resolution in 3D.

As in STED, GSD requires reversible switching between on- and off-states of the fluorophore. However, one of the major differences between the two methods lies in the nature of the off-state. Rather than by stimulated depletion, the off-

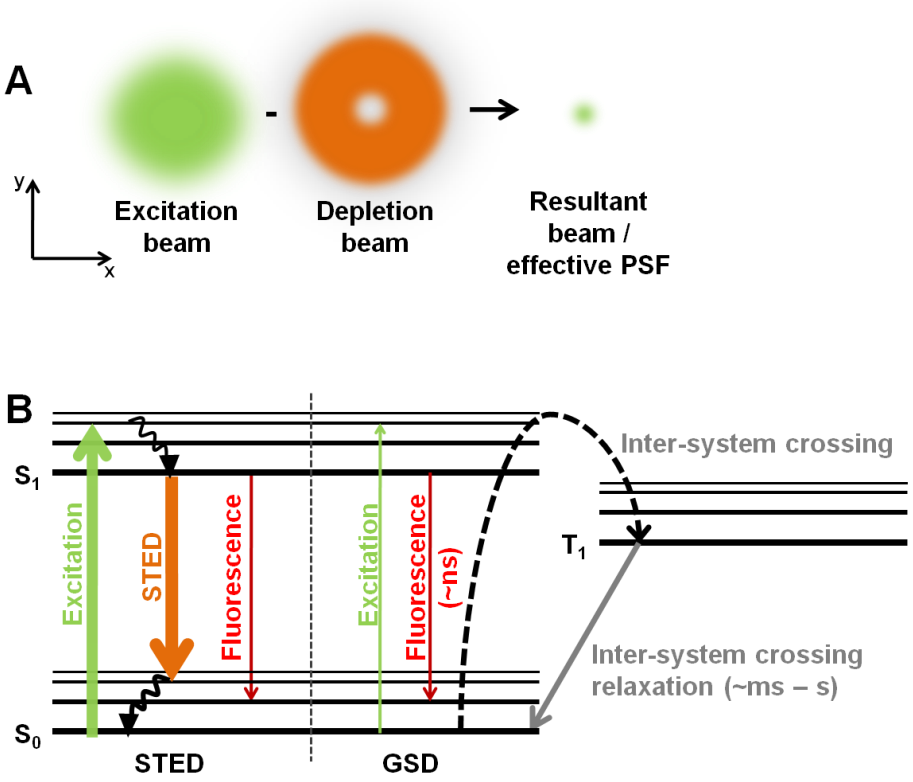

Figure 1.6. STED and GSD. (A) A 2D cross section of the excitation, depletion and resultant beams used in STED microscopy. The doughnut shape of the depletion beam can be achieved by placing a phase mask in the light path. (B) Jablonski diagram depicting STED and GSD. In STED, the depletion beam (labeled STED) de-populates the excited state (S_1). Fluorescence from very few fluorophores, which still remain in the excited state, is then recorded. In contrast, GSD works by 'optical shelving'. The electronic ground state (S_0) of fluorophores is depleted by pumping electrons into either the first triplet state (T_1) or other dark states. Electronic relaxations from these dark states occur at durations that are several orders of magnitude higher than that of fluorescence. At any given time, the ground state is thus sparsely populated, allowing only a few fluorophores to get excited.

state in GSD is induced via ground state depletion through increasing the triplet state population (**Fig. 1.6B**). Another difference between the two RESOLFT techniques is the use of a single continuous-wave laser for both excitation and depletion in GSD. A lateral resolution of ~50 nm has been demonstrated by applying GSD to the imaging of microtubules (152, 153) and to aggregates of SNAP-25 (152) or integrin-β proteins (153) in fixed cells. SPEM/SSIM is a wide-field super-resolution technique that excites a fluorescent sample by structured or patterned illumination (154, 155). This way unresolved information is first visible in the form of low-resolution moiré fringes, which are then computationally processed to obtain the final high-resolution image. Similar to other RESOLFT techniques, SSIM relies on the non-linear relationship between the fluorescence emission rate and excitation intensity, and the practical resolving power is determined by the SNR. The improvement in resolution is, however, only twofold over that obtained by conventional fluorescence microscopy, which is almost an order of magnitude less than that obtained by STORM/PALM/F-PALM. Nevertheless, SIM is currently the only subdiffraction high-resolution imaging technique that can produce multicolor 3D images of whole cells with enhancement of resolution in both lateral and axial directions while using conventional fluorescent probes and low intensity light sources. Upon implementing 3D-SIM to visualize interphase chromatin architecture and nuclear pore complex structure in formaldehyde-fixed cells, never-before seen details of these macromolecular structures were unraveled in their native nuclear milieu (158). In another report, Kner *et al.* (159) used a combination of speckle microscopy and SIM to observe the evolution of microtubules in living cultured cells with ~100-nm lateral resolution and ~100-ms time resolution. Recently, impressive time-lapsed 3D images of zebrafish and *Drosophila* embryos undergoing development were recorded using SIM based on a tunable light sheet, taking the potential of SIM to new heights (160). By utilizing multiple fluorescent tags and imaging embryos at multiple angles the group was able to generate a ‘digital’ fly embryo, highlighting the morphological changes of the entire embryo as it develops.

The theoretical resolution limit of RESOLFT techniques can be described by an extension of Abbe's law:

$$\Delta d = \frac{\lambda}{2n\sin\alpha\sqrt{1+\left(\frac{I_{\max}}{I_s}\right)}} \qquad \text{(Eq. 6)}$$

where I_{max} is the intensity of light bordering the centre and I_s is the saturation intensity required to outperform competing spectroscopic transitions (161). When $I_{max}/I_s \rightarrow \infty$, in theory "infinite" resolution can be achieved (i.e., down to a single molecule or even smaller), but this comes at the cost of using very high intensity beams that might damage sensitive samples like living cells. Due to this risk, RESOLFT is still generally implemented as an ensemble imaging technique, although single molecule detection is definitely possible (162).

Bridging the gap. The gap in attainable limits of resolution between traditional microscopy and electron microscopy (EM) has recently been bridged by several high-resolution imaging techniques. Ultra-high resolution microscopy, which for a long time was thought to be the realm of EM, near-field imaging or negative refractive index superlenses (163), has now become commonplace using microscope that bear conventional optics. Importantly, the ultimate contribution that these optical techniques will have to science depends on their accessibility to researchers. To this end, several 'out of the box' microscopes that implement PALM, and other high resolution microscopic techniques have recently been commercialized by manufacturers like Zeiss and Leica. Additionally, user-friendly software packages, both commercial and open-source (such as ImageJ), have made it easier to implement these powerful techniques without the need for technical proficiency or prior experience.

SMFM techniques are mainly limited by the number of observables accessible per experiment, imposing the need to perform multiple assays to study complex biological processes. The future of SMFM lies in the ability to

combine multiple tools into one adaptive instrument, such that the wealth of information obtained from a single sample is broadened. Techniques like 3D correlated EM (164), which combines the technical prowess of EM with the non-invasive nature of fluorescence microscopy, and SPT/single molecule FRET (165), have emerged as powerful tools to study the spatiotemporal evolution of molecules during various stages of cellular processes at very high resolution. The latter method can particularly probe conformational changes of proteins as they diffuse inside living cells.

Realizing the true potential of any technique relies on understanding its scope and limitations. However, factors considered as a bane in certain methods can be a boon in others. For instance, reactive oxygen species produced by fluorescent probes, which are considered to be toxic to living cells, can be used to oxidize certain contrast-enhancing agents to improve image quality in EM (166). Even non-fluorescent chromophores like heme, which typically contribute to high background in intracellular fluorescence imaging, can be imaged by STED microscopy to provide unique details on sub-cellular super-structures (167). In this fashion, molecules can be visualized label-free in their native cellular environment without the need for fluorophore conjugation.

Chu and coworkers recently improved the precision of wide-field imaging of biological samples by a factor of two through correcting for microscope drift with active feedback control, reaching sub-nm accuracy and resolution (168, 169). At such resolutions, it should become possible to obtain structural information of single molecules, for instance the distance between two subunits of a protein, even at very low molecule abundance and without the need to cool the sample below ambient temperatures (as required for EM and X-ray diffraction). The near future of SMFM will involve the implementation of such image acquisition and processing algorithms to spatially resolve the complex biological processes that enable life. Spatial resolution is, however, just one side of the coin since sufficient temporal resolution is also necessary; and both types of resolution are typically inversely related. Reaching higher (sub-millisecond) temporal resolution during biological imaging is mainly impeded by hardware limitations (e.g., the

maximal frame rate of the camera), limited photon collection at high frame rates, decreasing SNR, and fast diffusion of molecules inside the cell, which leads to image blurring. Stroboscopic imaging techniques, where laser excitation pulses are synchronized with the camera frame rate, have emerged as tools to address these limitations (170). Development of faster and more sensitive cameras may in the future enable higher resolution also during single-particle tracking based on simple optical and excitation schemes. Considering the large strides that SMFM has taken over the past two decades, one can easily envision that large-scale multiplexed imaging of biomolecules (e.g., proteins, DNA, RNA) at sub-nanometer and sub-millisecond spatiotemporal resolution within live cells or even animals will become possible within the next two decades.

1.5. Thesis Overview

The pervasive nature of miRNAs and the lack of an incisive tool to differentiate the various intracellular pathways these small ncRNAs follow warranted the utilization of SMFM; an unparalleled tool that has exposed molecular heterogeneities and short-lived and/or rare intermediates otherwise masked in the ensemble average. In Chapter 2, a novel single-molecule method was developed to visualize the diffusion and distribution of miRNAs in human cells. A combination of microinjection, HILO microscopy, SPT and stochastic photobleaching of fluorescent probes was used to measure the intracellular assembly and disassembly of fluorophore labeled miRNAs and their associated complexes. Single particles containing single or multiple miRNA molecules were visualized in live and formaldehyde-fixed cells. Their molecular stoichiometry, based on our single miRNA counting experiments, and diffusive behavior, based on SPT, is concordant with a heterogenous population of miRNA complexes bearing different molecular masses and following different cellular pathways. Moreover, time dependent changes in diffusive behavior and assembly states are suggestive of a miRNA-multiple turnover model. To the best of my knowledge, these data represent the first reported observation of intracellular miRNA complex assembly.

Next, I sought to further characterize the observed heterogeneous behavior of miRNA complexes using two-color single molecule (or particle) fluorescence microscopy as described in Chapter 3. The extent of colocalization (or interaction) between organic-fluorophore labeled miRNAs and fluorescent-protein labeled PBs, subcellular foci enriched in RNA degrading enzymes that are known to associate with miRNAs, were quantified with single molecule sensitivity. As reported by our single molecule counting experiments, only a small fraction of the total miRNA pool localized in PBs, with varying numbers of miRNA molecules per PB. Two-color SPT experiments in live cells showed that miRNAs either associated with PBs in a transient or stable fashion. Put together, these results predict the presence of a diverse set of miRNA complexes and PBs inside cells.

In chapter 4, I developed a single-molecule method to observe the interaction of miRNAs with mRNAs in an effort to quantify their binding stoichiometry *in vitro*. Mammalian cell extracts were used to assemble functional miRISC and miRISC-mRNA complexes. The number of miRNA molecules per mRNA was counted in a fashion similar to the miRNA counting experiments of chapters 2 and 3, which utilize the stochastic photobleaching of fluorescent probes. To our surprise, we found that a majority of mRNAs were either not bound or only bound by a single miRNA, even under conditions that led to maximum repression. This prompted us to hypothesize a low-probability binding model for miRNA-mRNA interaction as well. We further suggest that the relatively poor association of miRNAs with mRNAs could be mediated by mRNA structure and/or waek binding energies of miRNAs. These data, together with those in Chapter 3, seem to provide the molecular basis for the relatively weakly repressive capabilities of miRNAs as compared to siRNAs, which directly lead to target degradation. Finally, chapter 5 contains a summary of all salient results and future directions to be embarked upon by an upcoming student.

The data presented here advance our understanding of how miRNAs, ubiquitous small regulatory ncRNAs with profound implications in cellular sustenance and disease progression, function inside cells and assemble on their

mRNA targets to mediate gene regulation. The techniques developed for this purpose also provide a fundamental framework to probe other ncRNAs within the confines of the cell. In summary, this thesis provides the broader scientific community with new methods to visualize macromolecular complex assembly both *in vitro* and inside cells with single molecule sensitivity.

Chapter 2

Development of a Single-molecule Method to Probe miRNA Activity in Human Cells[1]

2.1 Introduction

Gene regulation by microRNAs (miRNAs) is an evolutionarily conserved RNA interference (RNAi) pathway wherein ~22-nucleotide-short non-coding RNAs assemble with components of the RNA induced silencing complex (RISC) so that their guide strand can bind partially complementary sequences in mRNA 3' untranslated regions (UTRs) to repress protein expression (11, 12). To date, over 1,000 mammalian miRNAs, generated from miRNA genes that account for over 1% of the entire genome (54), have been identified that are predicted to regulate over 50% of all protein coding genes (47). The ubiquitous nature of miRNAs implicates their involvement in all aspects of multi-cellular life (11, 12, 47), from general cellular processes such as cell differentiation and survival to pathologies such as cancer, thus creating an urgent need to understand the mechanism(s) by which miRNAs function.

While standard ensemble assays, including intracellular fluorescence microscopy (67, 171), have revealed a wealth of information (11, 12), the mechanism of gene repression by miRNAs is still debated (47). A major reason for this controversy is that an incisive tool for differentiating the various

[1] Sethuramasundaram Pitchiaya performed all experiments and analysis except for the fluorescence repression assay. John R. Androsavich created fluorescence reporter plasmids, performed the fluorescence repression assay and assisted with the bioinformatic analysis.

intracellular pathways that miRNAs follow so far has been lacking. We have therefore developed a unique approach to studying these molecules; by utilizing single molecule tools to investigate the location and mobility of single miRNAs within their native environment in pursuit of their still elusive mode of action.

Single molecule fluorescence microscopy (SMFM) has emerged as a powerful tool to quantify properties of biomolecules not accessible to conventional ensemble-averaging techniques (94, 172). In particular, SMFM has been applied to living cells to assess diffusive properties by single particle tracking (SPT) and the stoichiometry of molecular complexes by stepwise photobleaching (173). The main strategies for SPT in living cells either decorate the target molecule with endogenously expressed fluorescent protein(s) (138) or endocytosed nanoparticles (174), leading to high-molecular weight appendices that may impede function, or employ microinjection of target particles externally labeled with multiple fluorophores (175). These approaches so far have been applied to proteins, protein assemblies and large RNA:protein complexes. Complementary methods have recently been developed to assess the number and location of single intracellular molecules by fixing and permeabilizing a cell and incubating it with probes that are labeled with multiple fluorophores or nanoparticles (176), limiting this approach to the detection of relatively large protein and RNA molecules. Our intracellular single molecule high resolution localization and counting (iSHiRLoC) method overcomes these caveats by combining microinjection, optimal illumination, SPT and stepwise photobleaching of fluorophores to visualize the diffusive motions and distribution of singly fluorophore labeled functional small RNAs inside cells. Importantly, our data demonstrates the potential of iSHiRLoC to unravel both the dynamic nature and kinetics of intracellular complex assembly associated within an important gene regulatory pathway at single molecule sensitivity.

2.2 Materials and Methods

Plasmids, DNA and RNA olignucleotides. Luciferase reporter plasmids pmG-mH3U (wt) and pmG-mH3UM (mut) were engineered by inserting the wild-type

and mutant mouse HMGA2 3’ UTR sequences, respectively, downstream of the firefly luciferase ORF in the pmirGLO dual-luciferase expression vector (Promega). The wild-type and mutant 3’ UTRs were PCR amplified from plasmid templates received as a gift from David Bartel (Whitehead Institute, MIT) (48) using primers containing at their 5’ ends XhoI and NotI or XhoI and XbaI restriction sequences, respectively. Following restriction digestion, the amplicon insert was ligated to complementary ends in the pmirGLO vector. Fluorescence reporter plasmid pEF6-mCherry-mH3Um was constructed by first subcloning the mCherry ORF from the pRSET-mCherry vector, a gift from Roger Tsien (UCSD), into the multiple cloning site of the pEF6-myc-His-B (Invitrogen) vector using BamHI and EcoRI restriction sites. Then, using PCR cloning, the mutant HMGA2 3’ UTR was inserted downstream of the mCherry ORF between XhoI and NotI sites. pEGFP-C1 was purchased from Clontech.

Negative control siRNA used in transfection experiments was purchased from Ambion. SiLuc2 siRNA, a positive control siRNA, was designed towards the coding sequence of the firefly luciferase gene (*luc2*) and purchased from Dharmacon as a duplex. All other RNA oligonucleotides were purchased from the Keck Biotechnology Resource Laboratory at the Yale University School of Medicine with a 5’ phosphate (P) and, in the case of amine modified RNA, a 3’ amino group on a C7 carbon linker. RNA was purified as described (177) and the 3’ amine groups were labeled with Cy3 or Cy5 succinimidyl ester as described (177, 178). RNA sequences were as follows:

let-7-a1 guide: P-UGAGGUAGUAGGUUGUAUAGUU
let-7-a1-passenger: P-CUAUACAAUCUACUGUCUUUCC
let-7-a1 mut guide: P-UGCGUUAGUAGGUUGUAUAGUU
let-7-a1 mut passenger: P-CUAUACAAUCUACUGUCGUUCC
cxcr4 guide: P-UGUUAGCUGGAGUGAAAACUU
cxcr4 passenger: P-GUUUUCACAAAGCUAACACA
siLuc2 guide: GAAGUGCUCGUCCUCGUCCUU
siLuc2 passenger: GGACGAGGACGAGCACUUCUU

Guide and passenger strands were heat-annealed in a 1:1 ratio, resulting in duplex miRNAs, and frozen for further use. DNA oligonucleotide MS2 with four internal amine modifications was purchased from the Keck Biotechnology Resource Laboratory at the Yale University School of Medicine, purified and labeled as described above. A DNA oligonucleotide completely complementary to MS2 (C-MS2) with a 5' phosphate (P) was purchased from Invitrogen. The labeled and complementary strands were annealed in a 1:1 ratio and frozen for further use. DNA sequences were as follows:

MS2: AXGTCGACCTGCAGACAXGGGTGATCCTCAXGTTTTCTAGGCAATXA
(X represents an amine modified deoxy-uridine)
C-MS2:TAATTGCCTAGAAAACATGAGGATCACCCATGTCTGCAGGTCGACAT

Cell culture and media. HeLa cells (CCL-2, ATCC) were cultured in DMEM (GIBCO, Invitrogen) supplemented with 10% (v/v) fetal bovine serum (FBS) and non-essential amino acids (NEAA) at 37 ^{o}C. 1 - 1.25 x 10^5 cells were seeded onto delta-T dishes (Bioptechs) one day before microinjection, such that they were ~80% confluent at the time of microinjection. Regular medium was replaced with phenol red-free medium 4 h prior to microinjection and subsequently with a minimal medium (HBS), without serum and vitamins, but containing 20 mM HEPES-KOH pH 7.4, 135 mM NaCl, 5 mM KCl, 1 mM $MgCl_2$, 1.8 mM $CaCl_2$ and 5.6 mM glucose, immediately before microinjection. After microinjection, cells were incubated in phenol red-free DMEM containing 2% (v/v) FBS and 1x NEAA and in the presence of a 5% CO_2 atmosphere for the indicated amounts of time prior to imaging. For long incubations (4 h and greater), the medium was replaced every 4 h with fresh growth medium containing 2% (v/v) FBS. We found that cellular autofluorescence was a function of serum concentration; higher serum concentrations resulted in higher background and medium with no serum exhibited the least background. We used 2% (v/v) FBS to prevent conditions of serum starvation and simultaneously minimize cellular autofluorescence.

Microinjection. Microinjections were performed using a Femtojet pump (Eppendorf) and a microscope mounted Injectman NI2 micromanipulator

(Eppendorf). Solutions to be microinjected were centrifuged at 16,000 x g for 15 min at 4^{o}C just prior to microinjection. For a majority of the tracking and fixed cell experiments, the micropipette (Femtotips, Eppendorf) was loaded with 1.5 µM fluorophore labeled miRNA and 0.05% 10 kDa Fluorescein dextran (Invitrogen) in PBS. Fluorescein, which is spectrally distinct from Cy5, served as a marker to locate microinjected cells, mainly because Cy5 photobleached relatively quickly (within ~1.5 s). The focal plane to be imaged was adjusted during 488 nm (fluorescein) excitation and then quickly switched to 640 nm (Cy5) excitation for image acquisition. For (negative) control experiments, the miRNA was omitted and either 0.05% Fluorescein dextran (Invitrogen) in PBS or plain PBS were used. Microinjection of fluorescein dextran only resulted in very low background and false-positive particles. In some experiments, the fluorescein dextran was omitted and 2 µM Cy3 labeled miRNA in PBS was used. Although Cy3 labeled particles were visible for a longer time than those of Cy5, the majority of experiments were performed with Cy5 labeled miRNAs in conjunction with fluorescein dextran for two reasons: (i) cellular autofluorescence was higher upon 532 nm (Cy3) excitation as compared to 640 nm excitation; and (ii) it was easier to choose microinjected cells and check for microinjector clogging without photobleaching the dye conjugated to the miRNA. Co-microinjecting let-7-a1-Cy3 along with either fluorescein dextran or Alexa-647 dextran resulted in high background fluorescence and strong Cy3 fluorescence quenching, respectively, when illuminated with at 532 nm. The former background is largely contributed by the spectral overlap between fluorescein and Cy3. For MS2 DNA microinjections, 0.5 µM duplex DNA mixed with 0.05% (w/v) of 10 kDa fluorescein dextran was microinjected. All microinjections were performed at 100 hPa microinjection pressure for 0.5 s with 20 hPa compensation pressure. Using these conditions, microinjection volume was estimated to be ~0.02 pL or ~0.5% - 5% of the total cell volume, which translates to ~18,000 molecules of miRNA (at 1.5 µM working concentration). For plasmid microinjections, compensation pressure was increased to 40 hPa and plasmids were microinjected at a working concentration of 0.1 µg/µl in PBS (see **Repression Assays** for further details).

Fluorescence microscopy. Imaging was performed using a cell-TIRF system based on an Olympus IX81 microscope equipped with a 60x 1.45 NA oil-immersion objective (Olympus), nanometer-precision motorized stage (ASI Imaging), focal drift control module (zero drift control, Olympus), 1x – 4x magnification changer (Olympus) and an EM-CCD camera (Evolve, Photometrics). Solid state lasers with wavelengths of 488 nm (25 mW), 532 nm (100 mW) and 640 nm (100 mW), were directed through an acousto-optical tunable filter, split into different fiber-optic cables and then coupled to the cell-TIRF module. All laser lines had 10 nm bandwidth clean-up filters to ensure monochromatic illumination. Net powers of ~1.2 mW, 7 mW and 8 mW were achieved at the objective for the 488 nm, 532 nm and 640 nm laser lines, respectively. Laser beams were focused on the back-focal plane of the objective and made to travel parallel to the optic axis such that changing the distance from the optic axis controlled incident angle at the dish-media interface. Highly inclined laminar optical sheet (HILO) microscopy (100) was used to achieve deeper penetration into cells without compromising on signal-to-noise ratio. A dual band filter cube consisting of a z491/639rpc dichroic filter (Chroma) and z491/639m emission filter (Chroma) was used to detect fluorescein and Cy5 emission. Cy3 emission was detected using a Q570LP dichroic filter (Chroma) and HQ610/75m emission filter (Chroma). All videos were recorded at 100 ms camera exposure time using 120x magnification (60x objective and 2x additional magnification using the magnification changer) unless otherwise mentioned. Cells were maintained at 37 ^{o}C on the microscope stage while imaging using the DeltaT open dish system (Bioptechs) and a heated lid (Bioptechs). 5% CO_2 was supplemented to cells using the side port of the heated lid.

Live cell imaging and data analysis. The dish was washed several times with HBS immediately after microinjection. Cells were imaged in HBS consisting of 0.3 U/mL Oxyfluor (Oxyrase), 20 mM sodium succinate, 2 mg/mL ascorbic acid and 200 µM trolox (HBS-OSS). Oxyfluor and its substrate succinate act as an oxygen scavenging system, whereas ascorbic acid and trolox served as strong triplet state quenchers, effectively increasing the lifetime of the fluorophores

inside the cells. Single particle were tracked using the tracking module of Imaris (Bitplane). Only particles that lasted for more than 9 frames, in which case the error in the calculated diffusion coefficient will be ~50% (179), were used for further analysis. All tracks were visually inspected to ensure that they arose from well-isolated particles. In-house MATLAB routines were then used to calculate the mean squared displacement (MSD) and diffusion coefficients. Brownian diffusion coefficients were calculated by fitting the mean squared displacement for the first three time intervals to the equation (180):

$$\langle \boldsymbol{r^2} \rangle = \boldsymbol{4D\Delta t + offset}$$

An offset was used to account for the error in localization at t = 0. Localization precision was measured by tracking the variation in position of fixed miRNA particles (**Supplementary Fig. 2**). Relative deviation analysis (181) was performed on individual trajectories, based on the equation:

$$\boldsymbol{RD} = \frac{\boldsymbol{MSD}\ (\boldsymbol{n})}{\boldsymbol{4Dn\Delta t}}$$

where D is the instantaneous diffusion coefficient and n is a data point at a later time lag, not included in the original calculation of D. An RD value of 1 corresponds to pure Brownian motion. If the MSD time course were to deviate from linearity, such as those in anomalous, directed and corralled motions, RD values will deviate from 1. Thus, by comparing the distribution of RD values between multiple sample sets, we can gauge if a change in mobility of particles is due to the preponderance of one type of diffusive pattern over another.

The analytical forms of MSD time courses for different forms of motion:

$\langle \boldsymbol{r^2} \rangle = \boldsymbol{4D\Delta t + offset}$ (Brownian motion)

$\langle \boldsymbol{r^2} \rangle = \langle \boldsymbol{r_c^2} \rangle \left[\boldsymbol{1 - A_1 e^{(-4A_2 D\Delta t / \langle r_c^2 \rangle}} \right] + \boldsymbol{offset}$ (Corralled motion)

$\langle \boldsymbol{r^2} \rangle = \boldsymbol{4D\Delta t} + \ (\boldsymbol{Vt})^2 + \boldsymbol{offset}$ (Biased / directed motion with diffusion)

were used to derive diffusion coefficients from data points in Fig. 1e respectively.

Calculation of background intensity was done using ImageJ software (NIH). Briefly, a binary mask, using the background subtracted-thresholded image created by our intensity analysis software (see **Fixed cell imaging and data analysis**), was used to subtract all miRNA particles from an image and the total intensity from the resultant image was used to calculate the average background intensity. Intensity of regions outside the cell was used as the baseline to calculate the relative average background intensity. The 1 h and 32 h datasets were background subtracted, thresholded and deconvolved to accurately localize single particles. These images were subsequently also used to calculate the average number of particles visible for at least nine consecutive frames.

Fixed cell imaging and data analysis. Cells were first washed five times with PBS, fixed using 4% (w/v) paraformaldehyde in PBS for 20 min, washed five times with PBS after fixing and imaged in PBS consisting of the same OSS-antioxidant mix as mentioned above (PBS-OSS). Intensity analysis to determine number of photobleaching steps was performed using a custom written LabView (National Instruments) code (182). A Chung-Kennedy non-linear filter (183) was used to effectively average out the noise within intensity traces, yet preserving fast and sudden transitions, which aided in better visualization of photobleaching steps. The number of fluorophores per spot was estimated based on the number of photobleaching steps. The density of spots within cells was low enough (~0.1 - 0.25 spots/μm^2) to be confident that single particles were discerned.

Repression assays. For transfection repression assays 24 h prior to transfection, 100 µL of 15,000 HeLa cells were seeded per well of a 96 well plate. Cells were transfected with 60 ng of the indicated plasmid, 10 nM of the indicated dsRNA, 0.4 µL of Lipofectamine 2000 (Invitrogen) and 50 µL of OptiMEM (GIBCO). 6 h after transfection the growth medium was replaced with fresh medium. 24 h after transfection, medium was replaced with phenol red-free DMEM. Dual luciferase assays were performed using the Dual-Glo luciferase assay reagents (Promega) as per the manufacturer's protocol and luminescence

was detected using a Genios Pro (Tecan) plate reader. For microinjection repression assays, 0.1 µg/ul of both pEF6-mCherry-mH3UM and pEGFP-C1 plasmids were microinjected with 1.5 µM WT or MUT let-7 miRNA and 0.025% Alexa647 dextran (Invitrogen) in PBS. Following microinjection, cells were maintained under normal growth conditions for 24 h prior to imaging. Fluorescence signal were quantified using ImageJ software (NIH). The background subtracted mCherry signal was normalized with that of GFP for individual cells, which was then averaged over all cells. Using our filter sets (refer to **Microscopy**) we observed a small amount of mCherry bleed-through signal, ~14%, while imaging GFP. This bleed through was corrected for in our calculations. Repression was measured by normalizing the average relative intensity of mutant let-7-a1 injections with respect to that of wild-type let-7-a1 injections.

Cellular abundance of mRNA targets for let-7 and cxcr4. We first used targetscan 5.2© to identify potential mRNA targets of both let-7 and cxcr4 miRNAs. These targets were then compared to data from a HeLa cell mRNA expression profiling array (184) (dataset accessible at NCBI GEO database (185), accession GSM650992) using a custom written MATLAB code to identify endogenously expressed targets of both miRNAs. We found that ~10% of all predicted targets in either datasets were not expressed in HeLa cells. Comparing mRNA abundances of all potential targets for both miRNAs we deduced that let-7 is predicted to have ~10-fold more expressed target molecules than cxcr4.

Calculation of miRNA copy number in HeLa cells. We calculated the number of let-7 miRNA molecules per cell based on miRNA expression profiling data (186) and previously reported abundance of let-7a (187) and miR-21 (188) in HeLa cells. Fluorescence (187) and qRT-PCR (188) assays have estimated the copy number of let-7a and miR-21 to be ~4,000 copies and ~20,000 copies per cell, respectively. Deep sequencing data (186) (http://www.mirz.unibas.ch/cloningprofiles/) have predicted that let-7a, whose cellular fraction is 16.5% of the total let-7 population, and miR-21 are 1.6% and 13.2%, respectively, of the total

miRNA pool (~150,000 copies) in HeLa cells. Taking both these data sets into consideration, we calculated the abundance of let-7 to be approximately between 15,000 and 24,000 copies per HeLa cell.

2.3 Results

iSHiRLoC – a biologically relevant, intracellular, single-molecule method. In order to understand intracellular miRNA transport and localization, we microinjected mature double-stranded let-7-a1 or an artificial cxcr4 miRNA, labeled on the 3'-end of the guide strand with one Cy3 or Cy5 fluorophore, into human HeLa cervical cancer cells. Let-7-a1 miRNA is a member of the highly conserved, tumor suppressing let-7 family whose function is critical to cell proliferation (48). Let-7-a1 and cxcr4 have ~700 and ~70 predicted mRNA targets in HeLa cells, respectively (**Materials and Methods**) and both miRNAs have been reported to localize to processing bodies (PBs) (67, 189), sub-cellular ribonucleoprotein (RNP) complexes enriched in RNA processing enzymes. Microinjection allowed us to control the number of molecules introduced into the cytoplasm (~18,000) to be similar to the endogenous levels of let-7 miRNAs (**Materials and Methods**), minimizing cell perturbation and facilitating single miRNA detection as distinct point-spread functions upon imaging by highly inclined laminar optical sheet (HILO) microscopy (100). We supplemented cell medium with an oxygen scavenger system to delay photobleaching (**Materials and Methods**). Microinjected cells divided normally after 24 h and remained viable for at least 32 h, attesting to the low invasiveness of iSHiRLoC.

We further sought to ensure that microinjected, fluorophore-labeled miRNAs retain functionality. Transfection experiments showed that a luciferase reporter gene with seven let-7 target sequences was strongly repressed even without adding exogenous let-7-a1, most likely due to the fact that let-7 is one of most abundant miRNA families in HeLa cells. Accordingly, repression was moderately enhanced (by ~14%) upon co-transfection with let-7-a1 (**Fig. 2.1A**).

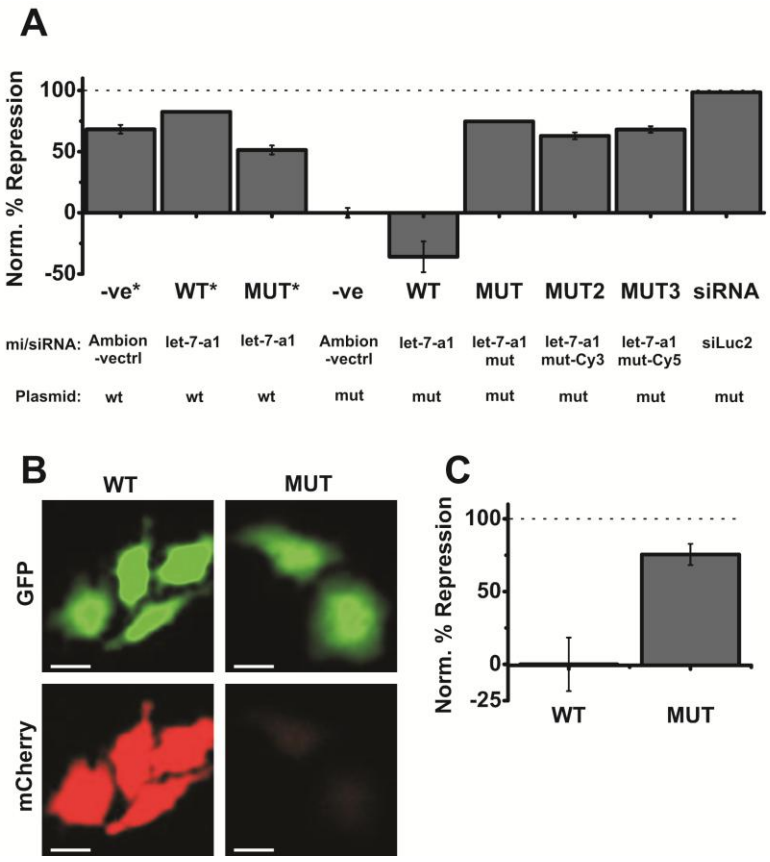

Figure 2.1. Effect of fluorophore modification and microinjection on miRNA function. (**A**) Luciferase reporter assays of HeLa cells co-transfected with luciferase reporter plasmids bearing the wild-type (wt) or a mutant (mut) 3`UTR of mouse HMGA2, and either a negative control siRNA (-ve's), wild-type let-7-a1 (WT's) or mutant let-7-a1 (MUT's) miRNA. An siRNA, Siluc2, was used as a positive control for repression. Renilla luciferase activity was used for internal normalization of each sample. All samples were normalized with respect to -ve. Results presented are from four replicates. Error bars, standard deviations. (**B**) Representative images of GFP fluorescence (top) and mCherry fluorescence (bottom) in cells co-injected with an mCherry reporter plasmid, a GFP control plasmid and, either the wild-type (WT) or mutant let-7-a1 (MUT) miRNA are shown. Scale bar, 20 μm. (**C**) Quantification of fluorescence data from panel **B**, normalized with respect to the WT sample. Results presented here are from duplicate experiments (n = 50 cells per experiment). Error bars, standard error of the mean.

To enhance the sensitivity of our assay, we included a mutant let-7-a1 that was previously shown to specifically repress a compensatory mutant of the target sequence (48). As expected, the repression of mutant target by mutant let-7-a1 was strong (~70%) and specific, consistent with previous observations (48). In this more sensitive assay, we then showed that attaching either a single Cy3 or Cy5 to the 3'-end of the let-7-a1 guide strand does not significantly compromise repression (**Fig. 2.1A**). Finally, we microinjected either mutant or wild-type let-7-a1 along with a mutant target and control fluorescent reporter gene plasmid and found that the intended target protein was specifically and strongly repressed, supporting the biological relevance of iSHiRLoC results (**Fig. 2.1B, C**).

Upon RNP assembly, microRNAs diffuse within well-resolved single particles. We next analyzed SPT trajectories of miRNA particles in cells injected with let-7-a1-Cy3 or let-7-a1-Cy5 (**Fig. 2.2A, B**) and found individual particles to undergo (at least) four distinct diffusive patterns (**Fig. 2.2C-E**). Control experiments showed that microinjection of PBS buffer alone or fluorescein-conjugated dextran, used as a marker for microinjection, contributed neither to the fluorescence signal (**Materials and Methods**) nor impacted the function and mobility of miRNA particles (**Fig. 2.1B** and **Fig. 2.2F**). Our SPT analysis reached a super-accuracy of ~30 nm at 100 ms temporal resolution (**Fig. 2.3**) with an observation window of, on average, ~3 s for let-7-a1-Cy3 (and cxcr4-Cy3) and ~1.5 s for let-7-a1-Cy5, before an individual particle went out of focus or photobleached (**Fig. 2.4**). Time-averaged mean squared displacement (MSD) analysis of individual SPT trajectories allowed us to characterize the distinct diffusive patterns as biased, corralled, fast or very slow Brownian diffusion, leading to a wide range of diffusion coefficients (**Materials and Methods**, **Fig 2.2E-G** and **Fig. 2.5**). Analysis of a large number of trajectories (**Table 2.1**) 4 h after microinjection revealed two distinct Gaussian distributions of diffusion constants, with average diffusion coefficients of ~0.26 $\mu m^2/s$ and ~0.034 $\mu m^2/s$ for both let-7-a1-Cy3 (**Fig. 2.2F**) and let-7-a1-Cy5 miRNA (**Fig. 2.2G**). These diffusion coefficients closely resemble those of messenger RNPs (87) and PBs (190), respectively, which are thought to be mechanistic intermediates of miRNA

Live cell analysis			
Experiment	**No. cells (no. particles*)**	**Initial no. particles*/frame**	**No. frames/video**
Cy3 labeled miRNAs	**4 h post-injection**		
Let-7a-1	4 (2115)	95	300
Cxcr4	3 (1038)	115	300
Let-7-a1-Cy5			
1 h post-injection	4 (240)	45	50
2 h post-injection	4 (1000)	251	50
4 h post-injection	4 (822)	295	50
8 h post-injection	6 (484)	90	50
32 h post-injection	4 (109)	21	50
Fixed cell analysis			
Experiment	**# cells (# particles)**	**Average # particles/cell**	**# frames/video**
	Let-7-a1, *cxcr4*		
1 h post-injection	5 (1125), *5 (1414)*	225 ± 121, *236 ± 71*	300, *500*
2 h post-injection	4 (1509), *5 (1500)*	377 ± 72, *300 ± 118*	300, *500*
4 h post-injection	3 (940), *5 (1210)*	313 ± 158, *242 ± 99*	300, *500*
8 h post-injection	4 (1168), 7 *(1825)*	292 ± 166, *261 ± 187*	300, *500*
32 h post-injection	8 (688), *9 (1294)*	86 ± 34, *144 ± 49*	300, *500*
MS2-Cy5 DNA	3 (702)	234 ± 125	300, *500*

*particles visible for greater than 9 frames

Table 2.1. Number of cells and particles used in both live and fixed cell analysis.

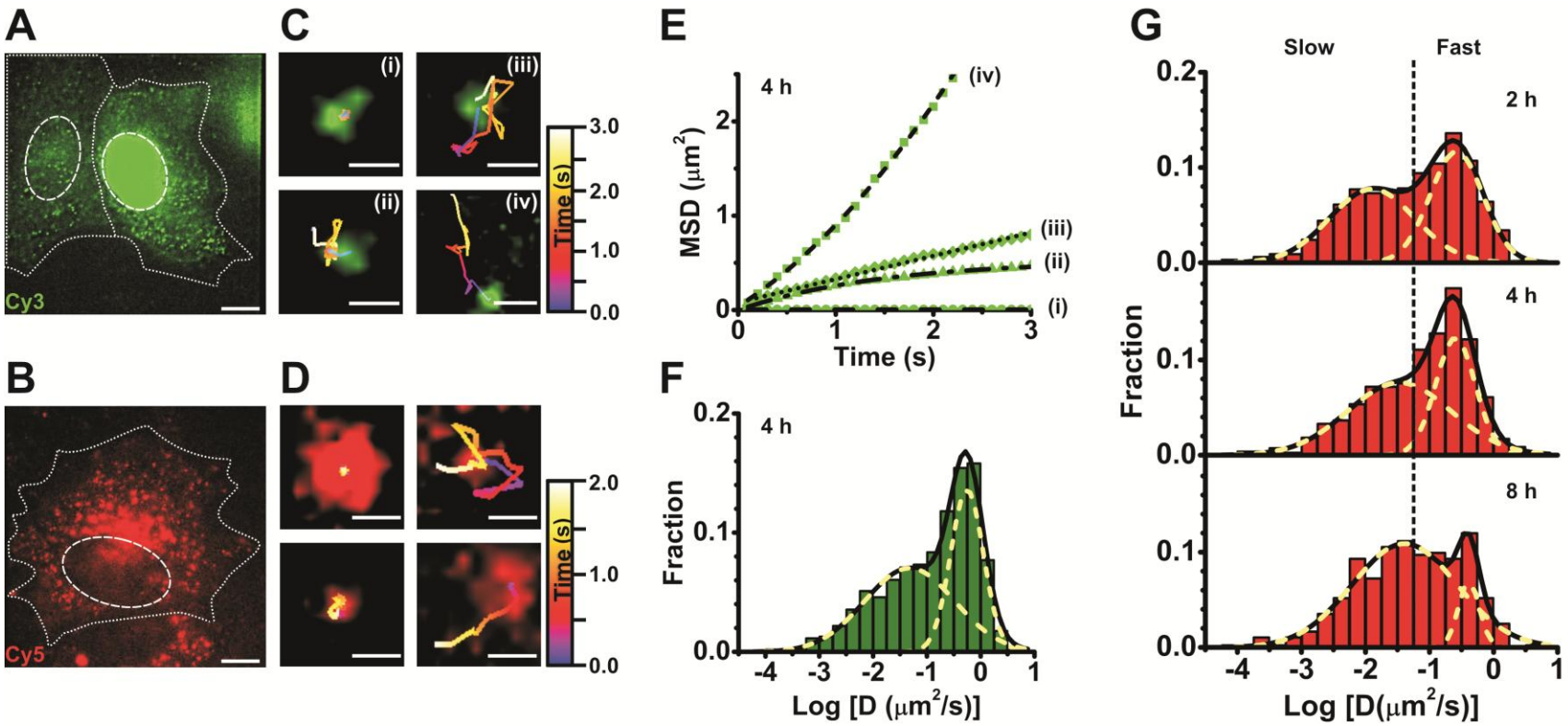

Figure 2.2. Single molecule high-resolution localization and tracking of miRNAs diffusing in living HeLa cells. Image of Cells microinjected with (**A**) let-7-a1-Cy3, (left, cytoplasmic injection; right, nuclear injection) and (**B**) let-7-a1-Cy5showing distinct particles of miRNA imaged 4 h and 2 h after microinjection respectively. Dashed and dotted lines indicate nuclear and cellular boundaries, respectively. Scale bar, 10 μm. Different types of diffusive motions exhibited by (**C**) let-7-a1-Cy3 and (**D**) let-7-a1-Cy5 miRNAs. Scale bars, 0.5 μm. (**E**) MSD plots of the let-7-a1-Cy3 particles shown in panel **C**. Data were fit with equations representing biased (iv), corralled (ii), fast (iii) and very slow (i) Brownian diffusion. Diffusion coefficients as derived from the fits are: D(i) = 0.0001 μm2/s; D(ii) = 0.06 μm2/s (corral radius = 0.52 μm); 15 D(iii) = 0.062 μm2/s; and D(iv) = 0.16 μm2/s (average velocity = 0.46 μm/s). (**F**) Distribution of diffusion coefficients calculated from

individual MSD plots of let-7-a1-Cy3 particles assuming Brownian diffusion. Cells were imaged 4 h after microinjection (n = 4 cells, **Table 2.1**). (**G**) Distribution of diffusion coefficients of let-7-a1-Cy5 at different time points after microinjection. Dotted lines represent demarcations of fast and slow particles to guide the eye, estimated based on segregation of the two Gaussian distributions 2 h after microinjection. Histograms represent data from multiple cells (n = 4, 4, 6 cells for data points corresponding to 2 h, 4 h and 8h, **Table 2.1**).

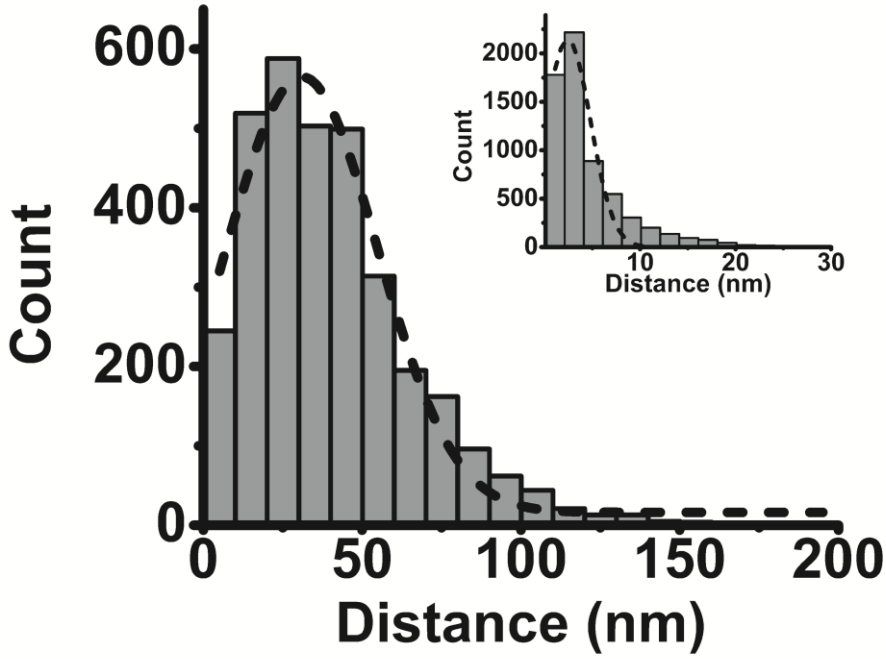

Figure 2.3. Precision of single particle localization. Histogram depicting the displacement of formaldehyde-fixed let-7-a1-Cy5 particles about their origin (n = 100 randomly selected particles). The location of each particle was tracked over time until it photobleached. The histogram was fit with a Gaussian function, which resulted in a mean of ~30 nm and a standard deviation of ~50 nm. Large jumps (>100 nm) were observed only when there were large fluctuations of intensity. Localization precision of immobilized beads (inset) was ~4 nm, largely owing to their higher signal-to-noise ratio (n = 100 randomly selected particles).

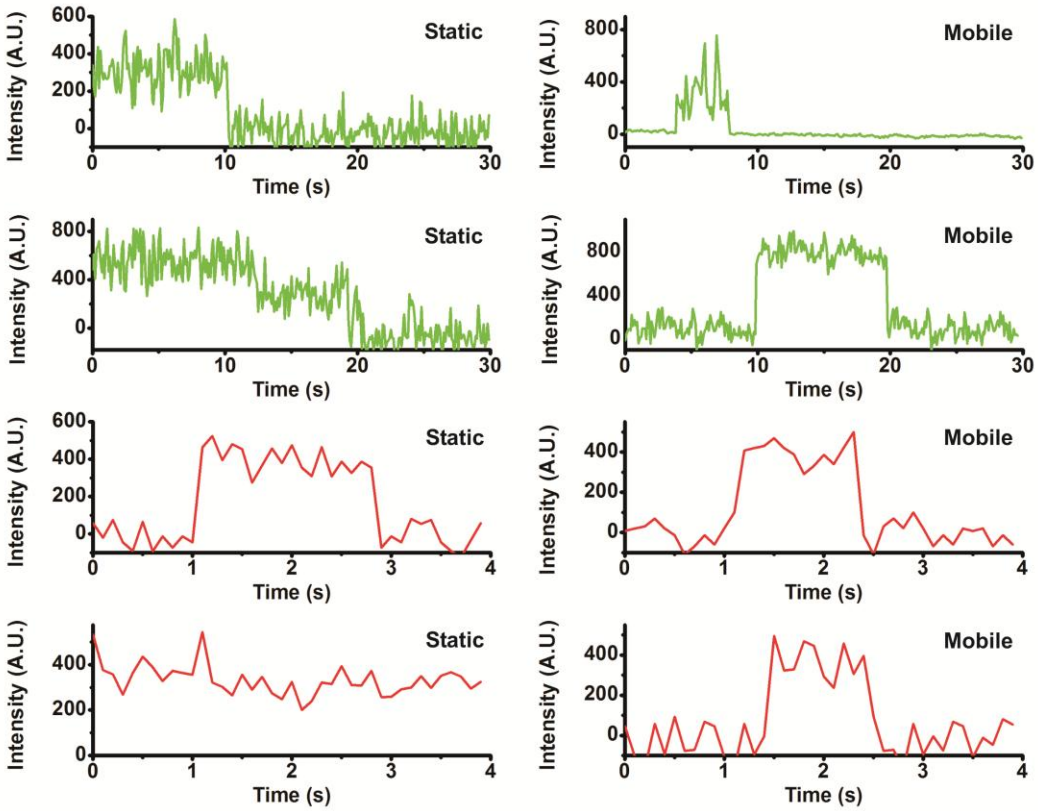

Figure 2.4. Intensity traces of particles undergoing diffusion in living cells. Intensity time trajectories of let-7-a1-Cy3 (green) and let-7-a1-Cy5 (red) particles are shown. Trajectories of both mobile and static particles are shown, as indicated in each trajectory. A significant proportion of particles had a relatively constant intensity during diffusion before disappearing. We infrequently observed large fluctuations in intensity as a particle was diffusing, possibly due to diffusion in the axial dimension (z-axis). We also occasionally observed stepwise changes in intensity of static particles, possibly due to photobleaching (see, for example, second trajectory from the top on the left side).

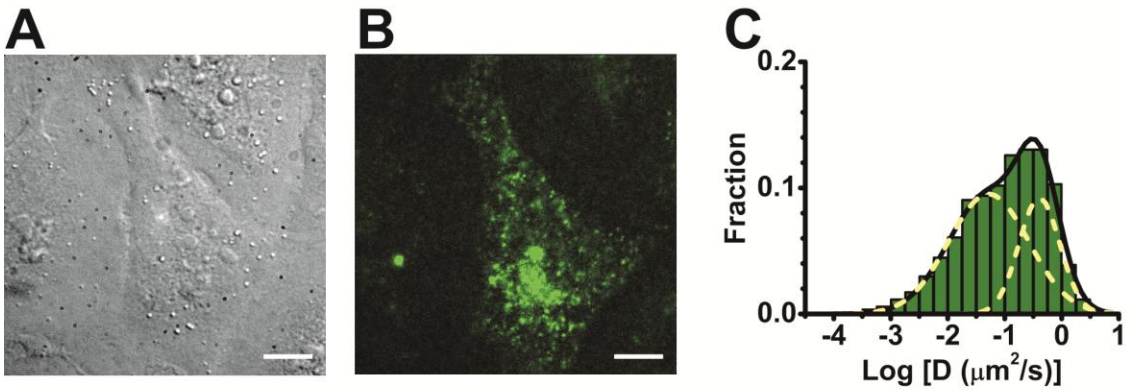

Figure 2.5. Intracellular diffusion of cxcr4 miRNA. (**A**) A DIC image and the corresponding (**B**) pseudocolored image of a cell microinjected with cxcr4-Cy3 and imaged 4 h after injection. Scale bar, 10 μm. (**C**) Distribution of diffusion coefficients calculated from individual MSD plots of cxcr4-Cy3. We observed two major Gaussian distributions, with different fractional abundance but similar average diffusion coefficients to those obtained with let-7-a1-Cy3.

repression. Given that we showed our miRNAs to be functionally active, at least some of the observed particles thus must contain miRNAs bound to and actively repressing target mRNAs.

The diffusion constants of miRNA containing RNPs increase over an 8-hour period. Next, we asked whether the diffusive properties of miRNA containing particles changed over time. Such changes may be expected for RISC-mediated loading of miRNAs onto mRNA targets and subsequent processing of the resulting mRNPs. To this end, we incubated let-7-a1-Cy5 microinjected cells for 1, 2, 4, 8 and 32 h prior to imaging. After 1 h and 32 h, high background and large inter-frame displacements of individual particles, respectively, precluded accurate tracking and this observation is consistent with the presence of fast diffusing free miRNAs and smaller miRNA-protein complexes that become blurred at our 100-ms time resolution (camera integration time). To quantify this effect, the relative average background intensity (**Fig. 2.6**) was calculated for each time point and the resultant curve was fitted with a single exponential function, yielding a rate constant of 0.82 ± 0.18 h^{-1}. The highest intensity is found at the 1 h time point, consistent with the notion that many miRNAs are not yet assembled into large and thus slowly diffusing RNPs, which become sufficiently localized to be visible at our 100-ms time resolution. We also determined the average number of particles visible for at least nine consecutive video frames for each time point, a threshold we used for our diffusion coefficient calculation. This criteria indirectly but faithfully reflects the number of large RNPs bearing a high molecular mass at each time point. The data fit well with a double exponential function with a rapid-rise phase characterized by a rate constant of 1.18 ± 0.62 h^{-1}, indicating assembly of miRNAs into larger RNPs (especially over the first 2 h of observation), and a slower decrease phase with a rate constant of 0.34 ± 0.13 h^{-1}, indicating an increase in RNP mobility of over the longer time frame (2 h – 32 h). For the intermediate time points (2 h, 4 h and 8 h) we again clearly discerned diffusing particles within two distinct Gaussian distributions, whose average Brownian diffusion constants systematically increased over time (**Fig.**

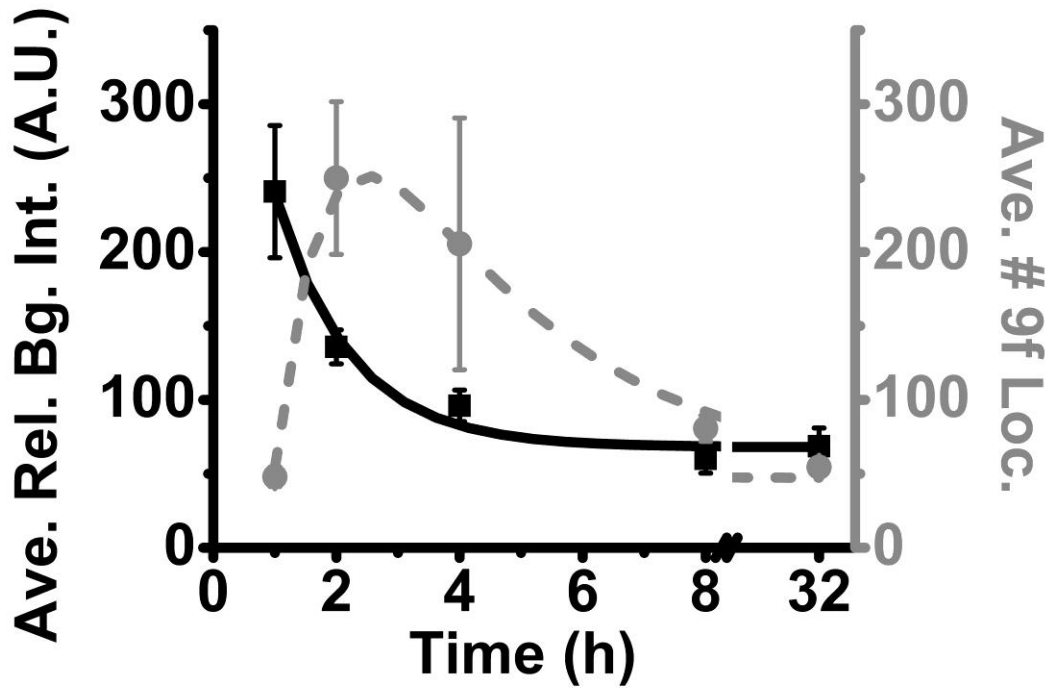

Figure 2.6. Analysis of background intensity and the average number of nine consecutive-frame localizations. The relative average background intensity (black, solid) was calculated for each time point and the resultant curve was fitted with a single exponential function. The average number of particles visible for at least nine consecutive video frames at each time point (grey, dashed), a threshold we used for our diffusion coefficient calculation, was obtained using the number of “trackable” particles in our single particle tracking experiments and the data fit well with a double exponential function. This trend (and rate constants) is very similar to that obtained in our fixed cell photobleaching analysis (**Fig. 2.8E**, black lines), further supporting our hypothesis that a relatively rapid initial assembly of miRNAs into large RNPs is followed by a slow disassembly at later times. Error bars, standard error of the mean.

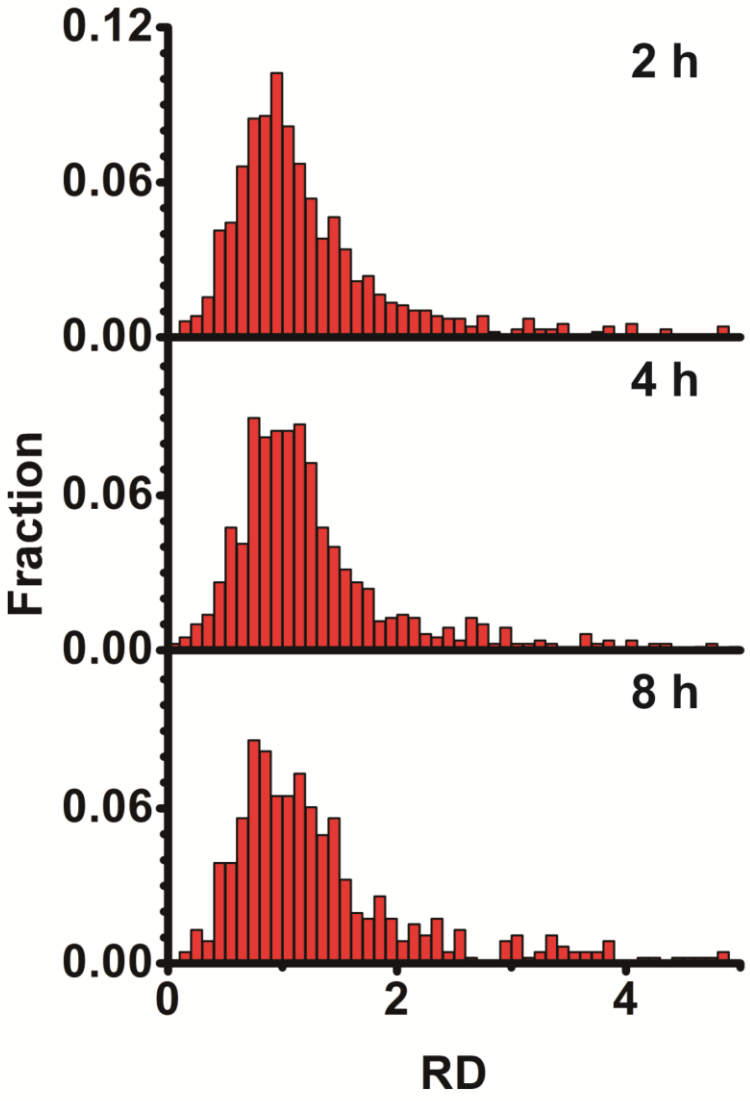

Figure 2.7. Relative deviation analysis of diffusion coefficients over time. Histograms depict the distribution of RD values (**Materials and methods**) at different times after let-7-a1-Cy5 microinjection (2 h, 4 h and 8 h, as indicated). RD values were calculated using MSD values corresponding to the sixth localization point and diffusion coefficients extracted from the first three points of the MSD time course. Although the distributions differ slightly, there is no significant increase in the fraction of higher RD values which, if present, would predict an increase in the fraction of particles undergoing directed motion (n = 4 cells for each, **Table 2.1**)

2.2G). This increase in mobility was not caused by an increase in the fraction of particles undergoing directed motion (**Fig. 2.7**), suggesting that, on average, the molecular weights of the RNPs decrease in the 2 to 8 h time frame.

Intracellular fluorophores can be counted accurately by stepwise photobleaching. The goal of iSHiRLoC is to measure both diffusion properties and assembly states of individual small RNA containing particles. To assess assembly, we utilized the relatively rapid stepwise photobleaching (135, 173) of single Cy5 fluorophores to quantify the number of miRNA molecules per particle. HeLa cells microinjected with either let-7-a1-Cy5 or cxcr4-Cy5 were formaldehyde-fixed and continuously illuminated until all fluorescent particles had photobleached (**Fig. 2.8A, B**). By counting the number of photobleaching steps for many particles (**Fig. 2.8C** and **Table 2.1**), we were able to deduce the distribution of their assembly states (**Fig. 2.8D**). While close to 50% of all particles contained a single miRNA 2 h after microinjection, a significant fraction held up to seven miRNAs (**Fig. 2.8C, D**). To test for bias from 'dark' (prebleached) Cy5, we microinjected a control DNA labeled with an average of 3.45 Cy5 fluorophores per molecule and counted a majority of 3 and 4 photobleaching steps in each particle (**Fig. 2.9**), as expected if prebleaching is negligible. In addition, we noted a strong overlap in the distribution of fluorescence intensities between particles observed in fixed and living cells (**Fig. 2.10**), together suggesting that our counting results in fixed cells accurately reflect the miRNA assembly states in living cells.

Time and mRNA dependent changes in miRNA assembly support a multiple target turnover model. Finally, we monitored miRNA assembly over time at the same time points as in our diffusion measurements. Similar to our observations in living cells, high background made it impossible to accurately localize single miRNA particles in cells that were fixed only 20 min after microinjection (**Fig. 2.11A**). At later time points (1 h to 32 h), we found two distinct assembly phases for let-7-a1 miRNA that fit well with a double-exponential function, suggesting the

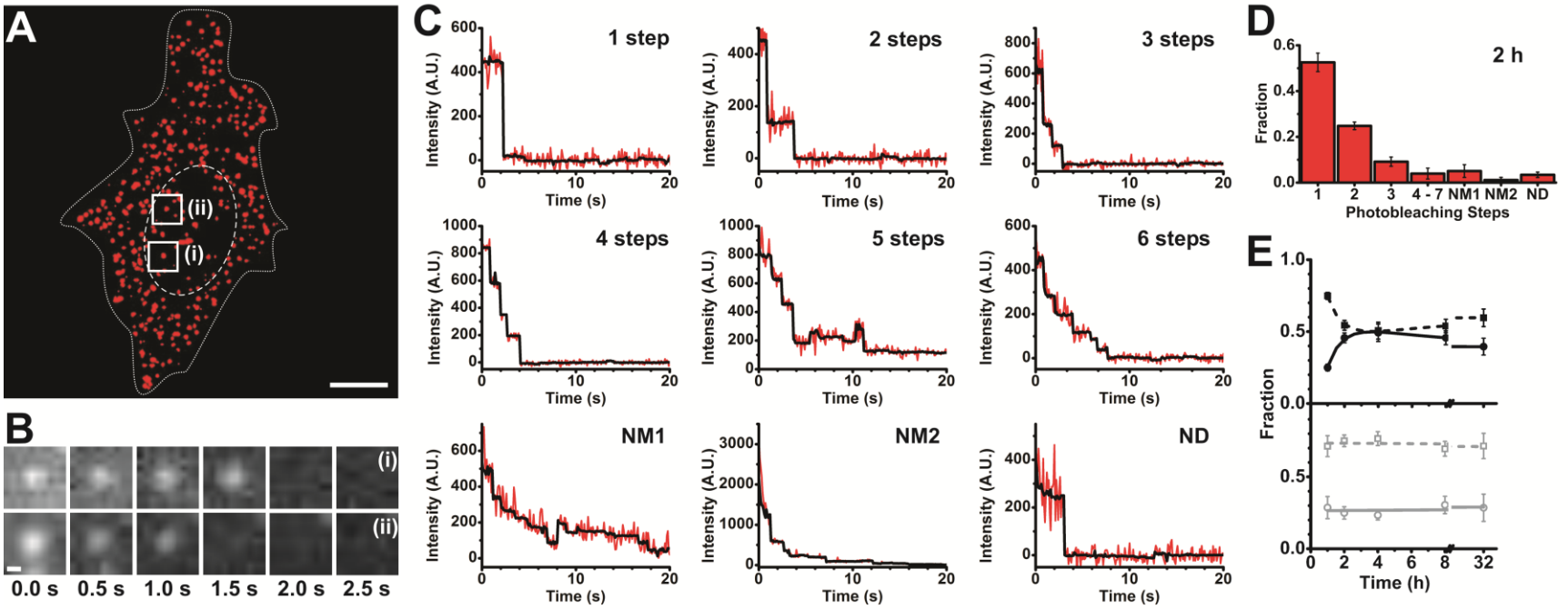

Figure 2.8. Counting of single miRNA molecules in fixed HeLa cells. (**A**) A pseudo-colored (background corrected) image of a formaldehyde-fixed HeLa cell showing the intracellular distribution of miRNAs 2 h after microinjection. Dashed and dotted lines indicate nuclear and cellular boundaries, respectively. Scale bar, 10 μm. (**B**) Sets of frames showing photobleaching of two different miRNA particles over the indicated time. The locations of the particles are labeled in panel **A**. Scale bar, 300 nm. (**C**) Representative stepwise photobleaching traces of individual miRNA particles within the cell shown in panel **A**. For some traces, the number of steps could not accurately be determined. These traces were further classified as either non-determinable multimer with indistinct steps (NM1); non-determinable multimer with initial peak intensity exceeding that expected from up to 7 fluorophores based on an average intensity of ~250 arbitrary units (A.U.)

per fluorophore bleaching step (NM2); or non-determinable as either monomer or multimer due to large fluctuations in intensity and rapid (< 3 frames) photobleaching (ND). (**D**) Distribution of miRNA photobleaching steps observed 2 h after microinjection (n = 4, **Table 2.1**). Error bars, standard deviation. (**E**) Change in the fraction of monomers (particles undergoing a single step of photobleaching, dotted line) and multimers (particles that bleach in two or more steps, solid line) of let-7-a1 (black) and cxcr4 (gray) miRNAs with time. Each data point is derived from multiple cells ($n_{let\text{-}7\text{-}a1}$ = 4, 4, 3, 4, 8 cells and n_{cxcr4} = 5, 5, 5, 7, 9 cells for 1 h, 2 h, 4 h, 8 h and 32 h, respectively; **Table 2.1**). Error bars, standard deviation.

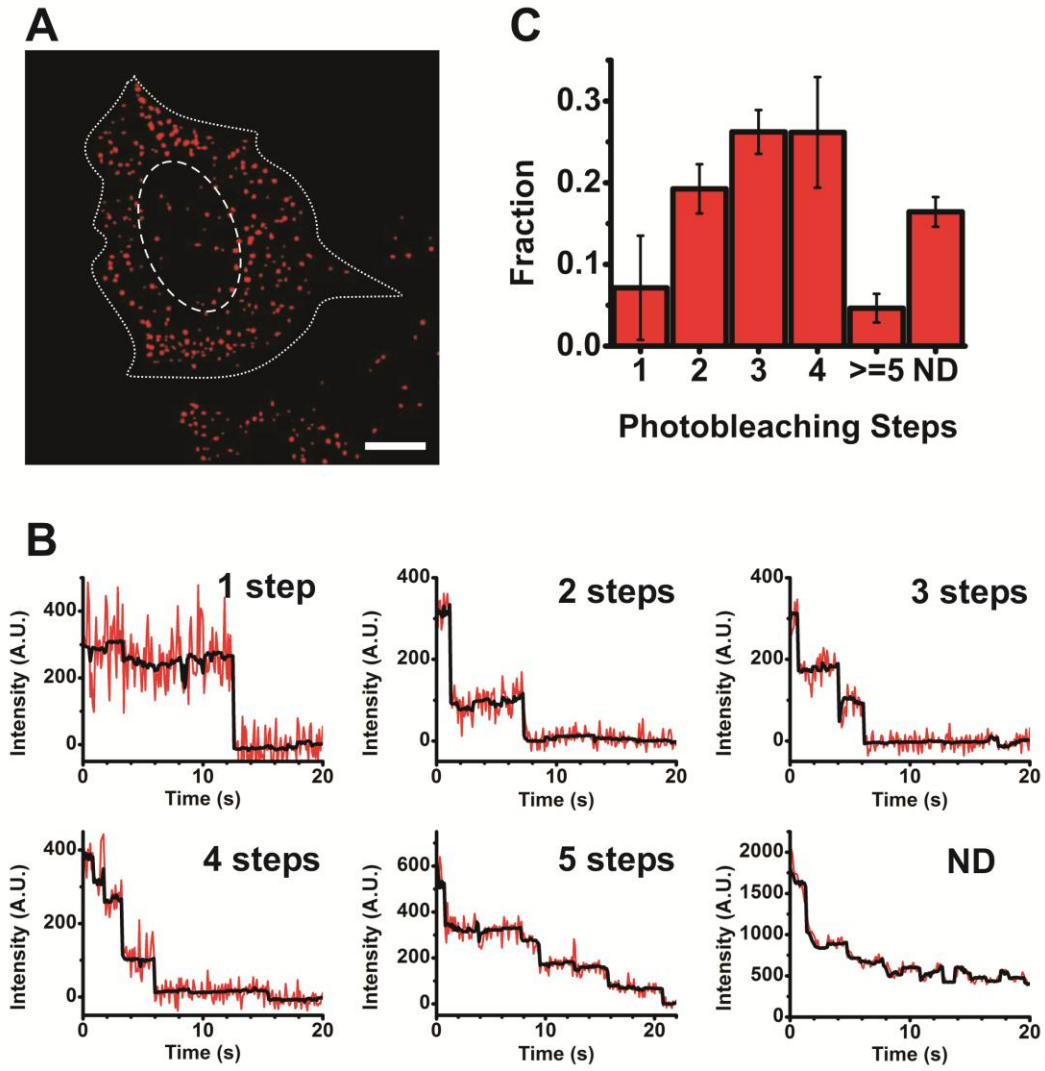

Figure 2.9. Stepwise photobleaching control. (**A**) Pseudo-colored, background subtracted image of cell microinjected with double-stranded DNA probe MS2 labeled with ~3.45 Cy5s per molecule. Outline of the cell (dotted) and its nucleus (dashed) are also shown. Scale bar, 10 μm. (**B**) Different types of photobleaching traces. (**C**). Distribution of photobleaching steps for MS2-Cy5 injections (n = 3 cells, **Table 2.1**).

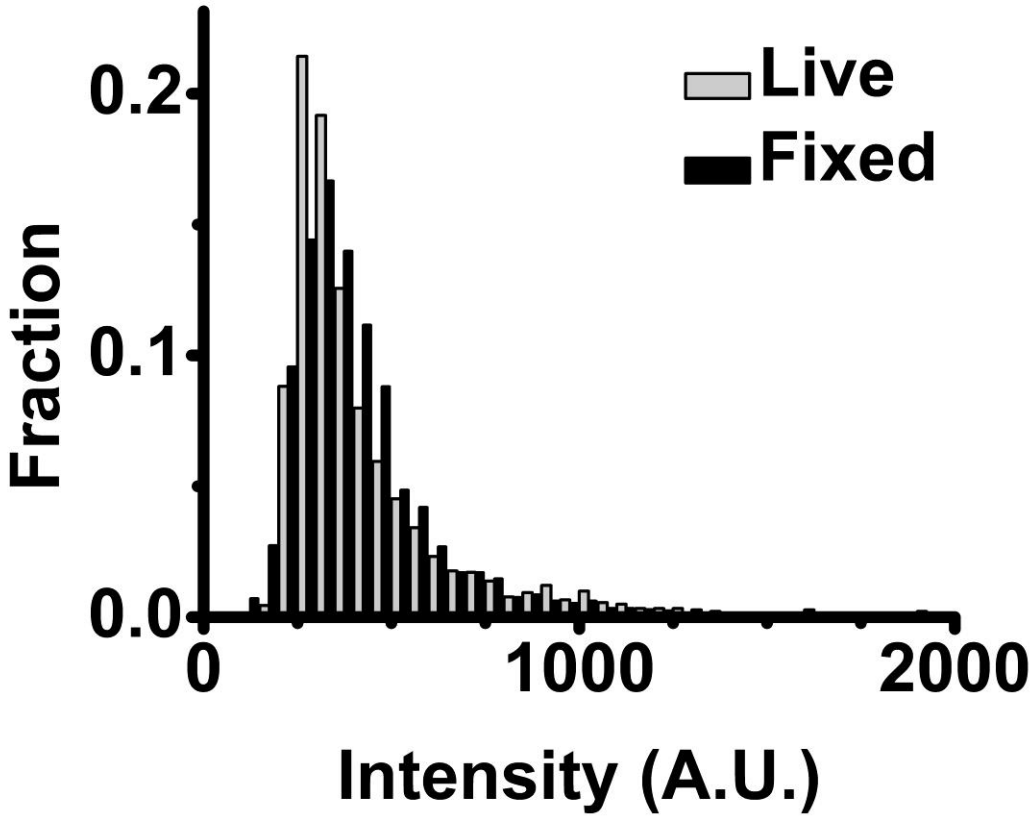

Figure 2.10. Comparison of fluorescence intensities. Intensity of Cy5-labeled miRNA containing particles was compared between living (grey) and fixed cells (black), imaged 2 h after microinjection. The intensity observed in the first frame of each video (100 ms exposure time) was used to create this histogram (n = 4 cells each).

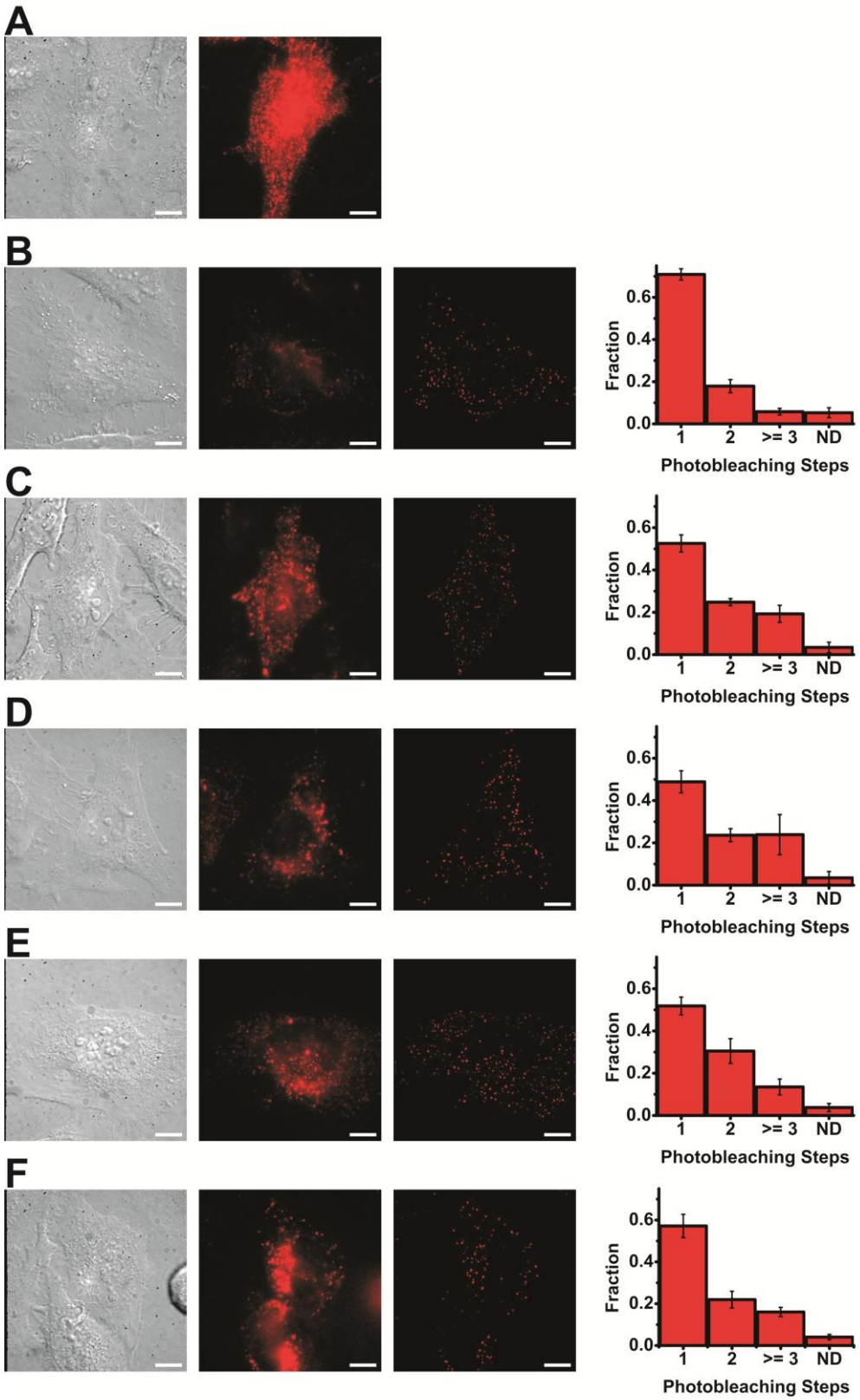
A
B
C
D
E
F
Fraction
0.0
0.2
0.4
0.6
1
2
>= 3
ND
Photobleaching Steps

Figure 2.11. Fixed cell images from various time points. Representative images of fixed cells incubated for various amounts of time after microinjection and their corresponding stepwise photobleaching distributions. Shown are (from left to right) DIC, pseudo-colored, pseudo-colored/background-subtracted images and photobleaching step distributions of cells injected with let-7-a1-Cy5 and fluorescein dextran. Images and distributions were taken from cells fixed (**A**) 20 min, (**B**) 1 h, (**C**) 2 h, (**D**) 4 h, (**E**) 8 h and (**F**) 32 h after microinjection (**Supplementary Table 1**). Scale bar, 10 μm. The background was very high in cells incubated for 20 min after microinjection, thus it was practically impossible to locate single molecules.

existence of two kinetic processes (**Fig. 2.8E**). The faster phase is characterized by a rate constant of 1.2 ± 0.2 h^{-1}, during which the number of RNPs containing more than one miRNA increases; we note that this time evolution resembles that of the initial assembly of miRNAs into RNPs observed over the earliest (1-2 h) live cell time points. The slower phase with a rate constant of 0.14 ± 0.08 h^{-1} leads to a modest increase in RNPs containing just a single miRNA and matches the timing of the increase in mobility of miRNA containing particles (**Fig. 2.2G** and **Fig. 2.6**) as well as that of miRNA-induced mRNA target degradation . Thus, our data support a multiple turnover model of miRNA-mediated gene repression, wherein miRNA:RISC (miRISC) complexes first assemble on their cognate mRNA targets, then associate with PBs where the mRNA is degraded and the miRNAs subsequently released back into the cytoplasm to bind additional mRNA targets (**Fig 2.12**). Consistent with this model, cells microinjected with the artificial cxcr4 miRNA, which is predicted to find 10-fold fewer mRNA target molecules in a HeLa cell, do not show these time dependent changes in the fractions of single and multiple miRNA containing particles (**Fig 2.8E**).

2.4 Discussion

Single miRNA molecules have been previously counted both *in vitro* (191-193) and *in situ* (194) but neither *in vivo* nor in a form that allowed them to still be functional. All prior methods required the hybridization of microscopically-detectable complementary oligonucleotides to miRNAs, after cell lysis or fixation, and were predominantly used to quantify endogenous miRNAs. Although efficient in understanding miRNA expression patterns, even at the single cell level (194), these methods cannot be used to visualize the intracellular assembly and transport of miRNA associated complexes, processes fundamental to their biological function. Here we report a novel method to visualize single, functional, fluorophore labeled miRNA molecules inside live as well as formaldehyde-fixed

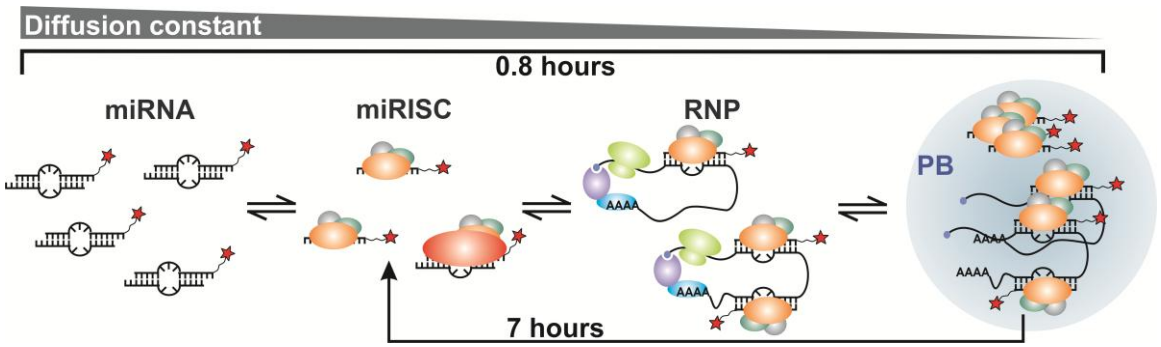

Figure 2.12. Model illustrating intracellular miRNA assembly. Model consistent with our data, depicting the sequential assembly of miRNA into miRISC complexes that bind translationally active mRNA targets to form large RNPs, associate with PBs, and are finally released upon PB mediated mRNA degradation to engage in multiple turnover of targets. The indicated timeframes were derived from the kinetics measured in the current study.

human cells, a technique laying the foundation for understanding their intracellular localization, assembly and diffusion.

Detection of single fluorophore labeled molecules inside living cells presents many challenges. Firstly, the concentration of the molecule under interrogation should be low enough to observe them as well isolated, diffraction-limited spots. Hence, we turned to microinjection, instead of other intracellular delivery methods such as transfection, which has the inherent disadvantage of trapping molecules in lipid vesicles. Microinjection also comes with the added advantage that the amount injected can be precisely controlled and even varied between different cells on the same dish. Secondly, autofluorescence is a major challenge for intracellular microscopy. Signal from fluorescent probes should be high enough to be visible above the autofluorescent background, which can be difficult to achieve. Using an appropriate medium formulation (113) and mode of illumination (100), we achieved high enough signal-to-noise ratios to reach single molecule detection sensitivity. Thirdly, photobleaching of fluorescent probes limits the number of photons that can be collected for efficient localization of single molecules. Although impossible to prevent entirely, photobleaching was delayed *in vivo* by using certain medium additives. Our imaging medium contains both an oxygen scavenging system, which prevents photobleaching mediated by oxidation, and a triplet state quencher, which prevents the formation of long-lived non-fluorescent excited states prone to oxidation and hence photobleaching (**Materials and methods**).

In our single particle tracking experiments, we typically observe brief sojourns of miRNAs in the imaging plane before they move out of focus or photobleach. Only few particles exhibited large variations in intensity along their trajectory (**Fig. 2.4**), potentially representing diffusion along the z-axis. In the case of random diffusion, all degrees of translational freedom are equivalent and movement along any two dimensions (2D) is a valid representation of the three-dimensional (3D) movements (195). A 2D diffusion coefficient is thus a good estimate of the mobility of a three-dimensionally diffusing particle. Limited by our

time resolution (100 ms) we cannot, however, rule out the possibility that miRNA particles undergo undetected diffusion along the z-axis between successive frames of imaging. Since we predominantly estimate the relative changes in mobility rather than absolute molecular mass, 2D diffusion coefficients suffice.

Schwille and coworkers (171) have previously characterized the localization and diffusion of fluorophore labeled silencing RNAs and EGFP labeled Ago2, an important component of RISC, in living cells using confocal microscopy and fluorescence cross correlation spectroscopy. They reported a cytoplasmic diffusion coefficient of ~5.4 $\mu m^2/s$ for RISC, which translates into an ~3 MDa complex. We do not observe such particles possibly due to limits in our time resolution (100 ms) and/or since they may not be visible for 9 frames, our threshold for diffusion coefficient calculation. We have evidence for the notion that we may be losing rapidly diffusing particles from our analysis in the fact that the diffusion coefficient distribution measured 8 h after microinjection becomes visibly curtailed above a diffusion coefficient of ~2 $\mu m^2/s$ (**Fig. 2.2G**). The main particles we do observe, however, have diffusion coefficients commensurate with those of miRNAs bound to mRNAs or miRNA localized in PBs, key mechanistic intermediates of mRNA repression by miRNAs, as both complexes bear a much higher molecular mass than that of RISC. We also note that the number of miRNAs we observe in the focal plane of a microinjected cell (~500 on average per fixed cell, considering both the number of distinct particles and their individual photobleaching steps; see **Table 2.1** and **Fig. 2.8D**) correlates well with the volume fraction of the cell in focus multiplied with the total number of microinjected miRNAs (~18,000), suggesting that we can account for a significant fraction of the microinjected miRNAs.

Based on our live and fixed cell data, we derive a model depicting the assembly of miRNAs into large RNPs (such as a miRISC bound to a ribosome-decorated mRNA or PB), followed by their release from the complex. On the one hand, our live cell data show that miRNAs start out as fast-moving, blurred particles (until ~1 h after microinjection), assemble into observable slow-moving

RNPs (between 1 h and 2 h), and once again become faster (and thus lower in molecular mass) as their residence time in cells increases (2 h – 32 h, **Fig. 2.2G** and **Fig. 2.6**). On the other hand, our fixed cell data clearly show a sharp decrease in the number of single miRNA containing particles within the first 1-2 hours, followed by a slow increase at later time points (**Fig. 2.8E**). This trend was not observed when cells were injected with the artificial cxcr4 miRNA, most likely due to its ~10 fold lower number of expressed mRNA target molecules as compared to let-7. As a result, the sharp decrease in monomeric miRNAs between 1 h and 2 h is expected to be ~10-fold smaller than that observed with let-7-a1 (down to ~2.5% from ~25%), thus making it indiscernible in our experiments (that have an estimated error in the decrease amplitude of ~±5%). Additionally, cells fixed 20 min after microinjection give rise to very high background fluorescence, which drastically decreases after 1 h (**Fig. 2.11A**)**.** Based on these observations, we propose the following chronological model for miRNA assembly (**Fig. 2.12**): At initial time points, less than 1 h after microinjection, a majority of miRNAs remains free or unbound, thus contributing to a large background in our live and fixed cell experiments. Between 1 and 2 h, most miRNAs assemble into miRISC-mRNA complexes, thereby depleting the free miRNA population. This assembly leads to relatively slowly moving complexes in living cells and a corresponding decrease in the population of single miRNAs containing particles in fixed cells. As time proceeds, miRNA mediated mRNA degradation occurs, releasing miRISC complexes to possibly elicit further rounds of repression, which is represented by an increase in the mobility of miRNA particles in live cells and an increase in the population of monomeric miRNAs in fixed cells. Time dependent changes in miRNA assembly were not observed for cxcr4, consistent with the lesser number of mRNAs it targets. We also observe a decrease in the number of miRNA particles at long incubation times (32 h), which may represent miRNA degradation, cleavage of the fluorophore from the miRNA, and/or even efflux of labeled miRNAs from the cell. In addition, dilution of microinjected miRNA through cell division has to be considered. Overall, our observations for the first time reveal a stepwise

assembly of miRNA containing complexes involving mRNAs or PBs, followed by the release of miRISC complexes from them into the cytoplasm due to mRNA degradation, possibly accompanied by miRNA (or fluorophore) degradation.

In conclusion, in iSHiRLoC we have developed a broadly applicable method that visualizes both diffusive properties and assembly states of functional small non-coding RNAs in cultured cells. We find that miRNAs exhibit different types of Brownian diffusion in living HeLa cells with (at least) two widely ranging Gaussian distributions of diffusion coefficients, representing two complexes of distinct molecular mass, consistent with messenger RNPs and processing bodies. Stepwise photobleaching revealed that the largest fraction of these particles contains single miRNA molecules. A still significant fraction of particles, however, contains multiple miRNA molecules, strongly invoking the formation of higher-order miRNA complexes either assembled on mRNA targets or associated with PBs. Time dependent changes in diffusion and assembly were observed in cells injected with let-7-a1 miRNA, supporting the multiple turnover model outlined in **Fig. 2.12**. In the future, iSHiRLoC can be extended by multicolor imaging (138, 172) to co-track a miRNA with its corresponding target mRNA, RISC or PB proteins and map the dynamic interaction network of RNAi, with the ultimate goal of understanding its mechanism through single molecule systems biology.

2.5 Acknowledgments

We thank D. Bartel and C. Mayr for a generous gift of plasmids containing the 3' UTR of HMGA2, R. Tsien for a generous gift of a plasmid containing the mCherry ORF, A. Manzo for MSD software development, H. Ding, A. Gafni and D. Steel for sharing their intensity analysis routine, the Microscopy and Image Analysis Laboratory at the University of Michigan for access to Imaris, and A. Mapp for access to her plate reader. This work was supported by NIH grant GM081025 to N.G.W.

Chapter 3

Quantitative Analysis of microRNA Localization within Processing Bodies at Single Molecule Sensitivity

3.1 Introduction

microRNA (miRNA) mediated gene regulation is an evolutionarily conserved cellular process wherein small RNAs, ~22 nt in length, typically repress eukaryotic protein expression post-transcriptionally (11, 12). miRNAs have been reported to employ several different mechanisms to elicit gene repression, however, these mechanisms are all under intense debate (47). Some data suggest that miRNAs interfere with initiation of messenger RNA (mRNA) translation (66, 70, 71), whereas others support the notion that repression occurs at post-initiation steps (74, 75, 196). More recent reports favor an mRNA destabilization model wherein miRNA induced silencing complexes (miRISCs), upon binding to the 3`UTR of mRNA targets, cause mRNA decay via deadenylation (78, 79). In contrast, Fabian *et al*. (197) had recently reported that miRNAs mediate target repression by a combination of both translational inhibition and mRNA decay. Their data suggest that miRNA mediated mRNA deadenylation and decay follow the initial inhibition of translation and thus alludes to the possibility for miRNA mediated mRNA decay to occur as a consequence of translational inhibition.

In eukaryotes, deadenylation of mRNAs is either closely followed by or simultaneously occurs with 3`-to-5` or 5`-to-3` mRNA degradation (80). Deadenylation is mediated by the exosome (198), whereas the latter

predominantly mandates an initial decapping step (199), involving the removal of the canonical 7-methyl guanosine ‘cap’ at the 5` end of mRNAs, followed by Xrn1 mediated mRNA degradation (200). Cap removal irreversibly tags an mRNA for degradation and this process is tightly regulated both spatially and biochemically. Although spatial compartmentalization of 5`-to-3` mRNA degradation was initially based only on the localization of Xrn1 exonuclease (201), decapping enzymes (202) and several other RNA processing enzymes (203) to distinct cytoplasmic foci; it was later proven that both decapping and mRNA degradation can indeed occur in these discrete areas (204). Notably, these foci do not contain ribosomes and are hypothesized to only contain translationally inactive messenger ribonucleoprotein complexes (mRNPs) (205). These cytoplasmic foci are now widely known as processing bodies (PBs).

PBs are dynamic structures, i.e. there is a continuous exchange of proteins and mRNAs between these foci and the cytoplasmic pool (189, 206). Additionally, the number (per cell) and size of PBs are cell cycle dependent (207). Previous research has shown that miRNAs and its associated proteins localize to PBs (67, 81, 173), and the inhibition of miRNA biogenesis or depletion of GW182 proteins, a central role player in miRNA mediated target repression (208, 209), causes the disappearance of PBs (210, 211). Conversely, depletion of certain PB components also prevented effective inhibition of mRNA targets (212). Moreover, a positive correlation exists between miRNA mediated mRNA repression and the accumulation of repressed mRNAs at PBs. As a specific example, cationic amino acid transporter (CAT-1) mRNA, a target of miR-122, localizes to PBs when Huh-7 hepatoma cells are enriched in miR-122 but exits PBs when repression is relieved either by stress or by the addition of miR-122 anti-miRs (213), chemically modified oligonucleotides that inhibit miRNA function by binding with complete complementarity. More general examples entail the distribution of PBs during embryogenesis and organ development wherein global suppression of miRNA function and reduction in miRNA abundance is coincident with loss of microscopically visible PBs (214, 215). These observations led to the hypothesis of yet another mechanism for the regulation of gene expression by

miRNAs. According to this hypothesis, PB assembly complexes release miRISC bound mRNPs from polysomes and promote association with other repressed mRNPs (205), thereby either mediating the formation of a PB or targeting these large complexes to PBs (81, 212). Repressed mRNPs are then stored or degraded within these foci, leading to the possibility for the spatial organization of gene regulation. This idea is very similar in concept to that of Fabian *et al.* (197), wherein mRNA degradation occurs as a consequence of translational inhibition. However, it is still not clearly understood whether PBs are indispensible for repression or miRNA repressed mRNPs localize to PBs as a consequence of other modes of repression, for example translational inhibition mediated by mRNA deadenylation (83). Regardless, PBs play an important role in miRNA mediated mRNA repression by, at the very least, sequestering previously repressed mRNPs and subjecting them to (further) degradation.

Not much is known about the distribution of miRNAs within PBs and the nature of miRNA:PB interactions *in vivo*. Previous work, based on ensemble intensity quantification, had estimated that only a very small proportion of cellular miRNAs and miRISC proteins localize to PBs (67, 189). In order to gain a deeper understanding on the dynamic and possibly heterogeneous nature of miRNA:PB interactions, and to more accurately quantify the distribution of miRNAs within PBs, we developed a method to observe single molecules of miRNAs (**Chapter 1**) and colocalize them with single PB particles inside human cells. To this end, miRNAs and PBs were labeled with spectrally different fluorescent probes and single particles (and molecules) of miRNAs were localized and tracked with respect to single PBs in the same cell. We then used spatial mapping software to colocalize the spectrally distinct fluorescent probes with ~10 nm resolution. Our single molecule counting by stepwise photobleaching of fluorophores (**Chapter 1**), performed subsequent to high-resolution colocalization of PBs and miRNAs, provides a robust quantification of miRNA distribution within PBs. With this added accuracy (in quantification) and resolution, we show that there is a heterogeneous distribution of miRNAs within PBs. We additionally show that

miRNAs interact either stably or transiently with PBs in live HeLa cells supporting the possibility for diversity in composition of miRNA complexes and PBs.

3.2 Materials and methods

Plasmids, DNA and RNA oligonucleotides. The EGFP ORF was PCR amplified from pEGFP-C1 (Clontech) using DNA primers bearing AgeI and XhoI restriction enzyme (RE) sites. Plasmid pEGFP-hDcp1a was created by removing the mRFP1 ORF from pmRFP1-hDcp1a (gift from Nancy Kedersha, Brigham Women's hospital) using AgeI and XhoI restriction enzyme digestion and replacing it with the PCR amplified, RE digested ORF of EGFP. pEGFP-hAgo2 was received as a generous gift from Phillip Sharp (MIT).

RNA oligonucleotides were purchased from the Keck Biotechnology Resource Laboratory at the Yale University School of Medicine with a 5' phosphate (P) and a 3' amino group on a C7 carbon linker. RNA was purified as described (177) and the 3' amine groups were labeled with Cy3 or Cy5 succinimidyl ester as described (177, 178). RNA sequences were as follows:

let-7-a1 guide: P-UGAGGUAGUAGGUUGUAUAGUU
let-7-a1-passenger: P-CUAUACAAUCUACUGUCUUUCC
Guide and passenger strands were heat-annealed in a 1:1 ratio, resulting in duplex miRNAs, and frozen for further use.

Cell culture and transfection. HeLa cells (CCL-2, ATCC) were cultured in DMEM (GIBCO, Invitrogen) supplemented with 10% (v/v) fetal bovine serum (FBS) and non-essential amino acids (NEAA) at 37 ^{o}C. For Ago2-Dcp1a colocalization experiments, 1.8 x 10^5 cells were seeded onto coverslip bottom dishes (Mat-tek) one day before transfection. Cells were transfected with pEGFP-Ago2, pmRFP1-hDcp1a or a combination of both using lipofectamine 2000 (Invitrogen) and imaged 24 h post transfection. Regular media was replaced with phenol red free growth media 4 h prior to imaging and cells were imaged in

phenol red free DMEM. For Dcp1a-miRNA colocalization and co-tracking experiments, 2.4 x 10^5 cells were reverse transfected with pEGFP-hDcp1a or pmRFP1-hDcp1a using Fugene HD (Roche) transfection reagent, in delta-T dishes (Bioptechs), one day before microinjection. Regular medium was replaced with phenol red-free medium 4 h prior to microinjection and subsequently with a minimal medium (HBS) immediately before microinjection. After microinjection, cells were washed several times with HBS and incubated in phenol red-free DMEM containing 2% (v/v) FBS and 1x NEAA and in the presence of a 5% CO_2 atmosphere for 2 h prior to imaging. Live cell and fixed cell imaging were done in HBS-OSS and PBS-OSS respectively (**Chapter1, MATERIALS AND METHODS, live cell imaging and data analysis** and **Fixed cell imaging and data analysis**).

Microinjection. Microinjections were performed using a Femtojet pump (Eppendorf) and a microscope mounted Injectman NI2 micromanipulator (Eppendorf). Solutions to be microinjected were centrifuged at 16,000 x g for 15 min at 4^{o}C just prior to microinjection. The micropipette (Femtotips, Eppendorf) was loaded with 1.5 µM let-7-a1-Cy5 labeled miRNA and optionally with 0.05% 10 kDa Fluorescein dextran or Alexa555-dextran (Invitrogen) in PBS. Fluorescein and Alexa555, spectrally distinct from Cy5, served as a markers to locate microinjected cells mainly because Cy5 photobleached relatively quickly (within ~1.5 s). All microinjections were performed at 100 hPa microinjection pressure for 0.5 s with 20 hPa compensation pressure.

Fluorescence microscopy. Ensemble hAgo2-hDcp1a colocalization experiments were performed on a Nikon TE2000 microscope equipped with a Cool-SNAP HQ CCD camera (Photometrics). Cells were imaged using a 40x objective at 0.5 – 1s camera exposure time. Light from a mercury lamp was spectrally filtered using 470/40x and 575/50X excitation filters to specifically excite EGFP and mRFP1 respectively via wide-field epi-illumination. Fluorescence from EGFP was detected using a 400DCLP dichroic filter and 460/50m emission filter; and that from mRFP1 was detected using a 605dxcru

dichroic filter and 625/30m emission filter. All filters were purchased from Chroma.

Super-accuracy single particle tracking was performed as described (**Chapter1, MATERIALS AND METHODS, Fluorescence microscopy**). EGFP and mRFP1 were imaged using the fluorescein and Cy3 filter sets respectively. Ago2 and Dcp1a particle tracking was done at 92x, 120x or 192x magnification using lower laser power and different camera gain settings as compared to single miRNA particle tracking. Signal from different fluorophores were recorded on the same region of the camera, one after another (not simultaneously) for multi-color imaging.

Data analysis. ImageJ (NIH) was used for image analysis in ensemble fluorescence microscopy. For single molecule microscopy, images from spectrally distinct fluorophores arising from the same particle were mapped onto one another using in-house MATLAB routines to correct for chromatic aberrations arising from the microscope optics. To this end, sparsely distributed (~100 beads per 68 x 68 μm^2), non-specifically immobilized ~200 nm tetraspek beads (Invitrogen) bearing four spectrally distinct fluorochromes were imaged using 488nm, 532nm and 640nm lasers respectively. The intensity distribution from each fluorohpore on the same bead were then independently fit with a 2D Gaussian function and localized with ~5 nm spatial accuracy. Combining the location of all beads thus determined, a local weighted mean transformation (136) was calculated to map the entire field of view for different fluorophore emissions. The resultant map thus created was then used as a template to co-localize EGFP/mRFP1 and Cy5 particles with ~10 nm spatial resolution. Single particle tracking and single molecule counting were done as described (**Chapter1, MATERIALS AND METHODS, live cell imaging and data analysis** and **Fixed cell imaging and data analysis**). Certain videos were deconvolved using a theoretical point spread function in AutoQuantX2 (MediaCybernetics) to artificially improve the signal to noise ratio.

As we use only a finite observation window, small observation time coupled with fluorophore photobleaching, to measure the dwell time of miRNAs in PB, a systematic bias is introduced in the calculation of observed dwell times. This was corrected for by measuring the rate at which single Cy5 fluorophores photobleached (k_{photo}) and subtracting this value along with the reciprocal of the observation window (t_w) from the observed rate ($k_{observed}$) (21):

$$\boldsymbol{k_{actual} = k_{observed} - k_{photo} - \frac{1}{t_w}}$$

3.3 Results

Ago2 and miRNAs colocalize with processing bodies. Previous reports had suggested that miRISC-bound mRNA complexes localize to PBs under both normal and stressed conditions (67, 189, 213). To test whether ectopically expressed Ago2 and microinjected miRNAs, core components of miRISC, localize to PBs we performed multi-color ensemble fluorescence microscopy (**Fig. 3.1**). Dcp1a, a decapping protein that localizes to PBs, fused to mRFP1 served as a PB marker. Under conditions of transient transfection, both EGFP-Ago2 and mRFP1-Dcp1a localized to distinct foci in the cytoplasm of HeLa cells (**Fig. 3.1A**). The distributions of the number of Ago2 foci and PBs (Dcp1a foci) per cell (**Fig. 3.1B, C**) were similar to those present endogenously (81, 189, 190). Notably, only ~50% of Ago2-EGFP expressing cells contained punctate structures of Ago2, whereas all cells expressing Dcp1a-mRFP1 contained foci enriched in Dcp1a (**Fig. 3.1B, C**). A majority of Ago2 foci (~82%) in cells co-expressing Ago2 and Dcp1a colocalized with Dcp1a foci, strongly suggesting that large punctae of Ago2 are themselves indicative of PBs. We additionally found that Cy5 labeled, microinjected miRNAs also formed punctate structures, which also colocalized (~72% of all Cy5 labeled punctuate structures respectively) with PBs (**Fig. 3.1D**). However, only ~15% of all Cy5 signal and ~10% of all EGFP signal, arising from miRNAs and Ago2 respectively, colocalized with PBs. These

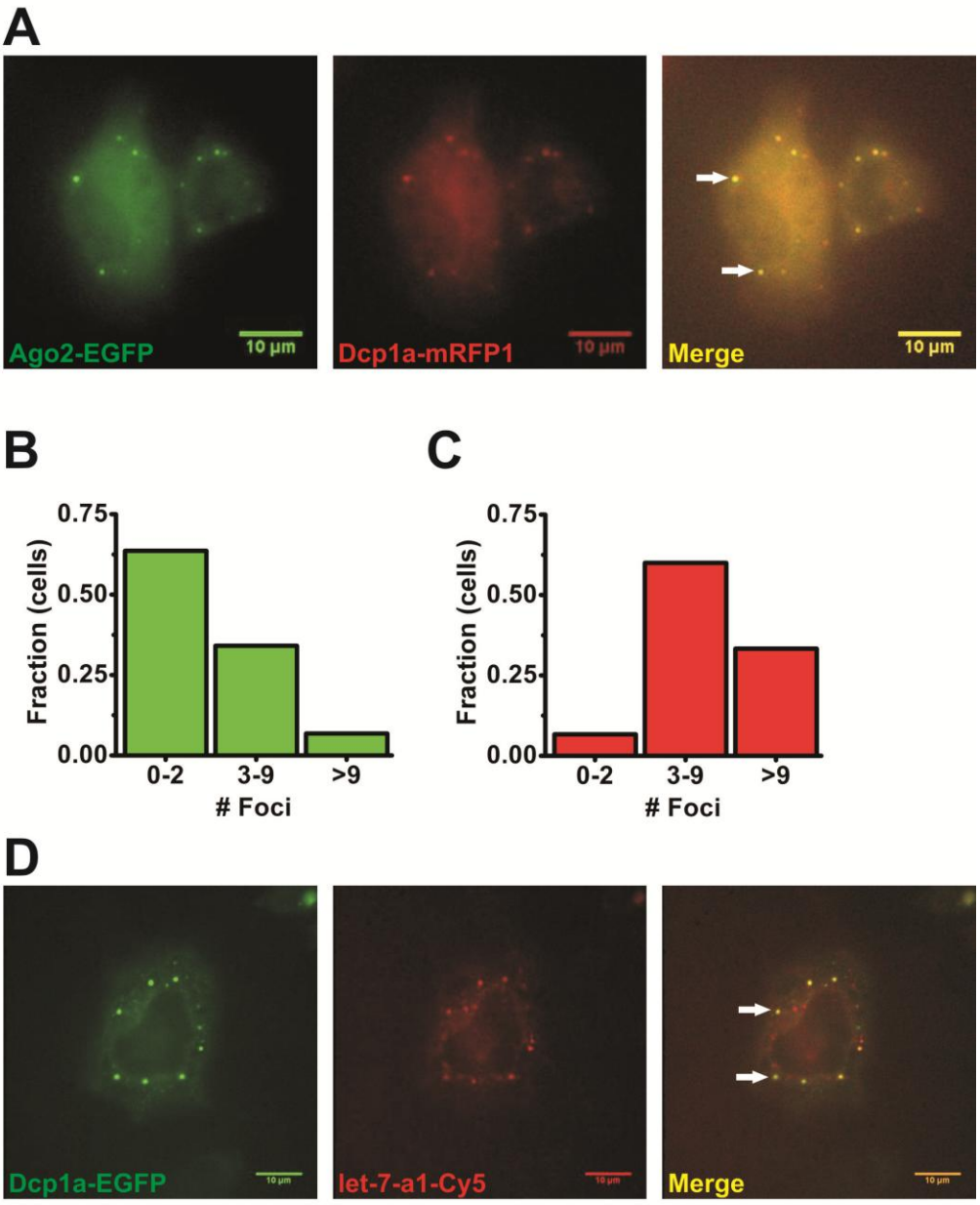

Figure 3.1. Ago2 and miRNAs colocalize with PBs. (A) Pseudo-colored images depicting the colocalization (Merge, right) of ectopically expressed Ago2-EGFP (left) and Dcp1a-mRFP1 (middle). Arrows show representative foci containing both Ago2 and Dcp1a. Scale bar 10 µm. (B) and (C) Distribution of the number of Ago2 and Dcp1a foci in HeLa cells (n = 55 cells). (D) Pseudo-colored images depicting the colocalization (Merge, right) of ectopically expressed Dcp1a-EGFP (left) and microinjected let-7-a1-Cy5 miRNA (middle). Arrows show representative foci containing both Dcp1a and miRNA. Scale bar 10 µm.

data suggest that only a small fraction both miRNAs and Ago2, potentially in the form of miRISC bound mRNPs, localize to PBs.

PBs diffuse much slower than micro-ribonucleoprotein complexes (miRNPs). Prior to performing multi-color tracking, we sought to understand the diffusive behavior of Dcp1a punctae in living HeLa cells. To this end, we transiently transfected HeLa cells with plasmids bearing Dcp1a tagged with a fluorescent protein (EGFP or mRFP1), and tracked the motion of individual fluorescent foci in live cells. Punctate structures were detected even at very low laser power and camera gain settings, as expected because each puncta should be composed of multiple Dcp1a molecules, and therefore fluorescent proteins. Particles were tracked for several minutes without observing significant photobleaching and diffusion coefficients of individual particles were determined using time-averaged mean squared displacement analysis (180).

We found that a majority of Dcp1a foci were either static (**Fig. 3.2A, C**) or exhibited confined motion; however, certain particles also demonstrated other types of diffusion (**Fig. 3.2B, C**). Diffusion coefficients of a majority of particles ranged between 10^{-2} and 10^{-4} $\mu m^2/s$ (**Fig. 3.2D**), consistent with those reported earlier (190), with good correlation between the size of punctae and their mobility. Based on our previous observations (**Chapter 2, Fig. 2.2**), a majority of diffusing miRNA particles, potentially in the form of miRNPs, bore diffusion coefficients ranging between 1 – 0.01 $\mu m^2/s$. The relatively slow diffusion of Dcp1a foci, compared to miRNPs, led us to devise a discontinuous illumination scheme wherein PBs were imaged immediately before and after visualizing miRNPs in live HeLa cells. Using such a scheme enabled us to track miRNPs without compromising on time resolution, which would have been reduced if miRNAs and PBs were visualized by continuously alternating excitation.

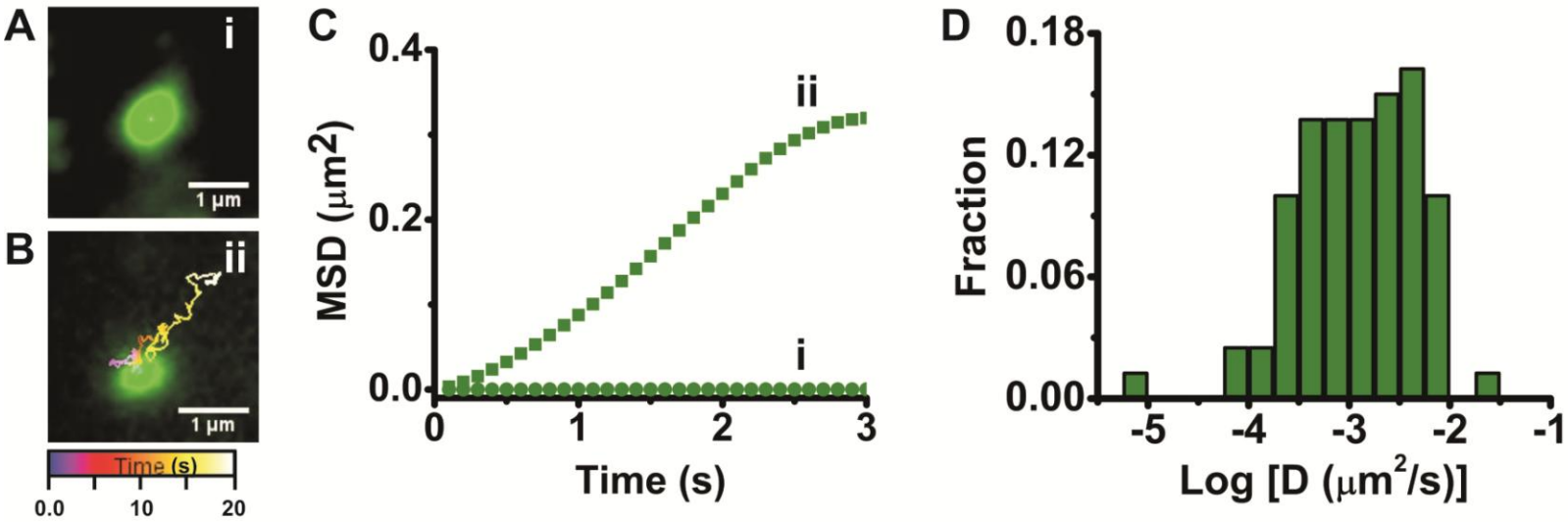

Figure 3.2. Mobility of PBs are much slower than that of miRNPs**.** Representative PBs demonstrating confined (A) and Brownian motion (B) respectively. (C) MSD vs time plots of particles in A and B. Diffusion coefficients calculated from the plot were D(i) = 0.0007 $\mu m^2/s$ and D(ii) = 0.1 $\mu m^2/s$ respectively. (D) Distribution of diffusion coefficients of Dcp1a foci in live HeLa cells (n = 8 cells, 80 particles).

Heterogeneous distribution of labeled miRNAs in processing bodies. To better understand the distribution of miRNAs within PBs, we performed single molecule miRNA counting experiments as described (**Chapter 1, Results, Intracellular single molecule counting**). More specifically, EGFP or mRFP1 and Cy5 fluorescence signal were mapped with ~10 nm spatial resolution and the intensity trajectories of Cy5 labeled miRNA particles, localized within ~300 nm from the periphery of PBs, were analyzed. Such a criterion was used to account for miRNAs that localized adjacent to PBs, which according to Pillai *et al.* (67) could potentially signify miRNA localization to distinct PB compartments. All localizations within (**Fig. 3.3A**) or adjacent (**Fig. 3.3B**) to PBs will be denoted by the term 'colocalization' from this point forward. We found that only ~20% of EGFP or mRFP1 labeled punctuate structures (i.e., PBs) colocalized with Cy5 labeled miRNA; and only ~10% of all miRNA molecules colocalized with PBs, consistent with earlier reports (67). Amongst the colocalized fraction, a majority of PBs (~83%) contained only 1 or 2 miRNA molecules (**Fig. 3.3A – C and E**) whereas the rest (~17%) contained three miRNA molecules or greater (**Fig. 3.3D, E**). We additionally found that PBs could either contain single (**Fig. 3.3A, C**) or multiple miRNA particles (**Fig. 3.3B, D**) suggestive of single or multiple miRISC-bound mRNPs. These findings reveal a surprising heterogeneity in the distribution of miRNAs within PBs (**Fig. 3.3F**), a phenomenon that was not observed using traditional fluorescence microscopy.

miRNPs localize to processing bodies stably or transiently. We further sought to understand the nature of the miRNP:PB interactions in live HeLa cells using single particle tracking microscopy. To this end, we injected Cy5 labeled miRNAs into HeLa cells expressing EGFP or mRFP-1 tagged Dcp1a and observed the mobility of each of these particles relative to one another. A discontinuous illumination scheme was employed; EGFP or mRFP-1 was imaged for 2 – 5 s before and after imaging Cy5 for 5 - 10 s, to track Dcp1a puncta and miRNA particles, respectively. We found that PBs, a majority of which were large particles with high molecular mass, moved very slowly (~100 – 150 nm) over the entire visualization period (9 – 20s) and thus were practically immobile during the

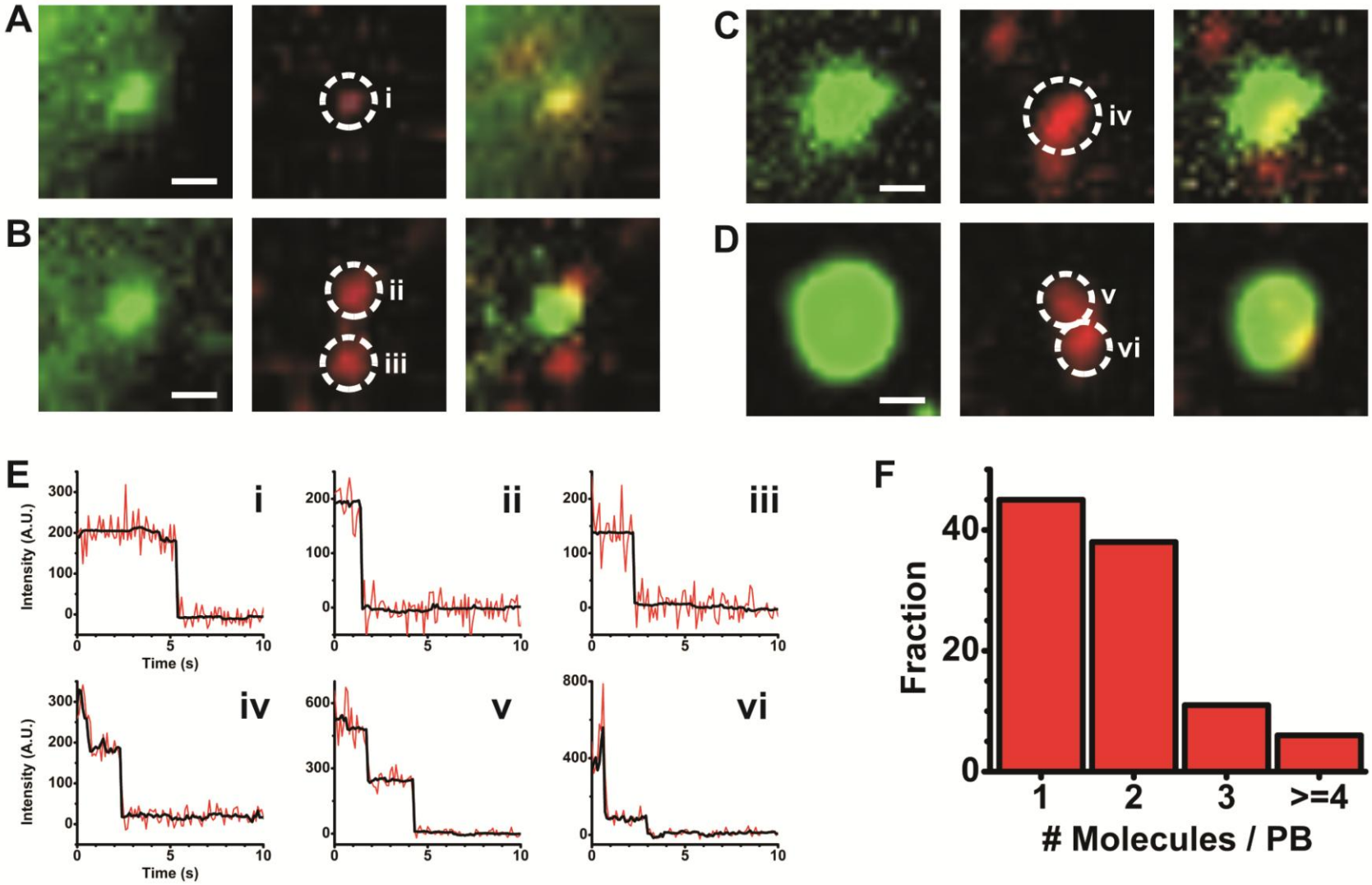
A
B
C
D
i
ii
iii
iv
v
vi
E
Intensity (A.U.)
Time (s)
F
Fraction
Molecules / PB
1
2
3
>=4

Figure 3.3. Heterogeneous distribution of miRNAs within PBs. (A - D) Pseudocolored images of EGFP labeled Dcp1a particles (left), Cy5 labeled miRNAs (middle) and their respective colocalized images (right), representing single mRNP bound by a single miRISC (A), two mRNPs bound by single miRISC each of which one is localized adjacent (iii) to the PB (B), single mRNP bound by two miRISCs (C) and two mRNPs each bound by two miRISCs (D) respectively. Scale bar, 0.6 µm (A, B) and 0.8 µm (C, D) respectively. (E) Representative single molecule intensity trajectories of Cy5 labeled miRNAs corresponding to those present in A-D. (F) Distribution of miRNA molecules colocalized with PBs (n = 12 cells, 110 particles).

miRNA visualization time. Only those miRNPs in the vicinity of large slowly moving PBs, whose displacements during miRNP imaging were less than 1 pixel (133 nm), were further analyzed. The EGFP/mRFP1 and Cy5 signals were mapped as described (**Data Analysis**), an average image of EGFP / mRFP1 puncta was created from videos corresponding to both pre- and post-miRNA imaging, and the localization of Cy5 labeled miRNPs in the vicinity of PBs was analyzed.

We predominantly observed two different types of interactions; one where miRNPs associated with PBs for short intervals of time before diffusing back into the cytoplasm (**Fig. 3.4A, B**), referred as 'transient' interactions from this point forward, and another where miRNPs remained colocalized with PBs until the Cy5 fluorescent probe on the miRNA photobleached (**Fig. 3.4C, D**) or the miRNP floated off to a different focal plane, denoted as 'stable' interactions. In the first type of interaction, a relatively fast moving cytoplasmic miRNP (~0.6 $\mu m^2/s$) transiently associated with a PB for ~0.2 – 3 s, observed as a reduction in miRNP mobility in the event of colocalization (~0.15 $\mu m^2/s$), and quickly dissociated to freely diffuse back into the cytoplasm (**Fig. 3.3A**). Transient interactions also included miRNPs that diffused away from PBs after being initially associated with one at the beginning of our observation window (**Fig. 3.3B**). In either case, we found that individual miRNPs interacted with the same PB multiple times. In contrast, stable colocalizations were observed as miRNPs associated with the periphery of a PB (**Fig. 3.3C**) or localized inside PBs (**Fig. 3.3D**). The average dwell time (or interaction times) of miRNPs in PBs, be it stable or transient associations, was ~ 0.62 ± 0.05 s, which after correcting for small observation time and photobleaching amounts to 1.18 ± 0.10 s. Upon further analysis, we found that miRNAs bind to PBs stably and transiently with equal probability, which in combination with the observations above, predicts diversity in composition of miRNPs and PBs.

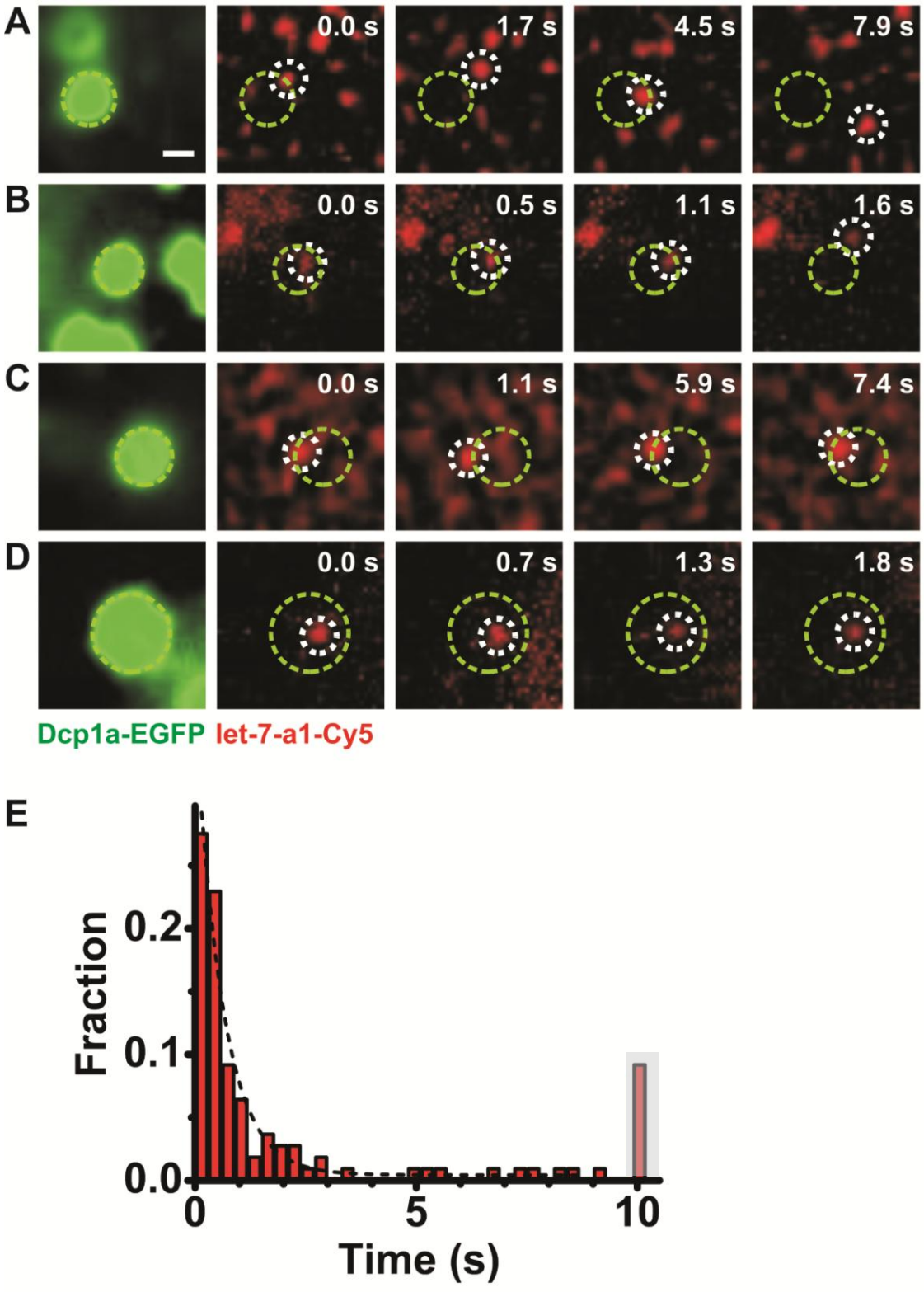

Figure 3.4. Interaction of miRNPs with PBs in live cells. (A) and (B) Representative images of let-7-a1-Cy5 miRNPs transiently interacting with EGFP

labeled Dcp1a foci, i.e. PBs, with average interaction times of 2.2 ± 1.3 s and 1.5 s respectively. The miRNP in (A) interacts multiple times with the PB before rapidly diffusing back into the cytoplasm (0.8s, 2.1s, 3.3s dwell times respectively). Scale bar, 0.5 µm. (C) and (D) Representative images of stable miRNP-PB interactions. The miRNP in (C) surveyed the periphery of the PB and that in (D) remained localized within the PB before photobleaching. Particles in (C) and (D) interacted with PBs for 8.4 s and 2 s respectively. Numbers in top right of each let-7-a1-Cy5 panels correspond to time since each particle was visible. Videos of let-7-a1-Cy5 in (A) and (C) were deconcolved. (E) Interaction (or dwell) time histogram of miRNPs (in) associating with PBs. Dotted line represents fit of the data to a single exponential function. (n = 8 cells, 108 interactions). Grey box at ’10 s’ time indicates an artificial enrichment of this dwell time as contributed by our limited observation window (10 s).

3.4 Discussion

Here we report on the distribution of miRNAs associated with PBs and the different modes of miRNA-PB interactions inside human cells with single molecule sensitivity. We find that majority of PBs contain very few fluorophore labeled miRNPs and that miRNPs can interact with PBs in stable or transient fashion. Taken together, these observations predict the existence of a diverse set of miRNA complxes and PBs varying in composition. Moreover, a stable miRNA:PB interaction may potentially require specific interacting proteins, such as GW182 (208, 209, 212, 216), whose presence either on the miRNP or the PB can strengthen the interaction. Additionally, our data clearly show the heterogeneity associated with molecular interactions, specifically in the context of a living cell, which are largely unobservable using ensemble biochemical and microscopic techniques.

We initially performed control experiments to confirm the colocalization of microinjected miRNA and ectopically expressed Ago2 with PBs. Consistent with previous work (67, 189) we found that only a small fraction of the total miRNA and Ago2 cellular pool colocalized with microscopically visible PBs. It is possible that miRNA mediated target repression occurs via multiple mechanisms and only a small fraction of repressed mRNPs are channeled through PBs. However, it is still unclear whether PB localization of repressed mRNPs is the cause for repression or occurs as a consequence of other modes of repression. Thus, an alternate hypothesis is that a majority of repression occurs in the cytoplasm through other mechanisms and only a very small fraction of these already repressed mRNPs aggregate to form PBs or are transported to PBs for further processing.

We also tracked the movements of single Ago2 and Dcp1a particles in live HeLa cells and found them to predominantly exhibit confined movements, as previously reported (190). Such restricted diffusion has been proposed to arise from the anchoring of PBs to certain cellular elements, like the cytoskeleton (190). Additionally, these particles diffused much slower than a majority of

miRNPs, largely owing to their high molecular mass. The large size and slow mobility of PBs enabled us to devise an illumination scheme to visualize both PBs and miRNPs, labeled with differently colored fluorescent probes, in the same region of a live cell. As a majority of miRNPs diffused at least an order of magnitude faster than PBs, it was absolutely necessary for us to image miRNPs at higher spatial and temporal resolution, which was easily achieved using our illumination and analysis methods. Continuous illumination schemes to image two fluorophores simultaneously (138) could potentially shed light on the interaction of miRNPs with fast moving PBs as well.

Very few quantitative data exist on the distribution and dynamics of miRNAs and miRISC proteins within PBs. On the one hand, Pillai *et al.*, using standard confocal microscopy, have shown that miRNAs can either localize within PBs or adjacent to PBs (67). This observation prompted them to hypothesize that miRNAs could potentially interact with PBs via different mechanisms, which were not resolvable by their visualization method. Photobleaching experiments, on the other hand, have shown that PB-localized miRISC components, especially Ago2, exchanged very slowly with their cytoplasmic pools compared to other PB components (189), strongly suggesting stable miRISC:PB interactions. These reports, upon comparing the signal intensity of fluorophore labeled miRNAs or Ago2 within PBs to the total fluorescent intensity within the cell have estimated that close to 20% of miRNAs and their associated mRNAs (67) and less than 2% of cellular Ago2 (189) localize to PBs. Quantifications such as these are often skewed by errors associated with ensemble intensity measurements arising due to fluorophore self-quenching (217), wherein the total intensity value of a particle with multiple fluorophores is not linearly related to that of a single fluorophore. To overcome these caveats, we used stepwise photobleaching of fluorescent probes for counting the number of miRNA molecules within PBs. This method does not rely on the absolute value of intensity per se, but uses the number of steps it takes for the intensity trajectory of an individual particle to reach background levels as a

direct count of the number of molecules within that spot, exploiting our single molecule sensitivity.

Our stepwise photobleaching intensity analysis showed that miRNAs are not equally distributed within PBs and, as reported earlier (67), localized either within or adjacent to PBs (**Fig. 3.3**). Certain foci contained more miRNAs than others, but surprisingly a majority of PBs contained either 1 or 2 fluorophore labeled miRNAs. Additionally, PBs colocalized with single mRNPs (**Fig. 3.3A, C**) or multiple distinct mRNPs each associated with one or more miRISCs (**Fig. 3.3B, D**). Notably, punctuate miRNA particles bearing greater than 6 miRNAs rarely colocalized with EGFP labeled PBs, possibly suggesting the presence of additional, unlabeled aggregates composed of different proteins that are undetectable in our experiments. Such heterogeneous distribution of miRNAs can potentially be explained by one or several of the following hypotheses; (i) depending on their composition and size, PBs can accommodate different numbers of miRNPs; (ii) based on their composition, miRNPs can interact with PBs to varying degrees; (iii) only punctuate structures of miRNAs are truly PB-localized, whereas the rest, containing only one or two miRNA molecules, represent transient miRNP:PB interactions; or (iv) PBs associated with small numbers of miRNA molecules are nucleating centers for miRNP aggregation.

Single molecule and particle tracking enabled us to clearly visualize the different modes of miRNP:PB interactions in live HeLa cells. We found that miRNPs either bound transiently or stably with PBs and those miRNPs that started out as freely diffusing particles in the cytoplasm were more likely to bind transiently than stably. These observations support the notion that miRNAs that localize adjacent to PBs in fixed cells represent either transient miRNP:PB interactions or miRNPs scanning over the surface of PBs to potentially locate a more stable docking site. As both stable and transient interactions, overall, were equally likely, our data strongly suggest a probabilistic miRNP:PB interaction model in which miRNPs do not show a constant (static) behavior, but can switch between being bound and unbound states, possibly depending on specific

biomolecular signals. This model coupled with the observed short dwell times, on the order of a few hundred milliseconds, of miRNPs in association with PBs suggests a transient role for PBs in mediating miRNA assisted gene repression. Alternatively, it may provide a more general explanation for the relatively low repression levels by miRNAs as opposed to silencing RNAs (siRNAs), which typically 'knock-down' protein expression almost completely. miRNAs predominantly bind with incomplete complementarity to their cognate mRNA targets, reducing protein expression by only a small fraction. Thus, low binding energy, in contrast to siRNAs that bind with complete complementarity to their targets, in addition to a low interaction probability of miRNPs with PBs, enables miRNAs to fine-tune protein expression instead of acting as binary switches. To further test such a model, the affinity of miRNAs for mRNAs will need to be investigated. Overall, our data shed light on the interaction between miRNPs and PBs inside living cells at single molecule sensitivity, thus paving the way for investigating biomolecular interactions in their native environment, one molecule at a time and highlighting the importance of heterogeneity and transient events in biomolecular processes.

3.5 Acknowledgements

We thank N. Kedersha for providing us the plasmid containing mRFP1-Dcp1a fusion protein, A. K. Leung for the plasmid containing EGFP-Ago2 fusion protein, A. Johnson-Buck for colocalization mapping routines, A. Manzo for MSD software development, H. Ding, A. Gafni and D. Steel for sharing their intensity analysis routine, and the Microscopy and Image Analysis Laboratory at the University of Michigan for access to Imaris. This work was supported by NIH grant GM081025 to N.G.W.

Chapter 4

Elucidating microRNA:mRNA Interactions *in vitro* Using Single Molecule Fluorescence Microscopy

4.1 Introduction

microRNAs (miRNAs) are small non-coding RNAs, ~22 nucleotides (nt) in length, that base pair with 3`UTRs of protein-coding mRNAs to mediate post-transcriptional repression (11, 12). The recognition of mRNAs by miRNAs is defined by a 6-8 nt region within the 5` end of the miRNA called the seed sequence (218-220). This sequence in the miRNA needs to be completely complementary to regions within the mRNA and this criterion, along with sequence conservation among organisms, has been traditionally used for the bioinformatic, genome-wide prediction of miRNA targets (219, 220). Reporter assays have suggested that seed pairing is not only important for recognition but, in some cases, is sufficient for efficient repression (64, 221). However, this does not hold true for all miRNA targets, and it has been shown that the degree of repression is highly variable in different UTR contexts (218). Such observations clearly suggest a role for mRNA structures and sequences outside of the seed region in target recognition and binding (218).

A majority of bioinformatically predicted miRNA targets contain only one seed sequence for a given miRNA, however, certain messages, especially those coding for transcription factors (222-224), contain multiple seed matches. Of particular importance is the mRNA coding for high mobility group AT hook 2 (HMGA2) proteins, a small, non-histone, chromatin architecture modulating

transcription factor. This mRNA contains seven seed matches for let-7, a miRNA that is evolutionarily conserved from the nematode *C.elegans* to humans, and the aberrant expression of this protein can lead to oncogenic transformation in mice (48, 222). Conversely, the 3` untranslated regions (UTRs) of several oncogenes, including HMGA2, are shortened in cancerous cells to evade miRNA mediated repression (225-227). These results suggest that mRNAs with long 3`UTRs are under evolutionary pressure for stringent regulation in order to evade cancer and that this is realized by the maintenance of multiple miRNA seed matches (226, 227).

Previous reports (48, 63, 64) have shown that all miRNA binding sites within a naturally occurring or artificial mRNA that contains multiple seed sequences are important *in vivo* (48, 63, 64); however, it is unclear whether: (i) all sites are occupied simultaneously; and (ii) “allostery” and/or cooperativity connect multiple miRNA binding sites. To this end, we developed a single molecule assay to count the number of miRNAs bound per mRNA molecule *in vitro*. We found that a majority of mRNAs are either unbound or singly bound by miRNAs, using each two different miRNA-mRNA pairs and cell extracts. Contrary to previous observations (63, 64, 228), our data together with computational analysis of RNA structure and free energy calculations of miRNA binding suggest that multiple seed matches within mRNAs provide a greater probability for miRNA binding, but not necessarily binding of multiple miRNA, thus providing a molecular framework for the relatively modest repressive abilities of miRNAs. Our results also suggest that miRNAs bind seed sequences independently from one another, with certain sites bound preferentially over others.

4.2 Materials and Methods

Plasmids, DNA and RNA oligonucleotides. cDNA of mouse HMGA2 containing a 5` untranslated region (UTR), coding sequence (CDS) and 3`UTR were removed from pcDNA-mH-2xwt plasmid bearing the cDNA of mouse

HMGA2 with two 3`UTRs (made by John Hoerter), using the BamHI and NotI restriction enzymes. The mouse HMGA2 cDNA was ligated into pEF6, which was also digested with the same restriction enzymes, downstream of the T7 promoter resulting in pEF6-mH. pRL-TK-cxcr4-6x (229), plasmid containing the renilla luciferase CDS and an artificial 3`UTR containing six binding sites for an artificial cxcr4 miRNA downstream of the T7 promoter, was purchased from Addgene ©.

All RNA oligonucleotides were purchased from the Keck Biotechnology Resource Laboratory at the Yale University School of Medicine with a 5' phosphate (P) and, in the case of amine modified RNA, a 3' amino group on a C7 carbon linker. RNA was purified as described (177) and the 3' amine groups were labeled with Cy3 or Cy5 succinimidyl ester as described (177, 178). RNA sequences were as follows:

let-7-a1 guide: P-UGAGGUAGUAGGUUGUAUAGUU
let-7-a1-passenger: P-CUAUACAAUCUACUGUCUUUCC
cxcr4 guide: P-UGUUAGCUGGAGUGAAAACUU
cxcr4 passenger: P-GUUUUCACAAAGCUAACACA
Guide and passenger strands were heat-annealed in a 1:1 ratio, resulting in duplex miRNAs, and frozen for further use.

Control DNA, BDCcxcr4N, containing a 5` biotin and 3` amino group was purified and labeled as described (177). Sequence is as follows:

BDCcxcr4N: AAAAAAAAGTTTTCACTCCAGCTAACATT

mRNA synthesis and labeling. Plasmids pEF6-mH and pRL-TK-cxcr4-6x were digested with NotI RE and purified by phenol-chlorofom extraction followed by ethanol precipitation. *In vitro* transcriptions were performed with 1 µg linearized plasmids using the MegaScript T7 kit (Ambion ©) according to manufacturer's protocol. Transcription reactions were then DNAse treated (turbo DNAse, Ambion ©) and the RNAs, mH or RL-cx6x transcribed from plasmids pEF6-mH and pRL-TK-cxcr4-6x respectively, were purified by LiCl precipitation. The RNAs were purified either from a 1.2% agarose gel, in the case of mH, or 5% urea poly-

acrylamide gel electrophoresis (PAGE), for RL-cx6x. Gel extracted RNAs were then modified by 7-methyl-(3`O-Methyl)-G capping and polyadenylation using the ScriptCap capping and polyA tailing kits respectively (Epicentre ©). 3`OMethyl GTP was used instead of GTP for capping reactions (**Fig. 4.2A**) to prevent periodate mediated oxidation and the subsequent biotinylation of the cap in addition to the 3` end. To estimate the length of the polyA tail, RNAs were separated on a 1.2% formaldehyde agarose gel. Capped and tailed RNAs were purified by gel filtration (Roche© RNA columns), and their 3`ends were biotinylated after periodate oxidation as described (230). Briefly, 1-10 µM RNA was oxidized using 100mM sodium periodate in a 100mM sodium acetate buffer, pH 5.3, for 90 min on ice and room temperature (RT) respectively. The oxidized RNA, purified by gel filtration and ethanol precipitation, was then reacted either with saturated biotin hydrazide or biocytin hydrazide (Thermo Pierce©) for 5 h at RT and purified by gel filtration (Roche© RNA columns) followed by ethanol precipitation. Biotinlyation efficiency was tested by adding a known amount of either a positive control RNA, a negative control non-biotinylated RNA or the biotinylated RNA to streptavidin beads (MyOne-C1 Streptavidin beads, Invitrogen©) and measuring the amount of RNA bound (**Fig. 4.2C**). Briefly, 50 pmol of biotinylated-let-7-a1 miRNA (+ve), capped and tailed RLcx6x mRNA (-ve) or capped, tailed, biotin tagged, Cy3 labeled, RLcx6x mRNA (CRTBCy3), suspended in 10 mM Tris.Cl, 1M NaCl and 0.1% Tween-20 buffer, were added to streptavidin coated magnetic beads and incubated for 0.5 h at RT to allow for RNA binding. Beads containing RNA were separated from unbound RNA using a magnet and the amount of RNA left in the supernatant was measured by the absorbance value at 260 nm. Amount left in the supernatant subtracted from the amount added was used to estimate the amount of RNA bound to the beads. In the case of RL-cx6x, the capped, tailed and biotinylated (using biocytin hydrazide, which had an extra amine functional group) RNA was further labeled with a Cy3 dye at the 3` end, as described (177). This dye labeled RNA was purified by gel filtration (Roche© RNA columns), ethanol purification and was used in single molecule assays.

Computational analysis of secondary structure and miRNA hybridization energies. Mfold version 2.3 (http://mfold.rna.albany.edu) was used to create and analyze secondary structures of mRNAs. The RNAs were folded at RT with 1 M Na^+ and no divalent ions. RNAhybrid was used to calculate the minimum free energy of hybridization between miRNAs and their corresponding seed sequences.

miRISC assembly and *in vitro* translation. miRISCs were assembled in HeLa cytosolic (S100) cell extracts (Jena Biosciences) with minor modifications to the protocol described earlier (231). Briefly, 1 nM Cy5 labeled let-7-a1miRNA was typically incubated with 50% HeLa cell extract supplemented with lysis buffer [23.7 mM HEPES.KOH, pH 7.5, 79 mM potassium acetate, 1.58 mM magnesium acetate, 5mM DTT and 1 mg/mL Pefabloc SC (Roche©)], RNAi mix (125mM creatine phosphate, 5mM ATP and 25mM DTT), 2% creatine kinase and 10% RNAse inhibitor (Applied Biosystems©), for 2 h at 4 ^oC.

Repression reactions in nuclease treated rabbit reticulocyte lysate (RRL, Promega) were performed as described (71, 229, 232). Briefly, 150 fmol of Cy5 labeled cxcr4 miRNA were mixed with 25 fmol of capped and tailed reporter mRNA (C-RLcx6x-T) and control luciferase RNA (firefly luciferase RNA, C-FL-T, Promega) to a total volume of 2.2 µL. The mixture was heated to 75 ^oC for 3 min, cooled to RT for 5 min and then added to ice to pre-anneal the miRNA with the reporter mRNA. 7.8 µL of a masrter mix containing 7 µL (70%) of RRL, 0.2 µL (4-8 U) of RNasin (Promega), 0.2 µL (20 µM) amino acid mix and 0.4 µL of water was added to the RNA mix and incubated at 30 ^oC for 15 min. Dual luciferase assays were performed using dual luciferase assay reagents (Promega) according to manufacturers protocol to quantify repression.

Single molecule microscopy. Slides and coverslips for single molecule microscopy were prepared as described (233). Briefly, clean quartz slides were functionalized using a commercially available aminosilane (Sigma) and reacted with a mixture of NHS-ester functionalized poly-ethylene glycol (PEG) and

biotinylated PEG (5000 MW, Laysan Biosciences). Coverslips were silanized and reacted only with PEG. Unreacted free amines on the slides and coverslips were then blocked with sulfo-DST (Laysan biosciences), thus creating a negatively charged surface that inhibits non-specific binding of negatively charges RNAs. Double sided tape was used to create a microfluidic channel between the coverslip and slide, which were then tightly glued together using epoxy.

For experiments with HeLa cell extracts, 50 – 350 pM capped, tailed and biotinylated mRNAs (C-mH-T-Bio or C-RLcx6x-T-Bio) were first immobilized on the streptavidin coated slides and assembled miRISC complexes (20 times more miRNA as compared to mRNA), as described above, were added to the immobilized mRNA. Complexes were allowed to bind to the mRNA, on the slide, at RT for 20 min and unbound complexes were washed off using a buffer containing the lysis buffer, RNAi mix, creatine kinase, RNAse inhibitor supplemented with an oxygen scavenging system (10 mM trolox, 100 mM protocatechuic acid and 1 µM protocatechuate-3,4-dioxygenase). Slides were imaged immediately after washing.

For experiments with RRL, repression reactions (described above) were assembled with capped and tailed biotinylated and Cy3 labeled reporter mRNA, (capped and tailed) control mRNA and the miRNA in the appropriate ratio. Repression reactions were then diluted 10-fold in the master mix (described above), added to streptavidin coated slides and incubated for 10-15 min at RT. Unbound complexes were washed using a buffer containing 50 mM HEPES.NaOH, pH 7.5, 80 mM potassium chloride, 20 mM sodium chloride, 1mM magnesium chloride and the oxygen scavenger system. Slides were imaged immediately after washing. Unfortunately, our attempts to image single miRNA molecules in the presence of cell extracts, both HeLa and RRL, within the microfluidic channel were marred by high background contributed by both the cell extract and unbound miRNAs.

Control experiments, to compute the percentage of bright fluorophores, were done by first annealing Cy3 labeled, biotin tagged DNA and Cy5 labeled

cxcr4 miRNA in a 1:10 ratio at 90 ^{o}C for 1 min, 75 ^{o}C for 3 min, and slow ramping of the temperature from 65 ^{o}C to 4 ^{o}C at 3^{o}C / min. The annealed solution was added to streptavidin coated slides and incubated for 10 min. Unbound duplexes and excess miRNA were then washed away with the using a buffer containing 50 mM HEPES.NaOH, pH 7.5, 80 mM potassium chloride, 20 mM sodium chloride, 1mM magnesium chloride and the oxygen scavenger system. Slides were imaged immediately after washing.

Imaging was done using a prism coupled total internal reflection fluorescence microscope based on an Olympus IX-71 microscope equipped with a 60x water immersion objective (Olympus) and a PentaMAX intensified CCD camera (Princeton Instruments). Cy3 and Cy5 fluorophores were excited using 532 nm and 635 nm lasers respectively and their fluorescence emission were detected using HQ580/60 and HQ710/130 bandpass filters (Chroma) respectively. Emission from Cy3 and Cy5 were spectrally separated using a dichotic filter and projected onto different regions (channels) of the same CCD chip. Positions on the Cy3 and Cy5 channels were spatially mapped using fiduciary markers [Red microspheres (Invitrogen)] as described (**Chapter 3**). Particles were Images were collected for 100 – 500 s at 10 frames/s (fps) camera exposure time and intensity trajectories were analyzed using custom written MATLAB routines. The density of spots on our passivated surfaces were low enough (~ 0.05 spots/μm^2) to be confident that single particles were visualized.

4.3 Results

mRNA secondary structure and thermodynamics of miRNA binding potentially play an important role in target recognition and binding. We first analyzed computationally predicted secondary structures of both C-mH-T and C-RLcx6x-T (**Fig. 4.1**) to check if secondary structure of mRNAs affected miRNA seed sequence accessibility. As expected, both mRNAs were highly structured, especially in their 3`UTRs. Seed sequences of let-7 miRNA in the 3`UTR of

mouse HMGA2 were found to be distributed between unstructured loops, structured stems that were completely base-paired with a different region of the mRNA, or a combination of both, wherein only a few bases were paired (**Fig. 4.1A**). Based purely on the general expectation that regions within loops are more accessible than ones that are base paired, we can immediately rank miRNA seed sequences with respect to their accessibility; seed sequence 5 is the most and seed sequences 2 and 6 are the least accessible. We also find that seed sequences 6 and 7, separated by just 13 nucleotides (nt), can potentially exhibit positive cooperativity, wherein binding of one miRNA melts the proximal structure of the mRNA, rendering the other miRNA binding site more accessible. All other binding sites are structurally well dispersed, inconsistent with synergistic miRNA binding. In contrast, all cxcr4 seed sequences within the relatively short 3`UTR of RLcx6x are closely located, both structurally and by sequence (separated by just 4 nt from one another), with correspondingly high propensity for cooperative miRNA binding (**Fig. 4.1B**), especially between seed sequences 2 and 6 as well as 3 and 5. Additionally, the lowest energy structure predicts that seed sequence 1 is the most accessible and the rest are equally of lower accessibility.

By contrast, computational prediction of the duplex stability of the miRNA:target site hybrid suggests an anti-correlation between minimum free energy of miRNA binding and seed sequence accessibility for mHMGA2 mRNA (**Fig. 4.1C**). It is possible that seed sequence accessibility is of primary importance, but upon seed matching, hybridization of ~4 – 8 nt in the 5`region of the miRNA with the mRNA, the extent of complementarity between the miRNA and mRNA can dictate affinity of miRISC complexes. Thus, both secondary structure and miRNA binding energy potentially play important roles in target recognition and miRNA binding, respectively, in addition to opening up the possibility for cooperative miRNA binding.

Synthesis of capped, tailed, biotinylated, dye labeled long mRNAs. To synthesize mRNAs with all the essential functionalities required for miRNA

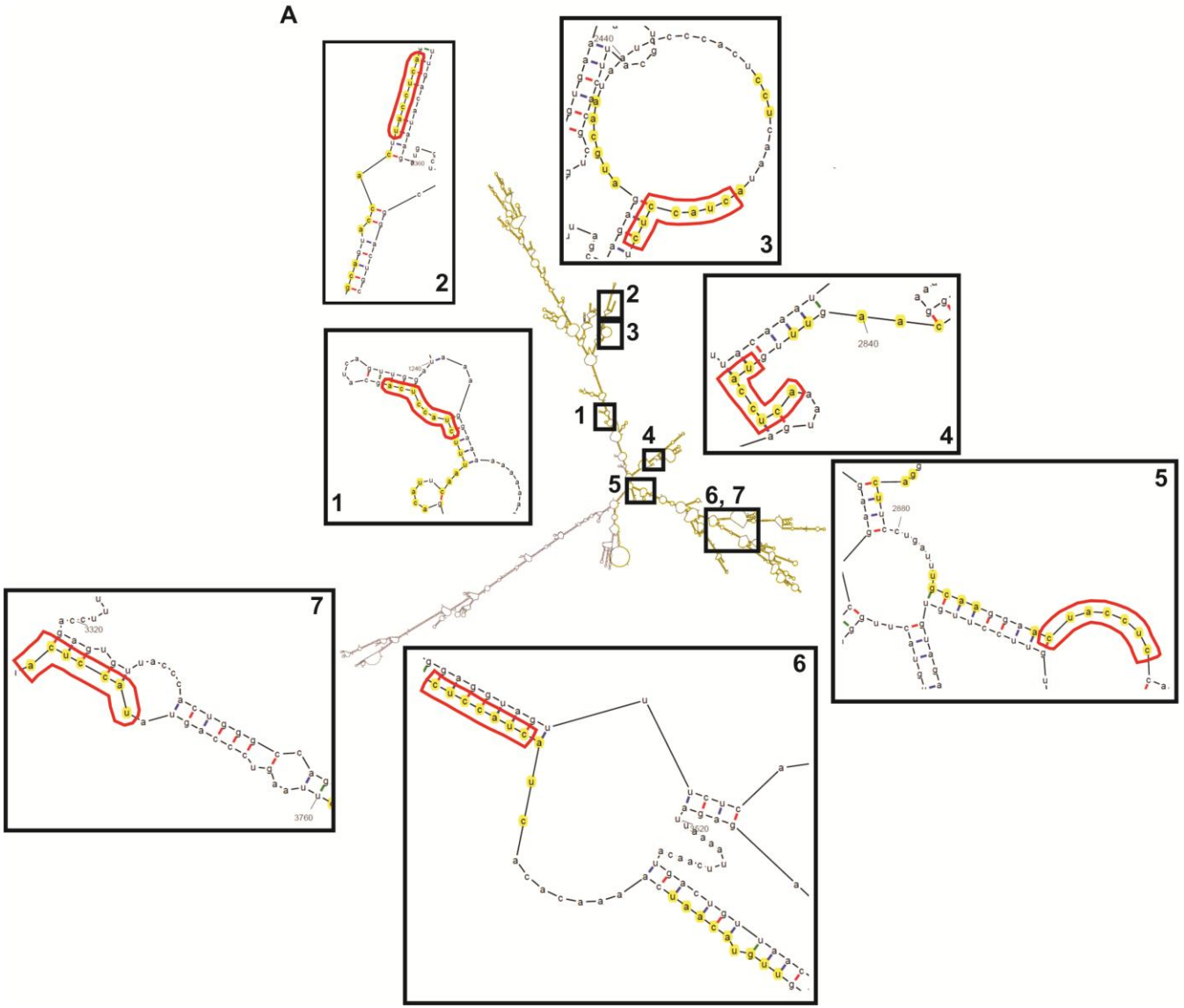
A
1
2
3
4
5
6, 7
2
3
1
4
5
6
7

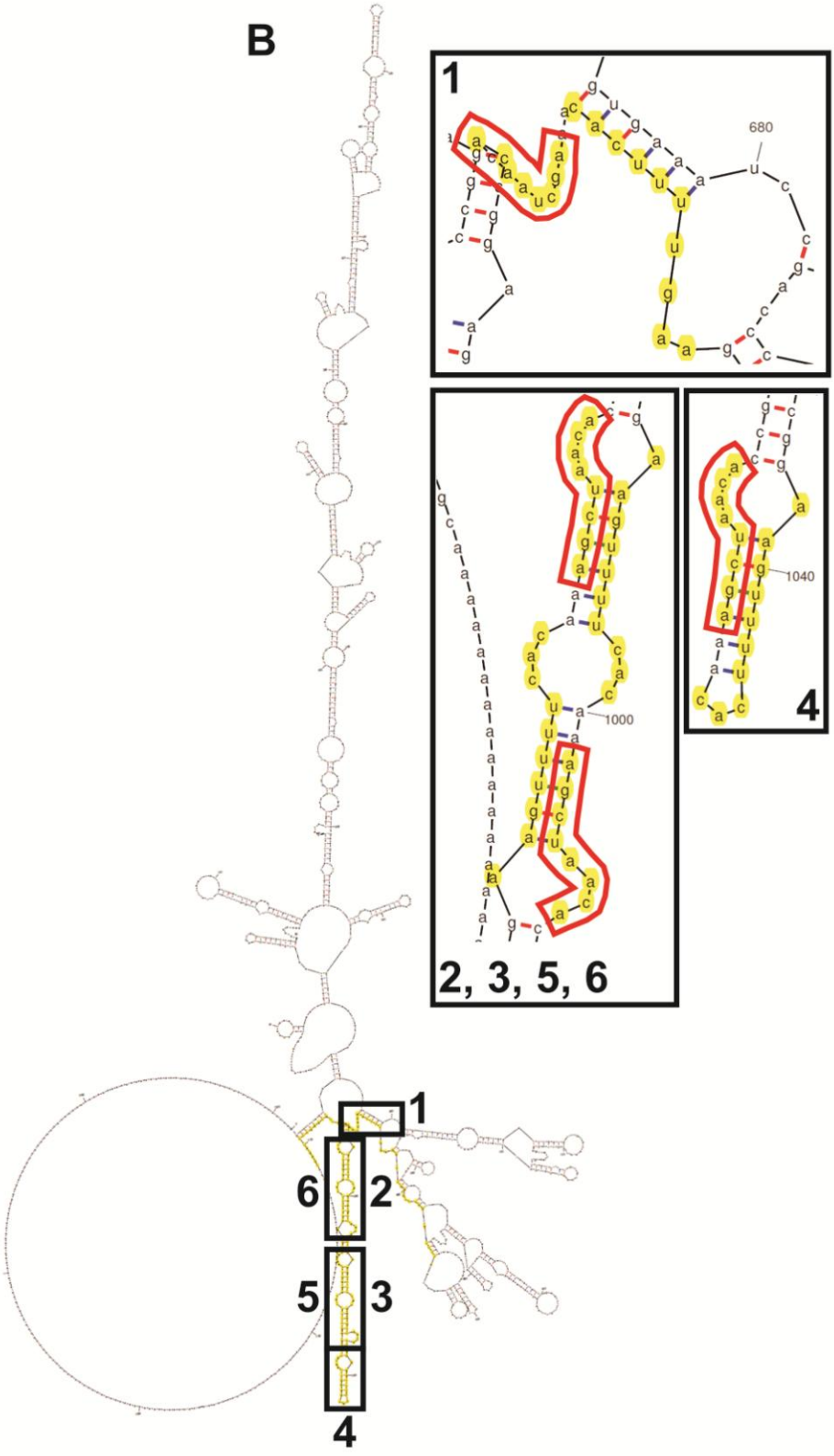
B
1
680
2, 3, 5, 6
1000
4
1040
1
6
2
5
3
4

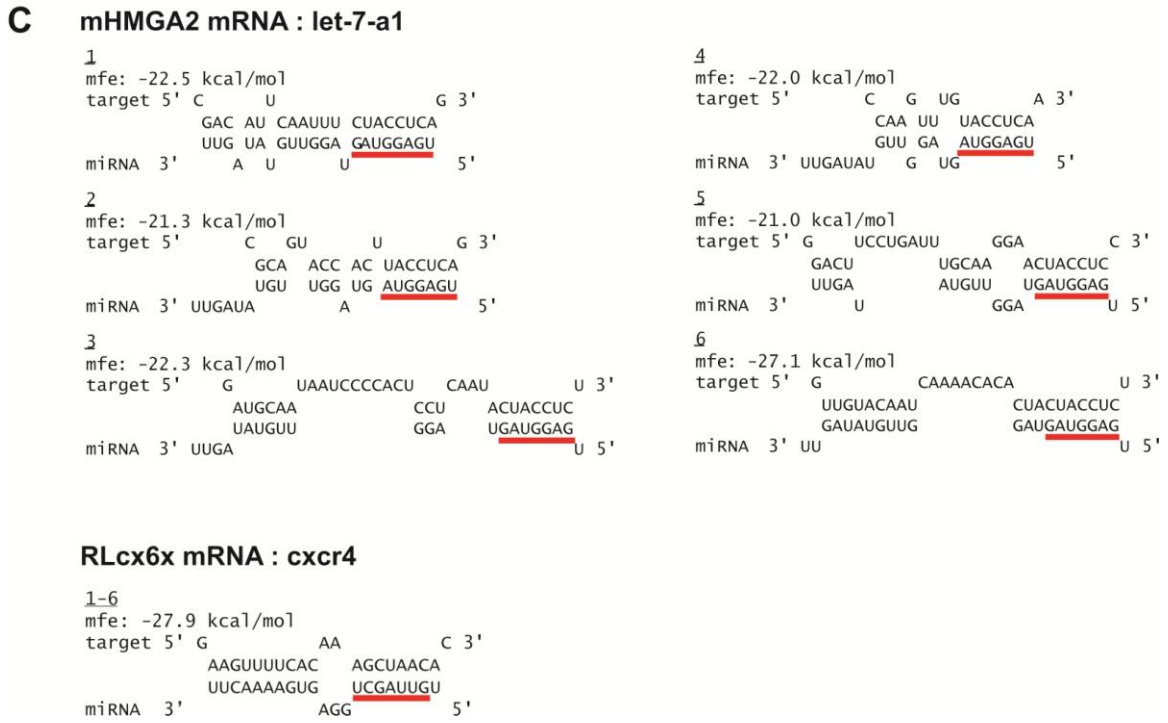

Figure 4.1. mRNA secondary structure and miRNA binding energy analysis. (A and B) Mouse HMGA2 and RLcx6x mRNAs folded in mfold. Highlighted region in the core structure denotes 3`UTR. Boxed structures show zoomed in sections of miRNA binding sites. Highlighted sequences inside zoomed-in sections denote regions complementary to let-7-a1 and cxcr4 miRNAs in mHMGA2 and RLcx6x mRNAs respectively. Regions circled in red represent seed sequences. (C) RNAhybrid results of mHMGA2 : let-7-a1 and RLcx6x : cxcr4, mRNA : miRNA pairs. Underlined numbers correspond to seed sequence numbers in (A) mHMGA2 and (B) RLcx6x mRNAs respectively. Sequences underlined in red denote seed pairing. Mfe denotes minimum free energy.

binding and single molecule visualization *in vitro*, we developed a multi-step mRNA synthesis and modification method. Based on previous reports (67, 229), which suggested the requirement for 5`caps and 3`tails on mRNAs for efficient miRNA mediated repression, we enzymatically capped (**Fig. 4.2A**) and tailed (**Fig. 4.2B**) our RNAs after *in vitro* transcription. These modified mRNAs were further functionalized with a biotin moiety, a requirement for surface immobilization in our single molecule assays; we used 3`end-specific, periodate-mediated oxidation of the vicinal diols to react with biotin or biocytin hydrazide. In certain cases, mRNAs coupled with biocytin hydrazide were also labeled with a Cy3 dye, which was needed for the visualization of single mRNA molecules. As mRNAs capped with regular GTP would contain vicinal diols at the 5` end, which can also get oxidized by periodate, we decided to use 3`O-methyl GTP instead of GTP in our capping reactions. We first sought to test whether RNAs can be capped by 3`O-methyl GTP. To this end, we set up capping reactions of small (29 nt) RNA oligonucleotides with 3`O-methyl GTP and compared their electrophoretic mobility to those of both uncapped and GTP-capped RNAs on a 20% denaturing PAGE that was capable of resolving RNAs differing in size by a single nt. As it would be impossible to resolve large RNAs (>100 nt) with single base sensitivity, we used a 29-nt RNA instead of mH or RLcx6x mRNA in these assays. Upon RNA staining and visualization, we found that these RNAs were capped by 3`O-methyl GTP with efficiencies similar to those capped by GTP (capping efficiency = ~90%) (**Fig. 4.2A**). We also systematically tested the mRNAs at the end of each step in our synthesis protocol to check for the presence of each modification and to quantify their respective efficiencies (**Fig. 4.2A - D**). For instance, we found that ~100 – 200 A's were added to the mRNA in our tailing reactions (**Fig. 4.2B**) and our biotinylation efficiency was ~30 – 60% (**Fig. 4.2C**). Capped, tailed, biotinylated and, in certain cases, Cy3 labeled mRNAs that passed our quality controls were then used for single molecule experiments.

mRNAs, containing multiple seed sequences for a particular miRNA, predominantly bind only one copy of the miRNA. Based on repression data

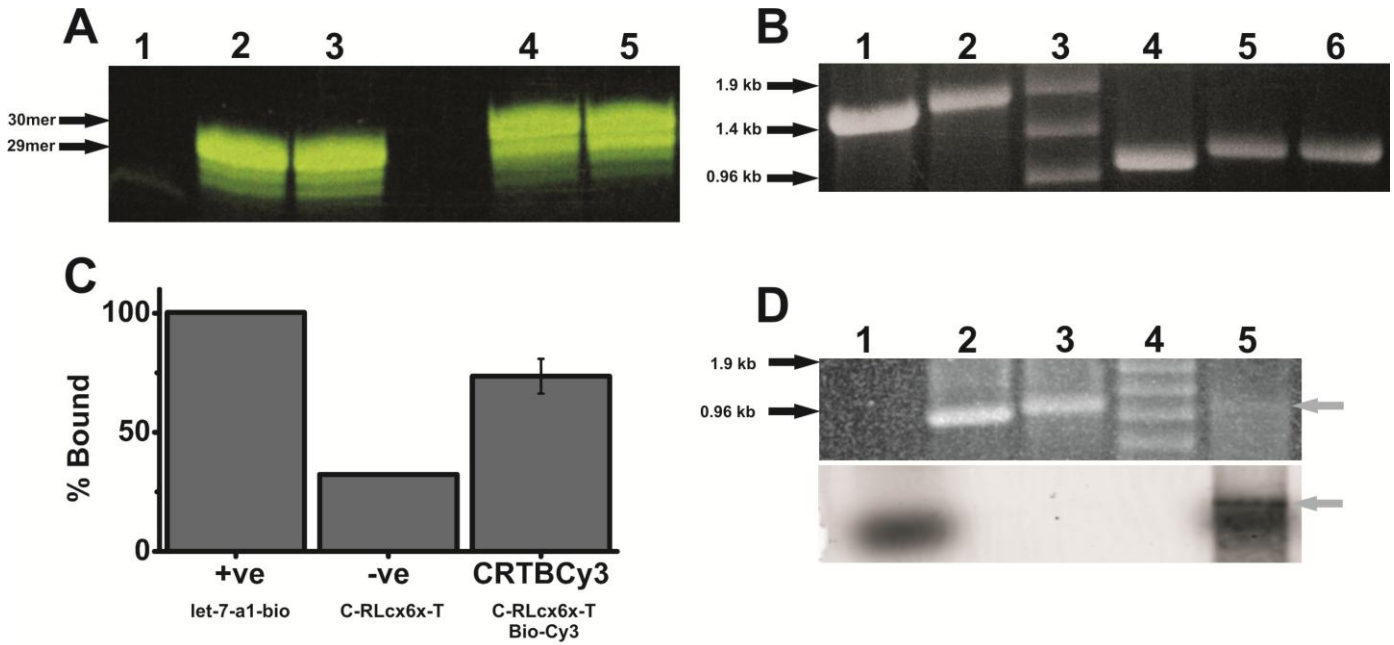

Figure 4.2. Quality control assays. (A) 20% denaturing PAGE loaded with a 25-mer (1), uncapped 29-mer (2), uncapped 29-mer with all components of capping reaction except for GTP (3), GTP-capped RNA (4), 3`OMethyl capped RNA (5). The RNA were stained with SYBR Gold nucleic acids stain (Invitrogen) and visualized under UV light. (B) 1.2% formaldehyde agarose gel stained with ethidium bromide and visualized under UV light. Samples correspond to, firefly luciferase RNA (FL, 1), capped and tailed FL (2), RNA ladder (Cat #G319A, Promega, 3), RLcx6x (4), capped and tailed RLcx6x (5), 3`OMethyl capped and tailed RLcx6x (6). (C) Quantification of biotinylation efficiency. Samples correspond to, biotinylated-let-7-a1 miRNA (+ve), capped and tailed RLcx6x mRNA (-ve) or capped-tailed-biotin tagged-Cy3 labeled RLcx6x mRNA (CRTBCy3). (D) 1.2% formaldehyde agarose gel loaded with Cy3 dye (1), RLcx6x mRNA (2), capped-tailed-biotin tagged RLcx6x mRNA (3), RNA ladder (Cat #G319A, Promega, 4), capped-tailed-biotin tagged-Cy3 labeled RLcx6x mRNA (5). Top panel shows eithidium bromide staining followed by visualization using UV light. Bottom panel shows fluorescent scan illuminating the Cy3 fluorophore.

several groups (63, 64, 218, 225, 228) had predicted that miRNAs bind to mRNAs with positive cooperativity, especially when the mRNA contains multiple seed matches for that specific miRNA. Thus, under conditions of miRNA excess, it is highly likely for an mRNA to be bound by multiple miRNAs. To test this hypothesis, we developed a single molecule assay that utilizes the stepwise stochastic photobleaching of single fluorophores to quantify the number of miRNAs bound per mRNA target in cell extracts under conditions where gene repression is observed.

We first tested for the binding stoichiometry between miRNAs and their mRNA targets in RNAi competent cytosolic HeLa cell extracts (231). Pre-assembled, Cy5 labeled miRISC complexes, assembled on let-7-a1 miRNAs, were incubated with surface-immobilized mH mRNAs (**Fig. 4.3A, right**) to allow for miRISC-mRNA complex assembly. As negative controls, miRISC complexes were also added to surfaces that either contained no mRNAs (negative, -ve) or were immobilized with a non-specific mRNA (RLcx6x, -veRNA) (**Fig. 4.3A, left and middle**). After washing the surface to remove any unbound miRISC complexes, the slide was illuminated until all the fluorophores had photobleached. By analyzing the number of photobleaching steps we were able to deduce the number of miRNA molecules within each particle. At first glance, miRISC bound mRNAs were visible as diffraction limited, well distributed particles in the field of view. We found (**Fig. 4.3A, B**) ~30 and ~5.5 fold more particles per field of view in slides immobilized with the specific mRNA (mH) compared to empty slides (-ve) and those immobilized with a non-specific (-veRNA) mRNA, respectively, attesting to the specificity of the miRNA:mRNA interactions in HeLa cell extracts. Upon further analysis, we found that a majority of the particles, ~ 70% in the mH sample, photobleached in a single step (**Fig. 4.3C, D**). Close to 30% of the particles, however, did contain anywhere between 2 to 5 miRNA molecules. Although the mouse HMGA2 mRNA contains seven let-7 seed sequences in its 3`UTR, we never observed any spots bleaching in seven steps, indicating the absence of fully loaded mRNAs. Thus, our observations

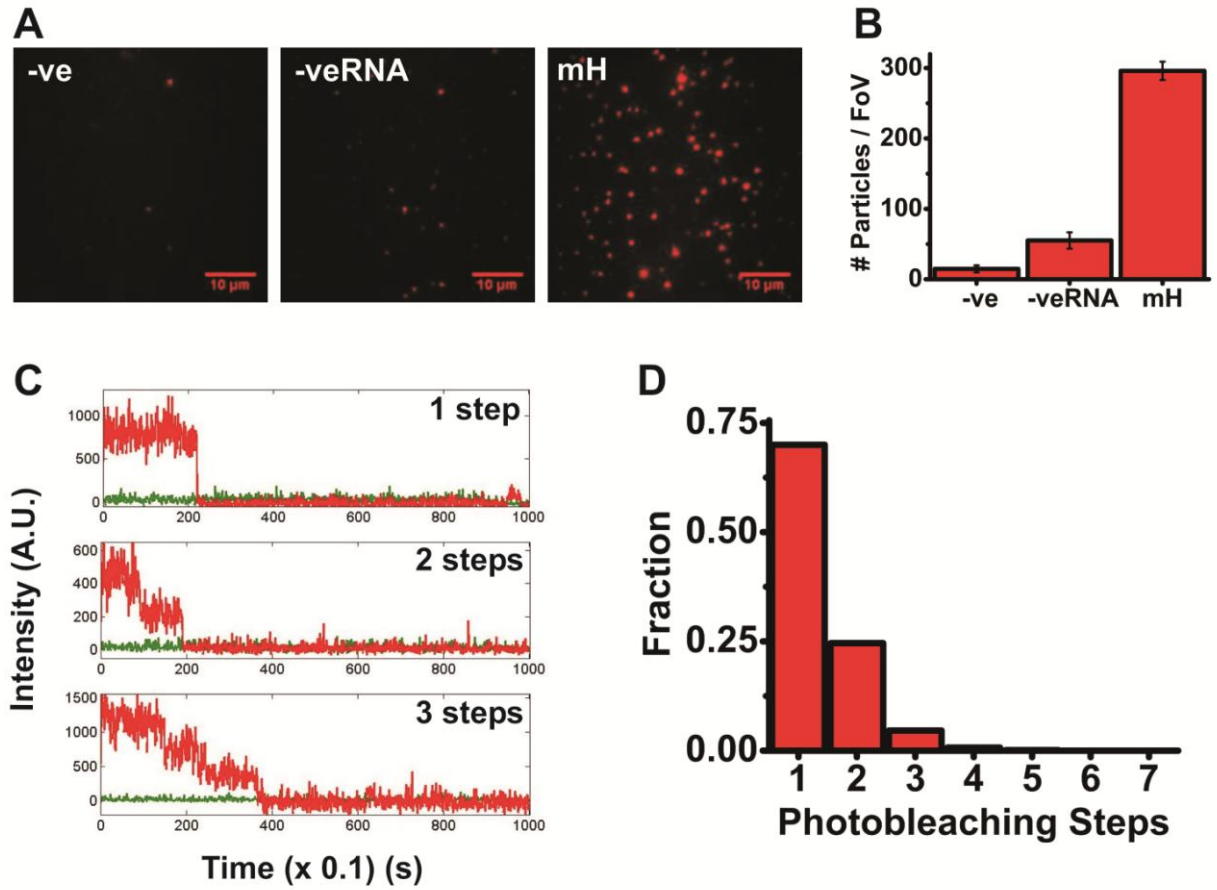

Figure 4.3. Single molecule miRNA counting experiments using HeLa cell extract. (A) Representative images of samples immobilized with no mRNA (-ve, left), a non-specific RLcx6x mRNA (-veRNA, middle) and a specific mouse HMGA2 mRNA (mH, right). (B) Number of particles per field of view (FoV) in each of the samples indicated in (A). (n = 5 slides and one FoV each) (C) Representative intensity trajectories showing one, two and three step photobleaching respectively. (D) Histogram depicting the distribution of photobleaching steps in the mH sample (n = 1576 particles).

suggest that mRNAs bind miRNAs at sub-stoichiometric ratios, even if they contain several seed sequences for the same miRNA.

We further sought to understand whether our previous observations were cell extract specific or were a general phenomenon associated with miRNA mediated target repression. To this end, we conducted photobleaching experiments with a different miRNA-mRNA pair in another cell extract, the rabbit reticulocyte lysate (RRL), which has been shown to faithfully recapitulate miRNA effecter function (71, 229, 232). As RRL is also translationally viable, its use offered a functional assay to correlate the amount of repression with miRNA binding. Ensemble luciferase assays showed that a Cy5 labeled cxcr4 miRNA repressed its cognate RLcx6x mRNA target both specifically and effectively (~50% repression, **Fig. 4.4A**) when pre-annealed to the mRNA (compare 'PA' to '-ve' and '-' in **Fig. 4.4A**) at stoichiometric ratios. In fact, the RLcx6x mRNA, which contains six cxcr4 seed sequences, was maximally repressed only when the mRNA was annealed with the miRNA at a ratio of 1:6 (229, 232), not higher or lower. As described previously (229, 232), addition of the antisense (guide) strand only (AS) or the miRNA duplex (DS) to the repression reaction resulted in lower amounts of repression than observed when the miRNA was pre-annealed to the mRNA. We then performed single molecule experiments using the same conditions that resulted in maximal repression to compare the distribution of miRNA binding stoichiometry with the extent of protein reduction. To our surprise, we found that a majority of Cy3 labeled RLcx6x mRNAs (~75%) were not bound by any miRNA (**Fig. 4.4B**), even when close to 50% reduction in protein expression was achieved in our repression assay. We additionally found that a majority of miRNA-associated mRNAs (~95%) bound just one copy of the miRNA (**Fig. 4.4C, D**). Based on our control experiment testing for bias from prebleached fluorophores, we found that close to 70% of all Cy5 labeled RNAs were fluorescent, as expected if prebleaching is negligible (**Fig. 4.4E**). These observations, in combination with our miRNA counting data in HeLa cell extracts, support the notion that sub-stoichiometric miRNA binding to mRNAs is a general

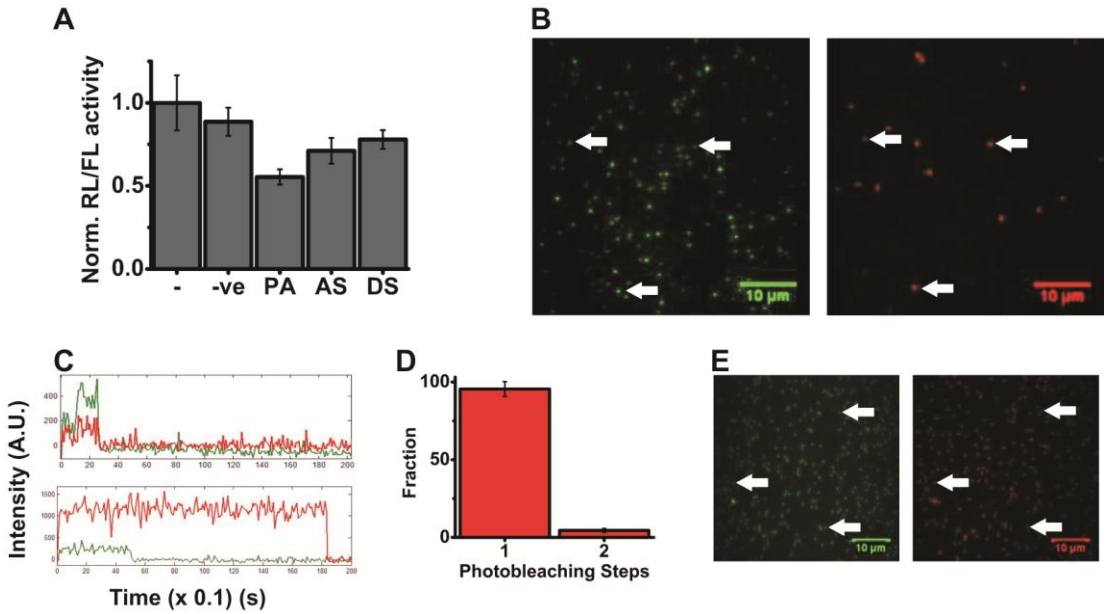

Figure 4.4. Luciferase assay**,** single molecule miRNA counting experiments using RRL and control single molecule experiment. (A) Dual luciferase assay of repression reactions that contain capped and tailed RLcx6x and FL mRNAs respectively, and either no miRNA (-), non-specific let-7-a1 miRNA (-ve), cxcr4 miRNA pre-annealed to mRNAs in a 1:6 miRNA:mRNA ratio (PA), anti-sense strand of cxcr4 miRNA (AS) or double stranded cxcr4 miRNA (DS). Renilla luciferase luminescence was normalized with that of firefly luciferase. All samples were normalized with respect to the no miRNA sample. Error bars, standard deviation (n = 6 independent trials). (B) Representative single-molecule image of Cy3 (left) and Cy5 (right) channels respectively. Arrows depict colocalized Cy3 and Cy5 spots. (C) Representative intensity trajectories showing single step photobleaching of both Cy3 (green) and Cy5 (red), which represents single mRNA molecules (green) bound by single miRNA molecules (red). (D) Histogram depicting the distribution of photobleaching steps in the RLcx6x sample (n = 694 particles). (E) Control experiment (**Materials and Methods**) to measure bias from dark fluorophores. Representative single-molecle image of Cy3 (left, green) and Cy5 (right, red) channels respectively. Arrows depict colocalized Cy3 and Cy5 spots.

phenomenon. Additionally, this notion potentially explains the relatively low repression potential of miRNAs as compared with silencing RNAs (siRNAs), a class of small RNAs that bind with complete complementarity to their mRNA targets to mediate mRNA cleavage.

4.4 Discussion

An ill-understood aspect of miRNA mediated mRNA repression is that of the binding stoichiometry between miRNAs and their mRNA targets, that is, to what extent any single binding site is occupied to affect mRNA regulation. Conversely, it is still unknown whether all binding sites within the 3`UTR of an mRNA containing multiple seed sequences are occupied by miRNAs simultaneously. To this end, we developed a single molecule assay that utilizes the stepwise photobleaching of single fluorophores to quantify the number of miRNAs bound per mRNA target *in vitro*. We first executed our assay in RNAi-competent (yet translation-inactive) HeLa cytosolic S100 extract. Let-7-a1 associated complexes were pre-assembled (**Materials and Methods**) and added to biotin-tagged mRNAs that were specifically immobilized on streptavidin coated surfaces. Surprisingly, a majority of mRNAs were bound by just one miRNA. In a complementary experiment, biotinylated and fluorophore labeled mRNAs were incubated with cell extracts that contained miRNAs labeled in a different color. miRNA-associated mRNAs were then immobilized on streptavidin coated quartz slides and the number of miRNAs bound per mRNA in rabbit reticulocyte lysate was deduced from the number of photobleaching steps of the miRNA fluorophore that colocalized with that of the mRNA. Our ability to fluorescently label large mRNAs allowed us to observe that a majority of mRNA molecules are either unoccupied or only singly occupied. Combining these results with *in vitro* repression assays, we conclude that repression indeed is achieved at sub-stoichiometric binding of miRNAs to their cognate mRNA target sites, contrary to previous reports.

The hypothesis that miRNAs bind to mRNAs in a cooperative manner has been largely based on the observation that mRNAs with a single miRNA binding site are repressed to lower levels as compared to an mRNA with multiple seed sequences (63, 64). However, these conclusions were derived from indirect repression reporter assays that are capable of only measuring functional cooperativity (synergistic effects that can be mediated either by cooperative binding or, in contrast, by increased probability for binding due to the presence of multiple binding sites), not binding cooperativity. In contrast, we directly visualized miRNA-mRNA interactions and our results suggest a relatively low propensity for binding of multiple miRNA to a total of seven seed sequences, suggesting the absence of positive cooperativity. A recent report (225) had suggested the incapability of small RNAs loaded into Ago2, unlike those loaded into other Ago isoforms (Ago1, 3 and 4 in mammals), in demonstrating positive cooperativity for binding to mRNAs. It is thus possible that both cell extracts we used are enriched in Ago2 (234), which in turn would be expected to lead to independent, non-cooperative binding of miRISCs onto mRNAs. Alternatively, the washing step in our single molecule assays, used to remove unbound miRISCs, may possibly cause the dissociation of loosely bound miRISCs and thus introduce a bias towards the visualization of only high-affinity binding events. We are currently in the process of implementing experiments that involve photo-induced cross-linking of miRISCs to mRNAs to further validate our conclusions.

Another possible explanation for our observations derives from our secondary structure and hybridization energy predictions (**Fig. 4.1**). Highly structured regions within an mRNA may be refractory to miRNA binding, thus leading to the prediction that seed sequence accessibility is a key factor determining miRNA occupancy; however, the limited stability of miRNA:target site hybridization also cannot be discounted. In both mRNAs we analyzed, only one seed sequence (seed sequences 5 and 1 in mH and RLcx6x, respectively) are located in their entirety within unstructured loops. These regions may possibly be the only ones to which miRISC binds with high propensity, consistent with previous reports (235, 236) that had suggested the need for at least four

unpaired bases within the mRNA seed sequence for efficient target site recognition and repression. In contrast, binding site 6 within the mH mRNA, which is almost completely hybridized with another region of the mRNA, binds with maximum complementarity to let-7-a1 miRNA, representing the potentially most stable association. Due to its strong secondary structure this, however, may not be the most favorable site, in the light of previous evidence (237) that active RISC is unable to unfold highly structured RNAs. Although it is still unclear whether the most accessible site or the most stably bound site is preferably occupied, it is likely that not all seed sequences within an mRNA can be bound with equal likelihood. Our finding that mRNAs containing multiple seed sequences are predominantly bound by just one miRNA, together with our computational analysis and previous reports thus may not only explain the relatively modest gene regulatory effect of miRNAs, but also why some mRNAs contain multiple (up to 7) redundant binding sites for the same miRNA; multiple miRNA binding sites simply provide a greater chance for effective miRNA engagement.

In summary, we have developed a novel single molecule assay to visualize and quantify the number of miRNA molecules bound per mRNA *in vitro*. To the best of our knowledge our data represent the first reported observations of a physical interaction between miRNAs and mRNA at the single molecule level. We predominantly observe only singly miRNA bound mRNAs, consistent with a probabilistic model for miRNA binding. We additionally hypothesize that mRNA structure and low miRNA binding energy may lead to sub-stoichiometric binding of miRNAs to mRNAs, which in turn serves as a plausible explanation for the relatively low repressive power of miRNAs. Comparing the binding profiles not only between different miRNAs, but also between miRNAs and siRNAs, will help us understand how mRNA structure and the extent of complementarity between mRNA targets and repressor RNAs affect repression, thereby providing a basic understanding of the molecular mechanism by which small regulatory RNAs mediate transcriptome-wide gene repression.

4.5 Acknowledgements

We thank C. Mayr and D. Bartel for providing us the plasmids containing the cDNA of mouse HMGA2, J. Hoerter for making the pcDNA-mH-2xwt clone, C. Novina for fruitful discussion of setting up repression assays in RRL and A. Mapp for access to her plate reader. This work was supported by NIH grant GM081025 to N. Walter.

Chapter 5

Summary and Future Outlook

5.1 Summary

The recently discovered pervasive nature of non-coding RNAs (ncRNA) in biology has highlighted their involvement in all aspects of multi-cellular life (6, 7, 9) and has prompted a fundamental reinterpretation of the central dogma of molecular biology. MicroRNAs are one such class of evolutionarily conserved small ncRNAs that act as master regulators of cellular gene expression (11, 12).

Standard biochemical assays have provided a wealth of information about the miRNA pathway at the ensemble level (11, 12, 65). The cell, however, is a complex mixture of many single molecules, each bearing distinct properties and specifically interacting with its local environment. Thus, it is very important to understand, if possible, the distribution of properties and behaviors of every single molecule, rather than just their average. Single molecule microscopy has the potential to reveal heterogeneity within a sample appearing homogenous at the ensemble level, thereby unraveling key outliers, transient species, and rare events (94). Given that several mechanisms have been proposed for miRNA mediated gene regulation and it is still debated which repression mode(s) are at work (62, 65), miRNA research clearly calls for investigation using single molecule tools. Two such novel single-molecule tools have been described in this thesis that: (i) probe miRNA diffusion and assembly in cultured cells; and (ii) quantify the binding stoichiometry between miRNAs and their targets *in vitro*. Both of these approaches have the potential to resolve long-standing

unanswered questions in the RNA silencing field that has recently spawned a multi-billion dollar biotech industry.

Chapter 2 describes a method to visualize miRNAs inside individual cells, with single molecule sensitivity. Previously reported methods of intracellular RNA observation, particularly an optimized illumination strategy (100), single particle tracking (SPT) and the probabilistic, step-wise photobleaching property of fluorescent probes (134, 135, 173), were all carefully 'packaged' together with microinjection into one widely usable single-molecule tool to specifically investigate the intracellular diffusion and distribution of miRNAs. Microinjection allowed for the homogeneous, controlled delivery of miRNAs directly into cells in an efficient and non-invasive fashion. Ensemble luciferase and fluorescent reporter gene assays (**Fig. 2.1**) showed that fluorophore modification and microinjection do not affect miRNA function, attesting to the low invasiveness of the method. In this fashion, each cell functions as an individual reaction vessel into which fluorophore labeled miRNAs are introduced. One hour or more after microinjection, miRNAs could be visualized as well isolated, diffraction limited particles that diffused with a wide range of diffusion coefficients (~0.7–0.0001 $\mu m^2/s$) and demonstrated multifarious diffusive patterns (Brownian, corralled and directed) in living cells (**Fig. 2.2**). Diffusion coefficients of miRNA particles were distributed within (at least) two distinct Gaussian populations and were indicative of miRNA-bound mRNAs (87) and PBs (190) respectively, functional intermediates of miRNA mediated gene regulation. The different modes of diffusion were consistent with the expectation that intracellular miRNAs follow multiple pathways. The nature of the diffusing particles was further probed in formaldehyde-fixed cells. Fixing immobilized all particles so that the number of miRNA molecules within individual particles could be quantified using the quantized photobleaching of fluorescent probes (**Fig. 2.8**). The number of photobleaching steps was used to quantify the number of miRNA molecules assembled within each particle (134, 135, 173). With unprecedented sensitivity, this single molecule counting assay showed that a majority of particles contained individual miRNA molecules; however, significant fractions of particles also held

multiple molecules (up to seven). Additionally, fluorescence intensity analysis showed that our fixed cell analysis reflects the situation in live cells (**Fig. 2.10**). Finally, the temporal changes observed in mobility of particles in live cells and their assembly states in fixed cells support a miRNA-induced multiple-turnover model of target mRNAs (**Fig. 2.12**), consistent with previous reports (238). Notably, our method breaks the diffraction limit and reaches a super-accuracy of ~30 nm for particle or molecule localization (**Fig. 2.3**) at a temporal resolution of 100 ms.

Transport of miRNA bound and suppressed mRNAs to processing bodies (PBs), cellular protein assemblies enriched in RNA processing enzymes (82), is considered one plausible mechanism by which miRNAs regulate protein expression (67, 81). Chapter 3 aimed (**Chapter 2**) to further quantify the extent of co-localization of miRNA-containing complexes and PBs, and thus estimate the fraction of miRNA bound mRNAs that are channeled though this pathway. To this end, high resolution (~10 nm) single molecule/particle tracking and single molecule counting were performed at two colors. Consistent with previous ensemble measurements (67) only a small fraction of miRNAs localized to PBs under conditions of cellular fixation. However, a surprising diversity in the number of miRNA molecules within individual PBs was observed (**Fig. 3.3**), strongly suggesting a heterogeneous composition of PBs and miRNA complexes and/or modes of miRNA-PB interaction. Further characterization of miRNA-PB interactions in live cells (**Fig. 3.4**) showed the presence of transient association, for on the order of a few hundred milliseconds, in addition to previously predicted stable association (189). Not only were such transient associations, hitherto unobserved, as frequent as the stable interactions, but individual miRNAs could switch between short and long residence times on the same PB. Taken together, our data suggests the presence of a diverse set of PB and miRNA complexes, and the potential role of an interacting protein or RNA partner that increases the affinity between the two complexes when present.

Finally, the studies described in Chapter 4 found that miRNAs interact inefficiently with their cognate mRNAs under conditions of maximal repression.

The extent of miRNA binding to mRNAs bearing multiple miRNA binding sites were measured *in vitro*, using RNA interference (RNAi) competent mammalian cell extracts (229, 231, 232) at the single-molecule level. Stepwise photobleaching analysis was again used to count the number of miRNA molecules on individual immobilized mRNA targets that were either labeled or unlabeled, under conditions of maximal repression (as assayed separately, **Fig. 4.4A**). In contrast to previous reports that had suggested positive cooperativity (35, 63, 64, 225), mRNAs with multiple seed sequences for a particular miRNA were predominantly bound by either no or just one miRNA (**Fig. 4.3 and 4.4**). The previous reports measured, however, functional cooperativity using reporter assays that indirectly quantify the increase in repression upon increasing miRNA concentration (35, 63, 64, 225). In contrast, our method visualizes actual association and has the potential to measure true binding cooperativity, if it exists. Furthermore, our observations are consistent different two cell extracts using two distinct miRNA:mRNA pairs. Our preliminary computational analysis of mRNA structure and miRNA binding energy coupled with previous reports (235-237) seem to corroborate our single-molecule results; structured regions in mRNAs render a majority of binding sites inaccessible to miRNAs and the binding to these sites with incomplete complementarity further decreases the propensity for miRNA binding to mRNAs. Our results strongly suggest that a miRNA has a higher total probability for binding to an mRNA with multiple seed sequences as compared to one with lower number of binding sites and this effect alone leads to the higher repression of the former.

Taken together, the data in both Chapters 3 and 4 offer a molecular understanding for the relatively modest repressive capability of miRNAs. Firstly, miRNAs bind with incomplete complementarity to their cognate mRNAs than their close cousins silencing RNAs (siRNAs) (12) that bind with higher complementarity to cause mRNA cleavage and thus stronger repression. Second, mRNA structure possibly renders a majority of miRNA binding sites inaccessible, thereby decreasing the propensity for miRNA binding. Conversely, siRNAs can better disrupt mRNA structure than miRNAs, which may further

enhance this effect. Finally, miRNA-bound mRNA complexes appear to bind to PBs with low affinity, decreasing the chance for the degradation of the target by PB components. This suggests that miRNAs work at the lower threshold of a multistep repression pathway, with low probabilities at each step, which culminates in a modest repressive ability that can quickly and substantially be ramped up if needed.

5.2. Future Outlook

Cell extracts provide the advantage of probing miRNA mediated repression events at much shorter time scales than transfection based cell culture assays, which can take hours or even days. Additionally, cell extracts offer ease of manipulation; it is relatively easy to add or remove specific molecular components at defined concentrations to observe dominant negative and loss-of-function phenotypes. In light of these advantages, future experiments to understand miRNA-mRNA interactions *in vitro* should include the addition of specific miRNA pathway proteins such as those of the Argonaute family, either in the form of their mRNA or as purified proteins. Such experiments can be used to verify whether miRNA association is modulated by titration of such proteins, which would indicate that they are limiting reagents. Additionally, experimental structure probing of mRNAs will be required to clearly predict the contribtion of mRNA structure and thus target site accessibility in miRNA binding. As binding of miRNAs to mRNAs is directly observed in our experiments, one can easily envision the determination of association and dissociation constants from such *in vitro* data, building a kinetic framework for miRNA mediated target repression.

The methods presented in this thesis (especially in **Chapters 2 and 3**) only present a glimpse at their future possibilities. Our ability to visualize single molecules and complex assembly with exceptional spatiotemporal accuracy and resolution inside cells lets us envision the application of this method to several other molecular systems. The first and most logical extension of the method

presented in Chapter 2 would be to observe the diffusion and distribution of other miRNAs or siRNAs in multiple cell lines. It would be especially interesting to compare the intracellular localization, transport and complex assembly of miRNAs in cancerous cells and healthy cells, cultured from animal tissues, given that miRNA levels, expression profiles (239) and even function are different between them (John Androsavich, unpublished data). These differences may explain the diversity of modes of miRNA action proposed based on a plethora of experimental approaches, and our tools promise to shed light on the relative importance of these pathways.

Based on our repression data (**Fig. 2.1**) it is highly likely that a significant proportion of our observed particles are functional, actively repressing miRISC-mRNA complexes. Further characterization of all particles by dual color tracking and colocalization, similar to that presented in Chapter 3, will aid in understanding the exact number of functional miRNAs. We can microinject miRNAs fluorescently labeled on both strands of the duplex and quantify the ratio of double-stranded to single-stranded miRNA. As only one strand of the miRNA duplex (guide) is preferentially retained in active RISC (**Fig. 1.2**), this experiment would serve to measure duplex unwinding and strand selection. As we can now also label and visualize single mRNA molecules (**Appendix 2**), it would be relatively easy to find the exact percentage of target bound miRNAs, and similar to the method presented in Chapter 4, find the number of miRNAs bound per mRNA target inside cells (as opposed to cell extracts). Furthermore, we may even be able to compare the intracellular activity of fluorophore labeled pre-miRNAs and mature miRNAs, as there is evidence for greater repressive capabilities of the former. We can, additionally, microinject pre-miRNAs specifically into the nucleus to monitor their nuclear export kinetics and investigate the effect of this step on pathway progression.

Apart from the canonical pathway, miRNAs can act as substrates of several other cellular pathways (47). For instance, certain miRNAs undergo degradation mediated by terminal uridyl transferase (TUT) (240, 241), whereas

still others have their sequences modified by adenosine deaminase acting on RNA (ADAR) (242). The latter, especially editing within seed sequences, can have an important impact on the targeting specificity of edited miRNAs (243). Using dual-color experiments (**Chapter 3**) we can exactly count the number of miRNA molecules within these off-(RNAi)-pathways. In this fashion, we will be able to monitor the progress of miRNAs though every step of the RNAi and other, competing cellular pathways at single molecule sensitivity, with the ultimate goal of understanding the RNAi mechanism through a novel single molecule systems biology.

Appendix 1

Purification and Functional Reconstitution of Monomeric μ-Opioid Receptors: Allosteric Modulation of Agonist Binding by G_{i2}[2]

A1.1 Introduction

Opioid receptors are members of the G protein-coupled receptor (GPCR) superfamily and are clinical mainstays for inducing analgesia. Three isoforms of opioid receptors, μ, δ, and κ, have been cloned and are known to couple to $G_{i/o}$ proteins to regulate adenylyl cyclase and K^+/Ca^+ ion channels (244-246). An ever growing amount of data suggests that many GPCRs oligomerize (247, 248), and several studies have suggested that μ-opioid receptors (MORs) and δ-opioid receptors heterodimerize to form unique ligand binding and G protein-activating units (249-253). Although intriguing, these studies utilize cellular overexpression systems where it is difficult to know the exact nature of protein complexes formed between the receptors.

To study the function of isolated GPCRs, our laboratory and others have utilized a novel phospholipid bilayer reconstitution method (254-259). In this approach purified GPCRs are reconstituted into the phospholipid bilayer of a high density lipoprotein (HDL) particle. The reconstituted HDL (rHDL) particles are monodispersed, uniform in size, and preferentially incorporate a GPCR monomer (258, 259). Previous work in our lab has shown that rhodopsin, a class A GPCR

[2] Adapted with permission from Kuszak, A.J., Pitchiaya, S., Anand, J.P., Mosberg, H.I., Walter, N.G., and Sunahara, R.K., *Journal of Biological Chemistry*, 284: 26732–26741. © 2009 by The American Society for Biochemistry and Molecular Biology, Inc. Sethuramasundaram Pitchiaya carried out the single-molecule assays and the ensuing analysis.

previously proposed to function as a dimer (260-262), is fully capable of activating its G protein when reconstituted as a monomer in the rHDL lipid bilayer (259). Moreover, we have demonstrated that agonist binding to a monomeric β_2-adrenergic receptor, another class A GPCR, can be allosterically regulated by G proteins (258). This led us to determine whether a monomer of MOR, a class A GPCR that endogenously binds peptide ligands, is the minimal functional unit required to activate coupled G proteins. We additionally investigated whether agonist binding to monomeric MOR is allosterically regulated by inhibitory G protein heterotrimer.

To study the function of monomeric MOR we have purified a modified version of the receptor to near homogeneity. A yellow fluorescent protein was fused to the N terminus of MOR, and this construct (YMOR) was expressed in insect cells for purification. After reconstitution of purified YMOR into rHDL particles, single-molecule imaging of Cy3-labeled and Cy5-labeled YMOR determined that the rHDL particles contained one receptor. This monomeric YMOR sample binds ligands with affinities nearly equivalent to those observed in plasma membrane preparations. Monomeric YMOR efficiently stimulates GTPγS binding to G_{i2} heterotrimeric G protein. G_{i2} allosteric regulation of agonist binding to rHDL●YMOR was also observed. Single-particle imaging of binding of [Lys^7, Cys^8]dermorphin-Cy3, a fluorophore-labeled agonist, to rHDL●YMOR supports the notion that the rHDL particles contain a single YMOR. Taken together, these results suggest that a monomeric MOR is the minimal functional unit for ligand binding and G protein activation and illustrate a novel method for imaging ligand binding to opioid receptors.

A1.2 Materials and methods

Materials. G protein baculoviruses encoding rat $G\alpha_{i2}$, His_6-$G\beta_1$, and $G\gamma_2$were provided by Dr. Alfred G. Gilman (University of Texas Southwestern, Dallas, TX). DNA encoding human -opioid receptor (NM 000914.2) was provided by Dr. John

R. Traynor (University of Michigan, Ann Arbor, MI). Expired serum was generously provided by Dr. Bert La Du (University of Michigan, Ann Arbor, MI). Spodoptera frugiperda (Sf9) and Trichoplusia ni (HighFive™) cells, pFastBac™ baculovirus expression vectors and Sf900™ serum-free medium were from Invitrogen. InsectExpress™ medium was purchased from Lonza (Allendale, NJ). N-Dodecyl-β-D-maltoside was from Dojindo (Rockville, MD). All of the lipids were from Avanti Polar Lipids (Alabaster, AL). [^{3}H]diprenorphine (DPN, 54.9 Ci/mmol) and [^{35}S]GTPγS (1250 Ci/mmol) were obtained from PerkinElmer Life Sciences. EZLink™ NHS-Biotin reagent was from Pierce. Ovomucoid trypsin inhibitor was purchased from United States Biological (Swampscott, MA). GF/B and BA85 filters, Cy3 and Cy5 NHSester mono-reactive dyes, Cy3-maleimide dye, and Source 15Q and Superdex 200 chromatography resins were from GE Healthcare. Talon™ resin was from Clontech. Bio-Beads™ SM-2 absorbant resin was from Bio-Rad. Chromatography columns were run using a BioLogic Duo-Flow protein purification system from Bio-Rad. Amicon Ultra centrifugation filters were from Millipore (Billerica, MA). Amino acids for ligand synthesis were obtained from Advanced ChemTech (Louisville, KY) or Sigma-Aldrich. All other chemicals and ligands were from either Sigma-Aldrich or Fisher Scientific.

YFP-μ-Opioid Receptor Fusion Protein Expression and Purification. Baculoviruses were created using transfer vectors (pFastBac™) that encoded a fusion protein of an N-terminal cleavable hemagglutinin signal sequence (MKTIIALSYIFCLVF), a FLAG epitope (DYKDDDD), a decahistidine tag, the monomeric and enhanced yellow fluorescent protein (Clontech), and the human MOR. High titer viruses (10^{7}–10^{8} plaque-forming units/ml) were used to infect Sf9 or HighFive™ suspension cultures at a multiplicity of infection of 0.25 to 1. FLAG-His_{10}-mEYFP-MOR (YMOR) was expressed for 48 –52 h in the presence of 1 μM naltrexone (NTX). The cells were resuspended in Buffer A (50 mM Tris●HCl, pH 8.0, 50 mM NaCl, 100 nM NTX, and protease inhibitors (3.2 μg/ml leupeptin, 3.2 μg/ml ovomucoid trypsin inhibitor, 17.5 μg/ml phenylmethanesulfonyl fluoride, 16 μg/ml tosyl-L-lysine-chloromethyl ketone (TLCK), 16 μg/ml tosyl-L-phenylalanine chloromethyl ketone (TPCK)) and lysed by nitrogen cavitation. Supernatants from

a 500 x g spin were then subjected to 125,000 x g spin for 35 min, and pellets containing membrane fractions were resuspended in Buffer A and either stored at -80 °C for later binding assays or further processed to purify receptor.

All of the purification steps were performed sequentially and at 4 °C or on ice. Membrane preparations were diluted to 5 mg/ml in Buffer A plus 1% DDM (w/v) and 0.01% cholesteryl hemisuccinate (CHS) (w/v) and gently stirred for 1 h to solubilize YMOR out of the membrane. Detergent extracted YMOR was enriched via Talon^{TM} metal affinity chromatography resin (Clontech) in Buffer A plus 0.1% DDM and 0.01% CHS and eluted with Buffer A plus 0.1% DDM, 0.01% CHS, and 150 mM imidazole. Fractions containing YMOR (based on Coomassie staining after SDS-PAGE separation) were pooled, diluted 5-fold in Buffer B (20 mM Hepes, pH 8.0, 5 mM MgCl2 , 0.1% DDM, 0.01% CHS, 100 nM NTX, and phenylmethanesulfonyl fluoride-TLCK-TPCK protease inhibitors), and eluted from a 1-ml Source 15Q strong anion exchange column with a 50 –300 mM NaCl linear gradient. Peak fractions were identified by radioligand binding assays using [^{3}H]DPN (2–4 nM). Peak fractions were then pooled and concentrated on Amicon Ultra centrifugation filters (10-kDa molecular mass cut-off). As a final purification step this YMOR sample was resolved based on size using a Superdex 200 gel filtration column (GE Healthcare) in Buffer C (20 mM Hepes, pH 8.0, 100 mM NaCl, 0.1% DDM, 0.01% CHS, 100 nM NTX, and protease inhibitors). Coomassie staining after SDS-PAGE was used to identify fractions containing YMOR, which were pooled and concentrated to ~1–2 μM. Glycerol was added to a final concentration of 10% (v/v), and the samples were flash-frozen in liquid nitrogen and then stored at -80 °C until further use.

ApolipoproteinA-1 Purification. Wild type human apoA-1 was purified from expired serum as previously described (258). A recombinant apoA-1 with an N-terminal 43-amino acid deletion and a histidine tag (Δ(1–43)-His_6 -ApoA-1) was expressed using a pET15b vector to transform competent Escherichia coli cells (BL21). The cells were resuspended and lysed by gentle vortexing in 10 mM Tris●HCl, pH 8.0, 100 mM NaH_2PO_4, 6 M guanidine hydrochloride, 1% Triton X-

100. Lysate was fractionated by centrifugation at 10,000 x g, and the supernatant was loaded onto a nickel-nitrilotriacetic acid column by gravity flow. The column was washed with 10 mM Tris●HCl, pH 8.0, 100 mM NaH_2PO_4, 6 M guanidine hydrochloride, 1% Triton X-100 and then with 50 mM NaH_2PO_4, pH 8.0, 300 mM NaCl, 1% Triton X-100. Bound Δ(1–43)-His_6-apoA-1 was eluted with 50mM NaH_2PO_4 , pH 8.0, 300 mM NaCl, 250 mM imidazole, 1%Triton X-100. Peak fractions were further purified on a Superdex 75 gel filtration chromatography column in 20 mM Hepes, pH 8.0, 100 mM NaCl, 1 mM EDTA, 20 mM sodium cholate. Pooled apoA-1 was then dialyzed against 20 mM Hepes, pH 8.0, 100 mM NaCl, 1 mM EDTA, 5 mM sodium cholate. Purified apoA-1 was concentrated to 10 mg/ml and stored at -80 °C until use.

In Vitro HDL Reconstitution. HDL particles were reconstituted according to previously reported protocols (258). Briefly, 21 mM sodium cholate, 7 mM lipids (1-palmitoyl-2-oleoyl-snglycero-3-phosphocholine (POPC) and 1-palmitoyl-2-oleoylsn-glycero-3-[phospho-rac-(1-glycerol)] (POPG) at a molar ratio of 3:2), purified YMOR (DDM-solubilized), and 100 µM purified apoA-1 were solubilized in 20 mM Hepes, pH 8.0, 100 mM NaCl, 1 mM EDTA, 50 mM sodium cholate. The final concentration of YMOR varied from 0.2 to 0.4 µM, but YMOR always comprised 20% of the total reconstitution volume. In some reconstitutions the lipid component was modified such that porcine polar brain lipid extract (Avanti Polar Lipids) was used in addition to POPC and POPG for a final concentration of 7 mM lipids at a molar ratio of 1.07:1.5:1 brain lipid: POPC: POPG. Following incubation on ice (1.5–2 h), the samples were added to Bio-Beads^{TM} (Bio-Rad, 0.05 mg/ml of reconstitution volume) to remove detergent and to form HDL particles. Particles containing YMOR were purified via M1 anti-FLAG immunoaffinity chromatography resin (Sigma) and eluted with 1 mM EDTA plus 200 µg/ml FLAG peptide. To assess the efficiency of HDL reconstitution, the total protein concentration of rHDL●YMOR was compared with the concentration of active reconstituted YMOR. FLAG affinity column-purified rHDL●YMOR was resolved from BSA and FLAG peptide on a Superdex 200 gel filtration column, and the peak fraction was analyzed for protein content with Amido Black staining

(263), whereas [^{3}H]DPN saturation assays were used to measure active YMOR content. YMOR reconstituted into HDL was stored on ice until further use.

G Protein Addition to rHDL●YMOR Particles. G_{i2} heterotrimer ($G\alpha_{i2}$- $His_6G\beta_1$-$G\gamma_2$) was expressed in Sf9 cells and purified as previously described (264). The concentration of active G protein was determined by filter binding of 20 μM [^{35}S]GTPγS (isotopically diluted) in 30 mM NaHepes, pH 8.0, 100 mM NaCl, 50 mM MgCl2, 1 mM EDTA, 0.05% $C_{12}E_{10}$, and 1 mM dithiothreitol after 1 h of incubation at room temperature. Purified G protein heterotrimer was added to preformed, FLAG-purified rHDL●YMOR particles at a molar ratio of 1:10 receptor to G protein. G_{i2} was purified in 0.7% CHAPS, and the final volume of G protein added to rHDL●YMOR was such that the final CHAPS concentration was well below its critical micelle concentration. Reconstituted receptor and G protein samples were then incubated in Bio-Beads^{TM} for 30 –45 min at 4 °C to remove residual detergent.

[^{3}H]DPN Saturation and Agonist Competition Binding Assays. Binding reactions were performed in 100-μl volumes. Membrane fractions prepared from Sf9 or HighFive^{TM} cells expressing YMOR (0.5–5 μg total protein, prepared as above) were incubated with [^{3}H]DPN (0.25 to 4 nM; 54.9 Ci/mmol) for 1 h at room temperature in 25 mM Tris●HCl, pH 7.7, 136 mM NaCl, 2.7 mM KCl (Tris-buffered saline) buffer. Nonspecific binding was determined in the presence of 20 μM NTX. Bound [^{3}H]DPN was separated from free by rapid filtration through GF/B filters and three 200-μl washes of ice-cold Tris-buffered saline. [^{3}H]DPN saturation binding reactions on YMOR incorporated into rHDL particles were prepared in Tris-buffered saline, pH 7.7, plus 0.1% BSA, and Sephadex G-50 Fine (GE Healthcare) gravity flow columns were used to separate bound from free [^{3}H]DPN. Agonist competition assays in insect membranes and rHDL particles were performed in 25 mM Tris●HCl, pH 7.7, 6 –7 mM NaCl. Competition assays in rHDL particles also included 0.1% BSA. [^{3}H]DPN binding assays on detergent solubilized YMOR were performed in 50 mM Tris●HCl, pH 7.7, 136 mM NaCl, 0.1% DDM, 0.01% CHS and separated on Sephadex G-50 gravity flow

columns. For agonist competition assays, receptor samples were incubated with 0.5–1 nM [^{3}H]DPN and increasing concentrations of agonist (1 pM to 1mM) in the absence or presence of 10 μM GTPγS. The samples were measured for radioactivity on a liquid scintillation counter, and the data were fit with one-site saturation, one-site competition, or two-site competition binding models using Prism 5.0 (GraphPad, San Diego, CA).

[^{35}S]GTPγS Binding Assay. 100-μl volume reactions were prepared containing 1 μg of total membrane protein from YMOR expressing HighFive^{TM} cells or ~50 – 60 fmol of YMOR incorporated into rHDL particles in 30 mM Tris●HCl, pH 7.4, 100 mM NaCl, 5 mM MgCl2 , 0.1 mM dithiothreitol, 10 or 1 μM GDP (membranes or HDL particles), and 0.1% BSA. Membrane assays and rHDL assays were incubated with 10 nM isotopically diluted [^{35}S]GTPγS (12.5 Ci/mmol). YMOR samples were incubated with increasing concentrations of agonists (1 pM to 1 mM) for 1 h at room temperature, then rapidly filtered through GF/B (membrane samples) or BA85 filters (HDL samples), and washed three times with 2 ml of ice-cold 30 mM Tris●HCl, pH 7.4, 100 mM NaCl, 5 mM MgCl2. The samples were measured for radioactivity on a liquid scintillation counter, and the data were fit with a log dose-response model using Prism 5.0.

Single-molecule Imaging of Reconstituted Cy3- and Cy5-YMOR. Purified YMOR (~200 pmol) was incubated with NHS-ester Cy3 or Cy5 mono-reactive dye (GE Healthcare) in 20 mM Hepes, pH 8.0, 100 mM NaCl, 5 mM MgCl2 , 6 mM EDTA, 0.1% DDM, 0.01% CHS, 100 nM NTX for 30 min at 25 °C and then 1 h at 4 °C. Conjugation reactions were quenched by the addition of Tris●HCl, pH 7.7 buffer (10 mM final). Cy-labeled YMOR was then separated from free dye using a 12-cm Sephadex G-50 column. The final dye to protein molar ratio was 3.8:1 for Cy3-YMOR and 3.7:1 for Cy5-YMOR, determined by absorbance at 280 nm for total protein, 550 nm for Cy3 dye, and 650 nm for Cy5 dye as measured on a NanoDrop ND-1000 spectrophotometer. A separate aliquot of YMOR was co-labeled with both Cy3 and Cy5 for final molar ratios of 2:1 Cy3: YMOR and 1.8:1 Cy5: YMOR. HDL reconstitutions of Cy3- YMOR alone, Cy5-YMOR alone,

a mixture of Cy3- and Cy5-YMOR, and Cy3-Cy5-YMOR were then performed. Reconstitutions were performed as previously described, using apoA-1 that had been biotinylated at a 3:1 molar ratio using EZ-Link NHS-Biotin according to the manufacturer's protocol (Pierce). Reconstituted samples were diluted 5000-fold in 25 mM Tris●HCl, pH 7.7, and injected into a microfluidic channel on a quartz slide that was previously coated with biotinylated polyethylene glycol and treated with 0.2 mg/ml streptavidin to generate a surface density of ~0.05 molecules/μm^2. An oxygen scavenging system of 10 mM Trolox (Sigma-Aldrich), 100 mM protocatechuic acid, and 1 μM protocatechuate-3,4-dioxygenase was included in the sample dilution (265). Following a 10-min incubation to allow binding of the biotin-HDL●CyYMOR complex to the streptavidin-coated slide, the channel was washed with ice-cold 25 mM Tris●HCl, pH 7.7, containing the oxygen scavenging system. An Olympus IX71 inverted microscope configured for prism-based total internal reflection fluorescence (TIRF) and coupled to an intensified CCD camera was used to image Cy3 and Cy5 fluorophores (CrystaLaser, 532 nm; Coherent CUBE laser, 638 nm; Chroma band pass filters HQ580/60 and HQ710/130 nm). Fluorophore intensity time traces were collected for 30 –100 s at 10 frames/s. Time traces were analyzed for photobleaching with in-house software (MatLab 7.0).

Synthesis of [Lys^7, Cys^8]Dermorphin and Labeling with Cy3 Dye. [Lys^7, Cys^8]dermorphin (Tyr-D-Ala-Phe-Gly-Tyr-ProLys-Cys-NH2) was synthesized on Rink resin (solid support) using an Applied Biosystems 431A peptide synthesizer and standard Fmoc (N-(9-fluorenyl)methoxycarbonyl) chemistry. The samples were characterized on a Waters reverse phase HPLC using a Vydac C18 (Protein and Peptide) 10-micron column. The samples were run on a linear gradient of 0 –45% acetonitrile in an aqueous phase containing 0.1% trifluoroacetic acid at 35 °C and monitored at 254 and 230 nm (**Fig. A1.1**). Peptides were similarly purified on a Waters semipreparative reverse phase HPLC using a Vydac C18 10-micron column at room temperature. The purified peptide was labeled with Cy3-maleimide (GE Healthcare) according to the manufacturer's instructions using a ratio of 1.5:1 peptide to fluorophore and

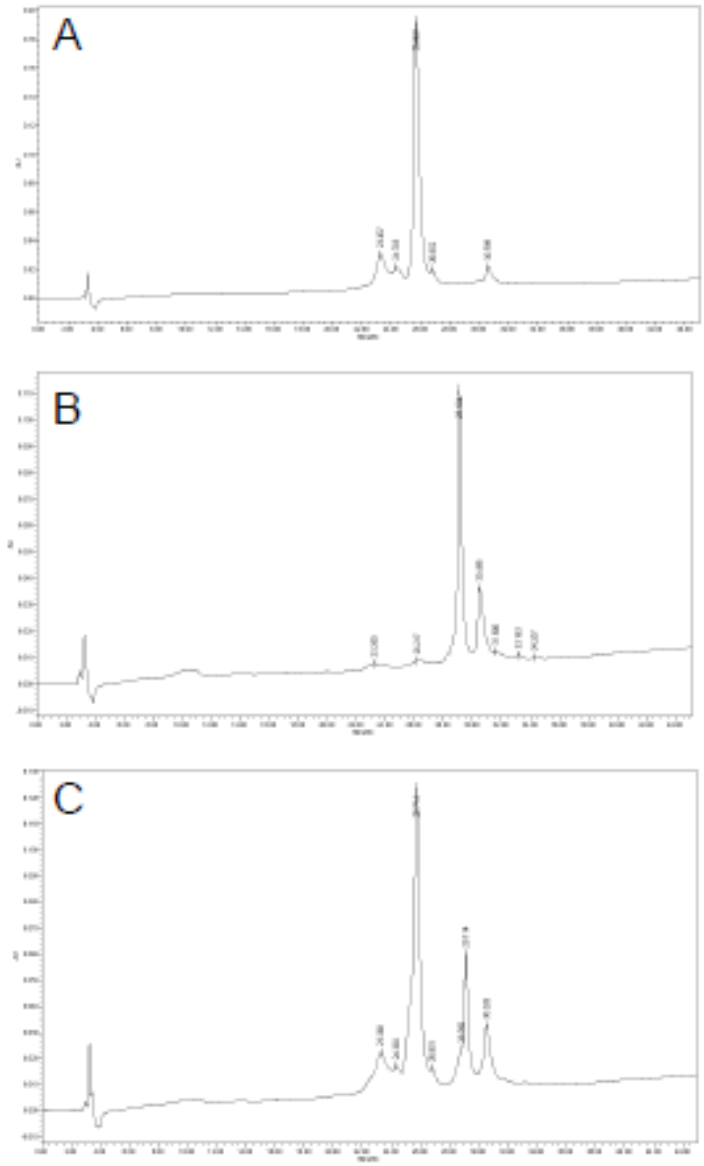

Figure A1.1. Synthesis and Purification of Lys^{7}, Cys^{8}]dermorphin. [Lys^{7}, Cys^{8}]dermorphin was synthesized on Rink resin using an Applied Biosystems Peptide Synthesizer and Fmoc chemistry. Samples were resolved on a Waters reverse phase HPLC using a Vydac C18 10 micron column, run on a linear gradient of 0 to 45% acetonitrile containing 0.1% TFA in an aqueous phase containing 0.1% TFA at 35^{o}C. Samples were monitored at 254 nm. [Lys^{7},Cys^{8}]dermorphin (A) has a retention time of 25.9 min and was determined to be 98% pure before labeling. [Lys^{7},Cys^{8}]dermorphin was labeled with Cy3-maleimide dye (GE Healthcare) at a ratio of 1.5:1 peptide:fluorophore. [Lys^{7},Cys^{8}]dermorphin-Cy3 (B) has a retention time of 29.2 min and was determined to be 91% pure before use in binding assays and imaging experiments. A mixture and co-elution profile (C) shows that the two compounds are well separated.

repurified by HPLC as before. The labeled peptide was further purified via semi-preparative HPLC using a 5-micron Vydac C18 column as described above. The potency and efficacy of [Lys^7, Cys^8]dermorphin-Cy3 at MOR were confirmed in radiolabeled [^{3}H]DPN competition and [^{35}S]GTPγS binding assays.

Prism-based Single-molecule TIRF and Step Photobleaching Analysis of [Lys^7, Cys^8]Dermorphin-Cy3 Binding to rHDL●YMOR + G_{i2}. Purified recombinant apoA-1 was biotinylated at a 3:1 molar ratio of biotin: apoA-1. Purified YMOR was then reconstituted with biotin-apoA-1, POPC, POPG, and brain lipid extract as above. Purified G_{i2} heterotrimer was added to reconstituted receptor as above, and coupling was confirmed by observing high affinity competition of [^{3}H]DPN binding by the agonist DAMGO. Five nanomolar biotin-HDL●YMOR+Gi2 was then incubated with 5 μM [Lys^7, Cys^8]-dermorphin-Cy3 for 45 min at 25 °C in 25 mM Tris●HCl, pH 7.7. The samples were diluted 100-fold in 25 mM Tris●HCl, pH 7.7, and imaged as described above with a surface density of ~0.25 molecules/μm^2. Fluorophore intensity time traces were collected for 30 – 100 s at 10 frames/s and analyzed for photobleaching with in-house software (MatLab 7.0).

A1.3 Results

Expression of a Functional μ-Opioid Receptor Fusion Protein in Insect Cells. Human YMOR (**Fig. A1.2A**) expressed in Sf9 and HighFive™ insect cells bound the nonspecific opioid antagonist [^{3}H]diprenorphine ([^{3}H]DPN) with high affinity in a saturable manner (Kd = 0.6 ± 0.1 nM; **Fig. A1.2B**). Maximal receptor levels of 12–40 pmol/mg were routinely observed.

The μ-selective agonist DAMGO ([D-Ala^2, N-MePhe^4, Gly^5-ol]enkephalin) stimulated [^{35}S]GTPγS binding to membranes co-expressing YMOR and $G\alpha_{i2}$-$His_6G\beta_1$-$G\gamma_2$ G protein heterotrimer (G_{i2}) in a concentration-dependent manner (**Fig. A1.2C**). DAMGO elicited strong activation of G_{i2}, stimulating [^{35}S]GTPγS

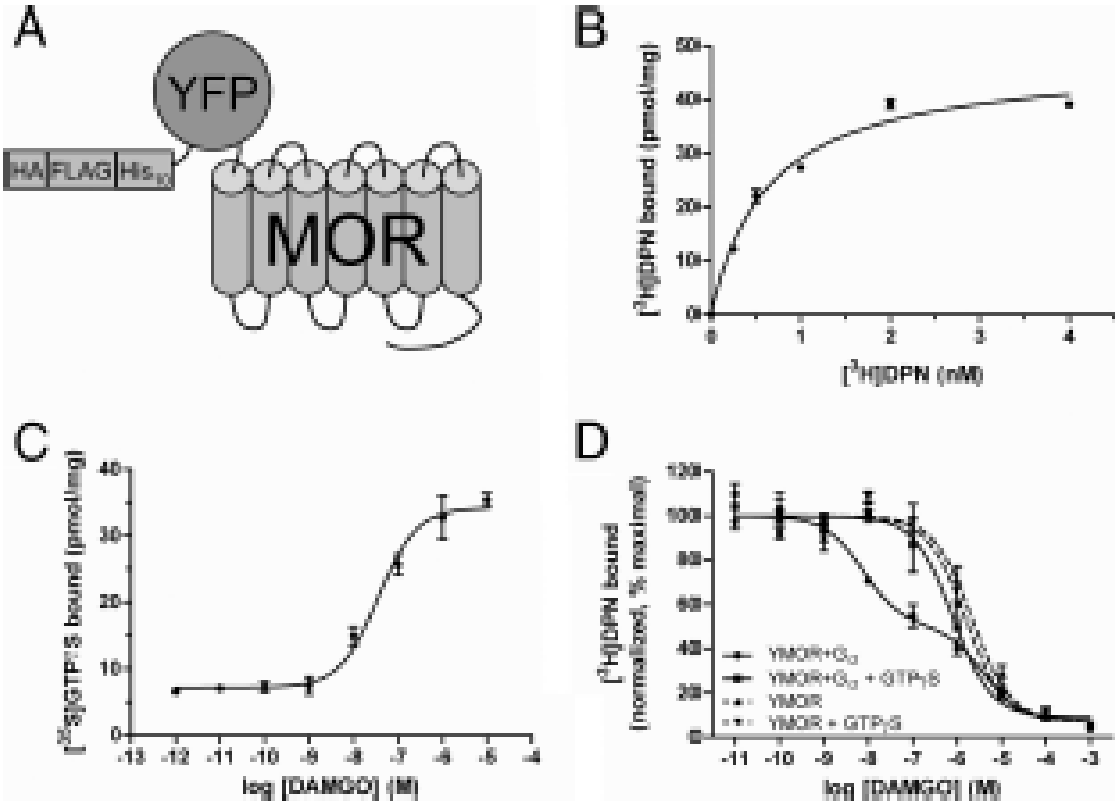

Figure A1.2. Functional expression of a modified MOR in insect cells. (A) schematic representation of the modified μ-opioid receptor expressed in insect cells. N-terminal modifications included a hemagglutinin signal sequence (HA), FLAG epitope, His_{10},and a YFP. This construct, termed YMOR, was expressed in Sf9 and HighFive™ insect cells using a recombinant Baculovirus system. (B) YMOR expressed in insect cells exhibits high affinity ligand binding. Plasma membrane preparations (5 μg) of HighFive™ cells expressing YMOR were used in [^{3}H]diprenorphine saturation binding assays. YMOR bound [^{3}H]DPN with a $B_{max}$of ~40 pmol/mg and a K_d of 0.6 ± 0.1 nM. (C) YMOR couples to G protein in insect cell membranes. Membrane preparations (2 μg) of HighFive™ cells co-expressing YMOR and G_{i2} heterotrimer were incubated with increasing concentrations of the μ-opioid agonist DAMGO in the presence of 10 nM [^{35}S]GTPγS (isotopically diluted). DAMGO stimulated [^{35}S]GTPγS exchange on $G\alpha_{i2}$ with an EC_{50} of 36 ± 0.1 nM. D, agonist binding to YMOR expressed in insect cells is allosterically regulated by G proteins. YMOR/G_{i2} membrane preparations (2–3 μg) were incubated with 0.8 nM [^{3}H]DPN and increasing concentrations of DAMGO in the absence or presence of 10 μM GTPγS. A high affinity binding site for DAMGO (●, $K_{i\ hi}$ =~2.9 nM) was disrupted in the absence of G protein coupling (with GTPγS, ■, K_i = ~300 nM). DAMGO also displayed low affinity binding to membranes not expressing G_{i2} (YMOR,▲, K_i =~580 nM; and YMOR + GTPγS, ▼, K_i=~800 nM). Binding data were normalized to the curve fit maximum. For all panels the data are representative of at least two experiments performed in duplicate, and the error bars represent the standard error of the mean.

binding nearly 4-fold over basal levels with an EC_{50} of 36 ± 0.1 nM. The potency and efficacy of DAMGO at insect cell expressed YMOR is well in line with its observed pharmacological characteristics in mammalian cell expression systems (266-268). Allosteric regulation of agonist binding to opioid receptors by G proteins has been well established in plasma membrane preparations of brain homogenates and overexpression systems (269-273) and was also observed for YMOR expressed in insect cells. In the absence of G_{i2}, DAMGO competed [^{3}H]DPN (0.5 nM) binding in a concentration-dependent manner with a K_i of ~580 nM (**Fig. A1.2D**). In membranes expressing both YMOR and G_{i2}, DAMGO exhibited a biphasic mode of inhibition of [^{3}H]DPN binding with a $K_{i\ hi}$ of ~2.9 nM and a $K_{i\ lo}$ of ~1.5 µM (fraction of $K_{i\ hi}$ ~0.53). The addition of 10 µM GTPγS to the YMOR + Gi2 membranes eliminated the high affinity DAMGO-binding site (Ki = ~300 nM), illustrating that YMOR is allosterically regulated by G proteins. Therefore, YMOR expressed in HighFive^{TM} cells proved fully functional in regards to G protein coupling.

YMOR Purification. The capacity of a variety of detergents (zwitterionic, polar, and nonionic detergents such as Triton X-100, digitonin, Nonidet P-40, CHAPS, $C_{12}E_{10}$, and n-octyl-β-glucoside) to solubilize YMOR from insect cell membranes was assessed by anti-FLAG Western blot analysis. Extraction of YMOR with DDM proved to be most efficient (data not shown). The addition of CHS (0.01% w/v) improved the stability of the solubilized receptor as measured by [^{3}H]DPN binding, consistent with the stabilizing effects of cholesterol moieties observed for solubilized β_2AR (274) (**Fig. A1.3**). The expression levels of YMOR and the efficiency of DDM solubilization, assessed by [^{3}H]DPN binding and anti-FLAG Western blots, were enhanced in the presence of naltrexone. Therefore this antagonist was present (100 nM) during all subsequent purification steps.

DDM-extracted YMOR was purified through a series of chromatographic steps including metal chelate (Talon^{TM}), anion exchange (Source 15Q), and size exclusion (Superdex 200) chromatography columns. Peak fractions from each column were determined by Coomassie staining, anti-FLAG antibody Western

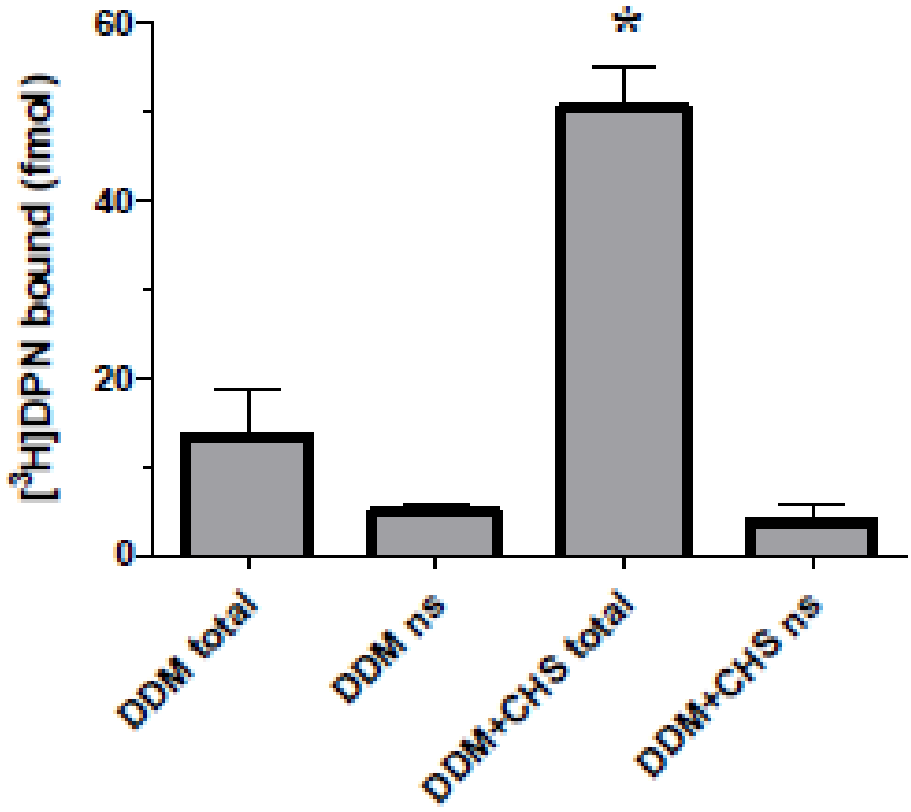

Figure A1.3. The inclusion of cholesteryl hemisuccinate (CHS) during n-dodecyl-β-D-maltoside (DDM) solubilization stabilizes YMOR. YMOR was solubilized from the plasma membranes of Sf9 cells with 1% DDM in the presence or absence of 0.01% CHS and then enriched on a Talon^{TM} IMAC column in either 0.1% DDM or 0.1% DDM plus 0.01% CHS. [^{3}H]DPN binding to these detergent solubilized YMOR samples was then measured in the absence (total) or presence (NS) of 20 µM naltrexone. Addition of CHS to solubilized YMOR increased [^{3}H]DPN ~3.8-fold, suggesting an improvement in the amount of receptor in an active conformation. Error bars represent the Standard Error of the Mean of two experiments performed in duplicate. *P<0.05, significantly different from DDM total as calculated by a Student's t-test.

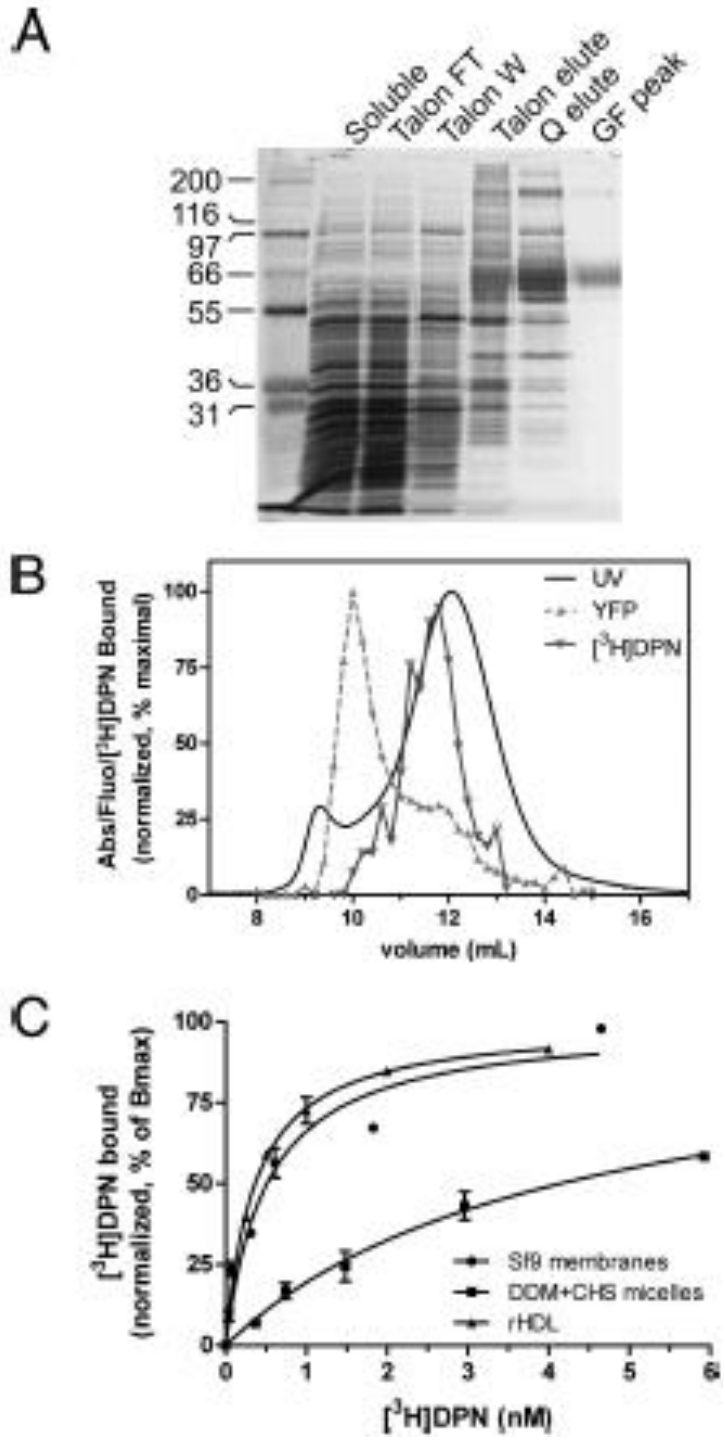

Figure A1.4. Purification of YMOR from HighFive™ insect cells and reconstitution into HDL particles. (A) YMOR was extracted from membranes in the presence of 100 nM naltrexone with 1% n-dodecyl-β-D-maltoside and 0.01% cholesteryl hemisuccinate and enriched on a Talon™ metal affinity column. The Talon™ pool containing YMOR (predicted 73-kDa molecular mass) was applied to a Source 15Q anion exchange column followed by a size exclusion gel filtration column (Superdex 200). Samples of the purification steps were resolved

by SDS-PAGE and silver-stained. YMOR was enriched to ~95% purity (GF peak). (B) purified YMOR was reconstituted into HDL particles (see "Experimental Procedures") and resolved by size exclusion chromatography (Superdex 200). Fractions were analyzed for total protein content (UV absorbance), active YMOR ([^{3}H]DPN binding), and YFP fluorescence. UV absorbance showed a major peak corresponding to rHDL particles (stokes diameter of ~10.5 nm). The elution volume of active YMOR corresponded with the rising slope of the rHDL peak. YFP fluorescence eluted as two peaks, corresponding to the active YMOR and a larger YMOR aggregate that was not incorporated into rHDL particles. This aggregated YMOR was not active based on [^{3}H]DPN binding. The data were normalized such that the maximal value for each parameter was set to 100%. [^{3}H]DPN binding measurements were performed in duplicate, and the error bars are omitted for clarity. (C) high affinity [^{3}H]DPN binding to YMOR is disrupted in detergent micelles but restored following reconstitution into rHDL particles. [^{3}H]DPN binding to YMOR in insect cell membranes (●, Kd=~0.5 nM), purified in DDM micelles (■, Kd=~4.1 nM), and in rHDL particles (▲, Kd=~0.4 nM). The data are representative of at least three experiments performed in duplicate, and the error bars represent the standard error of the mean. The binding data were normalized to the maximal binding level (B_{max}) as calculated by a one-site saturation curve fit (Prism 5.0,GraphPad).

blotting, and [^{3}H]DPN binding. Fractions displaying the highest [^{3}H]DPN binding capacity and appropriate molecular weight were pooled and subjected to the next chromatographic step. Superdex 200 peak fractions were pooled, concentrated, flash-frozen in liquid N2 , and then stored at -80 °C until later use. A representative silver-stained SDSPAGE separation of each enrichment step is shown in **Fig. A1.4A**. Yields of YMOR were typically ~50 µg of >95% pure receptor/liter of insect culture. YMOR, deemed pure based on silver staining, bound [^{3}H]DPN at ~20% of the predicted binding sites calculated from the molecular mass. This loss of activity is likely due to the detrimental freeze/thaw process.

Reconstitution of YMOR into High Density Lipoprotein Particles. The reconstitution of YMOR into high density lipoprotein (rHDL) particles was performed with a 500-fold molar excess of apoA-1 to YMOR (250-fold excess of rHDL) to favor reconstitution of a single YMOR molecule/rHDL particle. Resolution of rHDL particles containing YMOR (rHDL●YMOR) with size exclusion chromatography (SEC) suggested an apparent Stokes diameter of 10.5 nm (**Fig. A1.4B**). [^{3}H]DPN binding to the SEC fractions confirmed the presence of functional YMOR in particles that eluted slightly earlier than the main UV absorbance peak (Stokes diameter of ~10.3 nm), indicating the slightly larger size of rHDL●YMOR compared with rHDL. The YFP fluorescence of the SEC fractions indicated an additional peak that elutes near in the Superdex 200 void volume, suggestive of aggregated YMOR. Because these fractions did not bind [^{3}H]DPN, we surmised that this receptor population was inactive. This aggregated and inactive receptor is consistent with the previous observation that ~80% of the purified YMOR is inactive post freeze/thaw and prior to reconstitution into HDL.

The effectiveness of YMOR reconstitution into HDL is clear when comparing [^{3}H]DPN binding between detergent-solubilized receptor and rHDL●YMOR particles. Prior to reconstitution into HDL, DDM-soluble YMOR bound [^{3}H]DPN with a K_d of ~4.1 nM, whereas reconstituted YMOR bound

[^{3}H]DPN with a K_d of ~0.4 nM (**Fig. A1.4C**). This significant disruption of high affinity ligand binding for the soluble receptor is not surprising, because detergents are known to decrease the ligand affinity of opioid receptors (275) and disrupt GPCRs in general (276). Replacement of detergents with phospholipids reverses the deleterious effects of the detergent and restores YMOR conformation to one that binds [^{3}H]DPN with native, membrane-bound affinity.

YMOR Is Monomeric When Incorporated into rHDL. To determine the number of YMOR molecules present in each rHDL particle, we assessed the degree of receptor co-localization between Cy3- and Cy5-labeled YMOR using single-particle imaging. Purified YMOR was labeled with Cy3- or Cy5- reactive fluorescent dyes and reconstituted into HDL using biotinylated Δ(1–43)- His_6 -apoA-1. This biotin-rHDL●CyYMOR complex was then incubated on a streptavidin-coated microfluidic slide and excited with 532- and 638-nm lasers. Fluorescence emission was detected using prism-based SM-TIRF. Reconstituted Cy3-YMOR and Cy5-YMOR were visualized as mono-disperse fluorescent foci (**Fig. A1.5A and B**). When Cy3-YMOR and Cy5-YMOR were mixed prior to reconstitution (Cy3-YMOR+Cy5-YMOR), a low level of co-localization of the two fluorophores (3.4%) was observed (**Fig. A1.5C and E**). A false-positive co-localization signal of 2.8 and 2.2% was observed for the Cy3-YMOR and Cy5-YMOR samples, respectively (**Fig. A1.5E**). As a positive control, co-localization for YMOR labeled with both Cy3 and Cy5 was also measured (**Fig. A1.5D**). Considering that our method does not allow for the differentiation between YMOR labeled with multiple Cy probes of the same fluorophore versus co-localization of multiple YMORs labeled with the same Cy probe, we may underestimate colocalization by as much as a factor of 2. Thus we estimate an upper limit for co-localization, i.e. incorporation of two or more YMORs into a single rHDL particle, of ~1.8% ((3.4% x 2) - (2.8% + 2.2%)). These data suggest that HDL reconstitution resulted in a sample containing mostly monomeric YMOR. Therefore the ligand binding and G protein coupling characteristics of the HDL-reconstituted YMOR presented here are indicative of the properties of a monomeric receptor.

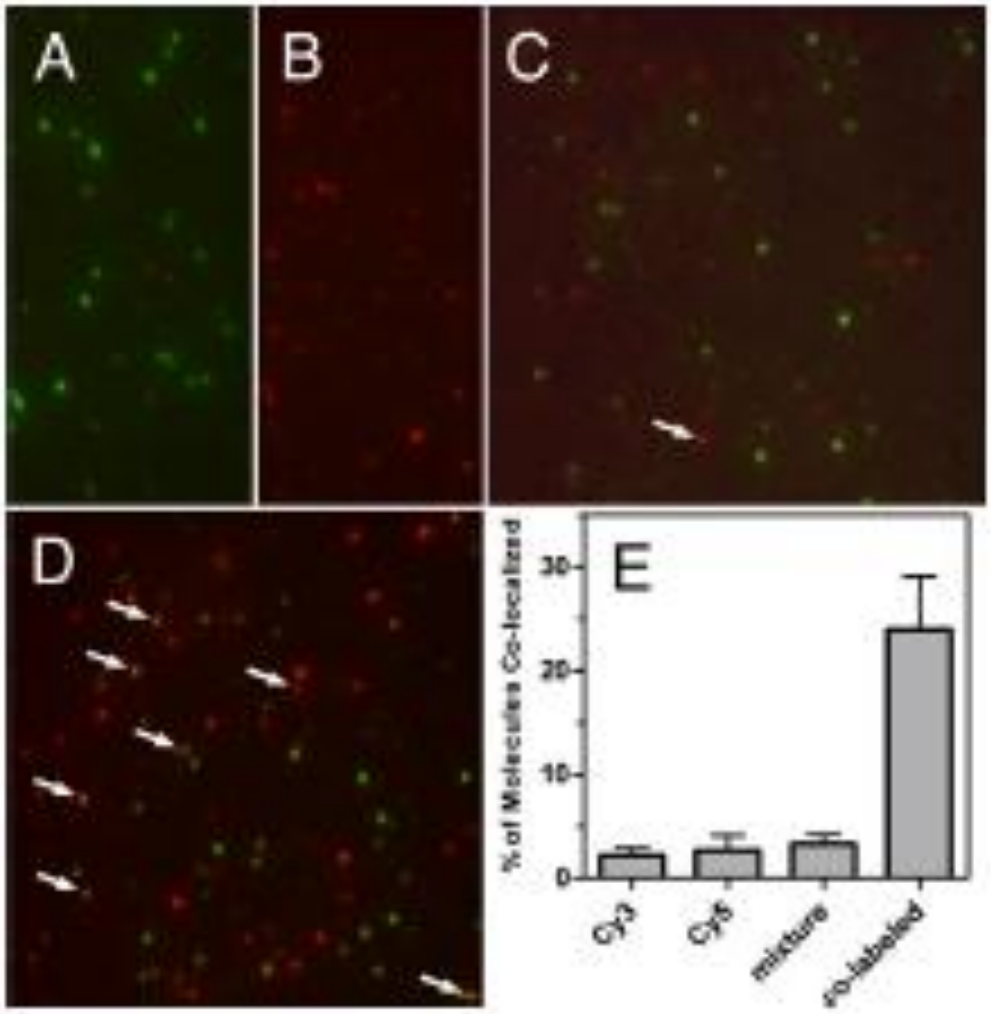

Figure A1.5. YMOR is monomeric when reconstituted into HDL particles. Purified YMOR was labeled with Cy3 or Cy5 fluorescent dyes and reconstituted separately or together into biotin-labeled rHDL. The particles were imaged using single-molecule total internal reflection fluorescence microscopy on quartz slides coated with streptavidin. Representative overlay images of reconstituted rHDL●Cy3-YMOR (A), rHDL●Cy5-YMOR (B), rHDL●(Cy3-YMOR Cy5-YMOR) (C), and rHDL●Cy3-Cy5-YMOR (D) are shown. Quantification of Cy3 and Cy5 co-localization (E) showed that when both Cy3-YMOR and Cy5-YMOR were mixed together prior to reconstitution (mixture, 4c), only ~3.4% of rHDL particles contained two labeled receptors, compared with a false-positive co-localization signal of 2.8 and 2.2% observed for the rHDL●Cy3-YMOR and rHDL●Cy5-YMOR samples. YMOR co-labeled with both Cy3 and Cy5 was also imaged as a positive control for co-localization. Approximately 24% of rHDL●Cy3-Cy5-YMOR particles (co-labeled, 4d) exhibited colocalization, indicating that not all YMOR received a secondary fluorescent dye under the labeling conditions.

To assess the amount of active versus inactive YMOR incorporated into rHDL, we compared the total protein concentration of purified rHDL●YMOR particles to the maximal concentration of YMOR based on [^{3}H]DPN saturation binding assays. Reconstituted YMOR was purified using FLAG affinity resin and resolved by SEC into a sample containing only apoA-1 and YMOR (based on SDS-PAGE and Coomassie staining). Amido Black staining of these peak fractions indicated a protein concentration of ~5.2 µg/ml. Considering that the protein sample consists of two apoA-1 molecules (molecular mass, ~25,500 Da) and one YMOR (molecular mass, ~73,500 Da), the rHDL●YMOR sample has a total molecular mass of 124,500 Da and therefore a molar concentration of ~42 nM. Saturation binding assays on the rHDL●YMOR SEC peak indicated a molar concentration of ~31 nM for YMOR which bound ligand. Given the inherent limitations of protein detection assays at the low concentration of our samples, these data suggest that at least 75% of the YMOR in rHDL is active based on [^{3}H]DPN binding.

Monomeric YMOR Binds Antagonists with High Affinity. Reconstituted and monomeric YMOR binds antagonists with affinities similar to those observed in the plasma membrane. The antagonists naloxone and naltrexone and the µ-specific peptide CTAP (D-Phe-Cys-Tyr-D-Trp-Arg-Thr-Pen-ThrNH2) compete [^{3}H]DPN binding in similar fashion when in HighFive^{TM} cell membrane preparations or in reconstituted HDL particles (**Fig. A1.6A**). Therefore reconstitution into HDL allows YMOR to adopt a conformation that appears identical to receptor in plasma membranes in terms of high affinity antagonist binding.

Monomeric YMOR Functionally Couples Inhibitory G Proteins. We next analyzed the capacity of monomeric YMOR to functionally couple to heterotrimeric G protein. Functional measurements included allosteric regulation of agonist binding (**Fig. A1.6B**) and agonist-mediated stimulation of [^{35}S]GTPγS binding (**Fig. A1.6C**). Anti-FLAG affinity column purification of rHDL●YMOR was performed to remove “empty” rHDL particles, and purified G_{i2} heterotrimer was

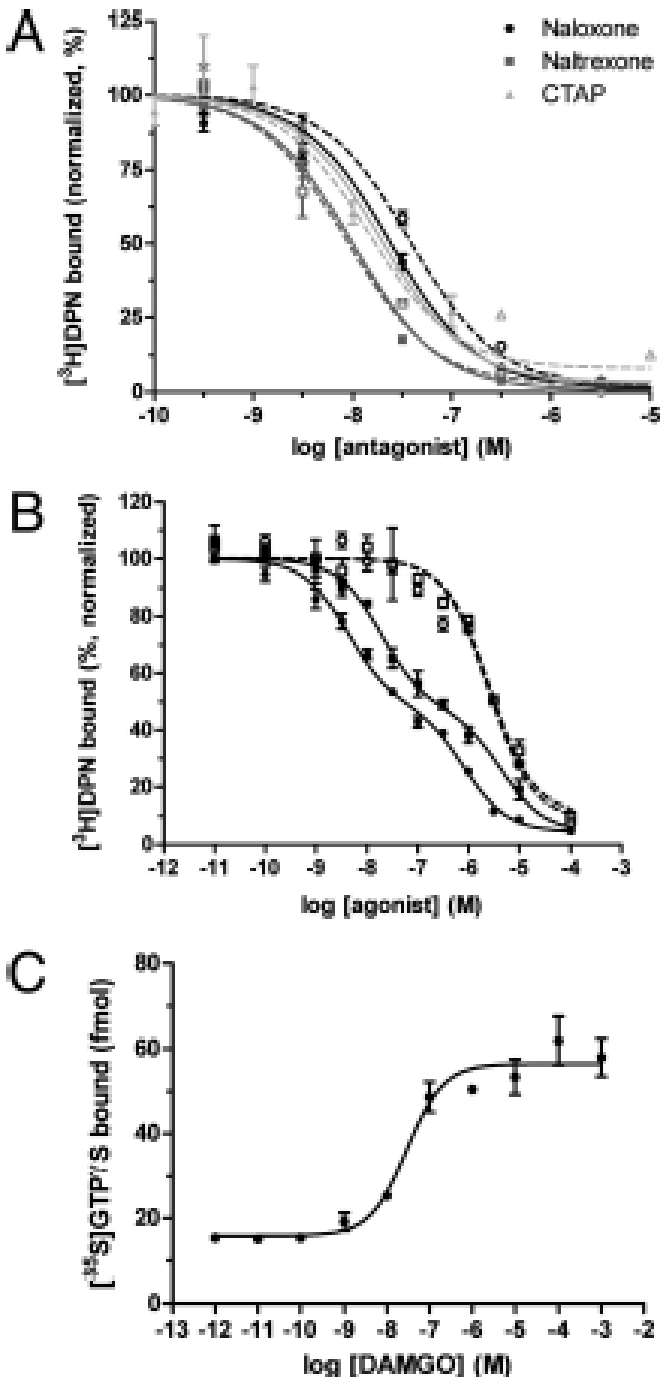

Figure A1.6. Monomeric YMOR binds ligands with high affinity and functionally couples to G_{i2} heterotrimer. (A) opioid antagonists bind YMOR in rHDL with affinities equivalent to those observed in membrane preparations. Competition binding assays were performed using plasma membranes of HighFive™ cells expressing YMOR and G_{i2} heterotrimer (dotted lines, open symbols) or rHDL●YMOR (solid lines, closed symbols). For CTAP binding assays in rHDL, YMOR was coupled to G_{i2} heterotrimer. Increasing concentrations of naloxone, naltrexone, or CTAP competed the binding of 1 nM [^{3}H]DPN in the rHDL system

or 0.5 nM [^{3}H]DPN in membrane preparations. The observed binding constants were: naloxone $K_{i\ mem}$ = ~19 nM, $K_{i\ rHDL}$ = ~7.8 nM; naltrexone $K_{i\ mem}$ = ~4.3 nM, $K_{i\ rHDL}$ = ~3.3 nM; CTAP $K_{i\ mem}$ = ~7.1 nM, $K_{i\ rHDL}$ =~7.6 nM. (B) binding of morphine to rHDL●YMOR is allosterically regulated by G proteins. Purified G_{i2} heterotrimer was added to rHDL●YMOR at a molar ratio of 10:1, G protein to receptor. DAMGO and morphine bound rHDL●YMOR with high affinity, competing the binding of 0.75 nM [^{3}H]DPN in a biphasic manner (DAMGO (■), $K_{i\ hi}$ = ~7.6 nM, $K_{i\ lo}$ = ~1.8 µM; morphine (●), $K_{i\ hi}$ = ~1.7 nM, $K_{i\ lo}$ = ~320 nM). High affinity agonist binding was lost with the addition of 10 µM GTPγS (DAMGO (□), K_i GTPγS = ~1 µM; morphine (○), K_i GTPγS = ~1 µM). In both A and B, data were normalized to the maximal binding level as calculated by a one- or two-site competition curve fit (Prism 5.0, GraphPad). © HDL-reconstituted YMOR activates G_{i2} in response to agonist binding. YMOR (an estimated 50 – 60 fmol) and associated G_{i2} heterotrimer were incubated with 10 nM [^{35}S]GTPγS (isotopically diluted) in the presence of increasing concentrations of DAMGO. DAMGO activated G_{i2} with an EC_{50} of 29 ± 1.4 nM, stimulating ~40 fmol of [^{35}S]GTPγS binding to $G\alpha_{i2}$ over basal levels, suggesting approximately a 1:0.7 coupling between YMOR and G protein. These results correlate with the estimated 53% high state observed in B. The data are representative of three experiments performed in duplicate. The error bars represent the standard error of the mean.

added at a 10:1 G_{i2}:rHDL●YMOR molar ratio. The concentration of purified G protein was determined by [^{35}S]GTPγS binding assays, and receptor concentration was measured with [^{3}H]DPN saturation assays of rHDL●YMOR samples. G_{i2} addition results in high affinity agonist binding (**Fig. A1.6B**). Morphine competed [^{3}H]DPN binding with a $K_{i\ hi}$ of ~1.7 nM and a $K_{i\ lo}$ of ~320 nM, whereas DAMGO inhibited with a $K_{i\ hi}$ of ~7.6 nM and a $K_{i\ lo}$ of ~1.8 μM. As in membranes the addition of 10 μM GTPγS to the monomeric rHDL●YMOR+G_{i2} uncouples the G protein and results in a single-site, low affinity agonist competition curve. Similarly, when rHDL●YMOR was not coupled to G_{i2}, DAMGO competed [^{3}H]DPN binding with micromolar affinity (**Fig. A1.7**).

Just as YMOR membrane preparations displayed DAMGO induced [^{35}S]GTPγS binding to G_{i2}, monomeric YMOR in rHDL particles showed strong DAMGO stimulation of nucleotide exchange (~4.7-fold stimulation with an EC_{50} of 31 ± 2.2 nM; **Fig. A1.6C**). A fluorescently labeled agonist, [Lys^{7},Cys^{8}]dermorphin-Cy3, was also tested and showed concentration-dependent stimulation of [^{35}S]GTPγS binding to G_{i2} by monomeric YMOR (EC_{50} of 32 ± 9.1 nM; **Fig. A1.8B**).

Although Gi2 was added to rHDL●YMOR at a 10:1 molar ratio in these reconstitutions, the observed high and low agonist affinities illustrate that not all YMOR was coupled to G_{i2}. In fact, the agonist competition assays indicate that ~54% of the receptor was coupled to G_{i2}. These data are consistent with previous studies on the β_2 AR where the addition of purified G protein heterotrimer to rHDL particles in the absence of detergents resulted in 90 –95% G protein loss, largely because of aggregation (258). Indeed, SEC analysis of rHDL●YMOR before and after G_{i2} addition confirmed that a large amount of the heterotrimer aggregates during its addition (data not shown). As such, the two populations of ~54% coupled and ~46% uncoupled YMOR correspond well with the expected final G protein to YMOR ratio of 0.5–1:1.

Single-particle Visualization of Agonist Binding to rHDL●YMOR. [Lys^{7}, Cys^{8}]dermorphin was used as an agonist probe to visualize binding to

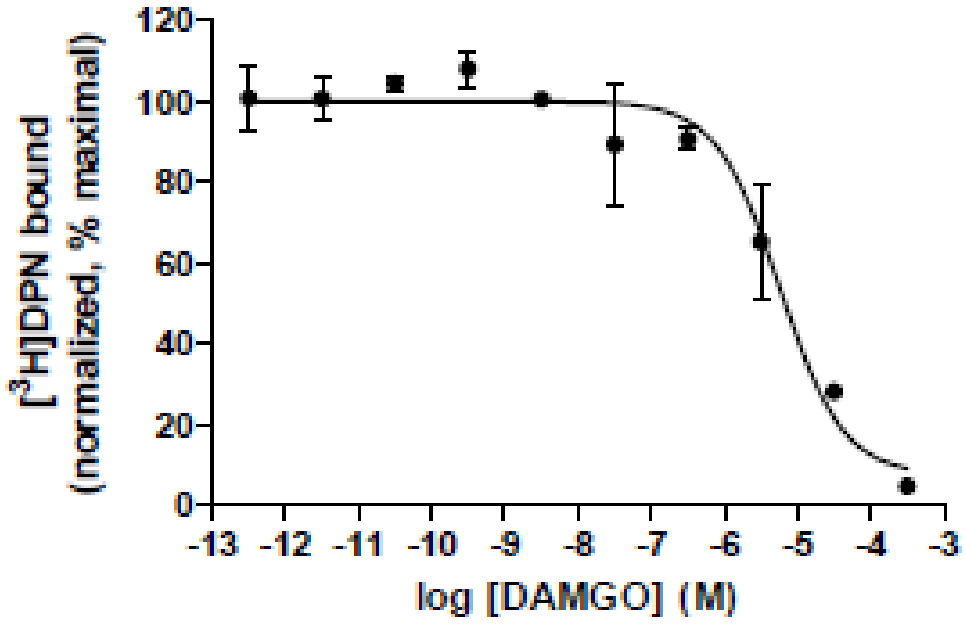

Figure A1.7. DAMGO displays low affinity binding to rHDL•YMOR. An estimated 15 fmoles of rHDL•YMOR was incubated with 1 nM [^{3}H]DPN and increasing concentrations of DAMGO in 25 mM Tris•HCl, pH 7.7, 100 mM NaCl, 0.1% BSA. DAMGO competed [^{3}H]DPN binding with a K_i of ~1.9 µM, indicating that in the absence of G protein heterotrimer coupling DAMGO binds YMOR with low affinity. These data corroborate those in **Fig. A1.2D and 6B**, which illustrated that DAMGO binds YMOR with low affinity when G_{i2} heterotrimer is uncoupled from the receptor by the addition of 10 µM GTPγS. Data is representative of three experiments performed in duplicate. Error bars represent the Standard Error of the Mean.

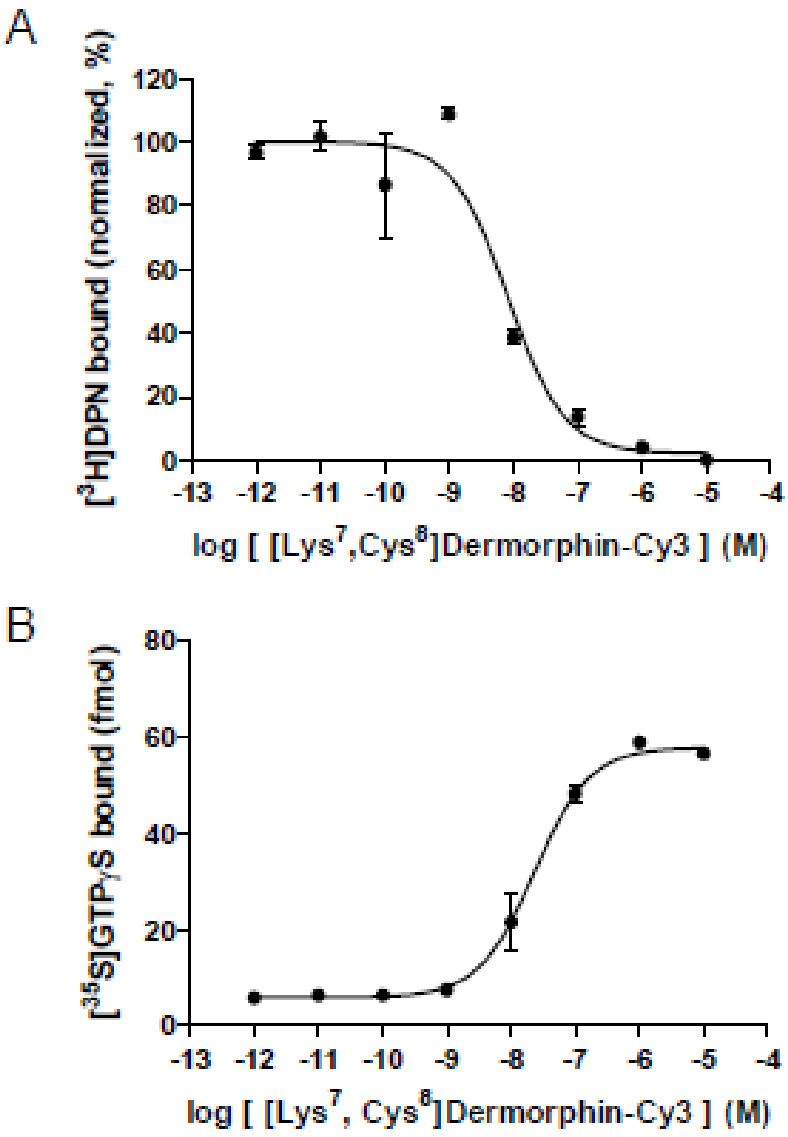

Figure A1.8. A Cy3-labeled [Lys^7, Cys^8]dermorphin retains agonist properties at YMOR. Approximately 50 fmoles of receptor in HDL particles were coupled to purified G_{i2} heterotrimer at a ratio of 30:1 G protein:YMOR. (A) [Lys^7, Cys^8]dermorphin-Cy3 binds rHDL•YMOR+G_{i2} with high affinity, displaying a K_i of 3.3 nM in competition assays against 0.75 nM [^{3}H]DPN. The single high affinity binding site suggested by the monophasic competition curve is due to the high molar ratio of G protein addition to YMOR, which results in nearly all of the receptor being coupled to G_{i2} heterotrimer. Data is normalized to the maximal binding level as calculated by a one-site competition curve fit (Prism 5.0, GraphPad). (B) [Lys^7, Cys^8]dermorphin-Cy3 stimulated [^{35}S]GTPγS binding to rHDL•YMOR+G_{i2} with an EC_{50} of 23.05 nM. Approximately 52 fmoles of [^{35}S]GTPγS binding was stimulated, suggesting a 1:1 YMOR:G_{i2} coupling, confirming the fact that adding G_{i2} at a 30:1 molar ration results in complete coupling of YMOR. Data are representative of three experiments performed in duplicate are shown. Error bars represent the Standard Error of the Mean.

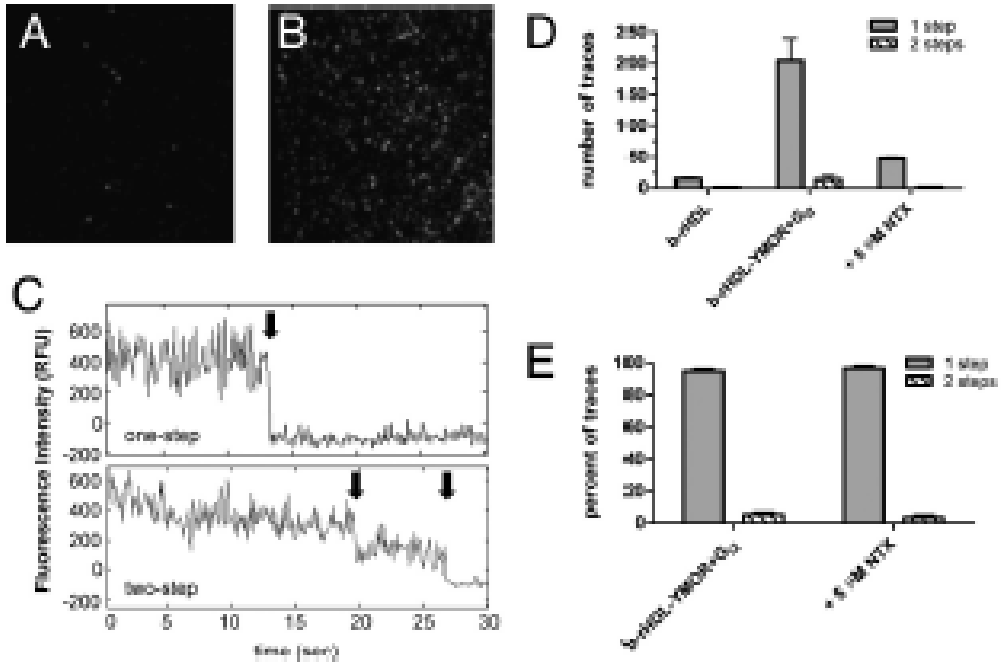

Figure A1.9. Single-molecule imaging of Cy3-labeled agonist binding to rHDL●YMOR + G_{i2} confirms that the majority of YMOR is monomeric when reconstituted into HDL. Binding of [Lys^7, Cys^8]dermorphin-Cy3, a fluorescently labeled MOR-specific agonist, to rHDL●YMOR+Gi2 was observed with prism-based total internal reflection fluorescence microscopy. YMOR was reconstituted into HDL particles using biotinylated apoA-1, followed by G_{i2} heterotrimer addition at a 30:1 G protein to receptor molar ratio. Reconstituted HDL (A) or rHDL●YMOR+G_{i2} (B) were then incubated with a saturating concentration (500 nM) of [Lys^7, Cys^8]dermorphin-Cy3, adhered to a streptavidin-coated quartz slide, and washed with ice-cold 25 mM Tris●HCl, pH 7.7 buffer. Bound [Lys^7, Cys^8]dermorphin-Cy3 was continuously excited at 532 nm to observe photobleaching of the fluorophore. C, representative fluorescence intensity traces for a one- and two-step photobleach event are shown. The arrows indicate photobleach events. D and E, quantification of photobleaching showed that ~95% of the bound [Lys^7, Cys^8]dermorphin-Cy3 bleached in a single step, suggesting that 95% of rHDL particles contained monomeric YMOR. [Lys^7, Cys^8]dermorphin-Cy3 binding was reversible, as shown the addition of 5 μM NTX. A minimum of four slide regions and 200 fluorescent spots were counted for each sample.

monomeric YMOR in rHDL at the single-molecule level with TIRF (**Fig. A1.9**). [Lys^7, Cys^8]-dermorphin was labeled with a Cy3 fluorophore (**Fig. A1.1**), and its ability to bind reconstituted YMOR with high affinity and stimulate [^{35}S]GTPγS binding to Gαi2 was confirmed (**Fig. A1.8**). YMOR was reconstituted with biotinylated Δ(1–43)-His$_6$ -apoA-1 (b-rHDL●YMOR), enriched on a FLAG affinity column, and added to G_{i2} heterotrimer at a 30:1 G_{i2}:YMOR molar ratio to ensure complete receptor coupling to G protein. Binding of a saturating concentration (500 nM) of [Lys^7, Cys^8]dermorphin-Cy3 to b-rHDL●YMOR+Gi2 was then imaged with SM-TIRF. Fifty picomolar b-rHDL or b-rHDL●YMOR+Gi2 (**Fig. A1.9A and B**) samples were continuously excited at 532 nm and fluorescence intensity traces (**Fig. A1.9C**) were analyzed for step photobleaching. Approximately 95% of the b-rHDL●YMOR+Gi2 fluorescence traces exhibited single-step photobleaching, suggesting that a single [Lys^7,Cys^8]dermorphin-Cy3 was localized within each fluorescent spot (**Fig. A1.9D and E**). Having shown that rHDL particles contain a single receptor, these photobleaching data indicate that only one dermorphin bound per receptor.

A1.4 Discussion

Intense research over the past decade has focused on the existence and functional consequences of GPCR oligomerization. Recently, our laboratory and others have taken advantage of a unique phospholipid bilayer platform in the form of rHDL particles (254, 255, 258, 259). Using this system we previously demonstrated the functional reconstitution of two prototypical GPCRs, rhodopsin and β_2AR (258, 259). Having illustrated that these receptors are monomeric following reconstitution, we observed complete functional coupling to their respective G proteins. For the β_2AR, agonist binding to monomeric receptor is allosterically regulated by the stimulatory heterotrimeric G protein $G\alpha_s\beta\gamma$. Therefore GPCR dimerization is not required for functional G protein coupling in the prototypical class A GPCRs rhodopsin and β_2AR.

In contrast, the accumulation of considerable biochemical and biophysical evidence suggests that the μ-, δ-, and κ-opioid receptors may function in a fashion that is dependent on their oligomerization. Analysis of receptor overexpression in co-transfected cells suggested the existence of δ-δ homodimers (277) and demonstrated unique pharmacology resulting from μ-δ (6, 7, 10) and δ-κ heterodimers (278). Bioluminescence resonance energy transfer studies have shown that homo- and heterodimers can be formed by all three opioid receptor isoforms (253). These findings have promoted the notion that opioid receptor oligomerization is important for function (279, 280). However, with co-transfection systems the final profiles of μ and δ monomers, homodimers, and heterodimers are unknown. In light of these reports, we rationalized that it was vital to determine whether the monomeric form of the MOR behaves in a pharmacologically similar manner as the native, membrane-bound form.

The HDL reconstitution system was used to investigate the function of monomeric MOR. Reconstitution of MOR required the purification of active receptor in large enough quantities for subsequent biochemical manipulation and analysis. Previous reports of MOR purification from endogenous or recombinant sources have yielded either low quantities (281-285) or poor agonist binding affinities (286-288). Several aspects were key to the expression and purification of YFP-MOR (YMOR): a cleavable hemagglutinin signal sequence at the N terminus of the receptor (289), the presence of naltrexone during expression, and the inclusion of cholesteryl hemisuccinate and naltrexone during the entire purification process. These modifications contributed to the stabilization of YMOR, leading to an increase in yields during the chromatography process as well as increasing the specific activity of the detergent solubilized receptor. Reconstitution into HDL facilitated the isolation of a monomeric form of YMOR that couples to and activates heterotrimeric G proteins. Furthermore, we illustrate that the inhibitory G protein $G\alpha_i\beta\gamma$ can allosterically regulate agonist binding to monomeric MOR. These results suggest that G protein regulation of monomeric receptors is likely a phenomenon common to all G proteins and class A GPCRs.

The capacity of MOR to couple to various isoforms of $G_{i/o}$ heterotrimers in a differential manner are currently under investigation in our laboratory.

Taken together our results demonstrate the functionality of monomeric MOR, illustrating that the opioid GPCR does not require dimerization to bind ligands and signal to G proteins. However, these data do not refute the existence of opioid receptor oligomerization in cells. It remains possible that homo- and heterodimerization create unique ligand binding entities that may be subject to differential regulation, desensitization, and internalization. One of our future goals is to isolate various oligomeric states of opioid receptors and other GPCRs in rHDL particles and compare their activities toward ligands and signaling partners directly. A major technical obstacle is the formation of “anti-parallel” receptor dimers, where the N termini for the reconstituted GPCRs in the oligomer are on opposite sides of the phospholipid bilayer. Indeed, reconstitution of two GPCRs in a single rHDL particle has been previously demonstrated for rhodopsin (254, 255, 258, 259), but a detailed analysis by nanogold labeling and single-particle electron microscopy of the reconstituted “dimers” reveals that a significant fraction were anti-parallel (254). It is plausible, and even likely, that an antiparallel GPCR dimer will result in suboptimal or disrupted G protein coupling. The development of approaches to ensure parallel GPCR dimer incorporation into rHDL particles to confidently study the functional relevance of opioid receptor dimerization is currently a major priority in the laboratory.

HDL reconstitution of YMOR also provided a platform for analysis of ligand binding using single-molecule microscopy. In this study we examined the reversible binding of a μ-opioid receptor specific agonist [Lys^7, Cys^8]dermorphin with SM-TIRF. To the best of our knowledge these data represent the first reported observation of a peptide agonist binding to an isolated GPCR in a lipid bilayer using single-particle imaging. We are currently refining our methods to resolve the kinetics of ligand binding to YMOR, as well as visualizing ligand binding to opioid receptors in intact cells. Peptide receptors such as the opioid family are particularly amenable to fluorescence spectroscopy because the

relatively large ligand size can tolerate the incorporation of fluorophores without drastically impairing binding affinities. This single-molecule visual approach of studying ligand binding to opioid receptors, utilizing labeled agonists and antagonists with unique binding affinities toward receptor homo- and heterodimers, may potentially address opioid receptor oligomerization in physiologically relevant tissue preparations.

A1. 5 Acknowledgements

We thank Drs. John Traynor and Richard Neubig for critical discussion of this work.

Appendix 2

Single mRNA Tracking in Human Cells

A2.1 Introduction

To exactly quantify the number of mRNA bound miRNA particles that were observed in Chapter 2, it was essential to label mRNAs with a complementary fluorescent probe. We validated the previously reported MS2-MCP system for this purpose (87, 138).

A2.2 Materials and methods

Plasmids, DNA and RNA oligonucleotides. pMCP-EGFP, plasmid bearing the ORF of MS2 coat protein fused to EGFP and SV-40 nuclear localization signal (NLS), and pSL-MS2_24x, plasmid bearing 24 copies of the MS2 stem loops, were received as gifts from Robert Singer (Yeshiva) (87). Luciferase reporter plasmids bearing the MS2 stem loops were created in two steps. First, the ORF of IF2, PCR amplified using a forward primer bearing SbfI and EcoRI RE sites and a reverse primer bearing NotI RE site, was cloned into the corresponding SbfI and NotI RE sites in the pmG (pmiR-GLO, Promega) or pmG-mH3UM plasmids. The latter plasmid contained the mutated 3`UTR of mouse HMGA2 which was unrepressed by wild-type let-7-a1 miRNAs but could be silenced by a mutant let-7-a1 miRNA. 24 copies of the MS2 stem loops (from pSL-MS2_24x) was then cloned into the EcoRI-NotI RE sites of the resultant plasmids, pmG-IF2 and pmG-mH3UM-IF2, to generate pmG-MS2 and pmG-mH3UM-MS2 respectively. We had to resort to this two step method because linearized

plasmids containing the MS2 stem loops often recombined with the genome of the bacterial competent cells we were using, thus resulting in clones bearing smaller plasmids. Clones containing the MS2 stem loops were created in SURE2 (Stratagene) bacterial cells to minimize recombination of the MS2 repeats with the bacterial genome. Negative control siRNA used in transfection experiments was purchased from Ambion. All other RNA oligonucleotides were purchased from the Keck Biotechnology Resource Laboratory at the Yale University School of Medicine with a 5' phosphate (P) and were purified as described . RNA sequences were as follows:

let-7-a1 guide: P-UGAGGUAGUAGGUUGUAUAGUU
let-7-a1-passenger: P-CUAUACAAUCUACUGUCUUUCC
let-7-a1 mut guide: P-UGCGUUAGUAGGUUGUAUAGUU
let-7-a1 mut passenger: P-CUAUACAAUCUACUGUCGUUCC
siLuc2 guide: GAAGUGCUCGUCCUCGUCCUU
siLuc2 passenger: GGACGAGGACGAGCACUUCUU

Guide and passenger strands were heat-annealed in a 1:1 ratio, resulting in duplex miRNAs, and frozen until used.

Repression assay. 24 h prior to transfection, 100 µL of 15,000 HeLa cells were seeded per well of a 96 well plate. Cells were transfected with 60 ng of the indicated plasmid, 10 nM of the indicated dsRNA, 0.4 µL of Lipofectamine 2000 (Invitrogen) and 50 µL of OptiMEM (GIBCO). 6 h after transfection the growth medium was replaced with fresh medium. 24 h after transfection, medium was replaced with phenol red-free DMEM. Dual luciferase assays were performed using the Dual-Glo luciferase assay reagents (Promega) as per the manufacturer's protocol and luminescence was detected using a Genios Pro (Tecan) plate reader.

Transfection, imaging and data analysis. 2.4 x 10^5 HeLa cells were reverse transfected by directly adding transfection complexes, containing 2 µg of the appropriate plasmid set and 7 µL of Fugene HD transfection reagent (Roche), to

trypsinzed cells. The 2 µg of total plasmid contained 1:1 molar ratio of the pMCP-GFP and either pmG, pmG-MS2 or pmG-mH3UM-MS2. Cells were grown on a DeltaT dish (Bioptech) for 24 h at 37 ^{o}C under conditions of 5% CO_2. The cells were then trypsinized and re-seeded onto DeltaT dishes in a 1:1 ratio of cells : growth media and re-grown for another 24 h. Regular medium was replaced with phenol red-free medium 4 h prior to imaging and subsequently with a minimal medium (HBS), without serum and vitamins, but containing 20 mM HEPES-KOH pH 7.4, 135 mM NaCl, 5 mM KCl, 1 mM $MgCl_2$, 1.8 mM $CaCl_2$ and 5.6 mM glucose, 0.3 U/mL Oxyfluor (Oxyrase), 20 mM sodium succinate, 2 mg/mL ascorbic acid and 200 µM trolox (HBS-OSS) immediately before imaging. Single particle tracking was performed as previously described (**Chapter 2, Fluorescence microscopy**) using the 488nm laser for GFP excitation and a dual band filter cube, consisting of a z491/639rpc dichroic filter (Chroma) and z491/639m emission filter (Chroma), for the detection of GFP fluorescence. Data analysis was done as previously described (**Chapter 2**, **Live cell imaging and data analysis**) with a minor modification of computing ensemble diffusion coefficients from mean squared displacement of all trajectories with a sample.

A2.3 Results and Discussion

Intracellular mobility of mRNAs as a good measure to predict 3`UTR 'loading'.** Ensemble reporter assays were first performed to validate the ability of MS2 tagged transcripts to undergo miRNA mediated gene silencing. We found that the transcript without the mutant HMGA2 3`UTR (compare all A's**, **Fig. A2.1A**) was not repressed by any miRNA whereas transcripts with the UTR (**compare all B's Fig. A2.1A**) were specifically and effectively repressed (**Fig. A2.1A**). We then performed single particle tracking (SPT) in HeLa cells co-transfected with the EGFP-MS2-NLS fusion protein containing plasmid and either a control plasmid containing no MS2 sequences (**-ve, Fig. A2.1B**), the pmG-MS2 plasmid (**luc2-MS2, Fig. A2.1B**) or the pmG-mH3UM-MS2 plasmid (**luc2-mH3UM-MS2, Fig. A2.1B**). In the absence of MS2 stem loops only the nucleus

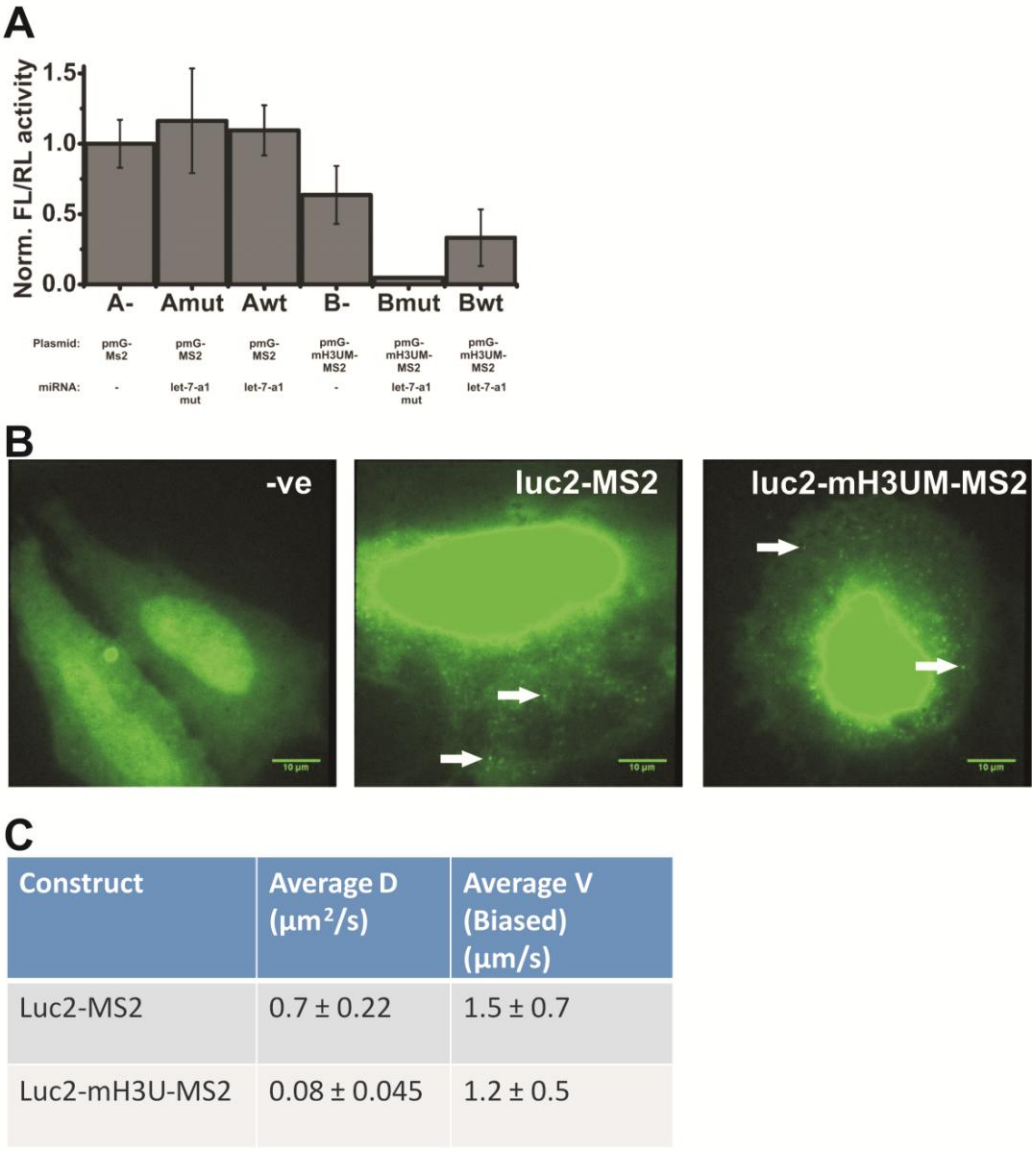

C

Construct	Average D ($\mu m^2/s$)	Average V (Biased) ($\mu m/s$)
Luc2-MS2	0.7 ± 0.22	1.5 ± 0.7
Luc2-mH3U-MS2	0.08 ± 0.045	1.2 ± 0.5

Figure A2.1. Establishment of the MS2-MCP system for dual-color intracellular single molecule microscopy. (A) Dual luciferase assay. Samples correspond to cells cotransfected with, pmG-MS2 and negative control siRNA (A-), pmG-MS2 and mutant let-7-a1 miRNA (Amut), pmG-MS2 and wild-type let-7-a1 miRNA (Awt), pmG-mH3UM-MS2 and negative control siRNA (B-), pmG-mH3UM-MS2 and mutant let-7-a1 miRNA (Bmut), pmG-mH3UM-MS2 and wild-type let-7-a1 miRNA (Bwt). (B) Pseudo-colored images of HeLa cells cotransfected with pMCP-EGFP and either pmG (-ve), pmG-MS2 (luc2-MS2) or pmG-mH3UM-MS2 (luc2-mH3UM-MS2). Arrows show representative cytoplasmic particles. (C) Ensemble diffusion coefficients of luc2-MS2 and luc2-mH3UM-MS2 transcripts. Velocity is calculated from particles moving in a biased fashion.

was fluorescent, representative of EGFP-MS2-NLS nuclear localization, and no cytoplasmic particles were seen. On the other hand cytoplasmic particles were seen for both of the latter two conditions. This was indicative of transcripts labeled with multiple copies of EGFP via the MS2 – MS2 stem loop interaction. Moreover, the ensemble diffusion coefficient of transcripts containing no UTR was almost ~7-fold larger than that with the UTR, even when the former was only 2-fold smaller than the latter (**Fig. A2.1C**). This data suggests that the molecular mass of the UTR containing transcripts are ~300 fold more than the ones without. Such a scenario is only possible if the UTR was bound by other protein factors. Consistent with this hypothesis, the mouse HMGA2 3`UTR contains several miRNA binding sites which could potentially be occupied by host miRNA induced silencing complexes (miRISC). These experiments, thus, open up the possibility for indirectly quantifying 3`UTR 'loading'. In this way, we can also express transcripts containing the wild-type 3`UTR of HMGA2 in let-7 rich HeLa cells and use the difference in mobility between mutant UTR transcripts and wild-type UTR plasmids as a measure of let-7-RISC loading. This measurement could further be used to quantify the number of let-7 miRNAs bound per mRNA target, indirectly. We can additionally use this labeling method in dual-color tracking and colocalization experiments, similar to that in Chapter 3, to find the extent of miRNA binding to mRNAs.

Appendix 3

Amenability of F9 Teratocarcinoma Cells for the Expression of Long 3`UTRs and Gene Repression Mediated by Modified microRNA

A3.1 Introduction

To shed light on the mechanism of microRNA (miRNA) action inside living cells (**Chapter 2**), we first sought to investigate the diffusive motions of miRNA bound messenger RNA (mRNA) complexes, assembled post-microinjection, in F9 teratocarcinoma cells. These cells were ideal for our experiments and were our initial cell line of choice due to their lack of endogenous let-7 miRNA. Thus, the cellular pool of let-7 miRNAs in these cells would be dictated by the amount that we microinject. A couple of reports (48, 290) had shown that the uncontrolled expression of the High Mobility Group AT-hook 2 (HMGA2) gene, which is the case in F9 cells, leads to several cancers in mouse and that let-7 miRNA can act as a tumor suppressor by repressing HMGA2, creating a strong need to understand the intracellular interaction between these two molecules. These findings along with the fact that the 3`UTR of HMGA2 has seven let-7-a1 miRNA binding sites (seed sequences) and that HMGA2 was shown to be repressed by let-7-a1 (48, 290) motivated us to choose HMGA2 mRNA as a preferred mRNA target and let-7-a1 miRNA as our probe. Our experiment was based on the assumption that upon microinjection, binding of several (up to seven) Cy3-labeled let-7-a1 miRNAs to a single HMGA2 mRNA would result in an inherent fluorescence amplification and will aid in tracking the particle. To further enhance the signal from a single mRNA, a target with more than seven let-7 seed

sequences was created by engineering two 3`untranslated regions (UTRs) of HMGA2 in tandem, downstream of its 5`UTR and coding sequence (CDS). Reverse Transcription followed by polymerase chain reaction (RTPCR) and Northern blotting indicated the presence of the endogenous HMGA2 mRNA, but an absence of our desired construct, i.e. the mRNA target containing tandem 3`UTRs. We, thus, decided to exploit endogenously expressed HMGA2 transcripts, ~ 8 – 80 copies / cell (based on absolute quantitative real-time PCR), as our mRNA target in single particle tracking (SPT) experiments. Unfortunately, control experiments (western blotting and dual luciferase assays) performed to test the repressive ability of fluorophore modified miRNAs showed that F9 cells, unlike HeLa cells, were incapable of using modified miRNAs for mRNA repression. Our observations can be explained either by technical issues related to transfection, wherein transfection efficiency or the intracellular availability (post-transfection) of modified miRNAs are different from those of un-modified miRNAs in F9 cells, or by a genuine difference in the molecular mechanism by which F9 cells (mouse) and HeLa cells (human) assemble miRNAs into repressive complexes.

A3.2 Materials and methods

Plasmids and DNA and RNA oligonucleotides. The coding sequence (CDS) of HMGA2 and two copies of its 3`-untranslated region (3`UTR) were cloned in tandem into the pcDNA4/TO/myc-His B plasmid (to yield pcDNA-mH-2xwt). pcDNA6/TR and the above plasmid were stably transfected into F9 teratocarcinoma cells. Together the two plasmids constitute the Tetracycline expression system (T-Rex, Invitrogen) wherein the gene in the pcDNA4 plasmid is under the inducible control of the tetracycline repressor (Tet-R), which is constitutively expressed by the pcDNA6 plasmid. Nine clones were generated and each was tested for expression of an mRNA bearing the CDS of HMGA2 followed by two copies of its 3`UTR, mH-2x-3`UTR. The above plasmids and clones were constructed by John Hoerter and Christine Mayr respectively.

Luciferase reporter plasmids pmG-mH3U was engineered by inserting the wild-type mouse HMGA2 3' UTR sequence downstream of the firefly luciferase ORF in the pmirGLO dual-luciferase expression vector (Promega). The wild-type 3' UTR was PCR amplified from plasmid templates received as a gift from David Bartel (Whitehead Institute, MIT) (48) using primers containing at their 5' ends XhoI and NotI restriction sequences, respectively. Following restriction digestion, the amplicon insert was ligated to complementary ends in the pmirGLO vector.

All DNA oligos were purchased from Invitrogen©. Cartridge-purified oligos were directly suspended in water and used for PCRs. For northern blotting, DNA oligos were size-selected and extracted from a 20% denaturing PAGE. DNA sequences are as follows,

Primers 175bp: Forward primer (FW-HMGA2), CCACAGAAGCGAGGACGCGGC and reverse primer (RV-HMGA2), CCTAGGTCTGCCTCTTGGCCG

Primers 282bp: Forward primer (FW-HMGA2-UTI), GCAGATATCCAGCACAGTGG and reverse primer (RV-HMGA2-3UTR), GTCCCCCGTGTTTACAGCAG

Probe1: Same sequence as RV-HMGA2

Probe2: CCACTGTGCTGGATATCTGC

Negative control siRNA used in transfection experiments was purchased from Ambion. SiLuc2 siRNA, a positive control siRNA, was designed towards the coding sequence of the firefly luciferase gene (*luc2*) and purchased from Dharmacon as a duplex. All other RNA oligonucleotides were purchased from the Keck Biotechnology Resource Laboratory at the Yale University School of Medicine with a 5' phosphate (P) and, in the case of amine modified RNA, a 3' amino group on a C7 carbon linker. RNA was purified as described (177) and the 3' amine groups were labeled with Cy3 or Cy5 succinimidyl ester as described (177, 178). RNA sequences were as follows:

let-7-a1 guide: P-UGAGGUAGUAGGUUGUAUAGUU
let-7-a1-passenger: P-CUAUACAAUCUACUGUCUUUCC
let-7-a1 mut guide: P-UGCGUUAGUAGGUUGUAUAGUU
let-7-a1 mut passenger: P-CUAUACAAUCUACUGUCGUUCC
siLuc2 guide: GAAGUGCUCGUCCUCGUCCUU
siLuc2 passenger: GGACGAGGACGAGCACUUCUU

Guide and passenger strands were heat-annealed in a 1:1 ratio, resulting in duplex miRNAs, and frozen for further use.

RT-PCR and northern blotting. Total RNA was extracted from both un-induced and doxycycline induced (0.2 – 1 µg/mL) stably transfected (tandem 3`UTRs) F9 cells using the QIAGEN RNeasy kit (QIAGEN). Reverse transcription and PCR were performed using the Taqman reverse transcription reagents (Applied Biosystems) and the SYBR green PCR mastermix (Applied Biosystems) respectively, according to manufacturer's protocol. DNA products after RT-PCR were resolved on a 2% Agarose gel. DNA was visualized by ethidium bromide staining and visualization under UV light.

For northern blotting, total RNA were separated on a 1.2% formaldehyde agarose gel along with an RNA ladder (Promega). The lane containing the RNA ladder was cut off the rest of the gel post-electrophoresis and was stained with SYBR gold (Invitrogen). RNA from rest of the gel was then transferred to a nylon membrane by capillary action. After oven-drying, the RNA was cross linked to the membrane by UV exposure. Transfer was confirmed by staining the RNA on a replicate membrane using a buffer containing 0.5 M acetic acid, pH 5.2 and 0.04% methylene blue (MB) for 10mins at room temperature. After multiple wash-steps and pre-hybridization, the membrane was then treated with ^{32}P labeled probe1 or probe2 and incubated at 55^{o}C for 24 h. After multiple wash steps the probe labeled RNA were visualized by exposing the radio-labeled RNA bands to a phosphor screen. The SYBR gold stained RNA marker as then used to estimate size of RNA bands.

Western blotting and luciferase assays. F9 cells were transfected either with no miRNA (No RNA), a negative control siRNA (-ve), let-7-a1 miRNA with an amine modification in the 3`end (let-7-a1 amine) or a mutant let-7-a1 miRNA with an amine modification in the 3`end (let-7-a1 mut amine) using lipofectamine 2000 (Invitrogen). miRNAs were added at a concentration of ~2 – 20nM. 24 h post-transfection cells were lysed using a RIPA buffer (50 mM Tris-HCl, pH 8.0, with 150 mM sodium chloride, 1.0% NP-40, 0.5% sodium deoxycholate, and 0.1% sodium dodecyl sulfate) and loaded onto a novex 16% tris-glycine pre-cast gel (Invitrogen). Size separated proteins were then transferred onto a polyvinylidene fluoride membrane (Millipore). Membranes were then probed with goat-anti-HMGIC polyclonal and mouse-anti-βactin monoclonal primary antibodies respectively. Rabbit-antigoat-HRP and goat-antimouse-Cy3 were used as secondary antibodies. Chemifluorescence, mediated by HRP and its substrate (ECL plus, GE Healtcare), was used to visualize HMGA2 and Cy3 fluorescene was used to visualize actin. Typhoon 9410 Variable Mode Imager (GE Healthcare Life Sciences) was used for imaging the membrane.

24 h prior to transfection, 100 µL of 15,000 HeLa cells were seeded per well of a 96 well plate. Cells were transfected with 60 ng of pmG-mH3U, 10 nM of the indicated dsRNA, 0.4 µL of Lipofectamine 2000 (Invitrogen) and 50 µL of OptiMEM (GIBCO). 6 h after transfection the growth medium was replaced with fresh medium. 24 h after transfection, medium was replaced with phenol red-free DMEM. Dual luciferase assays were performed using the Dual-Glo luciferase assay reagents (Promega) as per the manufacturer's protocol and luminescence was detected using a Genios Pro (Tecan) plate reader.

A3.3 Results and Discussion

**Long 3`UTR containing transcripts were not efficiently expressed in F9 cells.** We first performed RT-PCRs to test for the expression of transcripts containing the HMGA2 CDS with tandem 3`UTRs. Primer pairs were created to

amplify either a 175 base pair (bp) (Primers 175bp) or 282 bp (Primers 282bp) DNA sequence within the CDS or second 3`UTR of HMGA2, respectively (**Fig. A3.1A**). The former amplicon can result either from endogenous HMGA2 transcripts or those that contain two copies of the 3`UTR whereas the latter is specific to the tandem 3`UTR construct; the forward primer binds to a region in between the two 3`UTRs, unique to the mH-2x-3UTR cDNA, and the reverse primer binds within the 3`UTR of HMGA2. Even after doxycycline mediated induction, only the 175 bp DNA product was seen, the 282 bp product was not, suggesting the absence of tandem 3`UTR containing transcripts (**Fig. A3.1B, C**). To confirm the above results, we also performed northern blots with probes that either targets both endogenous and mH-2x-3UTR transcripts. Consistent with our previous observation, we only observed endogenous HMGA2 transcripts (**Fig. A3.1B, D**). These findings are in agreement with other recent work (226, 227), which have suggested the shortening of 3`UTRs in proliferating cells.

Modified miRNAs are non-functional in F9 cells. We then explored the possibility of utilizing the endogenous HMGA2 transcript for our SPT experiments in F9 cells. To test whether modified let-7-a1 miRNAs mediate repression of endogenous HMGA2, we first performed western blots. Surprisingly, amine modified let-7-a1 was incapable of repressing HMGA2 (compare, 'no RNA', '-ve', 'let-7-a1 amine' and 'let-7-a1 mut' in **Fig. A3.2A**). We performed luciferase reporter assays to confirm our previous observation. Similar to the western blots, modified miRNAs ('let-7-a1 amine', 'let-7-a1 Cy3', 'let-7-a1 Cy5', 'let-7-a1 bio') failed to elicit repression of a reporter gene that contained the 3`UTR of HMGA2 (**Fig. A3.2B**). In contrast, an unmodified siRNA (siLuc2) or miRNA (let-7-a1) were functional. These findings can be reconciled by two explanations, (i) transfection efficiency of modified miRNAs is much less than those of un-modified miRNAs, or (ii) modified miRNAs are incapable of being incorporated into the miRNA pathway. HeLa human cervical cancer cells, however, utilized modified miRNAs effectively to elicit repression (**Chapter 2, Fig. 2.1**) under similar conditions. This opens up the possibility that differences in the RNA interference machinery

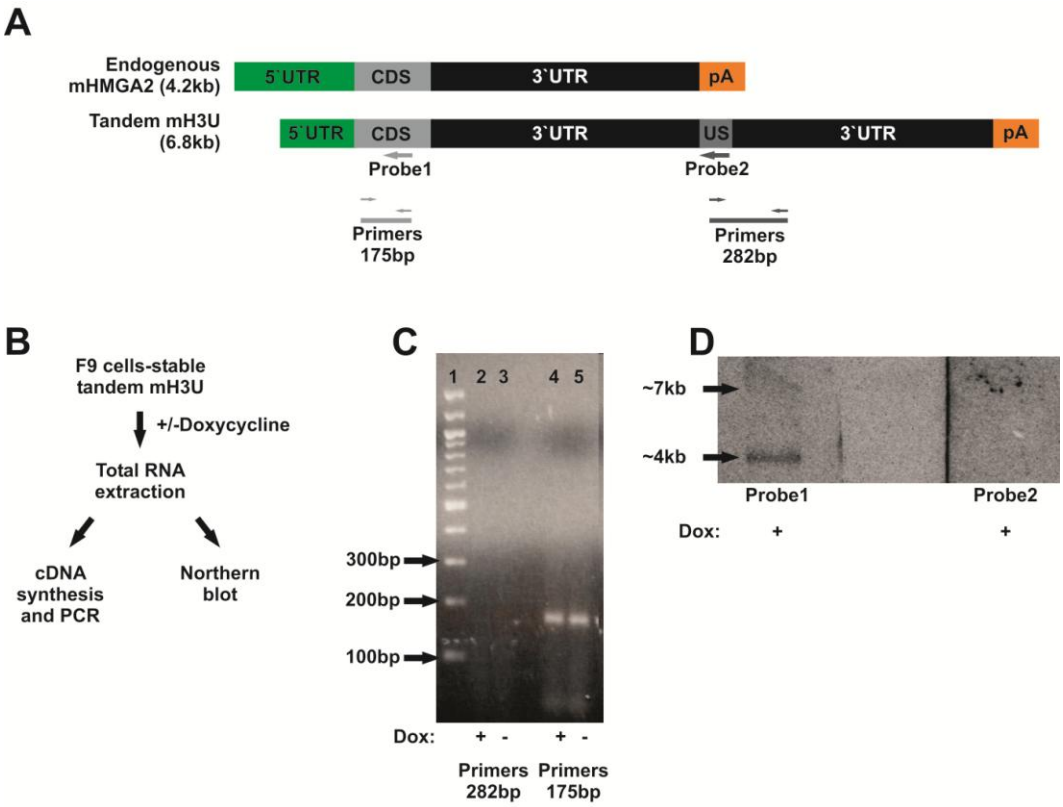

Figure A3.1. Tandem 3`UTR containing transcripts were not expressed in F9 cells. (A) Diagram depicting the transcript architecture of endogenous mouse HMGA2 (mHMGA2) and tandem 3`UTR containing mRNA (Tandem mH3U) respectively. Locations of PCR primers and northern blotting probes are shown using black and gray arrows. (B) Outline of our experiment. (C) 2% Agarose gel stained with ethidium bromide and visualized under UV. Samples separated on gel were, 100 bp ladder (NEB, lane 1), RT-PCR products amplified by primers specific to the tandem 3`UTR construct (lanes 2, 3) and products amplified by primers to the HMGA2 CDS (lanes 4, 5). (D) Northern blot showing RNAs detected with probe1 (left), which binds both endogenous and cloned transcripts, and probe2 (right), which is specific to the tandem 3`UTR construct.

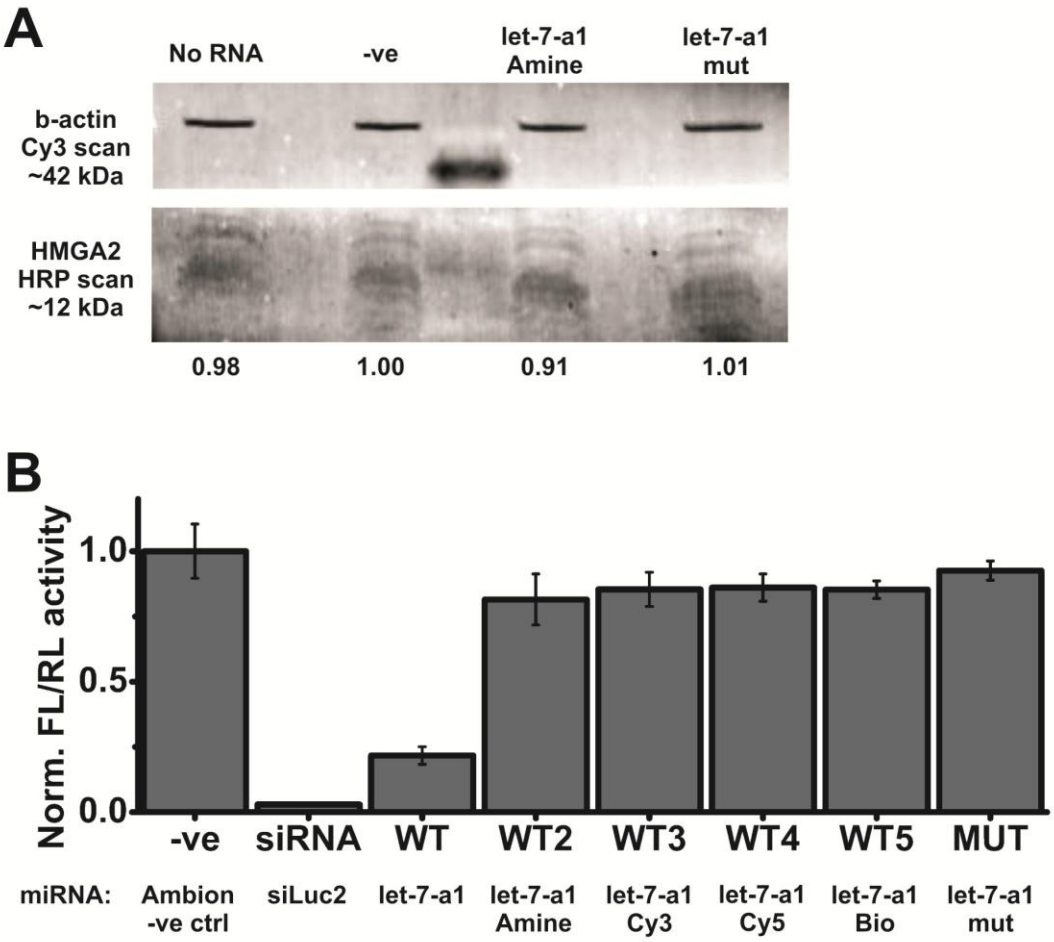

Figure A3.2. Modified miRNAs are repression incompetent in F9 cells. (A) Western blot of lysates from F9 cells, which were transfected with no miRNA (no RNA), ambion negative control siRNA (-ve), a specific amine modified let-7-a1 miRNA (let-7-a1 amine) or a mutated amine modified let-7-a1 that has been proven to not repress HMGA2 (let-7-a1 mut). Top panel shows actin and the bottom panel shows HMGA2. Numbers below represent quantification of bands, which was done in Image-quant©. Intensity of bands, used in quantification, were background subtracted and subsequently normalized to '–ve'. (B) Dual luciferase assay of F9 cells transfected with pmG-mH3U plasmid and any of the mentioned miRNAs. Firefly luciferase luminescence was normalized to that of renilla luciferase in all samples. Comparative activity of all samples were then normalized with that '–ve'. Error bars, standard deviation. (n = 6).

between humans and mice could mediate this effect; miRNA recognition and processing are different in these two cell lines (or even species) and therefore modified miRNAs are repression competent in one type of cells and not the other. Consistent with the above hypothesis, human and mouse Dicer, core components of the miRNA pathway with > 80% homology between two species, bear differences in their helicase domain, which has been implicated to unwind miRNA duplexes. It is highly possible that modified miRNAs are not efficiently unwound and thus are not functional in F9 cells. This claim can be confirmed by either incorporating compensatory mutations in the mouse dicer gene on trying to rescue miRNA mediated repression by overexpressing human Dicer in F9 cells.

A3.4 Acknowledgements

We thank C. Mayr and D. Bartel for providing us the plasmids containing the cDNA of mouse HMGA2, J. Hoerter for making the pcDNA-mH-2xwt clone, and A. Mapp for access to her plate reader. This work was supported by NIH grant GM081025 to N. Walter.

Appendix 4

miRNA Pulldown and Sequencing (miP-Seq): A High-throughput Method to Experimentally Validate miRNA Targets

A4.1 Introduction

Existing methods of miRNA target identification rely heavily on tools from bioinformatics, i.e., computational prediction (291). The predicted complementary binding or "seed" sequences within a 3' untranslated region (3'UTR), or potentially other segments, of an mRNA are then typically validated on an individual basis by experimental methods such as luciferase reporter gene assays that require cloning of the 3'UTR behind the reporter gene, co-transfection with the miRNA into a eukaryotic cell line, and careful comparison with control experiments (218). Such labor-intensive experimental tools have begun to unequivocally underscore the importance of matching seed sequences between a miRNAs and a specific mRNA target, however, they also have a number of severe drawbacks. We sought to overcome this caveat by developing a high-throughput technique that experimentally validates and quantifies *all* mRNA interactions of a given miRNA.

We will essentially combine HITS-CLIP (high-throughput sequencing of RNA isolated by crosslinking immunoprecipitation) (292) with an approach reported by Lund and co-workers to biochemically purify mRNA targets using a biotinylated miRNA "bait" (293, 294). The affinity purification of RNA-protein complexes in the protocol reported by Lund *et al*. (293, 294) is performed immediately after cell lysis without UV crosslinking, with the drawback that many

complexes will get lost during subsequent wash and dilution steps. Several other miRNA target isolation protocols have been published where either RISC proteins (e.g., Ago2) are used to immunoprecipitate the miRNA and the target mRNA (295, 296) or the miRNA itself is used as a primer for reverse transcription of the target mRNA (297). The former method is based on the assumption that the protein is associated to the target via the miRNA; although this is mostly the case, protein-mRNA interactions that are not miRNA mediated cannot be discounted. The latter method is inefficient in cases where the very 3` end of the miRNA does not canonically base-pair with its target.

Our miRNA Pull-down–deep-Sequencing approach (in short miP-Seq) will include CLIP (292), miRNA-mRNA complex purification, and deep-sequencing of RNA transcriptomes (**Fig. A4.1**). More specifically, A 3' biotin moiety will be attached to the guide strand of a miRNA duplex, leaving the functionally important 5' phosphate intact. The modified miRNA will be tested for its efficacy in RNAi using standard luciferase assays and Western blotting of the native *HMGA2* target. F9 cells will then be transfected with the biotinylated miRNA duplex and subjected to brief UV irradiation (3 times 400 mJ/cm^2 at 254 nm) on ice to form covalent bonds between RNA and any bound proteins (298). Proteins of RISC will form covalent bonds with both the bound miRNA and mRNA, covalently coupling the two. Alternatively, we will perform chemical crosslinking with formaldehyde or glutaraldehyde, but UV irradiation has the advantage that non-specific protein-protein and RNA-RNA crosslinking will be minimal. Cells will then be harvested, lysed, and streptavidin-coated magnetic beads will be used to affinity purify all miRNA-mRNA-protein complexes from the lysate. All RNA processing steps post-lysis and prior to cDNA synthesis will be done on-bead. Bound complexes will be partially digested with RNases (RNase A, RNase T1, etc.) dephosphorylated and ligated to a 3' RNA linker (3'RA). The RNA will then be 5' phosphorylated with polynucleotide kinase (PNK) to allow for the subsequent ligation of a second RNA adapter (5`RA) to the 5` end, essentially as described (292, 298). Bound complexes will then be eluted and covalently attached proteins will be removed from the adapter ligated RNA using proteinase

K. A DNA oligonucleotide (3`RDA) complementary to the 3` adapter will be used to reverse transcribe the RNA, and the resulting cDNA will be PCR amplified and subjected to high-throughput sequencing to generate several million sequence reads that will be assembled into an unbiased, genome-wide map of miRNA-associated RNAs. The frequency with which a particular sequence is found provides a quantitative measure of its occupancy potential.

Our proposed miP-Seq approach advances current miRNA target validation protocols in several important aspects:

1.) UV crosslinking will be used to covalently attach the miRNA to any proteins and to any mRNA target, ensuring that we will retain even transiently formed complexes through the purification procedure.
2.) Through affinity purification using the miRNA, a clear link is established between a specific miRNA and its RNA targets; this assignment is lost when immunoprecipitation is performed through a mediating protein component of RISC such as Ago2.
3.) High-throughput (deep) sequencing will be used to validate and annotate RNA targets, a technique that is more time efficient, sensitive and quantitative than competing techniques.

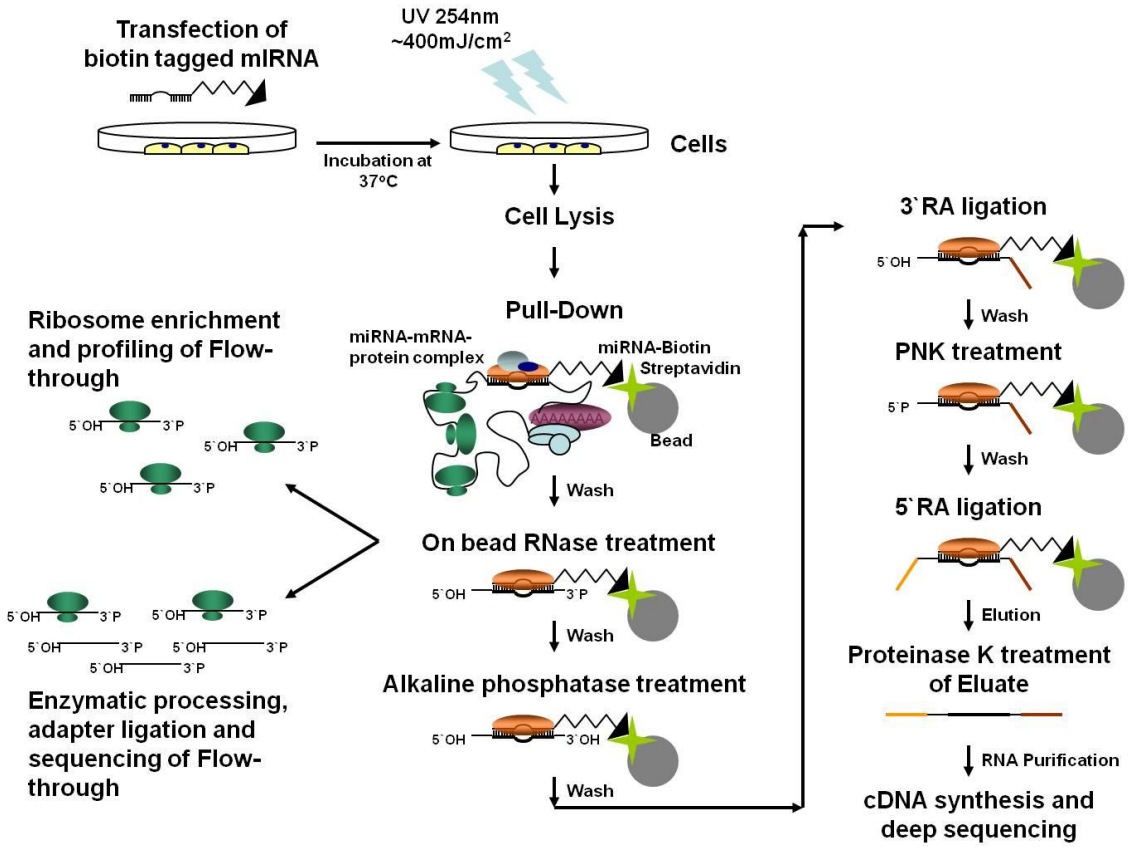

Figure A4.1. Schematic of miP-Seq.

So far, we have performed control experiments to (i) show that biotin tagged let-7-a1 miRNA maintain repressive abilities in HeLa cells and (ii) validate specificity of miRNA bound mRNA pulldown. Current members of the Walter Lab will be pursuing this approach in more detail to map all the mRNA targets of let-7-a1 in HeLa cells.

A4.2 Materials and Methods

Plasmids and RNA oligonucleotides. Luciferase reporter plasmids pmG-mH3U was engineered by inserting the wild-type mouse HMGA2 3' UTR sequence downstream of the firefly luciferase ORF in the pmirGLO dual-luciferase expression vector (Promega). The wild-type 3' UTR was PCR amplified from plasmid templates received as a gift from David Bartel (Whitehead Institute, MIT) (48) using primers containing at their 5' ends XhoI and NotI restriction sequences, respectively. Following restriction digestion, the amplicon insert was ligated to complementary ends in the pmirGLO vector.

Negative control siRNA used in transfection experiments was purchased from Ambion. SiLuc2 siRNA, a positive control siRNA, was designed towards the coding sequence of the firefly luciferase gene (*luc2*) and purchased from Dharmacon as a duplex. All other RNA oligonucleotides were purchased from the Keck Biotechnology Resource Laboratory at the Yale University School of Medicine with a 5' phosphate (P) and, in the case of biotin tagged RNA, a 3' biotin moiety on a C12 carbon linker. RNA was purified as described (177). RNA sequences were as follows:

let-7-a1 guide: P-UGAGGUAGUAGGUUGUAUAGUU
let-7-a1-passenger: P-CUAUACAAUCUACUGUCUUUCC
let-7-a1 mut guide: P-UGCGUUAGUAGGUUGUAUAGUU
let-7-a1 mut passenger: P-CUAUACAAUCUACUGUCGUUCC
siLuc2 guide: GAAGUGCUCGUCCUCGUCCUU
siLuc2 passenger: GGACGAGGACGAGCACUUCUU

Guide and passenger strands were heat-annealed in a 1:1 ratio, resulting in duplex miRNAs, and frozen for further use.

Luciferase assays. For transfection repression assays 24 h prior to transfection, 100 µL of 15,000 HeLa cells were seeded per well of a 96 well plate. Cells were transfected with 60 ng of pmG-mH3U, 10 - 30 nM of the indicated dsRNA, 0.4 µL of Lipofectamine 2000 (Invitrogen) and 50 µL of OptiMEM (GIBCO). 6 h after transfection the growth medium was replaced with fresh medium. 24 h after transfection, medium was replaced with phenol red-free DMEM. Dual luciferase assays were performed using the Dual-Glo luciferase assay reagents (Promega) as per the manufacturer's protocol and luminescence was detected using a Genios Pro (Tecan) plate reader.

Transfection, pull-down and RT-PCR. A schematic of the steps performed is shown in **Fig. A4.2A**. Cells were seeded onto 15 cm dishes ~2 days prior to transfections. 11 µg of the pmG plasmid, without any UTR, or 15 µg of pmG-mH3U were transfected along with 25nM of biotin tagged let-7-a1 miRNA using lipofectamine 2000 (Invitrogen). 6 h after transfection the growth medium was replaced with fresh medium. 24 h after transfection, cells were washed three times and suspended in cold phosphate buffered saline (PBS). UV cross-linking was performed by placing a hand-held UV illuminator (254nm), 1.5 cm above the dish surface for 15 min on ice. PBS was then replaced with cold lysis buffer (20 mM Tris.Cl pH7.5, 500 mM NaCl, 2.5 mM MgCl2, 0.05% NP-40, 60 U/mL Superase.In, 1x Roche© protease inhibitor capsule-EDTA free, 1mM DTT) and cells were scraped onto a tube using a rubber policeman (BD, Falcon). The tube was placed on ice for 10 min with intermittent vortexing, every 2.5 min. Lysates were then centrifuged at 10,000 x g for 15 min 4 ^{o}C and the supernatants, containing all the miRNA-mRNA complexes, were immediately used.

100 µL of streptavidin beads, washed with the lysis buffer, were blocked with 100 µg yeast tRNAs (Sigma) and 100 µg bovine serum albumin for 2 h at 4 ^{o}C. Beads were then washed multiple times with the lysis buffer. Lysates were added to blocked beads at a 1:1 ratio (vol:vol) and incubated for 4 h at 4 ^{o}C to

allow for binding of biotin tagged miRNA-mRNA complexes. Unbound complexes were washed using the lysis buffer and the beads, containing bound complexes, were DNAse (Turbo DNAse, Ambion) and proteinase K treated for 20 min each at 37 ^{o}C. This treated sample was then phenol-chlorofom extracted and the RNAs were ethanol precipitated. RNA pellets were dissolved in nuclease free water.

Reverse transcription and PCR were performed using the Taqman reverse transcription reagents (Applied Biosystems) and the SYBR green PCR mastermix (Applied Biosystems) respectively, according to manufacturer's protocol. DNA products after RT-PCR were resolved on a 2% Agarose gel. DNA was visualized by ethidium bromide staining and visualization under UV light.

A4.3 Results and Discussion

Proof of specific pulldown marred by DNA contamination. We, first, performed luciferase assays to test the repressive activity of biotin tagged let-7-a1. To this end HeLa cells were cotransfected with the pmG-mH3U plasmid and either a non-specific dsRNA (-ve), an un-modified let-7-a1 miRNA (WT), a biotin tagged let-7-a1 miRNA (WT1), a mutated let-7-a1 miRNA incapable of repressing let-7-a1 targets (let-7-a1 mut) or a specific siRNA (siRNA). As expected, the biotin tagged miRNA was capable of repressing its target (compare WT, WT1 and MUT), but to a slightly lower extent than the un-modified let-7-a1 (**Fig. A4.2B**).

To test whether we pulled down specific mRNA targets via the biotin tagged miRNA, we performed control experiments using plasmid encoded, validated let-7-a1 targets. Hela cells were transfected either with a plasmid encoding for an mRNA with no let-7 seed sequence (pmG) or a plasmid containing a valid target of let-7 (pmG-mH3U) along with the biotin lagged let-7-a1 miRNA. pmG-mH3U co-transfected with no miRNA was also included in our experiment to account for non-specific binding of mRNA targets to the beads. We

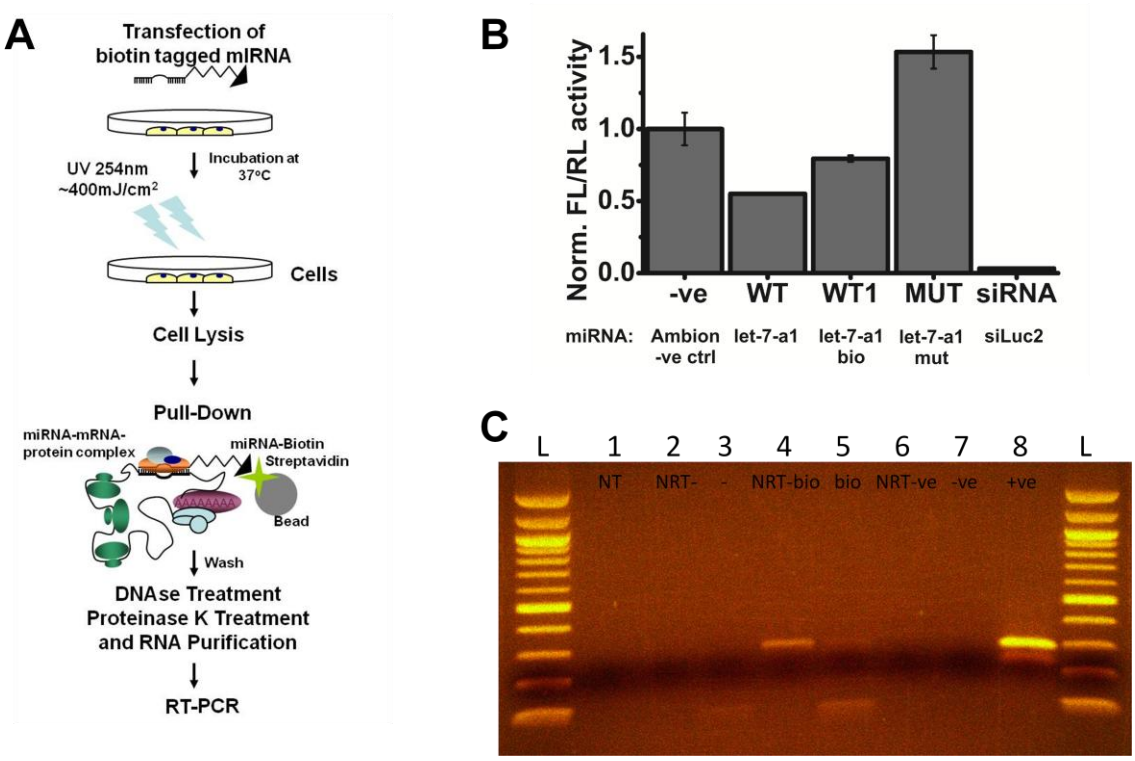

Figure A4.2. Validating biotin tagged miRNA function and its ability to pull-down specific targets. (A) Schematic of steps performed. (B) Dual luciferase assay of HeLa cells transfected with pmG-mH3U plasmid and any of the mentioned miRNAs. Firefly luciferase luminescence was normalized to that of renilla luciferase in all samples. Comparative activity of all samples were then normalized with that '–ve'. Error bars, standard deviation. (n = 6). (C) 2% Agarose gel loaded with RT-PCR products, stained with ethidium bromide and visualized under UV light. Samples correspond to no template control (NT, lane 1), no reverse transcriptase control and the actual RT-PCR sample from cells transfected with pmG-mH3U and no miRNA (NRT- and -, lanes 2 and 3), no reverse transcriptase control and the actual RT-PCR sample from cells transfected with pmG-mH3U and biotin tagged let-7-a1 miRNA (NRT-bio and bio, lanes 4 and 5), no reverse transcriptase control and the actual RT-PCR sample from cells transfected with pmG (NRT-ve and -ve, lanes 6 and 7), positive control for PCR, where PCR was set with DNA template, showing correct size of amplicon (+ve, lane 8) and 100 bp ladder (NEB, L).

then performed all the steps outlined in **Fig. A4.2A**. After RT-PCR, the DNA amplicons were separated on a 2% Agarose gel, stained with ethidium bromide and visualized under UV light. We did not detect any non-specific binding of mRNAs to the beads (lane 3, **Fig. A4.2C**) or non-specific pulldown by biotin tagged let-7-a1 (lane 7, **Fig. A4.2C**), but could clearly visualize the pulldown of a specific product (lane 5, **Fig. A4.2C**), which is indicative of efficient pulldown. However, we also detected a DNA band of the same molecular weight in the reverse transcription control sample, which does not contain any reverse transcriptase (lane 4, **Fig. A4.2C**). As no cDNA should be present in the absence of the reverse transcriptase, this band cold potentially arise from plasmid DNA contamination in our pull-down fraction, which could also serve as a template in the PCR reaction. This trend was present even after multiple rounds of DNAse treatment. Future experiments can include the RT-PCR of an endogenous target, which would not require the transfection of a plasmid DNA, and thus could potentially help in alleviating this problem. Alternatively, incomplete DNA digestion on-bead could potentially be the problem and the pull-down protocol can be tweaked to remove this step such that DNA digestion happens in solution.

A4.4 Acknowledgements

We thank C. Mayr and D. Bartel for providing us the plasmids containing the cDNA of mouse HMGA2, and A. Mapp for access to her plate reader. This work was supported by NIH grant GM081025 to N. Walter.

References

1. Dahm, R., Discovering DNA: Friedrich Miescher and the early years of nucleic acid research. *Hum Genet*, 2008. **122**(6): p. 565-81.
2. Campbell, K.H., et al., Implications of cloning. *Nature*, 1996. **380**(6573): p. 383.
3. Campbell, K.H., et al., Sheep cloned by nuclear transfer from a cultured cell line. *Nature*, 1996. **380**(6569): p. 64-6.
4. Gibson, D.G., et al., Creation of a bacterial cell controlled by a chemically synthesized genome. *Science*, 2010. **329**(5987): p. 52-6.
5. Kruger, K., et al., Self-splicing RNA: autoexcision and autocyclization of the ribosomal RNA intervening sequence of Tetrahymena. *Cell*, 1982. **31**(1): p. 147-57.
6. Carninci, P., Non-coding RNA transcription: turning on neighbours. *Nat Cell Biol*, 2008. **10**(9): p. 1023-4.
7. Mattick, J.S. and I.V. Makunin, Non-coding RNA. *Hum Mol Genet*, 2006. **15 Spec No 1**: p. R17-29.
8. Berretta, J. and A. Morillon, Pervasive transcription constitutes a new level of eukaryotic genome regulation. *EMBO rep*, 2009. **10**(9): p. 973-82.
9. Mercer, T.R., M.E. Dinger, and J.S. Mattick, Long non-coding RNAs: insights into functions. *Nat Rev Genet*, 2009. **10**(3): p. 155-9.
10. Mattick, J.S., The hidden genetic program of complex organisms. *Sci Am*, 2004. **291**(4): p. 60-7.
11. Bartel, D.P., MicroRNAs: target recognition and regulatory functions. *Cell*, 2009. **136**(2): p. 215-33.
12. Czech, B. and G.J. Hannon, Small RNA sorting: matchmaking for Argonautes. *Nat Rev Genet*, 2011. **12**(1): p. 19-31.
13. Wahl, M.C., C.L. Will, and R. Luhrmann, The spliceosome: design principles of a dynamic RNP machine. *Cell*, 2009. **136**(4): p. 701-18.
14. Schmeing, T.M. and V. Ramakrishnan, What recent ribosome structures have revealed about the mechanism of translation. *Nature*, 2009. **461**(7268): p. 1234-42.

15. Valadkhan, S. and J.L. Manley, Splicing-related catalysis by protein-free snRNAs. *Nature*, 2001. **413**(6857): p. 701-7.
16. Stark, B.C., et al., Ribonuclease P: an enzyme with an essential RNA component. *Proc Natl Acad Sci USA*, 1978. **75**(8): p. 3717-21.
17. Perreault, J., et al., Identification of hammerhead ribozymes in all domains of life reveals novel structural variations. *PLoS Comp Biol*, 2011. **7**(5): p. e1002031.
18. Webb, C.H., et al., Widespread occurrence of self-cleaving ribozymes. *Science*, 2009. **326**(5955): p. 953.
19. Doherty, E.A. and J.A. Doudna, Ribozyme structures and mechanisms. *Annu Rev Biophys Biomol Struct*, 2001. **30**: p. 457-75.
20. Ditzler, M.A., et al., A rugged free energy landscape separates multiple functional RNA folds throughout denaturation. *Nucleic Acids Res*, 2008. **36**(22): p. 7088-99.
21. Rueda, D., et al., Single-molecule enzymology of RNA: essential functional groups impact catalysis from a distance. *Proc Natl Acad Sci USA*, 2004. **101**(27): p. 10066-71.
22. Zhuang, X., et al., Correlating structural dynamics and function in single ribozyme molecules. *Science*, 2002. **296**(5572): p. 1473-6.
23. Salehi-Ashtiani, K., et al., A genomewide search for ribozymes reveals an HDV-like sequence in the human CPEB3 gene. *Science*, 2006. **313**(5794): p. 1788-92.
24. Teixeira, A., et al., Autocatalytic RNA cleavage in the human beta-globin pre-mRNA promotes transcription termination. *Nature*, 2004. **432**(7016): p. 526-30.
25. Tinsley, R.A., J.R. Furchak, and N.G. Walter, Trans-acting glmS catalytic riboswitch: locked and loaded. *RNA*, 2007. **13**(4): p. 468-77.
26. Winkler, W.C., et al., Control of gene expression by a natural metabolite-responsive ribozyme. *Nature*, 2004. **428**(6980): p. 281-6.
27. Mandal, M. and R.R. Breaker, Gene regulation by riboswitches. *Nat Rev Mol Cell Biol*, 2004. **5**(6): p. 451-63.

28. Frith, M.C., M. Pheasant, and J.S. Mattick, The amazing complexity of the human transcriptome. *Eur J Hum Genet*, 2005. **13**(8): p. 894-7.
29. Matlin, A.J., F. Clark, and C.W. Smith, Understanding alternative splicing: towards a cellular code. *Nat Rev Mol Cell Biol*, 2005. **6**(5): p. 386-98.
30. Brockdorff, N., et al., The product of the mouse Xist gene is a 15 kb inactive X-specific transcript containing no conserved ORF and located in the nucleus. *Cell*, 1992. **71**(3): p. 515-26.
31. Gupta, R.A., et al., Long non-coding RNA HOTAIR reprograms chromatin state to promote cancer metastasis. *Nature*, 2010. **464**(7291): p. 1071-6.
32. Moazed, D., Small RNAs in transcriptional gene silencing and genome defence. *Nature*, 2009. **457**(7228): p. 413-20.
33. Siomi, H. and M.C. Siomi, On the road to reading the RNA-interference code. *Nature*, 2009. **457**(7228): p. 396-404.
34. Lee, R.C., R.L. Feinbaum, and V. Ambros, The C. elegans heterochronic gene lin-4 encodes small RNAs with antisense complementarity to lin-14. *Cell*, 1993. **75**(5): p. 843-54.
35. Wightman, B., I. Ha, and G. Ruvkun, Posttranscriptional regulation of the heterochronic gene lin-14 by lin-4 mediates temporal pattern formation in C. elegans. *Cell*, 1993. **75**(5): p. 855-62.
36. Timmons, L. and A. Fire, Specific interference by ingested dsRNA. *Nature*, 1998. **395**(6705): p. 854.
37. Fire, A., et al., Potent and specific genetic interference by double-stranded RNA in Caenorhabditis elegans. *Nature*, 1998. **391**(6669): p. 806-11.
38. Napoli, C., C. Lemieux, and R. Jorgensen, Introduction of a Chimeric Chalcone Synthase Gene into Petunia Results in Reversible Co-Suppression of Homologous Genes in trans. *Plant Cell*, 1990. **2**(4): p. 279-289.
39. Romano, N. and G. Macino, Quelling: transient inactivation of gene expression in Neurospora crassa by transformation with homologous sequences. *Mol Microbiol*, 1992. **6**(22): p. 3343-53.

40. Elbashir, S.M., et al., Duplexes of 21-nucleotide RNAs mediate RNA interference in cultured mammalian cells. *Nature*, 2001. **411**(6836): p. 494-8.
41. Elbashir, S.M., W. Lendeckel, and T. Tuschl, RNA interference is mediated by 21- and 22-nucleotide RNAs. *Genes Dev*, 2001. **15**(2): p. 188-200.
42. Elbashir, S.M., et al., Functional anatomy of siRNAs for mediating efficient RNAi in Drosophila melanogaster embryo lysate. *EMBO J*, 2001. **20**(23): p. 6877-88.
43. Zamore, P.D., et al., RNAi: double-stranded RNA directs the ATP-dependent cleavage of mRNA at 21 to 23 nucleotide intervals. *Cell*, 2000. **101**(1): p. 25-33.
44. Dorsett, Y. and T. Tuschl, siRNAs: applications in functional genomics and potential as therapeutics. *Nat Rev Drug Discovery*, 2004. **3**(4): p. 318-29.
45. Ding, S.W. and O. Voinnet, Antiviral immunity directed by small RNAs. *Cell*, 2007. **130**(3): p. 413-26.
46. Kojima, K., et al., MicroRNA122 is a key regulator of alpha-fetoprotein expression and influences the aggressiveness of hepatocellular carcinoma. *Nat Comm*, 2011. **2**: p. 338.
47. Krol, J., I. Loedige, and W. Filipowicz, The widespread regulation of microRNA biogenesis, function and decay. *Nat Rev Genet*, 2010. **11**(9): p. 597-610.
48. Mayr, C., M.T. Hemann, and D.P. Bartel, Disrupting the pairing between let-7 and Hmga2 enhances oncogenic transformation. *Science*, 2007. **315**(5818): p. 1576-9.
49. Trajkovski, M., et al., MicroRNAs 103 and 107 regulate insulin sensitivity. *Nature*, 2011. **474**: p. 649–653.
50. Batuwita, R. and V. Palade, microPred: effective classification of pre-miRNAs for human miRNA gene prediction. *Bioinformatics*, 2009. **25**(8): p. 989-95.

51. Farh, K.K., et al., The widespread impact of mammalian MicroRNAs on mRNA repression and evolution. *Science*, 2005. **310**(5755): p. 1817-21.
52. Borchert, G.M., W. Lanier, and B.L. Davidson, RNA polymerase III transcribes human microRNAs. *Nat Struct Mol Biol*, 2006. **13**(12): p. 1097-101.
53. Lagos-Quintana, M., et al., Identification of novel genes coding for small expressed RNAs. *Science*, 2001. **294**(5543): p. 853-8.
54. Bartel, D.P., MicroRNAs: genomics, biogenesis, mechanism, and function. *Cell*, 2004. **116**(2): p. 281-97.
55. Ruby, J.G., C.H. Jan, and D.P. Bartel, Intronic microRNA precursors that bypass Drosha processing. *Nature*, 2007. **448**(7149): p. 83-6.
56. Diederichs, S. and D.A. Haber, Dual role for argonautes in microRNA processing and posttranscriptional regulation of microRNA expression. *Cell*, 2007. **131**(6): p. 1097-108.
57. Cheloufi, S., et al., A dicer-independent miRNA biogenesis pathway that requires Ago catalysis. *Nature*, 2010. **465**(7298): p. 584-9.
58. Cifuentes, D., et al., A novel miRNA processing pathway independent of Dicer requires Argonaute2 catalytic activity. *Science*, 2010. **328**(5986): p. 1694-8.
59. Czech, B., et al., Hierarchical rules for Argonaute loading in Drosophila. *Mol Cell*, 2009. **36**(3): p. 445-56.
60. Ghildiyal, M., et al., Sorting of Drosophila small silencing RNAs partitions microRNA* strands into the RNA interference pathway. *RNA*, 2010. **16**(1): p. 43-56.
61. Okamura, K., N. Liu, and E.C. Lai, Distinct mechanisms for microRNA strand selection by Drosophila Argonautes. *Mol Cell*, 2009. **36**(3): p. 431-44.
62. Chekulaeva, M. and W. Filipowicz, Mechanisms of miRNA-mediated post-transcriptional regulation in animal cells. *Curr Opin Cell Biol*, 2009. **21**(3): p. 452-60.

63. Doench, J.G., C.P. Petersen, and P.A. Sharp, siRNAs can function as miRNAs*. Genes Dev*, 2003. **17**(4): p. 438-42.
64. Doench, J.G. and P.A. Sharp, Specificity of microRNA target selection in translational repression*. Genes Dev*, 2004. **18**(5): p. 504-11.
65. Filipowicz, W., S.N. Bhattacharyya, and N. Sonenberg, Mechanisms of post-transcriptional regulation by microRNAs: are the answers in sight? *Nat Rev Genet*, 2008. **9**(2): p. 102-14.
66. Mathonnet, G., et al., MicroRNA inhibition of translation initiation in vitro by targeting the cap-binding complex eIF4F*. Science*, 2007. **317**(5845): p. 1764-7.
67. Pillai, R.S., et al., Inhibition of translational initiation by Let-7 MicroRNA in human cells*. Science*, 2005. **309**(5740): p. 1573-6.
68. Kiriakidou, M., et al., An mRNA m7G cap binding-like motif within human Ago2 represses translation*. Cell*, 2007. **129**(6): p. 1141-51.
69. Thermann, R. and M.W. Hentze, Drosophila miR2 induces pseudo-polysomes and inhibits translation initiation*. Nature*, 2007. **447**(7146): p. 875-8.
70. Chendrimada, T.P., et al., MicroRNA silencing through RISC recruitment of eIF6*. Nature*, 2007. **447**(7146): p. 823-8.
71. Wang, B., A. Yanez, and C.D. Novina, MicroRNA-repressed mRNAs contain 40S but not 60S components*. Proc Natl Acad Sci USA*, 2008. **105**(14): p. 5343-8.
72. Seggerson, K., L. Tang, and E.G. Moss, Two genetic circuits repress the Caenorhabditis elegans heterochronic gene lin-28 after translation initiation*. Dev Biol*, 2002. **243**(2): p. 215-25.
73. Kim, J., et al., Identification of many microRNAs that copurify with polyribosomes in mammalian neurons*. Proc Natl Acad Sci USA*, 2004. **101**(1): p. 360-5.
74. Maroney, P.A., et al., Evidence that microRNAs are associated with translating messenger RNAs in human cells*. Nat Struct Mol Biol*, 2006. **13**(12): p. 1102-7.

75. Nottrott, S., M.J. Simard, and J.D. Richter, Human let-7a miRNA blocks protein production on actively translating polyribosomes. *Nat Struct Mol Biol*, 2006. **13**(12): p. 1108-14.
76. Rehwinkel, J., et al., Genome-wide analysis of mRNAs regulated by Drosha and Argonaute proteins in Drosophila melanogaster. *Mol Cell Biol*, 2006. **26**(8): p. 2965-75.
77. Behm-Ansmant, I., et al., mRNA degradation by miRNAs and GW182 requires both CCR4:NOT deadenylase and DCP1:DCP2 decapping complexes. *Genes Dev*, 2006. **20**(14): p. 1885-98.
78. Wu, L., J. Fan, and J.G. Belasco, MicroRNAs direct rapid deadenylation of mRNA. *Proc Natl Acad Sci USA*, 2006. **103**(11): p. 4034-9.
79. Guo, H., et al., Mammalian microRNAs predominantly act to decrease target mRNA levels. *Nature*, 2010. **466**(7308): p. 835-40.
80. Parker, R. and H. Song, The enzymes and control of eukaryotic mRNA turnover. *Nat Struct Mol Biol*, 2004. **11**(2): p. 121-7.
81. Liu, J., et al., MicroRNA-dependent localization of targeted mRNAs to mammalian P-bodies. *Nat Cell Biol*, 2005. **7**(7): p. 719-23.
82. Parker, R. and U. Sheth, P bodies and the control of mRNA translation and degradation. *Mol Cell*, 2007. **25**(5): p. 635-46.
83. Eulalio, A., et al., P-body formation is a consequence, not the cause, of RNA-mediated gene silencing. *Mol Cell Biol*, 2007. **27**(11): p. 3970-81.
84. Lecuyer, E., et al., Global analysis of mRNA localization reveals a prominent role in organizing cellular architecture and function. *Cell*, 2007. **131**(1): p. 174-87.
85. Montero Llopis, P., et al., Spatial organization of the flow of genetic information in bacteria. *Nature*, 2010. **466**(7302): p. 77-81.
86. Oleynikov, Y. and R.H. Singer, Real-time visualization of ZBP1 association with beta-actin mRNA during transcription and localization. *Curr Biol*, 2003. **13**(3): p. 199-207.
87. Fusco, D., et al., Single mRNA molecules demonstrate probabilistic movement in living mammalian cells. *Curr Biol*, 2003. **13**(2): p. 161-7.

88. Merchant, K.A., et al., Characterizing the unfolded states of proteins using single-molecule FRET spectroscopy and molecular simulations. *Proc Natl Acad Sci USA*, 2007. **104**(5): p. 1528-33.
89. Schuler, B., E.A. Lipman, and W.A. Eaton, Probing the free-energy surface for protein folding with single-molecule fluorescence spectroscopy. *Nature*, 2002. **419**(6908): p. 743-7.
90. Solomatin, S.V., et al., Multiple native states reveal persistent ruggedness of an RNA folding landscape. *Nature*, 2010. **463**(7281): p. 681-4.
91. Lipman, E.A., et al., Single-molecule measurement of protein folding kinetics. *Science*, 2003. **301**(5637): p. 1233-5.
92. Kaufman, R.J., Overview of vector design for mammalian gene expression. *Mol Biotechnol*, 2000. **16**(2): p. 151-60.
93. Roy, R., S. Hohng, and T. Ha, A practical guide to single-molecule FRET. *Nat Methods*, 2008. **5**(6): p. 507-16.
94. Walter, N.G., et al., Do-it-yourself guide: how to use the modern single-molecule toolkit. *Nat Methods*, 2008. **5**(6): p. 475-89.
95. Toprak, E., C. Kural, and P.R. Selvin, Super-accuracy and super-resolution getting around the diffraction limit. *Methods Enzymol*, 2010. **475**: p. 1-26.
96. Edidin, M., Near-field scanning optical microscopy, a siren call to biology. *Traffic*, 2001. **2**(11): p. 797-803.
97. Lewis, A., et al., Near-field optics: from subwavelength illumination to nanometric shadowing. *Nat Biotechnol*, 2003. **21**(11): p. 1378-86.
98. Axelrod, D., Cell-substrate contacts illuminated by total internal reflection fluorescence. *J Cell Biol*, 1981. **89**(1): p. 141-5.
99. Konopka, C.A. and S.Y. Bednarek, Variable-angle epifluorescence microscopy: a new way to look at protein dynamics in the plant cell cortex. *Plant J*, 2008. **53**(1): p. 186-96.
100. Tokunaga, M., N. Imamoto, and K. Sakata-Sogawa, Highly inclined thin illumination enables clear single-molecule imaging in cells. *Nat Methods*, 2008. **5**(2): p. 159-61.

101. Nakano, A., Spinning-disk confocal microscopy -- a cutting-edge tool for imaging of membrane traffic*. Cell Struct Funct*, 2002. **27**(5): p. 349-55.
102. Rehemtulla, A., et al., Ultraviolet radiation-induced apoptosis is mediated by activation of CD-95 (Fas/APO-1)*. J Biol Chem*, 1997. **272**(41): p. 25783-6.
103. Gossen, M. and H. Bujard, Tight control of gene expression in mammalian cells by tetracycline-responsive promoters*. Proc Natl Acad Sci USA*, 1992. **89**(12): p. 5547-51.
104. Prescher, J.A. and C.R. Bertozzi, Chemistry in living systems*. Nat Chem Biol*, 2005. **1**(1): p. 13-21.
105. Lord, S.J., et al., DCDHF fluorophores for single-molecule imaging in cells*. Chemphyschem*, 2009. **10**(1): p. 55-65.
106. Lord, S.J., et al., A photoactivatable push-pull fluorophore for single-molecule imaging in live cells*. J Am Chem Soc*, 2008. **130**(29): p. 9204-5.
107. Davidson, M.W. and R.E. Campbell, Engineered fluorescent proteins: innovations and applications*. Nat Methods*, 2009. **6**(10): p. 713-17.
108. Heilemann, M., et al., Subdiffraction-resolution fluorescence imaging with conventional fluorescent probes*. Angew Chem Int Ed*, 2008. **47**(33): p. 6172-6.
109. Kapanidis, A.N. and S. Weiss, Fluorescent probes and bioconjugation chemistries for single-molecule fluorescence analysis of biomolecules*. J Chem Phys*, 2002. **117**(24): p. 10953-10964.
110. Dave, R., et al., Mitigating unwanted photophysical processes for improved single-molecule fluorescence imaging*. Biophys J*, 2009. **96**(6): p. 2371-81.
111. Aitken, C.E., R.A. Marshall, and J.D. Puglisi, An oxygen scavenging system for improvement of dye stability in single-molecule fluorescence experiments*. Biophys J*, 2008. **94**(5): p. 1826-35.
112. Olenych, S.G., et al., The fluorescent protein color palette*. Curr Protoc Cell Biol*, 2007. **Chapter 21**: p. Unit 21 5.

113. Bogdanov, A.M., et al., Cell culture medium affects GFP photostability: a solution. *Nat Methods*, 2009. **6**(12): p. 859-60.
114. Billinton, N. and A.W. Knight, Seeing the wood through the trees: a review of techniques for distinguishing green fluorescent protein from endogenous autofluorescence. *Anal Biochem*, 2001. **291**(2): p. 175-97.
115. Kredel, S., et al., Optimized and far-red-emitting variants of fluorescent protein eqFP611. *Chem Biol*, 2008. **15**(3): p. 224-33.
116. Magde, D., E. Elson, and W.W. Webb, Thermodynamic Fluctuations in a Reacting System—Measurement by Fluorescence Correlation Spectroscopy. *Phys Rev Lett*, 1972. **29**(11): p. 705-708.
117. Poo, M. and R.A. Cone, Lateral diffusion of rhodopsin in the photoreceptor membrane. *Nature*, 1974. **247**(441): p. 438-41.
118. Gelles, J., B.J. Schnapp, and M.P. Sheetz, Tracking kinesin-driven movements with nanometre-scale precision. *Nature*, 1988. **331**(6155): p. 450-3.
119. De Brabander, M., et al., The use of submicroscopic gold particles combined with video contrast enhancement as a simple molecular probe for the living cell. *Cell Motil Cytoskeleton*, 1986. **6**(2): p. 105-13.
120. Geerts, H., et al., Nanovid tracking: a new automatic method for the study of mobility in living cells based on colloidal gold and video microscopy. *Biophys J*, 1987. **52**(5): p. 775-82.
121. Moerner, W.E. and L. Kador, Optical detection and spectroscopy of single molecules in a solid. *Phys Rev Lett*, 1989. **62**(21): p. 2535-2538.
122. Ambrose, W.P., T. Basche, and W.E. Moerner, Detection and Spectroscopy of Single Pentacene Molecules in a p- Terphenyl Crystal by Means of Fluorescence Excitation. *J Chem Phys*, 1991. **95**: p. 7150-7163.
123. Ambrose, W.P. and W.E. Moerner, Fluorescence spectroscopy and spectral diffusion of single impurity molecules in a crystal. *Nature*, 1991. **349**: p. 225 - 227.

124. Orrit, M. and J. Bernard, Single pentacene molecules detected by fluorescence excitation in a p-terphenyl crystal. *Phys Rev Lett*, 1990. **65**(21): p. 2716-2719.
125. Van Oijen, A.M., et al., 3-Dimensional super-resolution by spectrally selective imaging. *Chem Phys Lett*, 1998. **292**(1-2): p. 183-187.
126. Yildiz, A., et al., Myosin V walks hand-over-hand: single fluorophore imaging with 1.5-nm localization. *Science*, 2003. **300**(5628): p. 2061-5.
127. Bobroff, N., Position measurement with a resolution and noise-limited instrument. *Rev Sci Instrum*, 1986. **57**(6): p. 1152-1157.
128. Thompson, R.E., D.R. Larson, and W.W. Webb, Precise nanometer localization analysis for individual fluorescent probes. *Biophys J*, 2002. **82**(5): p. 2775-83.
129. Hua, W., J. Chung, and J. Gelles, Distinguishing inchworm and hand-over-hand processive kinesin movement by neck rotation measurements. *Science*, 2002. **295**(5556): p. 844-8.
130. Forkey, J.N., et al., Three-dimensional structural dynamics of myosin V by single-molecule fluorescence polarization. *Nature*, 2003. **422**(6930): p. 399-404.
131. Yildiz, A., et al., Kinesin walks hand-over-hand. *Science*, 2004. **303**(5658): p. 676-8.
132. Gordon, M.P., T. Ha, and P.R. Selvin, Single-molecule high-resolution imaging with photobleaching. *Proc Natl Acad Sci USA*, 2004. **101**(17): p. 6462-5.
133. Qu, X., et al., Nanometer-localized multiple single-molecule fluorescence microscopy. *Proc Natl Acad Sci USA*, 2004. **101**(31): p. 11298-303.
134. Das, S.K., et al., Membrane protein stoichiometry determined from the step-wise photobleaching of dye-labelled subunits. *Chembiochem*, 2007. **8**(9): p. 994-9.
135. Kuszak, A.J., et al., Purification and functional reconstitution of monomeric mu-opioid receptors: allosteric modulation of agonist binding by Gi2. *J Biol Chem*, 2009. **284**(39): p. 26732-41.

136. Churchman, L.S., et al., Single molecule high-resolution colocalization of Cy3 and Cy5 attached to macromolecules measures intramolecular distances through time. *Proc Natl Acad Sci USA*, 2005. **102**(5): p. 1419-23.
137. Goshtasby, A., Image registration by local approximation methods. *Image and Vision Computing*, 1988. **6**(4): p. 255 - 261.
138. Grunwald, D. and R.H. Singer, In vivo imaging of labelled endogenous beta-actin mRNA during nucleocytoplasmic transport. *Nature*, 2010. **467**(7315): p. 604-7.
139. Kao, H.P. and A.S. Verkman, Tracking of single fluorescent particles in three dimensions: use of cylindrical optics to encode particle position. *Biophys J*, 1994. **67**(3): p. 1291-300.
140. Speidel, M., A. Jonas, and E.L. Florin, Three-dimensional tracking of fluorescent nanoparticles with subnanometer precision by use of off-focus imaging. *Opt Lett*, 2003. **28**(2): p. 69-71.
141. Schütz, G.J., et al., 3D imaging of individual ion channels in live cells at 40 nm resolution. *Single Molecules*, 2000. **1**(1): p. 25-31.
142. Toprak, E., et al., Three-dimensional particle tracking via bifocal imaging. *Nano Lett*, 2007. **7**(7): p. 2043-5.
143. Yajima, J., K. Mizutani, and T. Nishizaka, A torque component present in mitotic kinesin Eg5 revealed by three-dimensional tracking. *Nat Struct Mol Biol*, 2008. **15**(10): p. 1119-21.
144. Sun, Y., et al., Parallax: high accuracy three-dimensional single molecule tracking using split images. *Nano Lett*, 2009. **9**(7): p. 2676-82.
145. Sun, Y., et al., Single-molecule stepping and structural dynamics of myosin X. *Nat Struct Mol Biol*, 2010. **17**(4): p. 485-91.
146. Pavani, S.R., et al., Three-dimensional, single-molecule fluorescence imaging beyond the diffraction limit by using a double-helix point spread function. *Proc Natl Acad Sci USA*, 2009. **106**(9): p. 2995-9.

147. Thompson, M.A., et al., Localizing and tracking single nanoscale emitters in three dimensions with high spatiotemporal resolution using a double-helix point spread function. *Nano Lett*, 2010. **10**(1): p. 211-8.
148. Lang, M.C., J. Engelhardt, and S.W. Hell, 4Pi microscopy with linear fluorescence excitation. *Opt Lett*, 2007. **32**(3): p. 259-61.
149. Gustafsson, M.G., D.A. Agard, and J.W. Sedat, I5M: 3D widefield light microscopy with better than 100 nm axial resolution. *J Microscopy*, 1999. **195**(Pt 1): p. 10-6.
150. Hell, S.W. and J. Wichmann, Breaking the diffraction resolution limit by stimulated emission: stimulated-emission-depletion fluorescence microscopy. *Opt Lett*, 1994. **19**(11): p. 780-2.
151. Dyba, M., S. Jakobs, and S.W. Hell, Immunofluorescence stimulated emission depletion microscopy. *Nat Biotechnol*, 2003. **21**(11): p. 1303-4.
152. Bretschneider, S., C. Eggeling, and S.W. Hell, Breaking the diffraction barrier in fluorescence microscopy by optical shelving. *Phys Rev Lett*, 2007. **98**(21): p. 218103.
153. Folling, J., et al., Fluorescence nanoscopy by ground-state depletion and single-molecule return. *Nat Methods*, 2008. **5**(11): p. 943-5.
154. Heintzmann, R., T.M. Jovin, and C. Cremer, Saturated patterned excitation microscopy--a concept for optical resolution improvement. *J Opt Soc Am A Opt Image Sci Vis*, 2002. **19**(8): p. 1599-609.
155. Gustafsson, M.G., Nonlinear structured-illumination microscopy: wide-field fluorescence imaging with theoretically unlimited resolution. *Proc Natl Acad Sci USA*, 2005. **102**(37): p. 13081-6.
156. Willig, K.I., et al., Nanoscale resolution in GFP-based microscopy. *Nat Methods*, 2006. **3**(9): p. 721-3.
157. Schmidt, R., et al., Spherical nanosized focal spot unravels the interior of cells. *Nat Methods*, 2008. **5**(6): p. 539-44.
158. Schermelleh, L., et al., Subdiffraction multicolor imaging of the nuclear periphery with 3D structured illumination microscopy. *Science*, 2008. **320**(5881): p. 1332-6.

159. Kner, P., et al., Super-resolution video microscopy of live cells by structured illumination. *Nat Methods*, 2009. **6**(5): p. 339-42.
160. Keller, P.J., et al., Fast, high-contrast imaging of animal development with scanned light sheet-based structured-illumination microscopy. *Nat Methods*, 2010. **7**(8): p. 637-42.
161. Hell, S.W., Far-field optical nanoscopy. *Science*, 2007. **316**(5828): p. 1153-8.
162. Kasper, R., et al., Single-molecule STED microscopy with photostable organic fluorophores. *Small*, 2010. **6**(13): p. 1379-84.
163. Smolyaninov, II, Y.J. Hung, and C.C. Davis, Magnifying superlens in the visible frequency range. *Science*, 2007. **315**(5819): p. 1699-701.
164. Sun, M.G., et al., Correlated three-dimensional light and electron microscopy reveals transformation of mitochondria during apoptosis. *Nat Cell Biol*, 2007. **9**(9): p. 1057-65.
165. Sakon, J.J. and K.R. Weninger, Detecting the conformation of individual proteins in live cells. *Nat Methods*, 2010. **7**(3): p. 203-5.
166. Meisslitzer-Ruppitsch, C., et al., Photooxidation technology for correlated light and electron microscopy. *J Microscopy*, 2009. **235**(3): p. 322-35.
167. Min, W., et al., Imaging chromophores with undetectable fluorescence by stimulated emission microscopy. *Nature*, 2009. **461**(7267): p. 1105-9.
168. Pertsinidis, A., Y. Zhang, and S. Chu, Subnanometre single-molecule localization, registration and distance measurements. *Nature*, 2010. **466**(7306): p. 647-51.
169. Mortensen, K.I., et al., Optimized localization analysis for single-molecule tracking and super-resolution microscopy. *Nat Methods*, 2010. **7**(5): p. 377-81.
170. Elf, J., G.W. Li, and X.S. Xie, Probing transcription factor dynamics at the single-molecule level in a living cell. *Science*, 2007. **316**(5828): p. 1191-4.
171. Ohrt, T., et al., Fluorescence correlation spectroscopy and fluorescence cross-correlation spectroscopy reveal the cytoplasmic origination of

loaded nuclear RISC in vivo in human cells. *Nucleic Acids Res*, 2008. **36**(20): p. 6439-49.

172. Grunwald, D., R.H. Singer, and M. Rout, Nuclear export dynamics of RNA-protein complexes. *Nature*, 2011. **475**(7356): p. 333-41.
173. Leake, M.C., et al., Stoichiometry and turnover in single, functioning membrane protein complexes. *Nature*, 2006. **443**(7109): p. 355-8.
174. Pinaud, F., et al., Probing cellular events, one quantum dot at a time. *Nat Methods*, 2010. **7**(4): p. 275-85.
175. Babcock, H.P., C. Chen, and X. Zhuang, Using single-particle tracking to study nuclear trafficking of viral genes. *Biophys J*, 2004. **87**(4): p. 2749-58.
176. Itzkovitz, S. and A. van Oudenaarden, Validating transcripts with probes and imaging technology. *Nat Methods*, 2011. **8**(4 Suppl): p. S12-9.
177. Walter, N.G., Probing RNA structural dynamics and function by fluorescence resonance energy transfer (FRET). *Curr Protoc Nucleic Acid Chem*, 2003. **Chapter 11**: p. Unit 11 10.
178. Walter, N.G. and J.M. Burke, Fluorescence assays to study structure, dynamics, and function of RNA and RNA-ligand complexes. *Methods Enzymol*, 2000. **317**: p. 409-40.
179. Pinaud, F., et al., Dynamic partitioning of a glycosyl-phosphatidylinositol-anchored protein in glycosphingolipid-rich microdomains imaged by single-quantum dot tracking. *Traffic*, 2009. **10**(6): p. 691-712.
180. Saxton, M.J. and K. Jacobson, Single-particle tracking: applications to membrane dynamics. *Annu Rev Biophys Biomol Struct*, 1997. **26**: p. 373-99.
181. Kusumi, A., Y. Sako, and M. Yamamoto, Confined lateral diffusion of membrane receptors as studied by single particle tracking (nanovid microscopy). Effects of calcium-induced differentiation in cultured epithelial cells. *Biophys J*, 1993. **65**(5): p. 2021-40.
182. Ding, H., et al., Determination of the oligomer size of amyloidogenic protein beta-amyloid(1-40) by single-molecule spectroscopy. *Biophys J*, 2009. **97**(3): p. 912-21.

183. Chung, S.H. and R.A. Kennedy, Forward-backward non-linear filtering technique for extracting small biological signals from noise. *J Neurosci Methods*, 1991. **40**(1): p. 71-86.
184. Karnani, N., et al., Genomic study of replication initiation in human chromosomes reveals the influence of transcription regulation and chromatin structure on origin selection. *Mol Biol Cell*, 2010. **21**(3): p. 393-404.
185. Barrett, T., et al., NCBI GEO: archive for functional genomics data sets--10 years on. *Nucleic Acids Res*, 2011. **39**(Database issue): p. D1005-10.
186. Landgraf, P., et al., A mammalian microRNA expression atlas based on small RNA library sequencing. *Cell*, 2007. **129**(7): p. 1401-14.
187. Allawi, H.T., et al., Quantitation of microRNAs using a modified Invader assay. *RNA*, 2004. **10**(7): p. 1153-61.
188. Neilson, J.R., et al., Dynamic regulation of miRNA expression in ordered stages of cellular development. *Genes Dev*, 2007. **21**(5): p. 578-89.
189. Leung, A.K., J.M. Calabrese, and P.A. Sharp, Quantitative analysis of Argonaute protein reveals microRNA-dependent localization to stress granules. *Proc Natl Acad Sci USA*, 2006. **103**(48): p. 18125-30.
190. Aizer, A., et al., The dynamics of mammalian P body transport, assembly, and disassembly in vivo. *Mol Biol Cell*, 2008. **19**(10): p. 4154-66.
191. Chan, H.M., et al., Direct quantification of single-molecules of microRNA by total internal reflection fluorescence microscopy. *Anal Chem*, 2010. **82**(16): p. 6911-8.
192. Husale, S., H.H. Persson, and O. Sahin, DNA nanomechanics allows direct digital detection of complementary DNA and microRNA targets. *Nature*, 2009. **462**(7276): p. 1075-8.
193. Neely, L.A., et al., A single-molecule method for the quantitation of microRNA gene expression. *Nat Methods*, 2006. **3**(1): p. 41-6.
194. Lu, J. and A. Tsourkas, Imaging individual microRNAs in single mammalian cells in situ. *Nucleic Acids Res*, 2009. **37**(14): p. e100.

195. Grunwald, D., et al., Probing intranuclear environments at the single-molecule level. *Biophys J*, 2008. **94**(7): p. 2847-58.
196. Petersen, C.P., et al., Short RNAs repress translation after initiation in mammalian cells. *Mol Cell*, 2006. **21**(4): p. 533-42.
197. Fabian, M.R., et al., Mammalian miRNA RISC recruits CAF1 and PABP to affect PABP-dependent deadenylation. *Mol Cell*, 2009. **35**(6): p. 868-80.
198. Schaeffer, D. and A. van Hoof, Different nuclease requirements for exosome-mediated degradation of normal and nonstop mRNAs. *Proc Natl Acad Sci USA*, 2011. **108**(6): p. 2366-71.
199. Steiger, M., et al., Analysis of recombinant yeast decapping enzyme. *RNA*, 2003. **9**(2): p. 231-8.
200. Jinek, M., S.M. Coyle, and J.A. Doudna, Coupled 5' nucleotide recognition and processivity in Xrn1-mediated mRNA decay. *Mol Cell*, 2011. **41**(5): p. 600-8.
201. Bashkirov, V.I., et al., A mouse cytoplasmic exoribonuclease (mXRN1p) with preference for G4 tetraplex substrates. *J Cell Biol*, 1997. **136**(4): p. 761-73.
202. van Dijk, E., et al., Human Dcp2: a catalytically active mRNA decapping enzyme located in specific cytoplasmic structures. *EMBO J*, 2002. **21**(24): p. 6915-24.
203. Ingelfinger, D., et al., The human LSm1-7 proteins colocalize with the mRNA-degrading enzymes Dcp1/2 and Xrnl in distinct cytoplasmic foci. *RNA*, 2002. **8**(12): p. 1489-501.
204. Sheth, U. and R. Parker, Targeting of aberrant mRNAs to cytoplasmic processing bodies. *Cell*, 2006. **125**(6): p. 1095-109.
205. Erickson, S.L. and J. Lykke-Andersen, Cytoplasmic mRNP granules at a glance. *J Cell Sci*, 2011. **124**(Pt 3): p. 293-7.
206. Kedersha, N., et al., Stress granules and processing bodies are dynamically linked sites of mRNP remodeling. *J Cell Biol*, 2005. **169**(6): p. 871-84.

207. Yang, Z., et al., GW182 is critical for the stability of GW bodies expressed during the cell cycle and cell proliferation. *J Cell Sci*, 2004. **117**(Pt 23): p. 5567-78.
208. Chekulaeva, M., et al., miRNA repression involves GW182-mediated recruitment of CCR4-NOT through conserved W-containing motifs. *Nat Struct Mol Biol*, 2011. **18**(11): p. 1218-26.
209. Fabian, M.R., et al., miRNA-mediated deadenylation is orchestrated by GW182 through two conserved motifs that interact with CCR4-NOT. *Nat Struct Mol Biol*, 2011. **18**(11): p. 1211-7.
210. Chu, C.Y. and T.M. Rana, Translation repression in human cells by microRNA-induced gene silencing requires RCK/p54. *PLoS Biol* 2006. **4**(7): p. e210.
211. Pauley, K.M., et al., Formation of GW bodies is a consequence of microRNA genesis. *EMBO rep*, 2006. **7**(9): p. 904-10.
212. Jakymiw, A., et al., Disruption of GW bodies impairs mammalian RNA interference. *Nat Cell Biol*, 2005. **7**(12): p. 1267-74.
213. Bhattacharyya, S.N., et al., Relief of microRNA-mediated translational repression in human cells subjected to stress. *Cell*, 2006. **125**(6): p. 1111-24.
214. Ma, J., et al., MicroRNA activity is suppressed in mouse oocytes. *Curr Biol*, 2010. **20**(3): p. 265-70.
215. Suh, N., et al., MicroRNA function is globally suppressed in mouse oocytes and early embryos. *Curr Biol*, 2010. **20**(3): p. 271-7.
216. Liu, J., et al., A role for the P-body component GW182 in microRNA function. *Nat Cell Biol*, 2005. **7**(12): p. 1261-6.
217. Zhuang, X., et al., Fluorescence quenching: A tool for single-molecule protein-folding study. *Proc Natl Acad Sci USA*, 2000. **97**(26): p. 14241-4.
218. Grimson, A., et al., MicroRNA targeting specificity in mammals: determinants beyond seed pairing. *Mol Cell*, 2007. **27**(1): p. 91-105.

219. Lewis, B.P., C.B. Burge, and D.P. Bartel, Conserved seed pairing, often flanked by adenosines, indicates that thousands of human genes are microRNA targets. *Cell*, 2005. **120**(1): p. 15-20.
220. Lewis, B.P., et al., Prediction of mammalian microRNA targets. *Cell*, 2003. **115**(7): p. 787-98.
221. Lai, E.C., B. Tam, and G.M. Rubin, Pervasive regulation of Drosophila Notch target genes by GY-box-, Brd-box-, and K-box-class microRNAs. *Genes Dev*, 2005. **19**(9): p. 1067-80.
222. Hammond, S.M. and N.E. Sharpless, HMGA2, microRNAs, and stem cell aging. *Cell*, 2008. **135**(6): p. 1013-6.
223. Johnston, R.J., Jr., et al., MicroRNAs acting in a double-negative feedback loop to control a neuronal cell fate decision. *Proc Natl Acad Sci USA*, 2005. **102**(35): p. 12449-54.
224. Tsang, J., J. Zhu, and A. van Oudenaarden, MicroRNA-mediated feedback and feedforward loops are recurrent network motifs in mammals. *Mol Cell*, 2007. **26**(5): p. 753-67.
225. Broderick, J.A., et al., Argonaute protein identity and pairing geometry determine cooperativity in mammalian RNA silencing. *RNA*, 2011. **17**(10): p. 1858-69.
226. Mayr, C. and D.P. Bartel, Widespread shortening of 3'UTRs by alternative cleavage and polyadenylation activates oncogenes in cancer cells. *Cell*, 2009. **138**(4): p. 673-84.
227. Sandberg, R., et al., Proliferating cells express mRNAs with shortened 3' untranslated regions and fewer microRNA target sites. *Science*, 2008. **320**(5883): p. 1643-7.
228. Saetrom, P., et al., Distance constraints between microRNA target sites dictate efficacy and cooperativity. *Nucleic Acids Res*, 2007. **35**(7): p. 2333-42.
229. Wang, B., et al., Recapitulation of short RNA-directed translational gene silencing in vitro. *Mol Cell*, 2006. **22**(4): p. 553-60.

230. Newby Lambert, M., et al., Mg2+-induced compaction of single RNA molecules monitored by tethered particle microscopy. *Biophys J*, 2006. **90**(10): p. 3672-85.
231. Rawlings, R.A., V. Krishnan, and N.G. Walter, Viral RNAi suppressor reversibly binds siRNA to outcompete Dicer and RISC via multiple turnover. *J Mol Biol*, 2011. **408**(2): p. 262-76.
232. Wang, B., J.G. Doench, and C.D. Novina, Analysis of microRNA effector functions in vitro. *Methods*, 2007. **43**(2): p. 91-104.
233. Abelson, J., et al., Conformational dynamics of single pre-mRNA molecules during in vitro splicing. *Nat Struct Mol Biol*, 2010. **17**(4): p. 504-12.
234. Petri, S., et al., Increased siRNA duplex stability correlates with reduced off-target and elevated on-target effects. *RNA*, 2011. **17**(4): p. 737-49.
235. Long, D., et al., Potent effect of target structure on microRNA function. *Nat Struct Mol Biol*, 2007. **14**(4): p. 287-94.
236. Marin, R.M. and J. Vanicek, Efficient use of accessibility in microRNA target prediction. *Nucleic Acids Res*, 2011. **39**(1): p. 19-29.
237. Ameres, S.L., J. Martinez, and R. Schroeder, Molecular basis for target RNA recognition and cleavage by human RISC. *Cell*, 2007. **130**(1): p. 101-12.
238. Hutvagner, G. and P.D. Zamore, A microRNA in a multiple-turnover RNAi enzyme complex. *Science*, 2002. **297**(5589): p. 2056-60.
239. Chen, X., et al., Characterization of microRNAs in serum: a novel class of biomarkers for diagnosis of cancer and other diseases. *Cell Res*, 2008. **18**(10): p. 997-1006.
240. Heo, I. and V.N. Kim, Regulating the regulators: posttranslational modifications of RNA silencing factors. *Cell*, 2009. **139**(1): p. 28-31.
241. Heo, I., et al., TUT4 in concert with Lin28 suppresses microRNA biogenesis through pre-microRNA uridylation. *Cell*, 2009. **138**(4): p. 696-708.

242. Wu, D., A.T. Lamm, and A.Z. Fire, Competition between ADAR and RNAi pathways for an extensive class of RNA targets. *Nat Struct Mol Biol*, 2011. **18**(10): p. 1094-101.
243. Kawahara, Y., et al., Redirection of silencing targets by adenosine-to-inosine editing of miRNAs. *Science*, 2007. **315**(5815): p. 1137-40.
244. Blume, A.J., D. Lichtshtein, and G. Boone, Coupling of opiate receptors to adenylate cyclase: requirement for Na+ and GTP. *Proc Natl Acad Sci USA*, 1979. **76**(11): p. 5626-30.
245. North, R.A., et al., Mu and delta receptors belong to a family of receptors that are coupled to potassium channels. *Proc Natl Acad Sci USA*, 1987. **84**(15): p. 5487-91.
246. Waldhoer, M., S.E. Bartlett, and J.L. Whistler, Opioid receptors. *Annu Rev Biochem*, 2004. **73**: p. 953-90.
247. Bai, M., Dimerization of G-protein-coupled receptors: roles in signal transduction. *Cell Signal*, 2004. **16**(2): p. 175-86.
248. Milligan, G., et al., The role of GPCR dimerisation/oligomerisation in receptor signalling. *Ernst Schering Foundation Symposium Proceedings*, 2006(2): p. 145-61.
249. George, S.R., et al., Oligomerization of mu- and delta-opioid receptors. Generation of novel functional properties. *J Biol Chem*, 2000. **275**(34): p. 26128-35.
250. Gomes, I., et al., Oligomerization of opioid receptors. *Methods*, 2002. **27**(4): p. 358-65.
251. Gomes, I., et al., Heterodimerization of mu and delta opioid receptors: A role in opiate synergy. *J Neurosci*, 2000. **20**(22): p. RC110.
252. Martin, N.A. and P.L. Prather, Interaction of co-expressed mu- and delta-opioid receptors in transfected rat pituitary GH(3) cells. *Mol Pharm*, 2001. **59**(4): p. 774-83.
253. Wang, D., et al., Opioid receptor homo- and heterodimerization in living cells by quantitative bioluminescence resonance energy transfer. *Mol Pharm*, 2005. **67**(6): p. 2173-84.

254. Banerjee, S., T. Huber, and T.P. Sakmar, Rapid incorporation of functional rhodopsin into nanoscale apolipoprotein bound bilayer (NABB) particles. *J Mol Biol*, 2008. **377**(4): p. 1067-81.
255. Bayburt, T.H., et al., Transducin activation by nanoscale lipid bilayers containing one and two rhodopsins. *J Biol Chem*, 2007. **282**(20): p. 14875-81.
256. Leitz, A.J., et al., Functional reconstitution of Beta2-adrenergic receptors utilizing self-assembling Nanodisc technology. *BioTechniques*, 2006. **40**(5): p. 601-2, 604, 606, passim.
257. Nath, A., W.M. Atkins, and S.G. Sligar, Applications of phospholipid bilayer nanodiscs in the study of membranes and membrane proteins. *Biochemistry*, 2007. **46**(8): p. 2059-69.
258. Whorton, M.R., et al., A monomeric G protein-coupled receptor isolated in a high-density lipoprotein particle efficiently activates its G protein. *Proc Natl Acad Sci USA*, 2007. **104**(18): p. 7682-7.
259. Whorton, M.R., et al., Efficient coupling of transducin to monomeric rhodopsin in a phospholipid bilayer. *J Biol Chem*, 2008. **283**(7): p. 4387-94.
260. Fotiadis, D., et al., Atomic-force microscopy: Rhodopsin dimers in native disc membranes. *Nature*, 2003. **421**(6919): p. 127-8.
261. Jastrzebska, B., et al., Functional and structural characterization of rhodopsin oligomers. *J Biol Chem*, 2006. **281**(17): p. 11917-22.
262. Liang, Y., et al., Organization of the G protein-coupled receptors rhodopsin and opsin in native membranes. *J Biol Chem*, 2003. **278**(24): p. 21655-62.
263. Schaffner, W. and C. Weissmann, A rapid, sensitive, and specific method for the determination of protein in dilute solution. *Anal Biochem*, 1973. **56**(2): p. 502-14.
264. Carman, C.V., et al., Selective regulation of Galpha(q/11) by an RGS domain in the G protein-coupled receptor kinase, GRK2. *J Biol Chem*, 1999. **274**(48): p. 34483-92.

265. Patil, P.V. and D.P. Ballou, The use of protocatechuate dioxygenase for maintaining anaerobic conditions in biochemical experiments. *Anal Biochem*, 2000. **286**(2): p. 187-92.
266. Alt, A., et al., Stimulation of guanosine-5'-O-(3-[35S]thio)triphosphate binding by endogenous opioids acting at a cloned mu receptor. *J Pharm Exp Ther*, 1998. **286**(1): p. 282-8.
267. Clark, M.J., et al., Comparison of the relative efficacy and potency of mu-opioid agonists to activate Galpha(i/o) proteins containing a pertussis toxin-insensitive mutation. *J Pharm Exp Ther*, 2006. **317**(2): p. 858-64.
268. Emmerson, P.J., et al., Characterization of opioid agonist efficacy in a C6 glioma cell line expressing the mu opioid receptor. *J Pharm Exp Ther*, 1996. **278**(3): p. 1121-7.
269. Frances, B., C. Moisand, and J.C. Meunier, Na+ ions and Gpp(NH)p selectively inhibit agonist interactions at mu- and kappa-opioid receptor sites in rabbit and guinea-pig cerebellum membranes. *Eur J Pharm*, 1985. **117**(2): p. 223-32.
270. Kenakin, T., Principles: receptor theory in pharmacology. *Trends Pharm Sci*, 2004. **25**(4): p. 186-92.
271. Ott, S. and T. Costa, Guanine nucleotide-mediated inhibition of opioid agonist binding. Modulatory effects of ions and of receptor occupancy. *Bioch Pharm*, 1989. **38**(12): p. 1931-9.
272. Richardson, A., C. Demoliou-Mason, and E.A. Barnard, Guanine nucleotide-binding protein-coupled and -uncoupled states of opioid receptors and their relevance to the determination of subtypes. *Proc Natl Acad Sci USA*, 1992. **89**(21): p. 10198-202.
273. Werling, L.L., P.S. Puttfarcken, and B.M. Cox, Multiple agonist-affinity states of opioid receptors: regulation of binding by guanyl nucleotides in guinea pig cortical, NG108-15, and 7315c cell membranes. *Mol Pharm*, 1988. **33**(4): p. 423-31.

274. Rosenbaum, D.M., et al., GPCR engineering yields high-resolution structural insights into beta2-adrenergic receptor function. *Science*, 2007. **318**(5854): p. 1266-73.
275. Cho, T.M., B.L. Ge, and H.H. Loh, Isolation and purification of morphine receptor by affinity chromatography. *Life Sci*, 1985. **36**(11): p. 1075-85.
276. Ramon, E., et al., Effect of dodecyl maltoside detergent on rhodopsin stability and function. *Vision Res* 2003. **43**(28): p. 3055-61.
277. Cvejic, S. and L.A. Devi, Dimerization of the delta opioid receptor: implication for a role in receptor internalization. *J Biol Chem*, 1997. **272**(43): p. 26959-64.
278. Jordan, B.A. and L.A. Devi, G-protein-coupled receptor heterodimerization modulates receptor function. *Nature*, 1999. **399**(6737): p. 697-700.
279. Levac, B.A., B.F. O'Dowd, and S.R. George, Oligomerization of opioid receptors: generation of novel signaling units. *Curr Opin Pharm*, 2002. **2**(1): p. 76-81.
280. Milligan, G., G protein-coupled receptor dimerization: function and ligand pharmacology. *Mol Pharm*, 2004. **66**(1): p. 1-7.
281. Gioannini, T.L., et al., Purification of an active opioid-binding protein from bovine striatum. *J Biol Chem*, 1985. **260**(28): p. 15117-21.
282. Li, L.Y., et al., Purification of opioid receptor in the presence of sodium ions. *Life sciences*, 1992. **51**(15): p. 1177-85.
283. Massotte, D., et al., Characterization of delta, kappa, and mu human opioid receptors overexpressed in baculovirus-infected insect cells. *J Biol Chem*, 1997. **272**(32): p. 19987-92.
284. Obermeier, H., A. Wehmeyer, and R. Schulz, Expression of mu-, delta- and kappa-opioid receptors in baculovirus-infected insect cells. *Eur J Pharm*, 1996. **318**(1): p. 161-6.
285. Talmont, F., et al., Expression and pharmacological characterization of the human mu-opioid receptor in the methylotrophic yeast Pichia pastoris. *FEBS Letters*, 1996. **394**(3): p. 268-72.

286. Sarramegna, V., et al., Optimizing functional versus total expression of the human mu-opioid receptor in Pichia pastoris*. Protein Express Purif*, 2002. **24**(2): p. 212-20.
287. Sarramegna, V., et al., Solubilization, purification, and mass spectrometry analysis of the human mu-opioid receptor expressed in Pichia pastoris*. Protein Express Purif*, 2005. **43**(2): p. 85-93.
288. Sarramegna, V., et al., Green fluorescent protein as a reporter of human mu-opioid receptor overexpression and localization in the methylotrophic yeast Pichia pastoris*. J Biotechnol*, 2002. **99**(1): p. 23-39.
289. Guan, X.M., T.S. Kobilka, and B.K. Kobilka, Enhancement of membrane insertion and function in a type IIIb membrane protein following introduction of a cleavable signal peptide*. J Biol Chem*, 1992. **267**(31): p. 21995-8.
290. Lee, Y.S. and A. Dutta, The tumor suppressor microRNA let-7 represses the HMGA2 oncogene*. Genes Dev*, 2007. **21**(9): p. 1025-30.
291. Friedman, R.C., et al., Most mammalian mRNAs are conserved targets of microRNAs*. Genome Res* 2009. **19**(1): p. 92-105.
292. Licatalosi, D.D., et al., HITS-CLIP yields genome-wide insights into brain alternative RNA processing*. Nature*, 2008. **456**(7221): p. 464-9.
293. Orom, U.A. and A.H. Lund, Isolation of microRNA targets using biotinylated synthetic microRNAs*. Methods*, 2007. **43**(2): p. 162-5.
294. Orom, U.A., F.C. Nielsen, and A.H. Lund, MicroRNA-10a binds the 5'UTR of ribosomal protein mRNAs and enhances their translation*. Mol Cell*, 2008. **30**(4): p. 460-71.
295. Chi, S.W., et al., Argonaute HITS-CLIP decodes microRNA-mRNA interaction maps*. Nature*, 2009. **460**(7254): p. 479-86.
296. Easow, G., A.A. Teleman, and S.M. Cohen, Isolation of microRNA targets by miRNP immunopurification*. RNA*, 2007. **13**(8): p. 1198-204.
297. Andachi, Y., A novel biochemical method to identify target genes of individual microRNAs: identification of a new Caenorhabditis elegans let-7 target*. RNA*, 2008. **14**(11): p. 2440-51.

298. Ule, J., et al., CLIP: a method for identifying protein-RNA interaction sites in living cells. *Methods*, 2005. **37**(4): p. 376-86.